Families of control-volume distributed CVD (MPFA) finite volume schemes for the porous medium pressure equation on structured and unstructured grids.

Pal, Mayur

Families of Control-Volume Distributed CVD(MPFA) Finite Volume Schemes for the Porous Medium Pressure Equation on Structured and Unstructured Grids

Mayur Pal

Thesis submitted to the University of Wales Swansea
in candidature for the degree of Doctor of Philosophy

September 30^{th} 2007

Civil and Computational Engineering Centre
School of Engineering
University of Wales Swansea
Singleton Park, Swansea SA2 8PP
Wales, United Kingdom

ProQuest LLC.
789 East Eisenhower Parkway
P.O. Box 1346
Ann Arbor, MI 48106 – 1346

DECLARATION

This work has not previously been accepted in substance for any degree and is not being concurrently submitted in candidature for any degree.

Signed .. (Candidate)
Date.....2007-12-18.....

STATEMENT 1

This dissertation is being submitted in partial fulfilment of the requirements for the degree of PhD in the School of Engineering.

Signed . (Candidate)
Date.....2007-12-18.....

STATEMENT 2

This dissertation is the result of my own independent work/investigation, except where otherwise stated. Other sources are acknowledged by footnotes giving explicit references. A bibliography is appended.

Signed . (Candidate)
Date.....2007-12-18.....

STATEMENT 3

I hereby give my consent for my dissertation, if accepted, to be available for photocopying and interlibrary loan, and for the title and summary to be made available to outside organisations.

Signed . (Candidate)
Date.....2007-12-18.....

Families of Control-Volume Distributed CVD(MPFA) Finite Volume Schemes for the Porous Medium Pressure Equation on Structured and Unstructured Grids

Mayur Pal

What I have accomplished in life, is the result of the unconditional love and years of hard work and sacrifice of my loving parents, Namita and Randhir Singh Pal.

To my mother and father.

"I have nothing new to teach the world. Truth and non-violence are as old as hills." M.K. Gandhi

Contents

Acknowledgments

I am very grateful to my supervisor Dr Michael G. Edwards for his support, encouragement and guidance during all stages of my research. I have enjoyed working with him and the research discussions with him. It has been a great privilege to have worked under tutelage of such an accomplished academic and kind gentleman. I thank him especially for the confidence he had in me and allowing me to explore freely various areas related to my research.

I wish to thank all my friends in the department whose company has been very valuable in making my stay at Swansea a very pleasant one. I will specially like to thank my friends Derek, Sadok, Maziar, and Hongwen for giving me company during late hours of my PhD work. The staff at the School of Engineering has been fabulous. They have always been there to assist me with all administrative matter. I am also thankful to Exxon-Mobil for the financial support for my research.

Finally, My deepest gratitude goes to all my family for their help and moral support during my studies. It is the love of my wife, Disha which had made it possible, Disha has been very supportive through the difficult and enjoyable days we both have gone through. My parents, Namita and Randhir have inspired me to work hard and aim for the best. Thankyou for being there for me in times of need and advice, thankyou also for sharing with me in times of joy and celebration.

Summary

In this thesis, families of flux-continuous, locally conservative, finite-volume schemes are presented for solving the general geometry-permeability tensor pressure equation on structured and unstructured grids in two and three dimensions. The families of flux-continuous schemes have also been referred to in the literature as Multi-point Flux Approximation or MPFA schemes. The schemes are applicable to the general tensor pressure equation with discontinuous coefficients and remove the $O(1)$ errors introduced by standard reservoir simulation (two-point flux) schemes when applied to full, anisotropic and asymmetric permeability tensor flow approximation [1, 2, 3]. Such tensors may arise when fine scale permeability distributions are upscaled to obtain gridblock-scale permeability distributions.

A family of schemes is quantified by a quadrature parametrization where the position of continuity defines the quadrature and hence the family. In this work the family of flux-continuous schemes is presented in *Physical* space and *Transform* space, and has been tested for a range of quadrature points. A series of numerical test cases are presented and a numerical convergence study is conducted for the family of schemes using different types of two and three dimensional structured and unstructured grids. Specific quadrature points have been observed to yield improved convergence for the family of flux-continuous schemes on structured and unstructured grids in two and three dimensions.

This work also presents a complete extension of the family of control-volume distributed (CVD) multi-point flux approximation (MPFA) flux-continuous schemes for general three dimensional grids comprising of different element types e.g., hexahedra, tetrahedra, prism and pyramid. Discretization principles are presented for each element. The pyramid element is shown to be a special case with unique construction of the continuity conditions. The Darcy flux approximations are applied to a range

of test cases that verify consistency of the schemes. Convergence tests of the three-dimensional families of schemes are presented, with emphasis on use of quadrature parameterization.

A new family of locally conservative cell-centred flux-continuous schemes is presented for quadrilateral grids. The new family is defined by introducing a piecewise constant general geometry-permeability tensor approximation over the subcells of the control-volumes and ensures that the local discrete general-tensor is elliptic. A family of control-volume distributed subcell flux-continuous schemes is defined in terms of a quadrature parametrization, where the local position of flux continuity defines the quadrature point and each particular scheme. The subcell tensor approximation ensures that a symmetric positive definite discretization matrix is obtained for the base member of the formulation. The physical-space scheme has been shown to be non-symmetric for general quadrilateral cells [4]. A numerical convergence study of the schemes shows that the subcell tensor approximation reduces solution errors when compared to the cell-wise tensor scheme, and the subcell tensor approximation using the control-volume face geometry yields the best results. A particular quadrature point is found to improve numerical convergence of the subcell schemes for the cases tested [5].

When applying the family of flux-continuous schemes to strongly anisotropic heterogeneous media they can fail to satisfy a maximum principle (as with other FEM and finite-volume methods) and result in loss of solution monotonicity for high (full-tensor) anisotropy ratios causing spurious oscillations in the numerical pressure solution. In this work methods for obtaining optimal discretization with minimal spurious oscillations are investigated and the use of flux-splitting techniques [6] is extended to solve the discrete system for the problems with high anisotropy ratios to improve solution monotonicity [7, 8]. Flux-splitting schemes are presented together with a series of numerical results for test-cases with strong anisotropy ratios. In all cases the resulting numerical pressure solutions are free of spurious oscillations. Monotonicity

issues are also discussed and tests performed confirm optimal monotonicity of the schemes as determined by an M-matrix analysis [2, 3, 9, 10, 11].

This thesis also presents a double (q_1, q_2)-family of flux continuous schemes. Where, the double q_1, q_2-family is quantified by choosing a different quadrature parametrization or quadrature q on different faces of the sub-cell control-volume leading to a variable support scheme [10]. M-matrix analysis for double families [10] is then used to show a key result for general nine-point schemes, which exposes the limits on the schemes for ensuring solution monotonicity. The analysis is used to determine the upper limits for obtaining monotonic solutions and to aid the design of schemes that minimize the occurrence of spurious oscillations in the discrete pressure field.

Finally, the study of a locally conservative family of schemes is applied to upscaling. Equivalent upscaled permeability is used as a measure of performance of the family of schemes[12]. A series of upscaling examples is presented and convergence tests are performed for different upscaling techniques. Again the benefits of using the quadrature parametrization q are highlighted.

List of Figures

List of Tables

Chapter 1

Introduction and Background

1.1 What is Reservoir Simulation ?

Reservoir simulation is that process whereby the behavior of a hydrocarbon reservoir is inferred from the behavior of a mathematical model which describes it [13, 14]. The degree to which the model duplicates the actual reservoir is a function primarily of the input data used, and secondly the adequacy of the model to simulate the physical system.

1.1.1 A Brief Historical Overview

For many decades after the 1859, recognized as the beginning of our domestic oil industry, history reveals that finding and producing oil was conducted on a basis of feast or famine. The technologist was absent from the scene and it was not until the 1930s that people in the oil industry started looking at reservoir mechanics in any kind of a scientific way.

Reservoir simulators were first built as diagnostic tools for understanding reservoirs that yielded surprising or odd flow characteristics over years of production. The earliest simulators were physical models, such as sandboxes with clear glass sides for

viewing fluid flow, and analog devices that modeled fluid flow with electrical current flow [15]. These models, first documented in the 1930s, were constructed by researchers in an attempt to understand why water starts to be produced with oil and why the produced water-oil ratio increases with time [16, 17].

Some things haven't changed since the 1930s. Today's reservoir simulator generally solve the same equation studied 70 years ago-Material balance and Darcy's Law [14, 18, 19]. But other aspects of simulation have changed dramatically. With the advent of digital computers in the 1960s, reservoir modeling advanced from tanks filled with sand or electrolyte to numerical simulators. In numerical simulators, the reservoir is represented by a series of interconnected blocks, and the flow between the blocks is solved numerically. In the early days of reservoir simulation, computers had limited speed and memory, limiting the number of blocks that could be used. This required simplification of the reservoir model and allowed simulation to proceed with relatively small amount of input data.

The current state of the art in reservoir simulation is directly related to high speed computers, robust and efficient numerical techniques. There is no other way in which complex numerical calculations necessary to describe multi-phase flow in porous media can be performed economically or even realistically. Increased computer power has enabled engineers to create bigger, more geologically realistic models requiring much greater data input. This demand has been met by the creating of increasingly complex and efficient simulation programs. Computational efficiency has reached a stage that allows powerful simulation to be run frequently. Numerical simulation has become a reservoir management tool for all stages in the life of a reservoir.

1.1.2 Reservoir Simulation and Numerical Discretization

Petroleum reservoir simulation involves the use of numerical methods to obtain the solution of mass and /or energy conservation equations (in integral or partial differential form) governing fluid and /or heat flow in petroleum reservoirs. Any such

numerical procedure requires numerical discretization techniques. Hence, the Numerical discretization techniques have always been an integral part of reservoir simulation. The need for accurate and realistic reservoir simulation has always driven the field of research and development of efficient and robust numerical discretization techniques for reservoir simulation. There exists a number of different numerical discretization approaches which are used in reservoir simulation. One such approach is the Finite volume method (FVM). The main subject of this thesis is the use of flux-continuous finite-volume numerical discretization techniques for the reservoir simulation pressure equation. In this thesis, the finite volume formulation is used, to provide the general framework for the development of a number of novel and appealing schemes in the field of petroleum reservoir simulation. Most of the existing numerical reservoir simulators employ a pressure equation approximation that assumes a diagonal isotropic or anisotropic permeability tensor. A class of new schemes, which are called control-volume distributed multi-point flux approximations CVD(MPFA) are applicable to general geometry with diagonal of full permeability tensors and have been shown to give excellent results with removal of $O(1)$ errors introduced by standard schemes when applied to problems involving general full tensors in the pressure equation [1, 2, 9, 20, 3, 21, 6, 4, 22, 23, 5, 24, 12, 7, 8, 25, 10].

1.1.3 Recent Developments in Reservoir Simulation

Three basic problem areas have dominated much of the recent research in reservoir simulation.

First, the need for an effective model to describe the complex fluid and rock interactions that control recovery processes. Simulators are severely hampered by the lack of knowledge of reservoir properties, heterogeneities, and relevant length scales and of important mechanisms like diffusion, dispersion, and viscous instabilities. Russell and Wheeler [26] and Young [27] present excellent surveys of the influence of dispersion and attempts to incorporate it in present reservoir simulators. Since

the mixing and velocity variations are influenced at all relevant length scales by the heterogeneous properties of reservoir, there is a need for volume averaging of terms like porosity and permeability. Recently, developments have been made in homogenization [28, 29], renormalization [30, 20], scaled averaging [31], upscaling [32, 33], multi-scale methods [34, 35, 36, 37], and statistical methods have also been explored to obtain effective permeability [38, 39]. A review of different upscaling techniques used in petroleum reservoir simulation is also presented in [40]. Also, simulators are now used as an experimental tool to develop methods to model the interrelations between localized and large scale media effects.

Next, the need to develop accurate discretization techniques that retain the important physical properties of the continuous models. Recently, a variety of new discretization techniques have been developed for both the pressure and transport equations. Discontinuous Galerkin (DG)[41, 42], Mixed finite elements (MFEM) and related methods [26, 43, 44, 45, 46, 47, 48, 49, 50], and finite volume methods (FVM) [2, 9, 3, 21, 4, 51, 52, 53, 54, 55, 56] are being used to yield accurate mass-conservative approximations to the pressure and Darcy velocity of the fluid. Eulerian-Lagrangian techniques [57, 58, 59] have also been developed that not only conserve mass but also take advantages of the computed flow of the fluids to accurately model the transport phenomena and simultaneously symmetrize the model equations. Adaptive local grid refinement in space and time [60], [61] can be controlled by A posteriori error estimators. Then multi-grid or multilevel iterative techniques [62, 63] can be used to efficiently solve the discrete systems.

Finally, the need to develop efficient numerical solution algorithms that utilize the potential of the emerging computing architectures. Major potential advantages in computing lie in emerging parallel computer architectures and use of parallel computation for Large-Scale Reservoir Simulation[64]. Techniques such as domain decomposition e.g. [65], [66] that naturally split the big problem into smaller pieces to be addressed separately on distinct processors, which also allows modularized lo-

cal grid refinement and can play a significant role in developing effective and robust simulation codes.

1.2 Scope of Work and Research Contribution

The work documented in this thesis constituted a number of developments in numerical discretization techniques for the subsurface reservoir simulation pressure equation. A study of existing numerical discretization techniques was carried out. The advantages and limitations of some of these formulations are discussed and analyzed in this work with the help of numerical tests.

The major objective of this thesis is to address the important aspects of the existing families of control-volume distributed multi-point flux CVD(MPFA) finite volume approximation schemes [2, 3, 4, 5] employed for the solution of porous media pressure equation. And to extend the formulation of the families of CVD-MPFA schemes to overcome some existing limitations. The main contributions of this research work can be summarized as follows:

(i) A detailed numerical error convergence study for *Physical* and *Transform* space formulation of the families of CVD(MPFA) schemes was carried out on different types of 2D and 3D structured and unstructured grids, with emphasis on quadrature parametrization (where quadrature defines the point of flux-continuity and hence the family of scheme) [5, 12, 7, 25].

(ii) An extension of the family of CVD(MPFA) schemes in three dimensions is presented for different element types including hexahedra, tetrahedra, pyramid and prism, thereby providing flexibility in application of schemes for general geometry. Details of the formulation (in *Physical Space*) are documented and a series of cases are tested for numerical convergence [5, 12, 7, 8, 25].

(iii) Pressure field monotonicity issues are discussed for the families of CVD(MPFA)

schemes and novel methods are proposed for obtaining monotonic solutions with use of flux-splitting and specific discretization techniques based on choice of quadrature parameterization[7, 8, 25, 10].

The research outputs during the entire course of study period were documented and a number of publications, as a result, originated or are forthcoming and are listed in the bibliography of this thesis.

1.3 Organization of the Thesis

The thesis is subdivided into ten chapters, including an introduction and conclusion. The synopsis of each chapter is as follows:

Chapter 2 presents a brief review of previous work on flux-continuous finite volume numerical discretization schemes employed in petroleum reservoir simulation. Limitations of classical/standard five-point flux continuous finite volume schemes are discussed. The families of CVD(MPFA) schemes are introduced and recent advances for the family of CVD(MPFA) schemes are discussed.

The single and multi-phase flow mass conservation equations for fluid flow in porous media are presented in Chapter 3. Description of the problem to be solved with specified boundary conditions is also presented in this chapter.

Chapter 4 presents an overview of some of the existing numerical discretization techniques. Some of the methods mentioned include the finite difference method (FDM), the finite element method (FEM), the mixed finite element method (MFEM) and the finite volume method (FVM).

Chapter 5 is the largest chapter of this thesis, and is solely dedicated to the construction, analysis and testing of the family of control-volume distributed multi-point flux approximation CVD(MPFA) flux-continuous finite volume schemes for numerical discretization of elliptic pressure equation. Here, the discussion starts with essential fundamentals of finite-volume schemes. An overview of standard five-point

flux-continuous scheme is presented. Fundamentals of the family of schemes are presented with description of quadrature parametrization which essentially defines the family of schemes. Numerical formulation (*Physical Space*) of the scheme is presented on 2D structured and unstructured grids. Next, quadrature parametrization is presented in 3D and construction of the family of CVD-MPFA schemes is then presented for general 3D grids, for different element types including hexahedra, pyramid, prism and tetrahedra. The numerical flux calculation and global assembly of fluxes is presented for both 2D and 3D formulations. Finally, the chapter closes with a series of numerical convergence tests for 2D and 3D formulations of the schemes on different types of structured and unstructured grids.

Chapter 6 presents a new family of subcell-based, locally conservative cell-centred flux-continuous schemes, for quadrilateral grids [67]. A general geometry permeability tensor approximation is introduced that is piecewise-constant over the subcells of the control-volumes and ensures that the local discrete general tensor is elliptic. The subcell tensor approximation ensures that a symmetric positive definite discretization matrix is obtained for the base member of the formulation. Finally, a numerical convergence study is presented for a sub-cell based family of schemes. With the help of a numerical convergence study the subcell tensor approximation is compared to the cell-wise tensor scheme and the physical-space schemes. The numerical convergence comparison is then used to demonstrate the important benefits of using subcell tensor approximations with the control-volume face geometry.

Chapter 7 discusses pressure solution monotonicity issues relating to the family of CVD(MPFA) schemes in 2D and 3D for structured and unstructured formulations. Numerical cases are tested to demonstrate monotonicity behavior of the family of schemes. Novel methods are proposed, backed with numerical examples, to obtain monotonic solutions by combining flux-splitting techniques with CVD-MPFA schemes. Specific discretization issues are also discussed to obtain monotonicity preserving families of schemes in 2D and 3D on both structured and unstructured grids.

Chapter 8 presents a new double-family of flux continuous schemes parameterized by quadratures (q_1, q_2). There, the double family is quantified by choosing a different quadrature parametrization or quadrature on different faces of the sub-cell control-volume leading to a variable support scheme. M-matrix analysis for double families presented in [10] is used to establish a key result for general nine-point schemes and to exposes the limits on the schemes for ensuring that solutions are monotonic. The analysis is also used to determine the upper limits for obtaining monotonic solutions and to aid the design of schemes that minimize the occurrence of spurious oscillations in the discrete pressure field.

In chapter 9 the locally conservative family of CVD-MPFA schemes is applied to permeability upscaling. Equivalent upscaled permeability is used as a measure of performance of the family of schemes. A series of test cases are presented of upscaling, using slices of permeability data from SPE10 data-set. And convergence tests are performed using the family of CVD-MPFA schemes for different upscaling techniques. Where, again, the benefits of using the family of CVD-MPFA schemes are highlighted.

Finally, chapter 10 summarizes the novel research contributions of this work and recommendations are made for continuation of work through future research.

Chapter 2

Previous Work

2.1 Introduction

In this chapter, some background work related to the topic of this thesis is described. A brief overview of development of flux continuous schemes is presented in section 2.2. Flux-continuous finite volume discretization and the family of flux-continuous control-volume distributed (CVD) finite volume schemes are described very briefly in section 2.3. Numerical details of the methods, which are of direct importance to this work, are given later in Chapter 5. Finally, section 2.4 presents the recent advances for the family of flux-continuous finite volumes schemes outlining contribution made by work done in this thesis.

2.2 Flux-Continuous Finite-Volume Schemes

Edwards and Rogers [1, 2] presented a family of flux continuous scheme applicable to the general full tensor pressure equation to model fluid flow with quadrilateral type grids in 2D. These grids are nonorthogonal and use flux balance across the quadrilateral block boundaries by constraining the x and y direction fluxes. Pressure/Potential is constrained at specific points on the boundaries. Such potential

and flux constraints are used to obtain transmissibility coefficients which reduce to harmonic average transmissibilities used in standard diagonal tensor reservoir simulation. These schemes are equally applicable on either a cell vertex or a cell centred grid [9, 20, 3] and extension to general unstructured quadrilateral and triangular grids is presented in [4]. Verma and Aziz [52] presented numerical schemes for Voronoi grids having uniform properties inside the grid cell. This scheme uses flux constraints normal to the grid cell boundaries. This method can also be used with grids based on triangles(2D) and tetrahedra (3D) [68, 52].

Aavatsmark *et al.* [51] presented a method on nonorthogonal, curvilinear grids for multiphase flow. Aavatsmark *et al.* [53] have presented a similar scheme which belongs to the family of schemes presented by Edwards and Rogers [1, 2]for discretization on nonorthogonal quadrilateral grids for inhomogeneous and anisotropic media, while Aavatsmark *et al* [69, 54, 54] presented a discretization method on unstructured triangular grids for general media. This scheme is similar to that presented by Verma [52]. The flux continuous schemes are extended to mixed elements (grids of mixed cell type) in 2-D and 3-D [6, 4, 70, 71].

2.3 Flux-continuous Finite Volume Discretization

Rapid variation in permeability is common in oil reservoirs where permeability coefficients can jump by several orders of magnitude. Continuity of normal flux and pressure at local physical interfaces between grid blocks with strong discontinuities in permeability are fundamental laws that must be built into the discrete approximation of the pressure equation. Finite volume methods are a class of discretization schemes that have proven highly successful in approximating the solution of a wide variety of conservation laws. The primary advantages of these methods are improved numerical robustness through discrete maximum (minimum) principles, applicability on very general unstructured grids, and the intrinsic local conservation properties of

the resulting schemes.

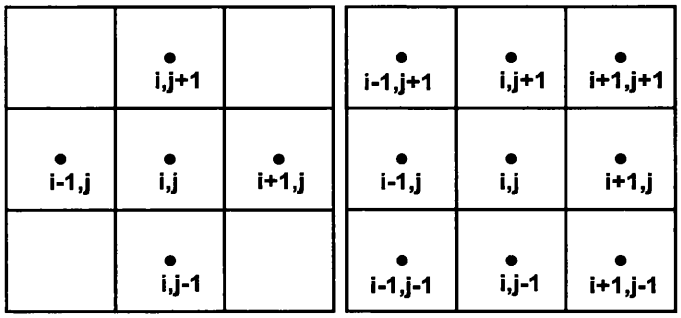

(a) (b)

Figure 2.1: (a) Five-Point Stencil in 2D. (b)Nine-Point Stencil in 2D.

2.3.1 The Family of Flux-Continuous Control-Volume Distributed Multi-Point Flux Approximation (CVD-MPFA) Schemes

Conventional reservoir simulation employs a standard five-point cell-centred stencil in 2D (seven in 3-D) for approximating the discrete diagonal tensor pressure equation, figure 2.1(a). Continuity of flux and pressure is readily incorporated into the standard discretization by approximating the interface coefficients with a harmonic average of neighbouring grid block permeabilities. Unfortunately, for an arbitrary heterogeneous domain the assumption of a diagonal tensor is not always valid at the grid block scale.

In general a full tensor equation arises whenever the computational grid is non-aligned with the principal axes of the local tensor field. A full tensor can occur when representing cross bedding, modeling any anisotropic medium that is non-aligned with the computational grid [19], using non **K**-orthogonal [72, 73] or unstructured grids and when upscaling rock properties from fine scale diagonal tensor simulation to the

grid block scale [33]. Consequently, standard five-point diagonal tensor simulator will suffer from an inconsistent $O(1)$ error in flux when applied to cases involving these major features. Accurate approximation of the full-tensor pressure equation requires nine-point support in two dimension (19 or 27 in 3-D), figure 2.1(b). The nine point formulation is possibly the most reliable method to counter grid-orientation effect, widen the simulator range of applicability to general non-orthogonal grids and full-tensors [74, 75, 76].

The derivation of local algebraic flux-continuity conditions for full tensor discretization operators has lead to efficient and robust locally conservative family of flux-continuous finite-volume schemes for determining the discrete pressure and velocity fields in subsurface reservoirs [3, 4, 6] where they are called flux-continuous control-volume distributed (CVD) schemes. The schemes constructed were aimed at achieving improved accuracy and reduced grid orientation. Increased applicability to general curvilinear grids is also gained for both diagonal and full tensor equations. Flux-continuous schemes are also presented in [53, 54, 55, 56] (for the fundamental member of the above family i.e. $q = 1$)where they are called multi-point flux approximation (MPFA) methods. Similar schemes of this type are also presented in [52, 77, 78]. All of the above schemes are applicable to the diagonal and full tensor pressure equation with generally discontinuous coefficients and remove the O(1) error introduced by standard reservoir simulation schemes when applied to full tensor flow approximation while maintaining a single degree of freedom per control-volume. Other schemes that preserve flux continuity have also been developed, using the mixed method e.g. [26, 48, 49, 79, 80, 81], or more recently Discontinuous Galerkin (DG) formulations have been presented [41, 42], however these methods introduce further degrees of freedom for fluxes which increase the size of the global system matrix when compared to the family of flux-continuous finite volume method presented in this thesis.

The premise of the families of flux continuous schemes presented here rests on

quadrature parametrization [5], where the quadrature point explicitly defines the position of imposed flux continuity. The local position of continuity defines the parameterized quadrature point and hence the whole family of flux-continuous schemes for a diagonal or full tensor pressure equation.

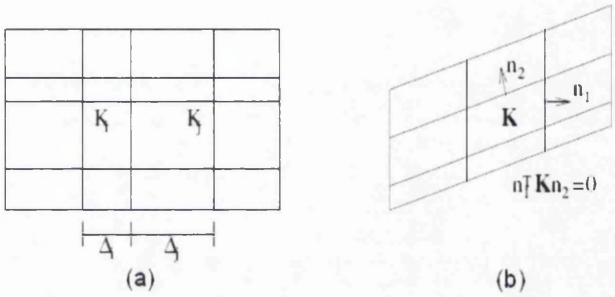

Figure 2.2: (a) The grid is orthogonal with gridlines aligned with the principal coordinate axes. (b) The grid is a **K**-Orthogonal grids

2.4 Recent Advances for The Family of CVD-MPFA Schemes

The recent advances with regards to the family of CVD-MPFA schemes discretization forms an integral part of the work presented in this thesis. The emphasis is on numerical pressure solution convergence, monotonicity and extension of the scheme to 3D. The convergence rates of the standard CVD-MPFA scheme has been discussed in [3, 82]. Improved convergence of the scheme with the use of quadrature parametrization for both 2D (structured and unstructured)and 3D formulation is noted in [5, 7, 25], and will be presented in the proceeding chapters of this thesis. Standard reservoir simulation uses two-point flux approximation or TPFA method. The TPFA approximation is only valid for **K**-orthogonal grids (figure 2.2) and hence has limited application. Whereas, the CVD(MPFA) schemes have extended reach

with applicability on general geometry with full heterogeneity and anisotropy. But, on the application of these CVD(MPFA) schemes to strongly heterogeneous media with combination of certain grids can result in failure to satisfy a maximum principle (as with other FEM and FVM) and results in loss of solution monotonicity [83, 7, 25, 84]. Efforts have been made to determine the limits of a monotonicity preserving scheme [2, 3, 9, 4, 10, 11, 25, 83, 84]. Novel methods are proposed in this work to obtain monotonic solutions using CVD(MPFA) schemes by combining reduced support discretization techniques and flux-splitting techniques [7, 8, 10]. The family of flux-continuous schemes is also used for upscaling techniques [12]. The formulation of the family of schemes (in physical space) results in a discretization matrix which is non-symmetric in general case. A new family of sub-cell flux-continuous CVD(MPFA) schemes is presented in this thesis in an effort to obtain symmetric positive definite pressure discretization [24]. Also, an extension of the *Physical space* CVD(MPFA) schemes to general 3D grids of any element type [25] is presented here allowing much greater flexibility in terms of gridding with regards to application of the scheme to general geometry.

Chapter 3

Flow Equations and Problem Description

3.1 Introduction

The purpose of this chapter is to introduce the principal equations governing the fluid flow in porous media, which are modelled throughout this thesis. Fluid flow in porous media is governed by the fundamental laws of conservation of mass, momentum and energy. A complete treatment of the dynamics and statics of the fluid flow in porous media is presented in [19]. Section 3.2 presents Darcy's Law and the flow equations governing single and multi-phase flow. The definition of the problem to be modelled in this thesis is presented in section 3.3. Section 3.4 presents a brief discussion on different types of boundary conditions applied to solve porous media pressure equation.

3.2 Flow Equations

3.2.1 Darcy's Law and Single Phase Flow

The movement of water, oil and natural gas through the subsurface, known as flow in a porous medium is a very complex phenomenon because of the involved scale and heterogeneity of the medium. Usually the velocity of the flow is so small ($Re << 1$) and the flow passages are so narrow that laminar flow may be assumed. Rigorous analysis of the flow is not possible because of complexity of the shape of the individual flow passages. Although, several theories have been formulated, credit is attributed to the French engineer *Henry Darcy* [18], who published his famous work on the public fountain of the French city of *Dijon.* In his work Darcy presented the result of his experiment on water flow through sand filters. He summarized his findings in the form of a mathematical relationship , in which he concluded that the rate of flow through a porous filter is inversely proportional to the length of the filter and proportional to the difference in pressure head across the medium, which is known as Darcy's Law [19]. In its most primitive form (1D Single phase flow with gravity neglected), the relations is expressed as:

$$\mathbf{v} = -k\frac{\partial \phi}{\partial x} \tag{3.1}$$

In this expression x refers to the average direction of flow, $\mathbf{v}$ and $\frac{\partial \phi}{\partial x}$ represent respective flow density or Darcy velocity and the gradient of pressure/hydraulic gradient [19]. The proportionality constant k is called as the permeability or conductivity of the medium. For flow in higher dimensions, the permeability will be spatially varying tensor $\mathbf{K}$. When the gravity is included, Darcy's law for single phase flow is expressed as:

$$\mathbf{v} = -\frac{\mathbf{K}}{\mu}(\nabla \phi + \rho g \nabla z) \tag{3.2}$$

Here, μ is the viscosity, g is the gravitational constant and z is the spatial coordinate in the upward direction. Darcy's law only considers the average flow behavior over a representative elementary volume (REV) of porous media that must be greater than several pores. This volume over which the flow is averaged is termed as a *control-volume*, figure 3.1. Using this control-volume approach, Darcy's law essentially bypasses both the microscopic level, at which we consider what happens to each fluid molecule, and the pore level, at which we consider the flow pattern within each pore and between pores. Observations of flow in porous media can then move to the macroscopic level at which only average phenomena over the control volume are considered. That is to say, Darcy's law is a macroscopic law. Thus the property defined at a point in Darcy's law represent an average property over a control-volume and the property at every point in space varies smoothly such that differential calculus applies.

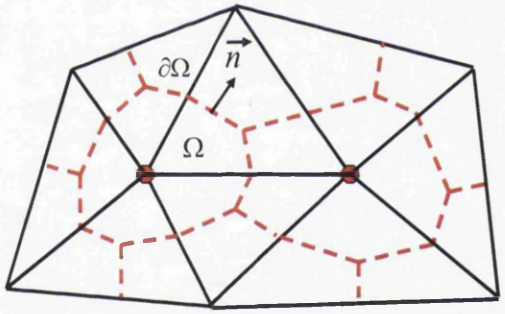

Figure 3.1: Primal grid (solid line), Control-volume Dual grid (dotted lines)

Continuity or mass conservation is another important law used in the development of the flow equations in porous media, i.e. For steady-state condition, continuity requires that the amount of fluid flowing into the control-volume must be equal to the amount flowing out. Therefore in integral form the mass conservation equation for single phase flow over the control-volume Ω (figure 3.1) is written as:

$$\int_{\Omega} \nabla \cdot \mathbf{v} d\tau = -\oint_{\partial_{\Omega}} \mathbf{K} \nabla \Phi \cdot \hat{\mathbf{n}} ds = M \tag{3.3}$$

Where $\mathbf{v}$ (defined by equation 3.2) is the Darcy velocity, $\mathbf{K}$ is the elliptic permeability tensor, ∂_{Ω} is the boundary of Ω, $\hat{\mathbf{n}}$ is the unit outward normal and ϕ is the pressure and M is a source term which is zero away from well locations.

3.2.2 Multi-phase Flow

When several phases or components are present in porous media, Darcy's law may be extended to describe simultaneous flow of more than one phase:

$$\mathbf{v}_{\mathbf{l}} = -\frac{k k_{rl}}{\mu_l} \left(\nabla \phi + \rho_l \frac{g}{g_c} \nabla z \right) \tag{3.4}$$

where $l = (o, w, g)$ (oil,water and gas phases, respectively) and k_{rl} is the relative permeability of phase l, which is used to account for the reduced permeability of each phase due to the presence of the other phases. In petroleum reservoirs different hydrocarbon components can exist in both a gas and a fluid phase, while water just exists in fluid phase. A large class of models that are widely used in porous media flow simulations fall within the *black-oil model*[85]. The name refers to the assumption that the hydrocarbon may be defined as two components: a heavy hydrocarbon component called *oil* and a light hydrocarbon component called *gas*. The two components can be partially or completely dissolved in each other depending on the pressure and the temperature, forming either one or two phases (liquid and gaseous). In general black-oil models, the hydrocarbon components are also allowed to be dissolved in water and the water component may be dissolved in the two hydrocarbon phases. The hydrocarbon fluid composition, however, remains constant for all time. The alternative, where the hydrocarbons are modelled using more than two components and hydrocarbons are allowed to change composition, is called a *compositional model* [86]. Since, emphasis here is on single phase flow further discussions on multi-phase

flow is refrained. A detailed discussion on flow equations involved in multi-phase flow is given in [14, 19].

3.3 Problem Description

While the methods presented in this thesis are for both single phase and multi-phase flow problems, specific discretization issues are considered here that arise with the finite volume approximation of the pressure equation in single phase flow, neglecting the effects of gravity.

3.3.1 Cartesian Tensor

The problem is to find the pressure ϕ satisfying

$$-\int_{\Omega} \nabla \bullet \mathbf{K}(x,y)\nabla\phi d\tau = \int_{\Omega} q d\tau = M \tag{3.5}$$

over an arbitrary domain Ω, subjected to suitable (Neumann/Dirichlet) boundary conditions on boundary $\partial\Omega$. The right hand side term M represents a specified flow rate and $\nabla = (\partial_x, \partial_y)$. Matrix $\mathbf{K}$ can be a diagonal or full cartesian tensor with general form

$$\mathbf{K} = \begin{pmatrix} K_{11} & K_{12} \\ K_{12} & K_{22} \end{pmatrix} \tag{3.6}$$

The full tensor pressure equation is assumed to be *elliptic* such that

$$K_{12}^2 \leq K_{11}K_{22} \tag{3.7}$$

The tensor can be discontinuous across internal boundaries of Ω. The boundary conditions imposed here are Dirichlet and Neumann. For incompressible flow pressure is specified atleast at one point in the domain. For reservoir simulation, Neumann

boundary conditions on $\partial\Omega$ requires zero flux on solid walls such that $(K\nabla\phi)\cdot\hat{n}=0$, where $\hat{n}$ is the outward normal vector to $\partial\Omega$.

3.3.2 General tensor equation

The pressure equation is defined above with respect to the *physical* tensor in the initial classical Cartesian coordinate system. Now we proceed to a general curvilinear coordinate system [3] that is defined with respect to a uniform dimensionless transform space with a (ξ,η) coordinate system, where $[0\leq(\xi,\eta)\leq 1]$. Choosing Ω to represent an arbitrary control volume comprised of surfaces that are tangential to constant (ξ,η) respectively, equation 3.5 is integrated over Ω via the Gauss divergence theorem to yield

$$-\oint_{\partial\Omega}(\mathbf{K}\nabla\phi)\cdot\hat{\mathbf{n}}ds=\mathbf{M} \tag{3.8}$$

where $\partial\Omega$ is the boundary of Ω and $\hat{n}$ is the unit outward normal. Spatial derivatives are computed using

$$\phi_x=J(\phi,y)/J(x,y),\phi_y=J(x,\phi)/J(x,y), \tag{3.9}$$

where $J(x,y)=x_\xi y_\eta-x_\eta y_\xi$ is the Jacobian. Resolving the x,y components of velocity along the unit normals to the curvilinear coordinates (ξ,η), e.g., for $\xi=$ constant, $\hat{\mathbf{n}}ds=(y_\eta,-x_\eta)d\eta$ gives rise to the general tensor flux components

$$F=-\int(T_{11}\phi_\xi+T_{12}\phi_\eta)d\eta,\quad G=-\int(T_{12}\phi_\xi+T_{22}\phi_\eta)d\xi, \tag{3.10}$$

where general tensor $\mathbf{T}$ has elements defined by

$$\begin{aligned}T_{11}&=(K_{11}y_\eta^2+K_{22}x_\eta^2-2K_{12}x_\eta y_\eta)/J,\\ T_{22}&=(K_{11}y_\xi^2+K_{22}x_\xi-2K_{12}x_\xi y_\xi)/J,\\ T_{12}&=(K_{12}(x_\xi y_\eta+x_\eta y_\xi)-(K_{11}y_\eta y_\xi+K_{22}x_\eta x_\xi))/J\end{aligned} \tag{3.11}$$

and the closed integral can be written as

$$\int\int_{\Omega} \frac{(\partial_\xi \tilde{F} + \partial_\eta \tilde{G})}{J} J d\xi d\eta = \triangle_\xi F + \triangle_\eta G = m \tag{3.12}$$

where e.g. $\triangle_\xi F$ is the difference in net flux with respect to ξ and $\tilde{F} = T_{11}\phi_\xi + T_{12}\phi_\eta$, $\tilde{G} = T_{12}\phi_\xi + T_{22}\phi_\eta$. Thus any scheme applicable to a full tensor also applies to non-K-Orthogonal grids (figure 2.2). Note that $T_{11}, T_{22} \geq 0$ and ellipticity of $\mathbf{T}$ follows from equations 3.7 and 3.11. Full tensors can arise from upscaling [33], and orientation of grid and permeability field [19]. For example by equation 3.11, a diagonal anisotropic Cartesian tensor leads to a full tensor on a curvilinear *orthogonal* grid.

3.4 Boundary Conditions

The two most common kinds of boundary conditions used in reservoir simulators to solve equation 3.5, are

3.4.1 Dirichlet

This boundary condition requires the specification of pressure at the reservoir boundaries or wells. Typically, this involves specifying flowing bottom hole pressure at a well and a constant pressure at physical boundaries of reservoir.

3.4.2 Neumann

This boundary condition requires specification of flow rates at reservoir boundaries. Typically, it involves specifying flow rates at wells and no-flow across physical boundaries of reservoir.

Chapter 4

Numerical Discretization Techniques

4.1 Introduction

Much of the theory of physical phenomena is described by differential and integral equations. Such equations appear not only in physical sciences, but in biology, sociology, and all scientific disciplines that attempt to understand these physical phenomena. But many of these equations have no exact solution. Therefore to find solutions to such equations we must resort to numerical techniques. The objective of any numerical method for solving a problem involving a differential or integral equation is to generate a set of algebraic equations involving a finite number of unknowns, whereby the solution of algebraic equations characterizes an approximation of the solution of the original problem.

In view of the complexity of the permeability and geometry of petroleum reservoirs, numerical methods are necessary for discretization of reservoir simulation elliptic pressure equation introduced in previous chapter. This chapter presents numerical methods suitable for discretization of heterogeneous elliptic equation with application to reservoir simulation. The methods discussed include the classical Finite differ-

ence method (FDM), Finite element method (FEM), Mixed finite element method (MFEM) and Finite volume method (FVM).

The chapter is organized as follows: Section 4.2 summarizes Finite difference methods with application to reservoir simulation. Section 4.3 presents a brief description of Finite element methods (Galerkin's formulation) applied to elliptic pressure equation of reservoir simulation. Mixed finite element method is described in section 4.4 along with a discussion of the benefits and drawbacks for application to reservoir simulation. Finally, details of Finite volume formulation are presented in section 4.5.

4.2 Finite Difference Method

The finite difference method (FDM) is probably the best known numerical method for solving differential equations. It is used extensively in conventional reservoir simulation [87, 88, 89, 89, 90, 91]. In this method the derivatives of the equation in consideration are replaced by finite differences. These can be derived from truncated Taylor series expansions. The values of the dependent variable at a discrete number of points in the grid become the unknowns. The FDM can be best illustrated by considering one dimensional version of elliptic pressure equation 3.3 with Neumann boundary on $\partial\Omega$ (zero flux on solid wall) such that $(K\nabla\phi)\cdot\hat{n} = 0$, where $\hat{n}$ is the outward normal vector to $\partial\Omega$. Assuming permeability tensor K is homogeneous in the problem domain. In this case equation 3.3 can be written as:

$$-\phi(x)'' = f \tag{4.1}$$

with f a known function. The boundary condition simply reduces to

$$\phi' = 0 \tag{4.2}$$

Let x_i denotes a point in an equidistance grid with spacing h and let ϕ_i , ϕ_{i+1} and ϕ_{i-1} denotes the unknown values of ϕ in the points x_i,x_{i+1} and x_{i-1} respectively.

Then, Taylor expansion of the function ϕ around x_i yields

$$\phi_{i+1} = \phi_1 + h\phi^{'}(x_i) + \frac{1}{2}h^2 h\phi^{''}(x_i) + \frac{1}{6}h^3 h\phi^{'''}(x_i) + O(h^4) \tag{4.3}$$

and

$$\phi_{i-1} = \phi_1 - h\phi^{'}(x_i) + \frac{1}{2}h^2 h\phi^{''}(x_i) - \frac{1}{6}h^3 h\phi^{'''}(x_i) + O(h^4) \tag{4.4}$$

adding equations 4.3,4.3 and dividing by h^2 gives

$$\frac{\phi_{i+1} - 2\phi_i + \phi_{i-1}}{h^2} = f_i \tag{4.5}$$

where $f_i = f(x_i)$. From the above it follows that this approximation is correct to order h^2.

However, for multidimensional problems with non-orthogonal grids and general permeability description, such FD schemes are not directly applicable as the differentiation now involves the permeability as well as the pressure i.e. in 1D permeability $k = k(x)$ and the equation 3.3 now will be written as

$$-(k(x)\phi(x)^{'})^{'} = f \tag{4.6}$$

hence, now the permeability should also be included in the FD scheme. This can be achieved by expressing $(k(x)\phi(x)^{'}) = \mathbf{\Phi}(\mathbf{x})$ and writing a discrete version of $\mathbf{\Phi}(\mathbf{x})$ in a similar fashion using Taylor series expansion.

Although, FDM may be classified as simplest of all available numerical methods and are very easy to program, but problems with FDM are well known. Classical FDM can be expected to break down near the discontinuities in the solution where differential equation does not hold and a special treatment is required [92]. For general non-orthogonal grids in 2D, and generally varying permeability tensors, discrete two-point finite difference method does not lead to a convergent scheme and the numerical solution converges to the wrong solution [93]. Also, FDM are well suited only for

regular domains and are limited in terms of application on irregular domains. Hence, the use of Finite-difference methods in reservoir simulation is not generally applicable.

4.3 Finite Element Method

The finite element method (FEM) is also one of the most popular method for solving partial differential equations. A number of different approaches may be adopted. Of these Rayleigh-Ritz (based on variational formulation) and Galerkin (based on the weak formulation) methods are probably the best known [94, 95]. The literature available on FEM is vast and the details of the methods and their applications can easily be found in e.g., [94, 95, 96, 97, 98, 99, 100].

In applying Galerkin approach to the elliptic pressure equation equation $(-\nabla \cdot (\mathbf{K}\nabla\phi) = m)$, the first step is to derive a *weak formulation* for the problem. This is obtained by multiplying the equation by an arbitrary test function ψ and then integrating by parts over the domain Ω. Using the Green's first identity for integration by parts in combination with the Neumann boundary condition $(\mathbf{K}\nabla\phi) \cdot \mathbf{n} = 0$ yields the weak formation as

$$\int_{\Omega} (\mathbf{K}\nabla\phi) \cdot \nabla\psi d\tau = \int_{\Omega} m\psi d\tau \tag{4.7}$$

which must hold for every differentiable test function ψ. In applying the Galerkin's FEM to equation 4.7 the domain Ω is divided into small volumes, called elements. These can be quadrilaterals or triangles in 2D and cubes,pyramids, prisms or tetrahedrons in 3D and can be chosen depending on complexity in geometry, which provides geometric flexibility. The computational points are identified by vertices or other characteristic points (e.g. cell/element-centre) in the network formed by the elements. The Unknown ϕ is approximated by

$$\phi = \sum_{i=1}^{N} \phi_i \psi_i \tag{4.8}$$

where $\{\psi_i\}_{i=1}^{N}$ denotes a set of interpolation function called basis functions and $\{\phi_i\}_{i=1}^{N}$ denotes set of unknown coefficients to be determined. The basis functions have local support, i.e. the area in which they are non-zero is limited to a few adjacent elements, and they span the space of piecewise polynomials functions. Further more they are defined to be equal to unity at a given computational point and equal to zero at all other computational points, e.g.

$$\psi_i(x) = \begin{cases} \frac{x - x_{i-1}}{x_i - x_{i-1}} & x \in [x_{i-1}, x_i], \\ \frac{x_{i+1} - x}{x_{i+1} - x_i} & x \in [x_i, x_{i+1}], \\ 0 & \text{otherwise.} \end{cases} \tag{4.9}$$

Subsequently each coefficient ϕ_i in the expansion of equation 4.8 corresponds to the value of unknown ϕ in the associated computational point. Substituting the expansion of equation 4.8 and the functions ψ_j for $j = 1, 2...., N$ as test functions in the weak formulation (equation 4.7) produces N equations in N unknowns $\{\phi_i\}_{i=1}^{N}$. These can be reformulated as single matrix equation

$$A_{i,j}\Phi_j = M_i \tag{4.10}$$

where

$$i = 1, ..., N \qquad \text{and} \qquad j = 1, ..., N$$

The matrix A can now be inverted to obtain the vector of unknowns ϕ. The use of FEM today, is widespread in many different fields of study. FEM enjoys its popularity due to advantages in modeling complex geometries, and its natural enforcement of Neumann boundary conditions. The FEM are known to be accurate on smooth data (homogeneous permeability) [99]. Whereas, in the case of application of Classical FEM to a medium involving discontinuities, which is common in petroleum

reservoir simulation, an undesired smearing effect occurs [101, 102, 70, 71]. This is a direct result of the loss of local conservation property of the method, due to lack in flux continuity across the interior interfaces across which the permeability can be discontinuous in general case, as discussed in [101, 102, 103, 104, 105, 106, 70, 71]. Advantages of CVD(MPFA) verses CVFE in terms of flow field resolution are shown in 2-D and 3-D in [70, 71]. Whereas, other finite element methods like Discontinuous Galerkin (DG) methods [107, 108, 109] and Mixed finite element methods (MFEM) [110] with improved resemblance of the physics of the problem and ability to handle discontinuous media are considered as a better choice.

4.4 Mixed Finite Element Method

The name "mixed method" indicates a finite element method which has more than one approximation space. The mixed finite element method [80, 26] uses both the fluxes and the pressure as primary unknowns simultaneously, whereas finite element method fluxes are computed from the discrete pressures in a post processing step. The method emphasizes the flow and in many cases gives a more accurate picture of the flow. Besides, the method fulfills the physics of the problem, with conservation of mass locally (where Galerkin FEM fails) as well as it is applicable to irregular domains with anisotropic, heterogeneous discontinuous permeability tensor [111, 112, 79].

To derive the mixed finite element formulation the second order reservoir simulation elliptic pressure equation is expressed in terms of two first order equations one for pressure and one for Darcy velocity, given as:

$$\mathbf{v} = -\mathbf{K}\nabla\phi \tag{4.11}$$

$$\nabla \cdot \mathbf{v} = m \tag{4.12}$$

The above two equations will now be used for weak formulation. To obtain a

weak formulation for the two equations, one multiplies by suitable test functions, and integrates over the domain Ω. The two equations can now be written as:

$$\int_{\Omega} \mathbf{K}^{-1}\mathbf{v} \cdot \psi d\tau = -\int_{\Omega} \phi \nabla \cdot \psi d\tau \tag{4.13}$$

$$\int_{\Omega} \varphi \nabla \cdot \mathbf{v} d\tau = -\int_{\Omega} \varphi m d\tau \tag{4.14}$$

For the equation 4.13 after applying Green's theorem and integrating by parts we obtain:

$$\int_{\Omega} \mathbf{K}^{-1}\mathbf{v} \cdot \psi d\tau = -\int_{\Omega} \nabla \cdot \psi \phi d\tau + \int_{\partial\Omega} \psi \cdot \mathbf{n} \phi ds \tag{4.15}$$

With no-flow boundary conditions the system of equations reduces to

$$\int_{\Omega} \mathbf{K}^{-1}\mathbf{v} \cdot \psi d\tau = -\int_{\Omega} \nabla \cdot \psi \phi d\tau \tag{4.16}$$

$$\int_{\Omega} \varphi \nabla \cdot \mathbf{v} d\tau = -\int_{\Omega} \varphi m d\tau \tag{4.17}$$

If all boundaries have no-flow boundary conditions imposed, an extra constraint must be added to make equations 4.16-4.17 well-posed. A common choice is to set the mean pressure to a constant where $\int_{\Omega} \phi d\tau = 0$, e.g. [86]. Here, we introduce $(\cdot, \cdot)$ for inner products in some inner product space. Using this inner product notation, the weak formulation of equations 4.16-4.17 reads: Find $(\mathbf{v}, \phi) \in H(div) \times L^2$ such that

$$(\mathbf{K}^{-1}\mathbf{v}, \psi) = (\phi, \nabla \cdot \psi) \qquad \forall \psi \in H(div), \tag{4.18}$$

$$(\nabla \cdot \mathbf{v}, \varphi) = (m, \varphi) \qquad \varphi \in L^2. \tag{4.19}$$

The discrete problem reads: Find $(\mathbf{v}_h, \phi_h) \in \mathbf{V}_h \times \Phi_h \subset H(div) \times L^2$ such that

$$(\mathbf{K}^{-1}\mathbf{v}, \psi) = (\phi, \nabla \cdot \psi) \qquad \forall \psi \in \mathbf{V}_h, \tag{4.20}$$

$$(\nabla \cdot \mathbf{v}, \varphi) = (m, \varphi) \qquad \varphi \in \Phi_h. \tag{4.21}$$

The discrete space Φ_h is the space of piecewise constants and the discrete space $\mathbf{V}_h$ is in many application chosen to be the lowest order Raviart Thomàs space [80] for triangular, tetrahedral, or regular parallelepiped grids. The mixed finite element methods are able to handle discontinuities in media with great ease because of inherent flux continuity condition (over the control-volume edges) in the formulation. The MFEM is shown to be locally mass conservative for medium involving discontinuities and hence, are well suited for petroleum reservoir simulation. The only drawback of the method is that it is computationally more expensive, because of solving for pressure and velocity simultaneously.

The mixed finite element framework has also been extended to account for a control volume formulation by Russel [113, 112] and co-workers. The expanded Mixed finite element method was developed by Wheeler, Yotov and co-workers [114, 111]. The relationship between the mixed finite element method and flux-continuous CVD(MPFA) schemes is given by Edwards in [4] (symmetric case) and [67] for the physical space (non-symmetric case), recently a proof of convergence of MPFA was presented in [115], which exploits this relationship. Discontinuous Galerkin method [41, 42] and Mixed Finite element method are frequently used in reservoir simulation [26, 43], but they prove to be computationally more expensive due to the additional degrees of freedom.

4.5 Finite Volume Method

The Finite volume methods (FVM) are related to the original integral equations, and are derived from conservation of physical quantities over cell volumes. To use the

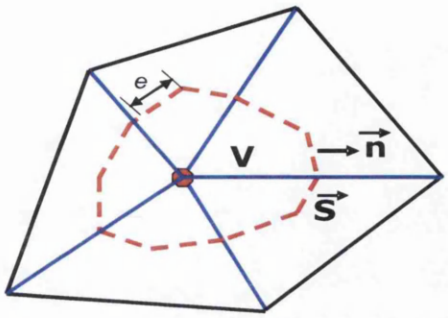

Figure 4.1: Control-volume Dual grid (dotted lines)

FVM, the problem domain Ω is divided into small volumes called as *control-volumes*, figure 4.1. The partial differential equations under consideration are then integrated over each control-volume to obtain a set of equations in the form of surface integrals. By way of illustration, integrating the elliptic pressure equation over a small control-volume V with surface S leads to

$$\int_S \mathbf{v} \cdot \mathbf{n} dS = \int_V m dV \tag{4.22}$$

where $\mathbf{n}$ is an outward unit normal vector to surface S (figure 4.1). What is left to be approximated is the flux for an edge e, which is part of the control-volume boundary S. This is given as

$$F_e = \int_S \mathbf{v} \cdot \mathbf{n} dS \tag{4.23}$$

Fundamental to FVM is the introduction of control-volume cell average. Godunov [116] introduced this interpretation in the discretization of the gas dynamics equations by assuming piecewise constant solution representation in each control-volume with values equal to cell average. The finite volume formulation is also suitable for discontinuity capturing and have been used in obtaining solution to nonlinear hyperbolic conservations laws [117, 118, 119, 93, 92].

Local conservation is a desirable property in numerical modeling of flow in porous

media. FVM are derived such that fluxes are conserved [120, 121, 122, 123] for both cell-centred and (dual grid) polygonal control-volume node based formulations. Numerical discretization techniques [2, 20, 3, 21, 4, 22, 23, 5, 24, 12, 7, 8, 25, 10] based on flux-continuous finite volume formulation forms the heart of this thesis and will be discussed extensively in the next few chapters. Advantage of using FVM over FDM and FEM can be stated respectively as: Relative ease by which FVM can solve problem on irregular geometries with discontinuities and its ability to conserve variable even on a coarse mesh.

4.6 Finite Volume Formulation

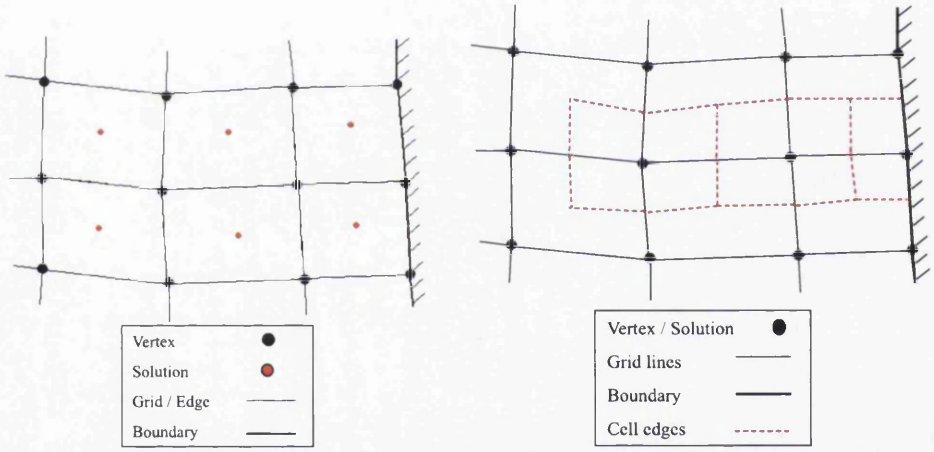

Figure 4.2: (a) Cell-centred Formulation. (b)Cell-Vertex Formulation.

The finite volume formulations considered in this thesis are for both cell-centred and cell-vertex control-volume distributed formulations e.g. [3, 4, 5]. In these formulations flow variables and rock properties, e.g., rock permeability tensor, share the same location within the control-volume. In the cell-centred formulation the control-volume is taken to be the cell of the primary grid imposed on the region Ω, flow and rock variables are located at the centre (velocity is computed on cell faces) 4.2(a). In

the cell-vertex finite volume formulation a control-volume is constructed by joining cell centres and edge midpoints around the common cell vertex and flow variables and rock properties are assigned to the vertices of the primal grid and are piecewise constant over each cell vertex control-volume, velocity is resolved locally on each control-volume subface at a chosen point leading to a (family) quadrature 4.2(b).

The 2D formulations of the flux-continuous schemes presented in this thesis involve cell-centred/control volume distributed formulation for structured quadrilateral grids and cell-vertex/control volume distributed formulation for both structured quadrilateral and unstructured triangular grids. The 3D formulation of the schemes will be cell-vertex/control volume distributed. However, it should be noted that on a structured grid the cell-centred/control volume distributed formulation of the family of flux-continuous schemes can easily be converted to cell-vertex/control volume distributed formulation by translating the operations onto a grid that is essentially a dual mesh.

Chapter 5

Families of Flux-Continuous CVD (MPFA) Schemes

5.1 Introduction

The main focus of this work is on the families of flux-continuous, locally conservative, control-volume distributed (CVD) finite volume schemes and the discretization issues related to these schemes. The complexity in geometry and geology of subsurface reservoirs continues to present a challenge to numerical methods for reservoir simulation. Rapid variation in permeability with strong anisotropy are common in subsurface reservoirs. Hence, continuity of flux and pressure are key properties for numerical methods employed for discretization of the reservoir simulation pressure equation. The families of locally conservative flux-continuous schemes have this property as they are built on the underlying principle of continuity in normal flux and pressure. These schemes have been developed for solving the general geometry-permeability tensor pressure equation on structured (cell-centred and cell vertex grids) and unstructured (cell vertex) grids and are control-volume distributed (CVD) [3, 6, 4, 22, 23, 24, 5, 12, 7, 8, 25]. The familes of schemes are classified by the quadrature parametrization $0 < q \leq 1$, where the scheme quadrature q defines

the point of continuity and hence the family of schemes [5].

In this chapter a detailed formulation of the family of flux-continuous schemes in *physical space*, with emphasis on variable quadrature point (defining the position of continuity) is presented for both, 2D (structured and unstructured) grids and 3D grids comprising of different element types (Hexahedra, Tetrahedra, Prism and Pyramid) [25]. Numerical convergence study is also presented for the family of schemes showing the benefits of using quadrature parametrization.

This chapter starts by dedicating section 5.2 to the details of flux-continuous formulation starting in 1-D followed by classical five-point schemes in 2D and the generalization of the flux-continuous schemes for 2D structured and unstructured grids, with discretization of the scheme in *physical space*. Section 5.3 starts with the motivation for the family of flux-continuous schemes and presents an overview of the family of schemes with emphasis on use of different quadrature point (quadrature parametrization) for imposing continuity of flux and pressure. The following section, section 5.4, presents a complete extension of the family of CVD (MPFA) flux-continuous schemes for general three dimensional grids comprising of any element types, hexahedra, tetrahedra, prism and pyramid elements. Discretization principles are presented for each element. The pyramid element is shown to be a special case with unique construction of the continuity conditions. Finally, in section 5.5 and 5.6 a detailed numerical convergency study is presented for the family of schemes with the help of series of test cases for 2D and 3D formulations respectively.

5.2 Flux Continuous Approximation

The key to any finite volume formulation lies in working with the integral form of flow equations. The Gauss divergence theorem is applied locally to the volume integral of divergence over each control volume. A unique discrete flux is then assigned to each control-volume face and each closed integral is approximated by sum of discrete

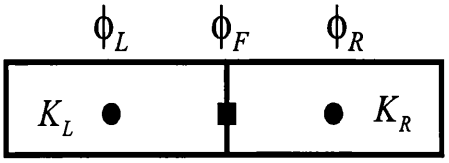

Figure 5.1: One dimensional Cell centered and Cell face pressures

outward normal fluxes. For a given face which is common to two neighbouring control-volumes, a unique flux is added to left hand control-volume while the same flux is subtracted from the right hand control-volumes leaving only the sum of global domain boundary fluxes. Thus the flux-continuous schemes considered here are locally conservative. The construction of the flux-continuous scheme is given below.

5.2.1 Flux-Continuous Approximation in 1D

We begin with classical cell centered formulation in one dimension where pressures and permeabilities are defined with respect to cell centres. In this case equation 3.3 reduces to

$$-\int (K(x)\phi_x)_x dx = m \tag{5.1}$$

Integration of the equation 5.1 over the cell i (referring to figure 5.1) results in the discrete difference of fluxes

$$F_{i+1/2} - F_{i-1/2} = m \tag{5.2}$$

where m is possible specified local flow rate, $F_{i+1/2} = -K\partial\phi/\partial x$ and the derivative remains to be defined. If the coefficient K is sufficiently smoothly varying it is possible to use linear interpolation between the centers of cells i and $i+1$ and approximates the flux by

$$F_{i+1/2} = -K_{i+1/2}(\phi_{i+1} - \phi_i)/\Delta x \tag{5.3}$$

where $K_{i+1/2}$ is a suitable average of the adjacent cell centered permeabilities. However if K is discontinuous then since normal flux and pressure are continuous the pressure gradient is in general discontinuous and thus linear interpolation is not valid across the cell faces separating jumps in permeability. The standard solution to this problem is described in [14]. Continuous pressure and normal flux are incorporated in the cell centered approximation by introducing a mean pressure ϕ_f at a cell face dividing neighbouring cells figure 5.1. Equating the resulting one sided flux approximation at the cell face results in

$$-K_r(\phi_r - \phi_f)/\Delta x_r = -K_l(\phi_f - \phi_l)/\Delta x_l \tag{5.4}$$

which ensures flux continuity. From equation 5.4 cell face pressure is given by

$$\phi_f = (\phi_l K_l/\Delta x_l + \phi_r K_r/\Delta x_r)/(K_l/\Delta x_l + K_r/\Delta x_r) \tag{5.5}$$

which is back-substituted into the discrete flux equation 5.4 to yield the classical cell face flux approximation

$$F = -2K_r K_l(\phi_r - \phi_l)/(K_r \Delta x_l + K_l \Delta x_r) \tag{5.6}$$

5.2.2 Flux-Continuous Approximation in 2D: Classical Five Point Scheme

As in one dimension pressures and permeabilities have a cell-wise distribution and cells act as control volumes. The equivalent two-dimensional discontinuous diagonal tensor five-point scheme on rectangular grid is derived by introduction of interface pressures and a sub-cell triangular support as indicated in figure 5.2(a). As in one dimension cell face pressures are eliminated in the flux continuity conditions to yield

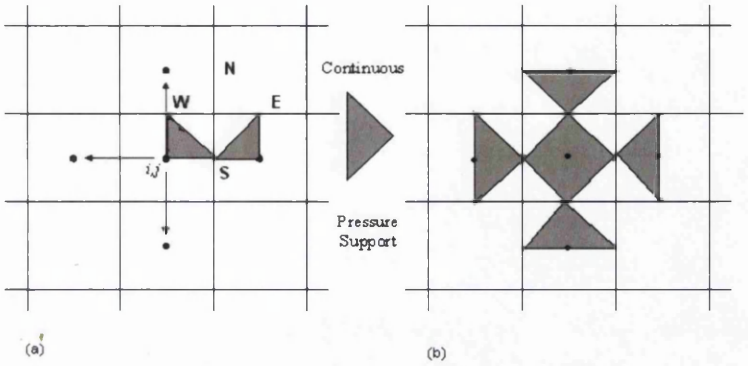

Figure 5.2: (a) Imposing continuity between the grid blocks in a five-point scheme(b)Cell-centered five-point support on a cartesian grid.

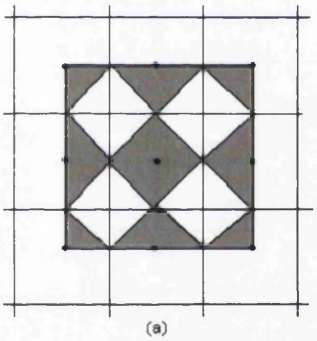

Figure 5.3: (a) Full tensor pressure support with standard default quadrature point q = 1

the classical five point scheme with harmonic mean coefficients in two dimensions, further details of the scheme can be found in [3]. The support for the classical five-point scheme is shown in figure 5.2(b),and shows that introduction of cell face pressures ($\Phi_f = (\phi_N, \phi_S, \phi_E, \phi_W,)$) enables the normal velocity and pressure to be point-wise continuous at the cell faces.

5.2.3 Full Tensor Flux Approximation

Continuous normal flux and pressure discretization of the reservoir simulation pressure equation is required in order to honour correct local physical interface conditions between grid blocks with strong discontinuities in permeability. A consistent full tensor flux approximation requires an increase in support compared to the standard two-point flux. In general a nine-point scheme is required for approximation of equation 5.1 with a full (or diagonal) tensor in two-dimensions, as indicated in figure 5.3(a) for a Cartesian grid and figure 5.5(a) for a quadrilateral grid respectively. Here we review the derivation of the family of flux-continuous schemes presented in [3, 4, 5]. Emphasis is on the comparison and benefits of different quadrature points (explained in section 5.3 below) that belong to the family of flux continuous schemes derived in physical space. There are multiple motivations for the families of schemes for both full and diagonal tensor formulations and these are stated below. This is followed by a presentation of the quadrature parameterization on which the schemes are based.

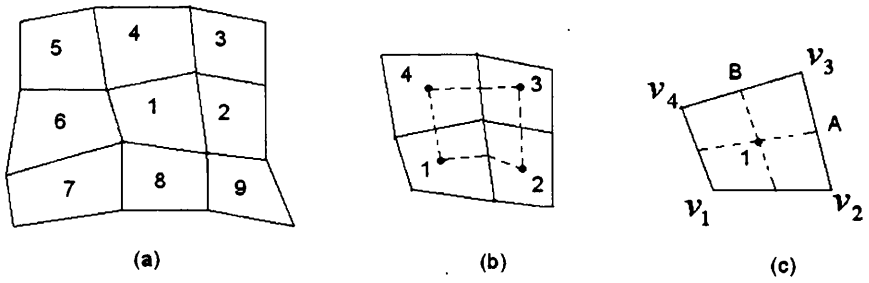

Figure 5.4: (a) Nine-point scheme support. (b) Dual-cell. (c) Four Sub-cells of cell 1, vertices $V_i, i = 1, ..4$

5.3 Family of Flux-Continuous Finite Volume Schemes - 2D Formulation

Local conservation, flux and pressure continuity are physical properties satisfied by the solution of equation 3.3. Local conservation is the basis upon which every finite volume scheme is built and relies on a flux balance, where relative to a given control-volume face, flux is subtracted from the left volume and the same flux is added to the right volume. We note that while flux continuity ensures local conservation, the converse is not necessarily true. Consequently we must therefore build flux continuity into the approximation of equation 3.3. The families of flux-continuous locally conservative control-volume distributed (CVD) finite volume schemes presented in [3, 6, 4, 22, 23, 24, 5, 12, 7, 8] have been developed for different gird types including cell vertex structured, unstructured and cell centred formulations in physical and transform space. Numerical convergence for a range of quadrature rules in physical space are presented in [5].

In this section we present the framework for the physical space formulation specialized to the structured cell centred quadrilateral grids (the formulation has also been developed for cell vertex structured and unstructured grids e.g. [4, 5, 7], also see Appendix C).

The nine node support of the scheme is indicated in figure 5.4(a). The scheme has cell centred flow and rock variables, so that the approximation points (or nodes) are shared by both variables and are at the centres of the primal grid cells. Thus in this case the primal grid cells are the control-volumes and the schemes are control-volume distributed CVD with respect to the primal grid cells, where the central control-volume is the cell with vertex position vectors $\mathbf{r}_{V_1}, \mathbf{r}_{V_2}, \mathbf{r}_{V_3}, \mathbf{r}_{V_4}$ and the scheme is centred on node 1, figure 5.4(c).

Dual-Cell

Each group of four cell centred nodes surrounding a primal grid vertex defines the fundamental corners of a *dual-cell*, as indicated by the dashed line in figure 5.4(b). The perimeter of each dual cell is defined by joining cell centres to cell edge mid-points as shown in figure 5.4(b).

Subcells

The dual-cells partition the primal quadrilateral grid cells (or control-volume) into sub-quadrilateral cells, which are called subcells [4]. Each control-volume and each dual-cell are comprised of four subcells, figure 5.4(b). Each subcell has one corner attached to a cell centre node and the opposite corner attached to a control-volume corner (a primal grid vertex). A subcell is illustrated in figure 5.4(c) with corner position vectors $\mathbf{r}_1, \mathbf{r}_A, \mathbf{r}_{V_3}, \mathbf{r}_B$. The two faces of a subcell attached to the primal grid vertex define two *sub-faces* of a parent control-volume, refer to the top right corner of the cell in figure 5.4(c), over which $(0 < q \leq 1]$, see figure 5.5.

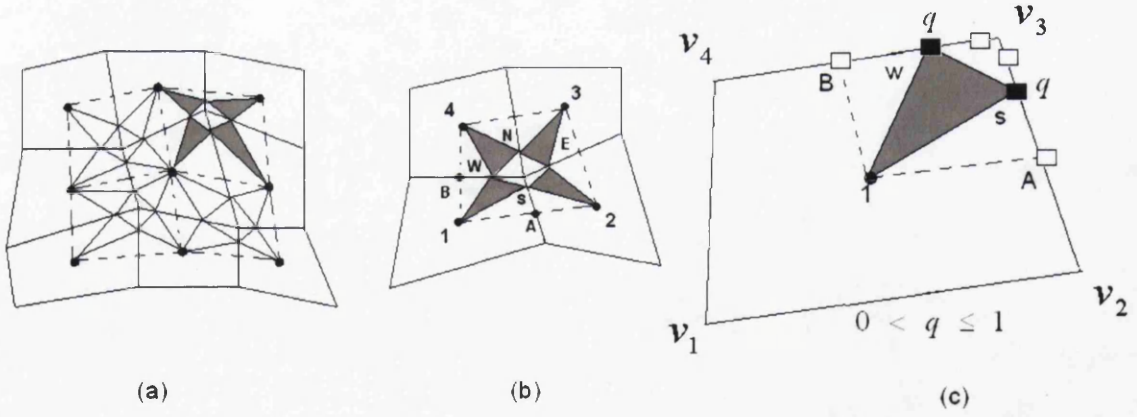

Figure 5.5: (a)Nine-point continuous pressure support, highlighted *dual-cell* dashed line. (b) Points of Flux-Continuity (N,S,E,W) on subcell faces of a *dual-cell* (c) Quadrature points on subcell faces *q=0.1*, $q = 1$ hollow squares, general q bold squares.

Pressure Sub-triangles

Pressure sub-triangles are defined within subcells as follows: Interface pressures $\phi_N, \phi_S, \phi_E, \phi_W$ are introduced on the four *sub-faces* inside each dual cell at specified positions (N, S, E, W), as defined in figure 5.5(b). Sub-triangles are then formed by connecting cell centres to the interface pressure positions and the sub-triangles indicate local piecewise linear support of pressure. For example figure 5.5(c) shows a subcell with sub-triangle $(1, S, W)$ inside the subcell, points (S, W) are indicated with solid squares. Introduction of interface pressures $\phi_N, \phi_S, \phi_E, \phi_W$ (figure 5.5(b)) automatically ensures point-wise pressure continuity across control-volume interfaces in a locally coupled system. Pressure gradients are therefore piecewise constant over the sub-triangles and are linear functions of discrete cell-centre and cell interface pressures.

5.3.1 Motivation for the Family of Schemes

Motivation for the family of flux-continuous schemes and flexibility in location of quadrature point with $0 < q \leq 1$ is to allow for improvement in accuracy e.g. *q=1/2* yields a significant gain in accuracy with order $O(h^6)$ truncation error for the Laplacian operator and $O(h^4)$ for an anisotropic constant diagonal tensor [3]. A nine point scheme will also reduce grid orientation effects [21] and flux-continuous nine-point schemes can improve upscaling even in the case of a diagonal tensor by detecting cross-flow [20, 12]. Variable q can also improve diagonal dominance of the full tensor approximation [3].

5.3.2 Family of CVD (MPFA)Schemes - Quadrature parameterization

The family of schemes is formed when imposing normal flux and pressure continuity conditions at the four positions (N, S, E, W), figure 5.5(b)) on the *sub-faces*, where

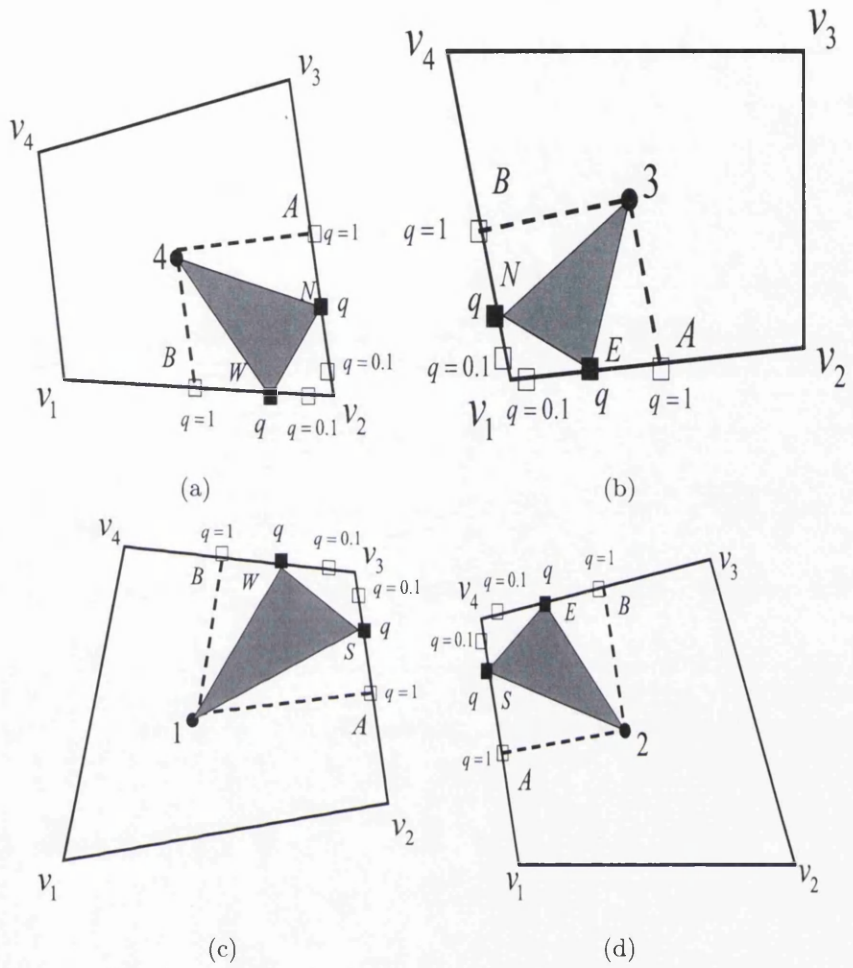

Figure 5.6: Quadrature parametrization on the sub-cell faces - exploded view of figure 5.5(b).

the four shaded triangles meet in a dual cell. On each *sub-face* the point of continuity is parameterized with respect to the subcell face by the variable q where referring to figure 5.5(c) the range of q is given by $(0 < q \leq 1]$. Specific quadrature points $q = 0.1,\ 1$ are illustrated in figure 5.6 (hollow squares) together with the subcell triangle construction for a generic value of q (solid squares). The quadrature point $q = 1$ corresponds to the point of intersection between the *sub-faces* and the *dual-cell* perimeter. Hence, for a given subcell, the points of continuity can lie anywhere in

the intervals $(0 < q \leq 1]$ on the two faces of a subcell inside a dual cell, that coincide with the control-volume *sub-faces*, and the value of q defines the quadrature point and hence the family of flux-continuous finite-volume schemes. Cell face pressures $\phi_N, \phi_E, \phi_S, \phi_W$ are introduced at N, E, S, W locations (figure 5.5(b)). Pressure sub-triangles are then defined with local triangular support within each quarter (*sub-cell*) of the *dual-cell* as shown (shaded triangle) in figure 5.5(b). Pressure ϕ, in local cell coordinates, then assumes a piecewise linear variation over each triangle. The most primitive member of the family of schemes (illustrated in figure 5.3(a)) corresponds to the quadrature point position coincident with the cell face mid-point i.e. $q = 1$. The general cell-centred flux-continuous schemes support is shown in figure 5.5(a).

The parametric variation in q is illustrated further using the sub-cell example of figure 5.5(c), with sub-cell containing sub-triangle $(1, S, W)$. Let $\mathbf{r}_1 = (x_1, y_1)$ denote the coordinates of the cell-centre and $\mathbf{r}_S = (x_S, y_S)$, $\mathbf{r}_W = (x_W, y_W)$ denote the local continuity coordinates. Then it is understood that the continuity position is a function of q with $\mathbf{r}_S(q)$ and $\mathbf{r}_W(q)$. The coordinate system of a physical cell is illustrated in figure 5.5(c), where the origin ($q = 0$) is the top right hand corner of the cell and $q = 1$ is the cell-face mid-point and is given as e.g. along the right hand cell face

$$\mathbf{r_V}(q) = \mathbf{r_{V_3}} + \frac{q}{2}(\Delta \mathbf{r_{V_{23}}}) \tag{5.7}$$

where

$$\Delta \mathbf{r_{V_{23}}} = ((x_{V_2} - x_{V_3}), (y_{V_2} - y_{V_3})), \quad \mathbf{r_{V_2}} = (x_{V_2}, y_{V_2}), \quad \mathbf{r_{V_3}} = (x_{V_3}, y_{V_3}) \tag{5.8}$$

However,it should be noted that a different parametric value could also be chosen along each subface so that $\mathbf{r}_S(q_1)$ and $\mathbf{r}_W(q_2)$ which leads to a variable support scheme, presented in [10].

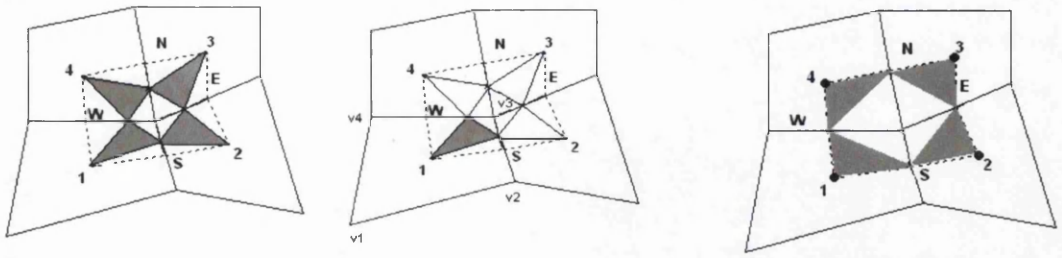

(a) (b) (c)

Figure 5.7: (a) Dual cell- Dashed line: Flux and pressure continuity at N,S,E,W, Quadrature q = 1/2 (b) Subcell of the Dual cell with pressure support. (c) One-sided quadrature (*Quadrature q = 1*).

5.3.3 Formulation of Scheme in *Physical Space*

Full tensor *transform* space and *physical* space flux approximations has been previously presented in [3, 4]. Here, we now consider the full tensor flux approximation in *physical* space. Note that while normal flux is continuous across an interface tangential flux can be discontinuous. As described in previous section, with respect to each *dual-cell* primal grid cell-face pressures $\Phi_f = \phi_N, \phi_E, \phi_S, \phi_W$ are introduced at the N, S, E, W locations indicated in figure 5.7(a). A local triangular support is introduced within each quarter of the *dual-cell* (sub-cell) as shown in figure 5.7(b). Pressure ϕ and the cell coordinates assume a piecewise linear variation over each triangle, for example, over the triangle of cell 1(figure 5.7(b)), given as:

$$\begin{aligned} \phi &= \xi\phi_S + \eta\phi_W + (1-\xi-\eta)\phi_1, \\ x &= \xi x_S + \eta x_W + (1-\xi-\eta)x_1, \\ y &= \xi y_S + \eta y_W + (1-\xi-\eta)y_1, \end{aligned} \tag{5.9}$$

(ξ, η) are area coordinates and $(x_S(q), y_S(q))$,$(x_W(q), y_W(q))$ are local continuity

coordinates and pressure is piece-wise continuous over each triangle. Piecewise constant Darcy fluxes are now constructed on each of the pressure sub-triangles belonging to the sub-cells of the *dual-cell* as shown in figure 5.7(b). The local linear pressure ϕ, is expanded in sub-triangle coordinates. The Darcy flux approximation for sub-triangle $(1, S, W)$ is given below.

$$\begin{pmatrix} \phi_\xi \\ \phi_\eta \end{pmatrix} = \begin{pmatrix} \phi_S - \phi_1 \\ \phi_W - \phi_1 \end{pmatrix} \tag{5.10}$$

and

$$\begin{pmatrix} x_\xi(q) \\ x_\eta(q) \end{pmatrix} = \begin{pmatrix} x_S(q) - x_1 \\ x_W(q) - x_1 \end{pmatrix}, \begin{pmatrix} y_\xi(q) \\ y_\eta(q) \end{pmatrix} = \begin{pmatrix} y_S(q) - y_1 \\ y_w(q) - y_1 \end{pmatrix} \tag{5.11}$$

Using equations 3.9, 5.10 and 5.11 the discrete Darcy velocity is defined as

$$v_h = -\mathbf{K^1} \nabla \phi_h = -\mathbf{K^1} \mathbf{G}(q) \begin{pmatrix} \phi_\xi \\ \phi_\eta \end{pmatrix} \tag{5.12}$$

Where $\mathbf{K^1}$ is the local permeability tensor of cell 1 and dependency of $\nabla \phi_h$ on quadrature point arises through

$$\mathbf{G}(q) \begin{pmatrix} \phi_\xi \\ \phi_\eta \end{pmatrix} = \begin{pmatrix} y_\eta(q) & -y_\xi(q) \\ y_\eta(q) & x_\xi(q) \end{pmatrix} \frac{1}{J(q)} \begin{pmatrix} \phi_S - \phi_1 \\ \phi_w - \phi_1 \end{pmatrix} \tag{5.13}$$

where approximate $r_\xi(q)$ and $r_\eta(q)$ are defined by equation 5.11. $J(q)$ is the jacobian matrix as a function of quadrature q. Note that (x_1, y_1) is the position vector of the cell centre of cell 1 in figure 5.4, $\mathbf{r}_{V_3} = (x_{V_3}, y_{V_3})$ is the position vector of the corner vertex V_3 of the cell. The normal flux at the left hand side of S(figure 5.7(a)) is resolved along the outward normal vector $dL_S = \frac{1}{2}((y_{V_3} - y_{V_2}), -(x_{V_3} - x_{V_2}))$ (figure 5.7(b)) and is expressed in terms of the general tensor T as

$$F_S^1 = v_h \cdot dL_S = -(T_{11}^1 \phi_\xi + T_{12}^1 \phi_\eta)|_S^1 \tag{5.14}$$

where it is understood that the resulting coefficients of $(\phi_\xi, \phi_\eta)|_S^1$ are denoted by $T_{11}|_S^1$ and $T_{12}|_S^2$ and are sub-cell approximations in *physical space*, of the general tensor

components given in equation 3.11 at the left hand face of S. A similar expression for flux is obtained at the right hand side of S from cell 2(figure 5.7(b)). Similarly sub-cell fluxes are resolved on the two sides of the other faces at W,N and E. Flux continuity is then imposed across the cell interfaces at the specified positions N,S,E and W (figure 5.7(a))for a specified quadrature point q (section 3.3.2 above). The local *physical space* flux continuity conditions are now defined in the dual cell and expressed as

$$\begin{aligned} F_N &= -(T_{11}\phi_\xi + T_{12}\phi_\eta)|_N^3 = -(T_{11}\phi_\xi + T_{12}\phi_\eta)|_N^4, \\ F_S &= -(T_{11}\phi_\xi + T_{12}\phi_\eta)|_S^1 = -(T_{11}\phi_\xi + T_{12}\phi_\eta)|_S^2, \\ F_E &= -(T_{12}\phi_\xi + T_{22}\phi_\eta)|_E^2 = -(T_{12}\phi_\xi + T_{22}\phi_\eta)|_E^3, \\ F_W &= -(T_{12}\phi_\xi + T_{22}\phi_\eta)|_W^1 = -(T_{12}\phi_\xi + T_{22}\phi_\eta)|_W^4 \end{aligned} \tag{5.15}$$

Where e.g.

$$-(T_{11}\phi_\xi + T_{12}\phi_\eta)|_S^1 = -(T_{11}|_S^1\phi_\xi|^1 + T_{12}|_S^1\phi_\eta|^1) \tag{5.16}$$

and $T|_\sigma^i$ denotes the *physical space* tensor approximation as a function of quadrature point q for subcell i and interface point $\sigma = \sigma(q)$ resulting from normal Darcy velocity resolution on the control-volume faces.

Using the local piecewise linear variation of pressure over each sub-triangle in the dual cell equation 5.15 can be expressed explicitly with respect to potential differences as

$$
\begin{aligned}
F_N &= -(T_{11}|_N^4(\phi_N - \phi_4) + T_{12}|_N^4(\phi_4 - \phi_W)) = -(T_{11}|_N^3(\phi_3 - \phi_N) + T_{12}|_N^3(\phi_3 - \phi_E)) \\
F_S &= -(T_{11}|_S^1(\phi_S - \phi_1) + T_{12}|_S^1(\phi_W - \phi_1)) = -(T_{11}|_S^2(\phi_2 - \phi_S) + T_{12}|_S^2(\phi_E - \phi_2)) \\
F_E &= -(T_{12}|_E^2(\phi_2 - \phi_S) + T_{22}|_E^2(\phi_E - \phi_2)) = -(T_{12}|_E^3(\phi_3 - \phi_N) + T_{22}|_E^3(\phi_3 - \phi_E)) \\
F_W &= -(T_{12}|_W^1(\phi_S - \phi_1) + T_{22}|_W^1(\phi_W - \phi_1)) = -(T_{12}|_W^4(\phi_N - \phi_4) + T_{22}|_W^4(\phi_4 - \phi_W))
\end{aligned}
\tag{5.17}
$$

Where, e.g., for sub-cell 4 in figure 5.7 (c) $\phi_\xi = (\phi_N - \phi_4)$. The linear system of equation can be written as

$$F = A_L\Phi_f + B_L\Phi_v = A_R\Phi_f + B_R\Phi_v \tag{5.18}$$

where $F = (F_N, F_S, F_E, F_W)$ are the fluxes defined in the dual-cell and $\Phi_f = (\phi_N, \phi_S, \phi_E, \phi_W,)$ represents interface pressures. Similarly $\Phi_v = (\phi_1, \phi_2, \phi_3, \phi_4,)$ represents cell centered pressures. Thus the four interface pressures are expressed in terms of the four cell centered pressures. From equation 5.18 Φ_f is eliminated to obtain the flux coefficient matrix given as

$$F = (A_L(A_L - A_R)^{-1}(B_R - B_L) + B_L)\Phi_v \tag{5.19}$$

This illustrates a key advantage of the method as in one dimension, the cell-face pressures are determined locally in terms of the cell centered pressures in a preprocessing step thus avoiding introduction of the interface pressure equations into the assembled discretization matrix. Therefore flux continuity in the case of a general tensor is obtained while maintaining the standard single degree of freedom per cell. Since the continuity equations depend on both ϕ_ξ and ϕ_η(unless a diagonal tensor is assumed with cell-face midpoint quadrature resulting in a 2-point flux), the interface pressures $\Phi_f = (\phi_N, \phi_S, \phi_E, \phi_W,)$ are locally coupled and each group of four interface pressures is determined simultaneously in terms of the four cell centered pressures whose union contains the continuity positions.

5.3.4 Discrete Flux Approximation for Structured Grids

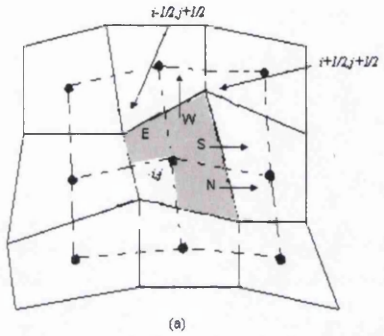

Figure 5.8: (a) Control volume quadrant fluxes on a cartesian grid.

Once the flux coefficient matrix has been calculated (equation 5.19) the discrete scheme is defined by approximating equation 3.12 with the sum of eight fluxes, two per control volume quadrant as in figure 5.8(a), the top right hand *dual-cell* has index $i+1/2, j+1/2$. The net flux for the respective right hand side and top cell faces (in a global assembly)is given by

$$\begin{aligned} F_{i+1/2,j} &= F_{N_{i+1/2,j-1/2}} + F_{S_{i+1/2,j+1/2}} \\ F_{i,j+1/2} &= F_{E_{i-1/2,j+1/2}} + F_{W_{i+1/2,j+1/2}} \end{aligned} \tag{5.20}$$

Finally, the discrete scheme is completed by defining the closed integral of net flux over the control-volume *(i,j)* which results in

$$F_{i+1/2,j} - F_{i-1/2,j} + F_{i,j+1/2} - F_{i,j-1/2} = M \tag{5.21}$$

where M is the specified flow rate. It should also be noted here that for any quadrature point q, other than the cell face mid-point *(q=1)*, a nine point flux-continuous scheme is always obtained regardless of whether the tensor is full or diagonal.

Although, the formulation of the family of flux-continuous finite-volume schemes in *physical space* leads to a discretization matrix which is non-symmetric in the general

case. However, it is possible to derive an alternative formulations in *transform space* [3, 24] that yield a symmetric positive definite (SPD) discrete matrix. And it will form the basis for next chapter, where it be described in detail.

5.3.5 Formulation of Scheme in *Physical Space*- On Unstructured Grids

This section presents a brief summary of the formulation of flux-continuous schemes for unstructured grids (for detailed formulation see Appendix C). In this case pressures and permeabilities are vertex centered. A control-volume is constructed around each vertex by joining cell edge mid-points to cell centers for all cells common to a given vertex. The physical permeability is assigned to the control-volume. Using an analogous procedure to that for the structured grids the flux continuity formulation is carried over directly to treat unstructured triangular grids [4]. For a triangular grid three flux continuity conditions are imposed within each triangle where a local coordinate system is associated with each subcell of a given triangle, figure 5.9(a). Interface pressures $\Phi_f = (\phi_N, \phi_S, \phi_E)$ are introduced in a similar fashion to section 5.2.2 and three subcell triangular basis functions are formed joining vertex pressures $\Phi_v = (\phi_1, \phi_2, \phi_3)$ with adjacent interface pressures Φ_f. The pressure assumes a piecewise linear variation over each subcell triangle and the derivatives ϕ_x and ϕ_y are linear functions of Φ_f and Φ_v.

5.3.6 Discrete Flux Approximation for Unstructured Grids

Similar to the structured case the system of fluxes for unstructured grids are rearranged in the form

$$F = A_L\Phi_f + B_L\Phi_v = A_R\Phi_f + B_R\Phi_v \tag{5.22}$$

where $\Phi_f = (\phi_N, \phi_S, \phi_E)$ represents the interface pressures for triangular grids.

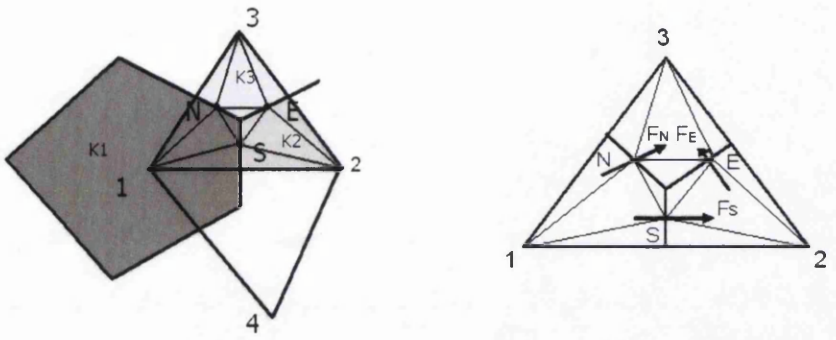

(a) (b)

Figure 5.9: (a)Control-volume , Flux and pressure continuity positions at N, S, E shown on a Triangle. Quadrature q = 1/2. (b)Sub-cell triangular basis functions and fluxes at interface.

Similarly $\Phi_v = (\phi_1, \phi_2, \phi_3)$ represents cell vertex pressures for triangular grids. Thus the interface pressures can now be expressed in terms of the cell vertex pressures. From equation 5.22 Φ_f can be eliminated to obtain the flux coefficient matrix as for structured grid and is given as

$$F = (A_L(A_L - A_R)^{-1}(B_R - B_L) + B_L)\Phi_v \tag{5.23}$$

After calculating the flux coefficient matrix the Gaussian integral of divergence over each control-volume is obtained by global flux assembly.

5.4 Family of Flux-Continuous CVD (MPFA) Schemes - 3D Formulation

Subsurface reservoir dimensions can have very different length scales in the vertical and horizontal directions. Moreover, layers, fractures and faults all give rise to complex physical geometries and grid-blocks that represent the underlying geology are rarely orthogonal. This requires flexible gridding for a consistent numerical

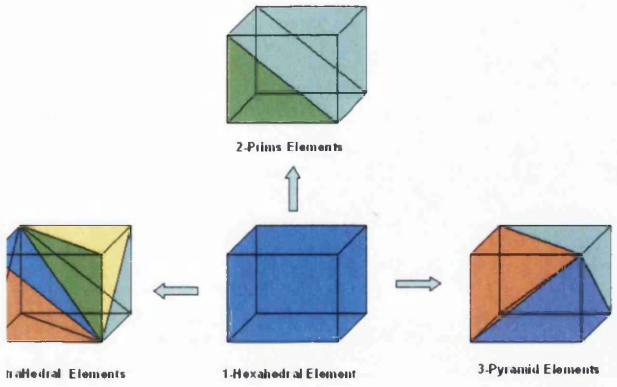

(a)

Figure 5.10: (a) Decomposition of hexahedral element into 2-prism, 6-tetrahedral and 3-pyramid elements

method to be applicable. Maximum flexibility in grid generation is achieved when allowing grids to be comprised of any connecting combination of hexahedra, tetrahedra, prism and pyramid elements [25]. This is an important motivating factor for the schemes presented here. For illustration of element types a regular hexahedral (block) element can easily be decomposed into either two-prisms, five or six-tetrahedral or three-pyramid elements as shown in figure 5.10.

The schemes presented here are vertex centred, where for a given control-volume surrounding a grid vertex, flow variables and rock properties are assigned to grid vertices and rock properties are piecewise constant with respect to the associated control-volumes and thus the schemes are control-volume distributed or CVD. Therefore, discontinuities in rock properties occur over control-volume faces. The physical constraints that must be enforced are continuity of pressure and continuity of normal flux across each interface that separates a change in the geological medium, therefore the continuity conditions must be applied across the control-volume faces.

The initial or primal grid considered here is comprised of elements i.e. combinations of tetrahedra, prisms, pyramids and hexahedra elements (also called cells), with

corners defined by grid vertices. A polyhedral control-volume is built around each grid vertex, which generates a *primal-dual* grid.

Control-volume

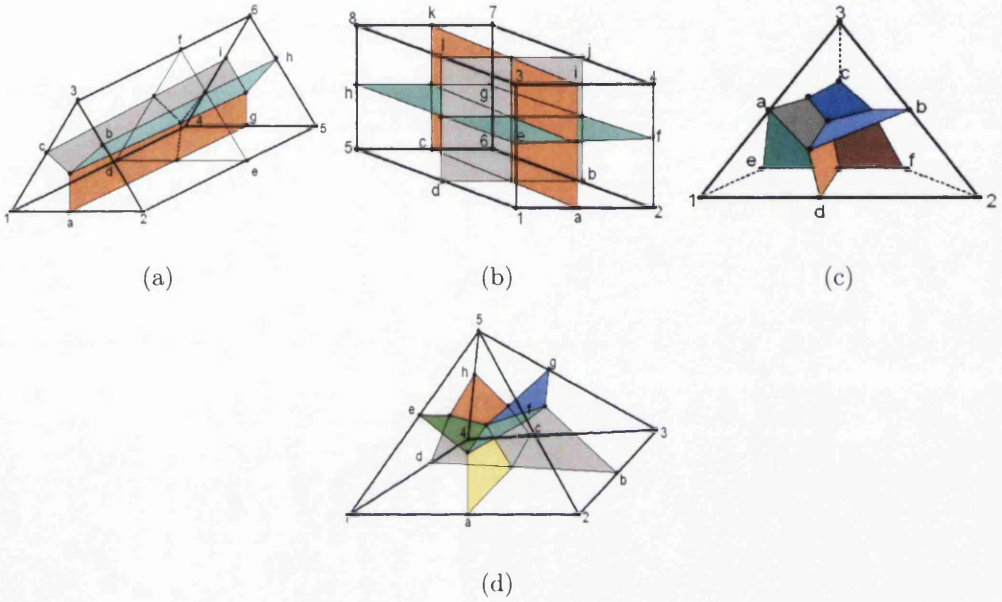

(a) (b) (c)

(d)

Figure 5.11: (a) Constraint points and boundary for a prism element. (b) Constraint points and boundary for a hexahedra element. (c) Constraint points and boundary for a pyramid element. (d) Constraint points and boundary for a tetrahedral element. (Quadrature q = 1)

Construction of the control-volume starts in a primal grid cell. The cell centre (or circumcentre) is joined to cellface mid-points, cellface mid-points are joined to cell-edge mid-points. As a result the primal grid cells are decomposed into sub-hexahedra or subcells [7] figure 5.11. In each case the number of subcells corresponds to the number of vertices defining the primal element. A hexahedra element has eight vertices and thus eight sub-cells, one for each vertex. Similarly, a prism element has six, the pyramid element has five and the tetrahedral element has four sub-cells respectively as shown in figure 5.11. Note each subcell is always a hexahedra. Each

subcell belongs to the control-volume of the unique vertex to which it is attached. Cell vertex control-volumes are defined by a local assembly or recomposition at each primal grid vertex of all subcells that are attached to the vertex. The resulting set of polyhedral control-volumes defines a dual grid relative to the primal grid which we call the primal-dual.

5.4.1 3D-Finite Volume Approximation

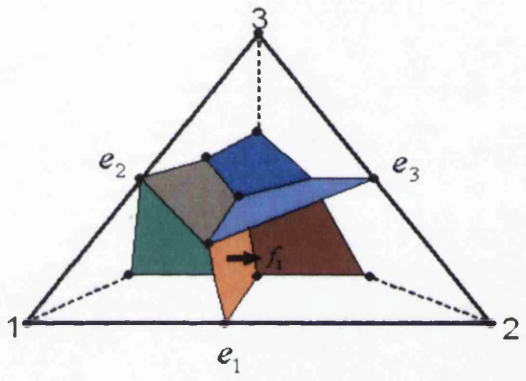

(a)

Figure 5.12: (a) Control-volume faces and edges of primal cell in tetrahedral element.

As with all finite volume schemes we begin with application of the Gauss divergence theorem to the integral of divergence, over a given control-volume. A unique discrete flux is then constructed for each control-volume face and the closed integral of flux is approximated by the sum of discrete outward normal fluxes. For a given face between two neighbouring control-volumes, the unique flux is subtracted from the left-hand control-volume and added to right-hand control-volume leading to a locally conservative scheme with respect to the polyhedral control volumes that contain the discrete permeability tensors with flow variables defined at their vertices. Within the flux build process, fluxes are approximated on control-volume subcell faces inside each primal grid cell, in analogous step to 2-D [3, 4, 5]. The construction of flux-continuity

conditions are presented below. Each subcell flux is associated with a unique cell edge, and the number of primal cell fluxes constructed inside each primal cell is equal to the number of cell edges, 12 for hexahedra, 9 for prism, 8 for a pyramid and 6 for tetrahedra.

The subcell fluxes are accumulated with respect to their primal cell edges within an assembly process. The edge index $e(i,j)$ refers to the j^{th} primal edge attached to vertex i, e.g. figure 5.12. The net edge based single phase flux $F_{e_{i,j}(\phi)}$ associated with edge $e(i,j)$ is comprised of the sum of adjacent subcell fluxes that belong to the primal grid cells with common edge $e(i,j)$, with

$$F_{e_{i,j}(\phi)} = \sum_{\sigma=1}^{N_{SCE}} F_{\sigma}(\phi) \tag{5.24}$$

where N_{SCE} is the number of subcells attached to the edge $e(i,j)$. After assembly of net edge-based flux, the discrete scheme for each vertex i is completed with closed integral of net Gaussian flux approximated by sum of net edge-based fluxes connected to the i^{th} vertex. For single phase flow on unstructured grids the assembled finite volume scheme at vertex i can be written concisely as:

$$\sum_{j=1}^{N_{edV}} F_{e(i,j)}(\phi) = M_i \tag{5.25}$$

where summation is over all N_{edV} edges passing through the i^{th} grid vertex, (M_i denotes a specified flow rate at vertex i, or is zero otherwise).

5.4.2 Flux Continuity in Hexahedra, Tetrahedra and Prism Elements

In this section a continuous flux and pressure family of schemes (*q-family*) formulation is presented for hexahedra, tetrahedra, prism and pyramid elements. This work is based on the flux continuous schemes of [3, 4] and 3-D cell vertex formulations

presented in [52, 70]. The continuity conditions for the hexahedra, tetrahedral and prism elements follow an analogous procedure described below. There is an important exception in the case of the pyramid element and this treatment is discussed in the next section.

By definition of a cell-vertex CVD formulation any variation in permeability will occur inside the primal grid cell across interior subfaces of adjacent control-volumes, which also correspond to faces of the subcells. Thus continuity of flux and pressure must be imposed across the interior subfaces.

Interface pressures are introduced in a 3D grid element, at one point on each control-volume subface, establishing point-wise continuity in pressure (figure 5.11), which is also the point at which normal flux continuity is enforced. The local position of flux continuity is parameterized in the local subcell-face coordinate systems with parametric variables (q1,q2).

Quadrature parameterization q-family in 3D

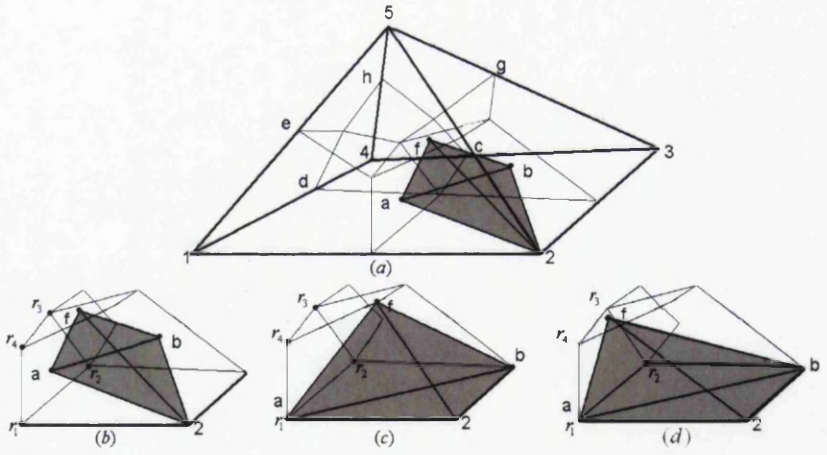

Figure 5.13: (a) Pyramid cell with pressure support. (b) Pressure support on a subcell of pyramid element for quadrature $q = \frac{1}{2}$. (c) Pressure support on subcell of pyramid element for quadrature $q = 1$. (d) Pressure support on subcell of pyramid element for variable quadrature q.

Similar to two-dimensional construction of the flux continuous schemes [3, 4, 5] a quadrature parameterization is introduced in the three-dimensional formalism, where local position of continuity defines scheme quadrature as function of q, where q varies over (0, 1], consequently the co-ordinates of the continuity position define the flux-continuous *q-family of schemes.* The co-ordinate system of a physical pyramid cell is illustrated in figure 5.13. Referring to the subcell face defined by coordinates (r_1, r_2, r_3, r_4), the origin $(q = 0)$ is at the top right hand corner of the figure 5.13(b). The subcell face mid-point quadrature $q = \frac{1}{2}$ with a variable quadrature q is shown in figure 5.13(b) and 5.13(d) respectively. The quadrature $q = 1$ refers to the left hand bottom corner of the subcell face shown in figure 5.13(c) and is given by

$$r_a = r_1(1-\xi)(1-\eta) + r_2\xi(1-\eta) + r_3\xi\eta + r_4(1-\xi)\eta \tag{5.26}$$

where

$$r_i = (x_i, y_i, z_i), i = 1, ...4 \tag{5.27}$$

While the quadrature parametrization $q_1 = (1-\xi), q_2 = (1-\eta)$ can vary differently on three different faces of the subcell, in this chapter a symmetric variation is considered on each subcell face with $q_1 = q_2 = q$, though in [10] unequal is explored, which will be further discussed in chapter 8.

As in [3, 4, 5] parameterization of the continuity points leads to a general choice for flux quadrature thus defining the *q-family of schemes.* The number of interface pressures matches the number of edges of the primal cell, thus the number of components of vector ϕ_f is equal to 12 for a hexahedra, 9 for prism, 8 for a pyramid and 6 for a tetrahedra. The local vector of primary variables (global degrees of freedom) of the pressure system with respect to a primal element are denoted by $\phi_v = (\phi_1, ...\phi_{N_V})$, where N_V is equal to the local number of vertices, 8 for a hexahedra, 6 for a prism, 5 for a pyramid and 4 for a tetrahedral element as shown in figure 5.11.

The inward view from a primary corner vertex attached to a hexahedral, tetrahedral or prism element, looking *inside* the respective element is of the three interior subcell faces on which the interface pressures lie. Joining each vertex with its 3 adjacent interface pressures creates a set of subcell tetrahedral basis functions. (While the same is true for the 4 base nodes of a pyramid, the summit node view sees four interfaces, figure 5.11(c). And as a consequence construction of the scheme on pyramid element needs special consideration (see section 5.4.3).

Construction of Scheme

Piecewise constant subcell physical space fluxes are approximated using the local tetrahedral basis functions over which pressure is linear and gradients are piecewise constant. For each subcell

$$v_i = -\mathbf{K_i}\nabla\phi_\mathbf{i}, \qquad i = 1, ...N_v \tag{5.28}$$

where K_i and $\nabla\phi_i$ are the i^{th} subcell permeability tensor and gradient respectively.

First the formulation is illustrated for a primal hexahedra element, figure 5.11(b) shows the eight subcells and permeabilities inside a primal hexahedral cell with the 8 vertex pressures. The potential gradient approximation $\nabla\phi_1$ in subcell 1 is expressed as

$$\begin{pmatrix} \phi'_{x1} \\ \phi'_{y1} \\ \phi'_{z1} \end{pmatrix} = \begin{pmatrix} A_{x1}(q) & A_{x2}(q) & A_{x3}(q) \\ A_{y1}(q) & A_{y2}(q) & A_{y3}(q) \\ A_{z1}(q) & A_{z2}(q) & A_{z3}(q) \end{pmatrix} \begin{pmatrix} \phi_a - \phi_1 \\ \phi_d - \phi_1 \\ \phi_e - \phi_1 \end{pmatrix} \tag{5.29}$$

Where the coefficients follow from the piecewise linear tetrahedral basis functions (alternatively via Taylor series) and are well known [124]. The discrete physical space flux corresponding to subcell 1 at interface a figure 5.11(b) is then defined by

$$F_{1a} = A_a \vec{v_1} \cdot \hat{n_a} \tag{5.30}$$

Where $\hat{n_a}$ is the outward normal on the interface at a pointing away from vertex 1. Note that the flux can also be expressed in terms of the approximate general tensor where

$$F_{1a} = -\frac{1}{4}(T^1_{11}(\phi_a - \phi_1) + T^1_{12}(\phi_d - \phi_1) + T^1_{13}(\phi_e - \phi_1)) = -\frac{1}{4}\sum_{j=1}^{3} T^1_{1j}\Delta\phi_{f_{j,1}} \quad (5.31)$$

Where $T^1_{1j}, j = 1, 2, 3$ are defined at a and are functions of subcell 1 geometry and $\triangle\phi_{f_{j,1}}, j = 1, 2, 3$ are the differences between interface pressures at (a, d, e) and local vertex 1.

Expressions for the other physical space subcell fluxes are obtained in a similar fashion. Fluxes resolved on each side of the common subfaces are now equated to obtain a set of flux continuity conditions with number matching that of the number of local interface pressures (and thus edges) within the primal element. For the primal hexahedra element, fluxes are defined at interfaces $a, b, c, d, e, f, g, h, i, j, k$ and l at a physical position on each subface that determines the quadrature, defined by q. The equations of continuity at these points are:

$$\begin{array}{lll}
\vec{v_1}\cdot\vec{n_a} = \vec{v_2}\cdot\vec{n_a} & \vec{v_6}\cdot\vec{n_c} = \vec{v_5}\cdot\vec{n_c} & \vec{v_3}\cdot\vec{n_e} = \vec{v_1}\cdot\vec{n_e} \\
\vec{v_2}\cdot\vec{n_b} = \vec{v_6}\cdot\vec{n_b} & \vec{v_5}\cdot\vec{n_d} = \vec{v_1}\cdot\vec{n_d} & \vec{v_4}\cdot\vec{n_f} = \vec{v_2}\cdot\vec{n_f} \\
\vec{v_8}\cdot\vec{n_k} = \vec{v_7}\cdot\vec{n_k} & \vec{v_8}\cdot\vec{n_g} = \vec{v_6}\cdot\vec{n_g} & \vec{v_3}\cdot\vec{n_i} = \vec{v_4}\cdot\vec{n_i} \\
\vec{v_7}\cdot\vec{n_l} = \vec{v_3}\cdot\vec{n_l} & \vec{v_7}\cdot\vec{n_h} = \vec{v_5}\cdot\vec{n_h} & \vec{v_4}\cdot\vec{n_j} = \vec{v_8}\cdot\vec{n_j}
\end{array} \quad (5.32)$$

Where $\vec{n_a}, \vec{n_b}, \vec{n_c}, \vec{n_d}\vec{n_e}, \vec{n_f}, \vec{n_g}, \vec{n_h}, \vec{n_i}, \vec{n_j}, \vec{n_k}$ and $\vec{n_l}$ are the outward normals. The continuity conditions of equation 5.32 are next expressed (in a similar fashion as 2D formulation) as

$$F = A_L\phi_f + B_L\phi v = A_R\phi_f + B_R\phi_v \quad (5.33)$$

Where ϕ_f are the interface pressures and ϕ_v are vertex pressures defined above. A_L, B_L, A_R and B_R are matrices whose entries are also functions of quadrature parametriza-

tion q. The interface pressure ϕ_f in equation 5.33 can now be expressed in terms of cell vertex pressures ϕ_v (as in 2D formulation) yielding:

$$F = (A_L((A_L - A_R)^{-1}(B_R - B_L)) + B_L)\phi_v \tag{5.34}$$

Thus the cell-face pressures are eliminated from the flux by being determined locally in terms of the primal cell vertex pressures in pre-processing step, avoiding introduction of the interface pressures equation into the assembled discretization matrix. By expressing the continuity conditions as at a

$$F_a = -\frac{1}{4}\sum_{j=1}^{3} T_{1j}^1 \Delta\phi_{f_{j,1}} = -\frac{1}{4}\sum_{j=1}^{3} T_{1j}^2 \Delta\phi_{f_{j,2}} \tag{5.35}$$

where j sums over the 3 interior subcell face potential values, leads to the alternative form

$$AF = -\Delta\phi_v \tag{5.36}$$

where the entries of matrix A are local inverse tensor element combinations and

$$\Delta\phi_v = (\phi_{21}, \phi_{31}, \phi_{43}, \phi_{42}, \phi_{84}, \phi_{73}, \phi_{51}, \phi_{75}, \phi_{86}, \phi_{87}, \phi_{62}, \phi_{65}) \tag{5.37}$$

are the differences of vertex pressures. An analogous procedure is used for prismatic and tetrahedral elements. Consistency of the formulation follows from equation 5.37 which shows that flux is zero for constant potential. The relationship with the mixed method can also be deduced from equation 5.36, see [4, 24] for details. The above systems equations 5.36,5.37 represent the generalisation of the standard flux with harmonic coefficients to general elements with families of schemes defined by quadrature point q.

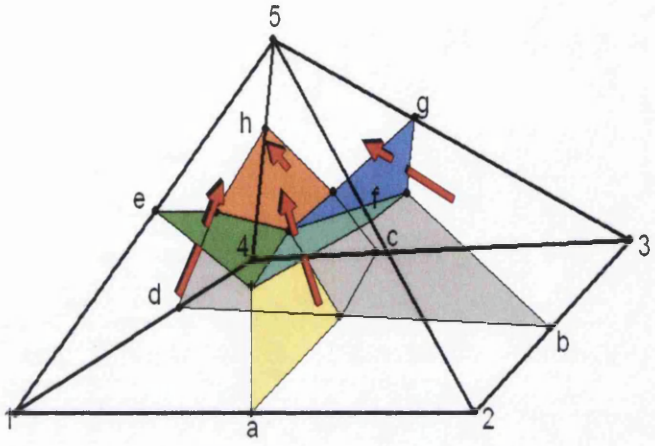

Figure 5.14: Control-volume faces, Flux and pressure continuity positions at a, b, c, d, e, f, g and h shown on a Pyramid element. (*quadrature q = 1)*

5.4.3 Continuous Flux in the Pyramid Element

The pyramid element is comprised of 4 sub-hexahedra and 1 octahedral sub-cell, where 4 hexahedral sub-cells belong to the 4 base node control volumes and the octahedral sub-cell belongs to the summit node control volume, figure 5.14. Unlike hexahedra, tetrahedral and prism elements where each node view inside the respective element sees three interior subcell faces, for the pyramid, the summit node view sees four subcell faces, figure 5.14. Hence, construction of the scheme on a pyramid element needs special consideration.

There are eight interfaces inside each pyramid element and there is one flux corresponding to each interface. For construction of the scheme in 3D a face potential is introduced at each interface (total of 8) to impose continuity in pressure. The face potentials along with the vertex potentials are used to define potential gradients inside each of the sub-control volumes in the pyramid which are used to define velocity at each interface. Velocities are then used to approximate flux at each interface. For the base vertex subcells, flux continuity is imposed across each subinterface between control volumes as above where

$$\begin{aligned} \vec{v_1} \cdot \vec{n_a} = \vec{v_2} \cdot \vec{n_a} \quad \vec{v_3} \cdot \vec{n_c} = \vec{v_4} \cdot \vec{n_c} \\ \vec{v_2} \cdot \vec{n_b} = \vec{v_3} \cdot \vec{n_b} \quad \vec{v_4} \cdot \vec{n_d} = \vec{v_1} \cdot \vec{n_d} \end{aligned} \tag{5.38}$$

The special case of the scheme is illustrated here for the summit node and subcell for quadrature $q = 1$, and is generalized for any continuity position on each interface.

For region 5 (where we have 4 interfaces around the node 5) we have one extra degree of freedom. In order to treat this case we couple three interfaces at a time to the summit node and obtain equations similar to equation 5.38 with a total of 4 sets of equations involving node 5, where the interfaces attached to node 5 involve (in anti-clockwise direction) *h-e-f, e-f-g, f-g-h* and *g-h-e*, figure 5.14. The normal fluxes across the interfaces are based on velocities at points a, b, c, d, e, f, g and h. The constraint equations at these points are:

$$\begin{aligned} \vec{v_1} \cdot \vec{n_e} = \vec{v_5} \cdot \vec{n_e} \quad \vec{v_3} \cdot \vec{n_g} = \vec{v_5} \cdot \vec{n_g} \\ \vec{v_1} \cdot \vec{n_f} = \vec{v_5} \cdot \vec{n_f} \quad \vec{v_4} \cdot \vec{n_h} = \vec{v_5} \cdot \vec{n_h} \end{aligned} \tag{5.39}$$

Equations 5.38 and 5.39 then define 8 algebraic flux continuity equations for the interface pressures. These equations can then be expressed in the form of equation 5.34 or equation 5.36. Thus three sub-cell fluxes are obtained with respect to each base vertex and four sub-cell fluxes with respect to the summit vertex. Consistency of the formulation is verified below, using a linear test case with homogeneous permeability tensor and using uniform and perturbed pyramid grid elements, exact values for numerical pressure and velocities are obtained.

5.5 Numerical Convergence Study

The aim of this study is to test the effect of quadrature point on convergence. While, numerical convergence tests in transform space have previously been performed by Edwards and Rogers in [3] and Eigestad *et al.* in [82] presents numerical convergence of the default member of the family of flux-continuous schemes considered

here i.e for q=*1*. A study of numerical convergence for the family of flux-continuous schemes in terms of a range of quadrature points was first presented in [5] and forms part of this work and is presented here. In this section firstly, a *physical* space numerical convergence study is presented for structured and unstructured grids in 2D followed by *physical* space numerical convergence study in 3D, for a series of test cases.

In all test cases the permeability field remains fixed under grid refinement, ensuring that each problem is invariant with respect to each grid level for the convergence study.

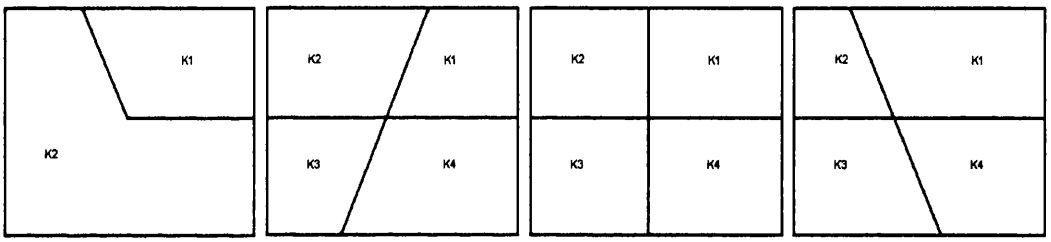

Figure 5.15: Different subdomains with internal discontinuous permeabilities. 3(a) Subdomain with discontinuity along $\theta = 2\pi/3$. 3(b) Subdomain with discontinuity along $\theta = \pi/3$. 3(c) Subdomain with discontinuity along $\theta = \pi/2$. 3(d) Subdomain with discontinuity along $\theta = 2\pi/3$.

5.5.1 Convergence results on 2D structured grids (*physical space*

In this section convergence study results for the family of flux-continuous schemes for a range of quadrature points are presented ($q = 0.1, 0.5, 0.287, 1$). where $q = 0.287$ is the *Gauss quadrature point.* A numerical convergence study is performed for each of the domains illustrated in figure 5.15 where subdomain $K_1 ... K_4$ indicates the variation in the permeability field. The different types of grid used are shown in figure 5.16. The Discrete L_2 *norm* is used to investigate pressure and velocity errors, which is

defined for pressure and velocity as

$$||\phi_h - \phi||_{L_2} = \Big(\frac{\sum_i (V_i(\phi_{h,i} - \phi_i)^2)}{\sum_i V_i}\Big)^{1/2} \tag{5.40}$$

$$||f_h - f||_{L_2} = \Big(\frac{\sum_j (Q_j(f_{h,j} - f_j)^2)}{\sum_j Q_j}\Big)^{1/2} \tag{5.41}$$

Here, $f = -\mathbf{v} \cdot \mathbf{n}$ (where $\mathbf{v} = \mathbf{K}\nabla\phi$) is the edge normal flow velocity. Subscript h refers to numerical solution. Further V_i is the volume of the grid cell i,and Q_j is the volume associated with edge j (where two cells are separated by edge j). The grid refinement levels used for the L_2 *norm* calculation were 8x8, 16x16, 32x32, and 64x64 and were used for all test cases in 2D. In each case dirichlet boundary conditions are prescribed via the exact solutions.

CASE 1:

The first example involves uniform flow over a rectangular domain. The medium is divided into two parts as shown is figure 5.17(a). The permeability field is discontinuous and permeability ratio is 1/10 across the medium discontinuity. The discontinuity is aligned along the line $rx + sy = 0$, where $r = tan(\pi/3)/(1 + tan(\pi/3))$ and $s = 1/(1 + tan(\pi/3))$.The pressure field is piecewise linear and varies as

$$\phi(x, y) = \begin{cases} rx + sy, & rx + sy < 0, \\ 10(rx + sy), & rx + sy > 0. \end{cases} \tag{5.42}$$

The diagonal permeability tensor $\mathbf{K} = c\mathbf{I}$, where $c = 10$ for $rx + sy < 0$ and $c = 1$ for $rx + sy > 0$. The numerical solution shown in figure 5.17(b) was obtained using a grid aligned along the discontinuity. The numerical solution was found to be exact for *any* quadrature point q, which is a result of using piecewise linear variation in pressure over each subcell and exact (physical space) geometry representation in the piecewise constant fluxes.

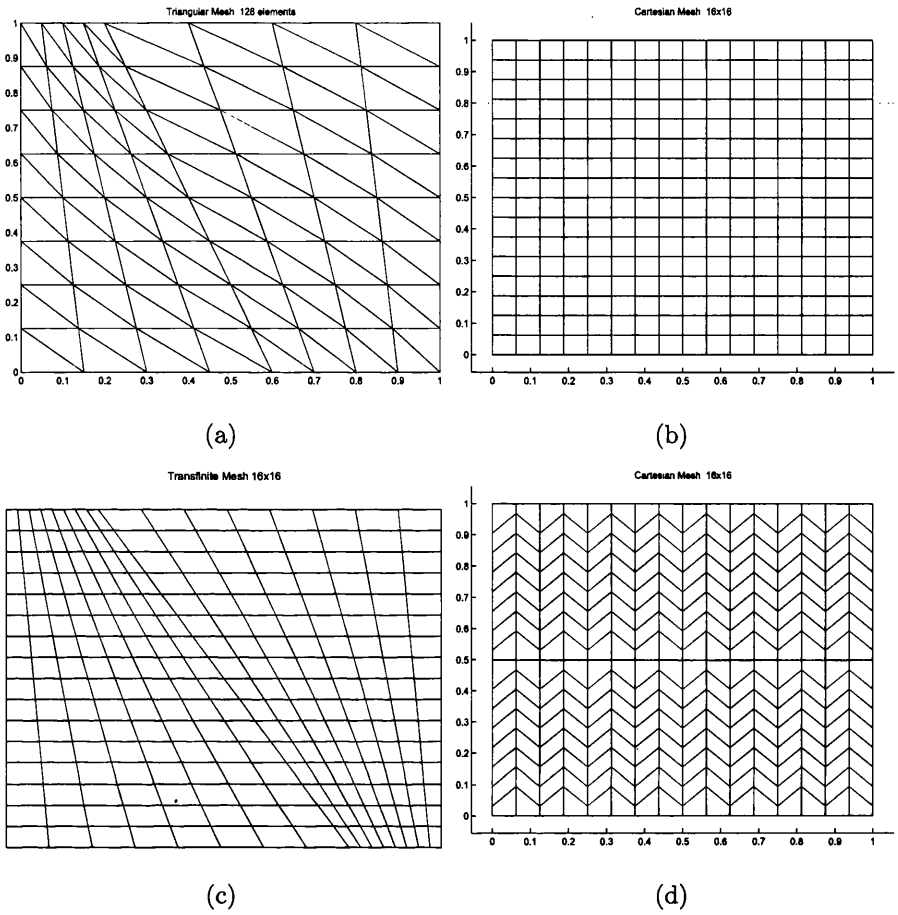

Figure 5.16: Different girds used to test numerical cases. (a) Unstructured transfinite Mesh aligned along $\theta = 2\pi/3$ discontinuity,(b) Cartesian Mesh, (c) Transfinite mesh aligned along $\theta = 2\pi/3$ discontinuity (d) Zigzag grid honoring internal discontinuity.

Similar cases were tested by Edwards and Rogers [3] and Eigestad *et al.* [82]. Edwards and Rogers [3] obtained the exact solution for a discontinuous medium when a uniform parallelogram grid is used (where $\mathbf{T}$ is exact). Eigestad *et al.* used a random grid and obtained the exact solution in physical space (for $q = 1$).

The aim of this study is to investigate convergence of flux-continuous schemes and exploit the flexibility in quadrature point by testing for a possible optimal quadrature point of the family of schemes. The above example shows that uniform linear

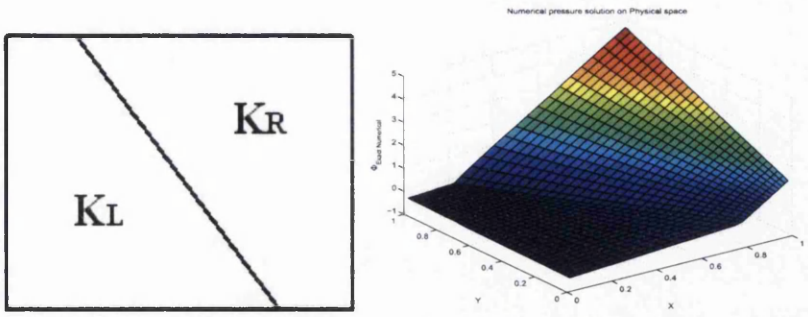

(a) (b)

Figure 5.17: CASE 1: (a) Medium discontinuity. (b) Exact Numerical pressure - *Physical space.*

or piecewise linear flows are reproduced exactly by the numerical scheme for any quadrature point consistent with the piecewise linear approximation. The following numerical examples test the numerical convergence of the family of flux-continuous schemes for a range of quadratures for more challenging examples where an exact solution is available and where the scheme cannot obtain an exact solution.

CASE 2:

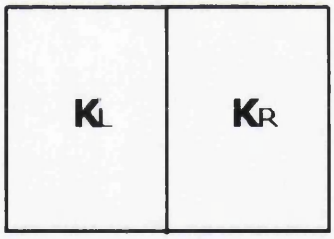

Figure 5.18: Discontinuous Tensor field

This example is taken from Edwards and Rogers [3]. In this case the pressure field is piecewise quadratically varying over the domain shown in figure 5.18. The domain

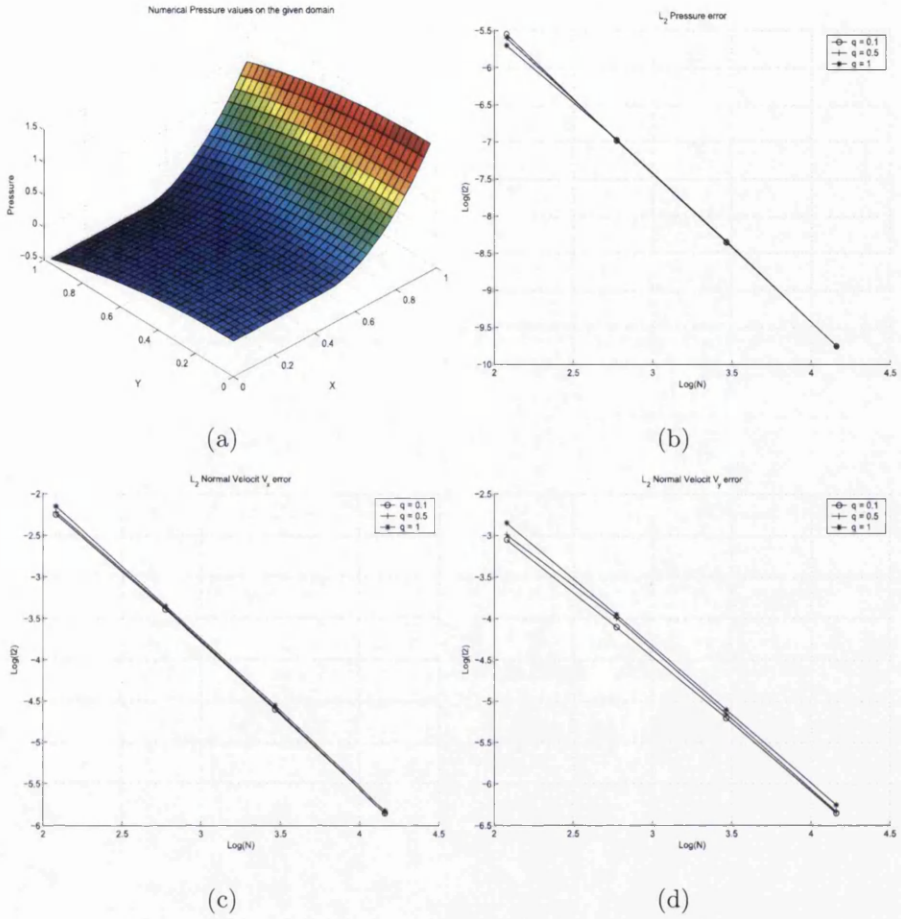

Figure 5.19: CASE 2: (a) Numerical Pressure Solution. (b)Convergence of Pressure with variable quadrature points. (c) Velocity convergence of velocity along X direction. (d) Velocity convergence of velocity along Y direction.

discontinuity is aligned along the line $x = 1/2$, and the analytical solution is given by

$$\phi(x,y) = \begin{cases} c_l x^2 + d_l y^2, & x < 1/2, \\ a_r + b_r x + c_r x^2 + d_r y^2, & x \geq 1/2, \end{cases}$$

$$
\begin{aligned}
K &= \begin{cases} \begin{pmatrix} 50 & 0 \\ 0 & 1 \end{pmatrix}, & x < 1/2, \\ \begin{pmatrix} 1 & 0 \\ 0 & 10 \end{pmatrix}, & x \geq 1/2, \end{cases} \\
\alpha &= K_{11}|_r / K_{11}|_l, \\
\beta &= K_{22}|_l / K_{22}|_l, \\
a_r &= 1, \\
f &= 4a_r/((\alpha-2)\beta+1), \\
b_r &= (\beta-1)f, \\
c_r &= f, \\
d_r &= -c_r K_{11}|_r / K_{22}|_r, \\
c_l &= \alpha\beta c_r, \\
d_l &= d_r
\end{aligned} \tag{5.43}
$$

The imposed top boundary flux is also discontinuous at $x = 1/2$, resulting in a discontinuous tangential flux across the domain. The computed numerical solution and the plots showing L_2 norm of pressure and velocity errors for the quadrature range $(0 < q \leq 1)$ are shown in figure 5.19. For this test case the best numerical convergence for pressure was obtained for quadrature $q = 0.1$. The numerical convergence rates for pressure and velocity for this case are presented in table 5.1.

Quadrature q	ϕ_h Convergence	f_{h_x} Convergence	f_{h_y} Convergence	f_h Convergence
$q = 0.1$	$O(h^2)$	$O(h^{1.77})$	$O(h^{1.62})$	$O(h^{1.69})$
$q = 0.5$	$O(h^{1.98})$	$O(h^{1.77})$	$O(h^{1.64})$	$O(h^{1.70})$
$q = 1$	$O(h^{1.95})$	$O(h^{1.78})$	$O(h^{1.68})$	$O(h^{1.73})$

Table 5.1: Numerical Convergence rates for Pressure and Velocity: CASE 2.

The next cases test the effect of discontinuous permeability with a corner in the

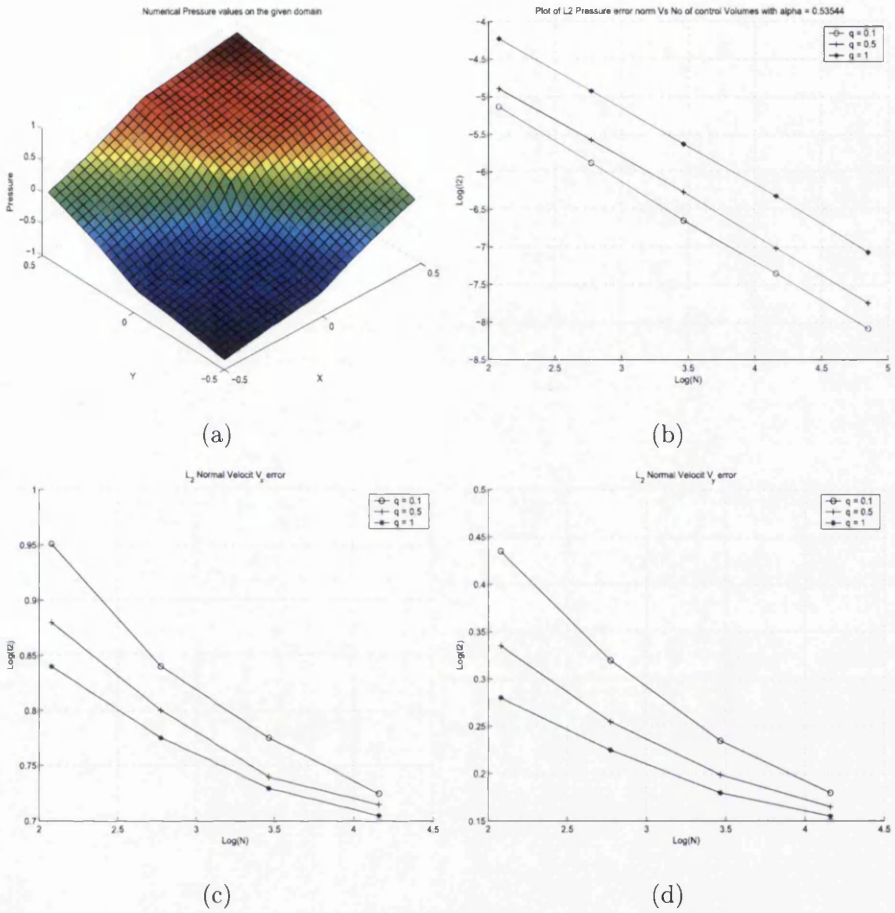

Figure 5.20: CASE 3: (a) Numerical Pressure Solution. (b) Convergence of Pressure with variable quadrature points. (c) Convergence of Velocity along X direction. (d)Convergence of Velocity along Y direction.

field upon convergence. In each of the following test case (case 3-7) taken from Eigestad *et al.*[82] and B.Riviere [41] the problem involves a rectangular domain with discontinuous permeability variation as indicated in figure 5.15.The exact solution in each case takes the form

$$\phi(r,\theta) = r^{\alpha}(a_i sin(\alpha\theta) + b_i cos(\alpha\theta)) \tag{5.44}$$

Difference between problems are in terms of strength of the coefficients, permeability tensor and orientation, which also determine the level of difficulty in each case.

CASE 3:

For this case analytical pressure solution is given by equation 5.44 and the domain discontinuity shown in figure 5.15(c) has an internal angle $\theta = \pi/2$. The permeability tensor is given as $\mathbf{K_i} = k_i\mathbf{I}$ where k_i is a scalar, for $i = 1, ..., 4$, taking values $k_1 = 5, k_3 = k_1$ and $k_2 = 1, k_4 = k_1$. Cartesian and Zig-zag grids shown in figure 5.16(b), 5.16(d) were used to test this problem. The coefficients that describe the analytical solution are given by

$$\begin{aligned} \alpha &= 0.53544095, \\ a_1 &= 0.44721360, \quad b_1 = 2.33333333, \\ a_2 &= -0.74535599, \quad b_2 = 1.0, \\ a_3 &= -0.94411759, \quad b_3 = 0.5555556, \\ a_4 &= -2.40170264, \quad b_4 = -0.481481481. \end{aligned} \tag{5.45}$$

The L_2 norm of pressure and velocity errors along with the numerical pressure solution obtained on a Cartesian grid are shown in figure 5.20. From the numerical convergence rates for pressure and velocity (for all quadrature points q) shown in table 5.2, it can be seen that the best numerical convergence of pressure and velocity on Cartesian grid was obtained for quadrature $q = 0.1$, where numerical pressure converges in the discrete L_2 norm with order $h^{1.0653}$ and numerical velocity (f_x, f_y) converges with order $h^{0.109}$ and $h^{0.12}$ respectively.

Quadrature q	ϕ_h Convergence	f_{h_x} Convergence	f_{h_y} Convergence	f_h Convergence
$q = 0.1$	$O(h^{1.0635})$	$O(h^{0.109})$	$O(h^{0.12})$	$O(h^{0.11})$
$q = 0.5$	$O(h^{1.02})$	$O(h^{0.082})$	$O(h^{0.081})$	$O(h^{0.081})$
$q = 1$	$O(h^{1.02})$	$O(h^{0.068})$	$O(h^{0.063})$	$O(h^{0.065})$

Table 5.2: Numerical Convergence rates for Pressure and Velocity: CASE 3.

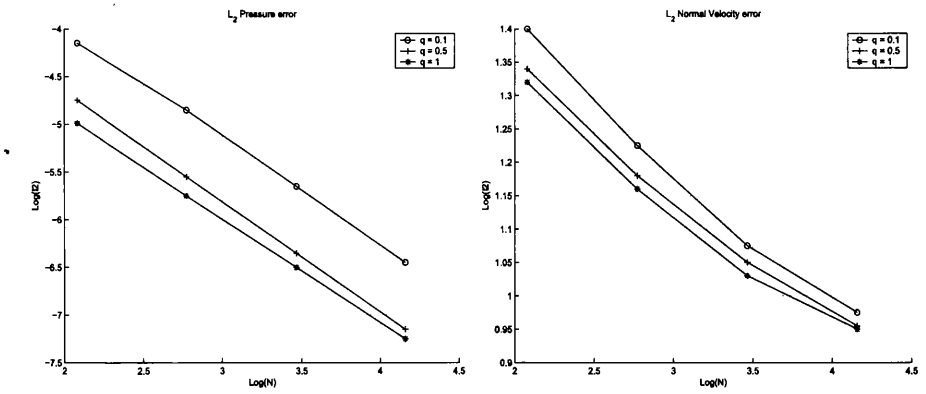

(a) (b)

Figure 5.21: CASE 3: (a) Numerical Pressure convergence with variable quadrature. (b) Numerical velocity convergence with variable quadrature.

Using Zigzag/Chevron grids shown in figure 5.16(d) the numerical pressure converges with order $h^{1.09}$ and numerical velocity converges with order $h^{0.205}$ for quadrature $q = 0.1$ as shown in table 5.3. The plots of L_2 norm for numerical pressure and velocity errors for different quadrature points using Zig-zag grids are shown in figure 5.21.

Quadrature q	ϕ_h Convergence	f_h Convergence
$q = 0.1$	$O(h^{1.09})$	$O(h^{0.205})$
$q = 0.5$	$O(h^{1.12})$	$O(h^{0.186})$
$q = 1$	$O(h^{1.07})$	$O(h^{0.175})$

Table 5.3: Numerical Convergence rates for Pressure and Velocity on Zig-zag grids: CASE 3

CASE 4:

For this case analytical solution for pressure is again given by equation 5.44 and the domain discontinuity is shown in figure 5.15(c) with an internal angle $\theta = \pi/2$. The permeability tensor is given by $\mathbf{K_i} = k_i\mathbf{I}$ where k_i is a scalar, for $i = 1, ..., 4$, taking values $k_1 = 100, k_3 = k_1$ and $k_2 = 1, k_4 = k_1$. This problem is tougher

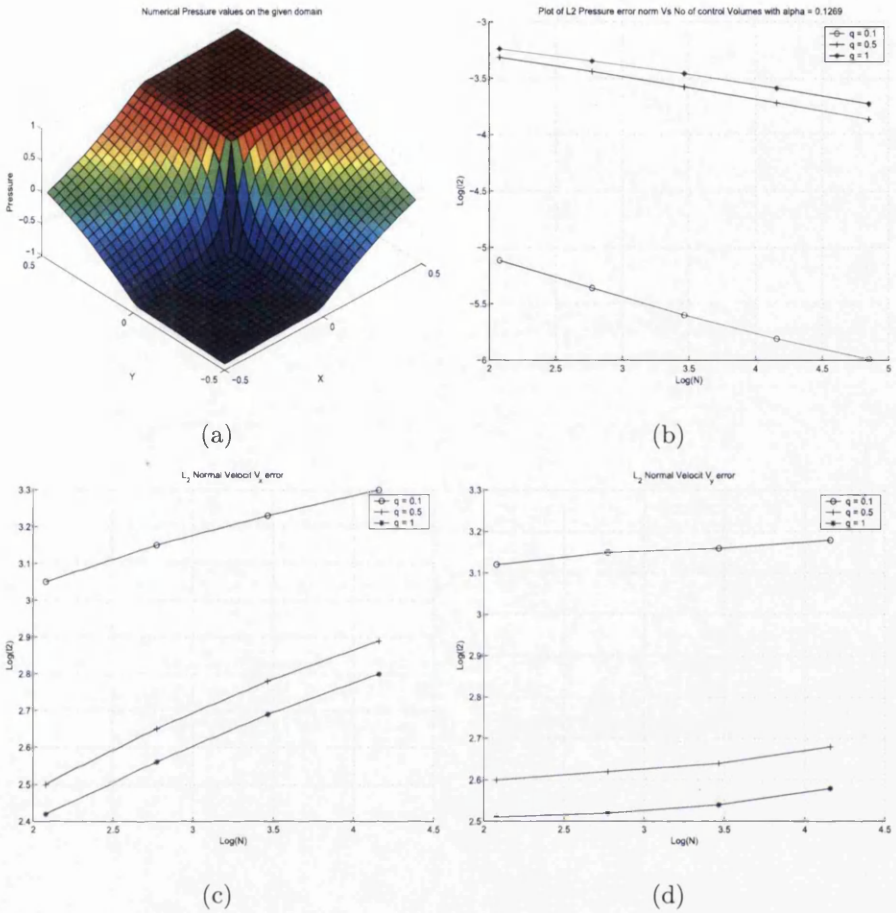

Figure 5.22: CASE 4: (a)Numerical Pressure solution. (b) Numerical convergence of Pressure with variable quadrature points. (c) Numerical convergence of Velocity along X direction. (d) Numerical convergence of Velocity along Y direction.

compared to the previous one as there is a large variation in permeability across the discontinuity and α value is small comparatively. The problem is tested on Cartesian as well as Zig-zag grids, shown in figure 5.16(b),5.16(d). The coefficients that describe

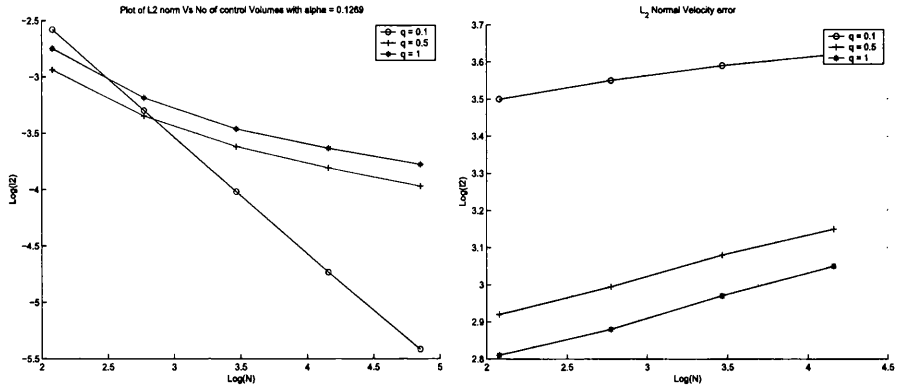

(a) (b)

Figure 5.23: CASE 4: (a) Numerical convergence of Pressure with variable quadrature. (b)Numerical Convergence of Velocity with variable quadrature.

the analytical solution are given by

$$\begin{aligned} \alpha &= 0.126902097221, \\ a_1 &= 0.1, & b_1 &= 1.0, \\ a_2 &= -9.603960396, & b_2 &= 2.960396040, \\ a_3 &= -0.4803548672, & b_3 &= -0.8827565925, \\ a_4 &= 7.701564882, & b_4 &= -6.456461752. \end{aligned} \tag{5.46}$$

L_2 norm of pressure and velocity errors obtained on a Cartesian grid are shown in figure 5.22. The best numerical convergence for pressure and velocity on a Cartesian grid was again obtained for quadrature $q = 0.1$, where numerical pressure solution converges in the discrete L_2 norm with order $h^{0.326}$ and numerical velocity (f_x, f_y) were found to be diverging. For these cases pressure converges with exponent $\alpha \leq 1$, since velocity is proportional to pressure gradient, therefore velocity can be expected to have a negative exponent. The divergence of velocity is also observed by Eigestad *et al.*[82]. The convergence rate of pressure for $q = 0.5$ and $q = 1$ is of the order of $h^{0.194}$ and $h^{0.166}$ respectively. Convergence rates are also shown in table 5.4

Quadrature q	ϕ_h Convergence	f_h Convergence
$q = 0.1$	$O(h^{0.326})$	*Diverge*
$q = 0.5$	$O(h^{0.194})$	*Diverge*
$q = 1$	$O(h^{0.166})$	*Diverge*

Table 5.4: Numerical Convergence rates for Pressure and Velocity on Cartesian Grids: CASE 4

Quadrature q	ϕ_h Convergence	f_h Convergence
$q = 0.1$	$O(h^{1.02})$	*Diverge*
$q = 0.5$	$O(h^{0.285})$	*Diverge*
$q = 1$	$O(h^{0.287})$	*Diverge*

Table 5.5: Numerical Convergence rates for Pressure and Velocity on Zig-zag grids : CASE 4

Using Zigzag/chevron grids (shown in figure 5.15(d)) numerical pressure and velocity convergence rates are shown in table 5.5. Improved convergence is seen for quadrature $q = 0.1$ with order $h^{1.02}$, showing a clear advantage in pressure convergence when using $q = 0.1$. However, velocity diverges. As before, such a diverging behavior of velocity is consistent with Eigestad *et al.*[82]. Figure 5.23 shows the plots of numerical pressure and velocity convergence with variable quadrature points on Zig-zag grids. The pressure convergence results known for this test case from Eigestad *et al.*[82] is of the order of $h^{0.22}$.

CASE 5:

In this case analytical solution is given by equation 5.44 and the domain discontinuity is along the line $2\pi/3$, shown in figure 5.15(a). The domain is divided into two parts with the permeability tensor $\mathbf{K_i} = k_i\mathbf{I}$ where k_i is a scalar, for $i = 1, 2$ taking values $k_1 = 100$ and $k_2 = 1$. The grid used to test this case was aligned along the discontinuity. The coefficients that describe the analytical solution are given by

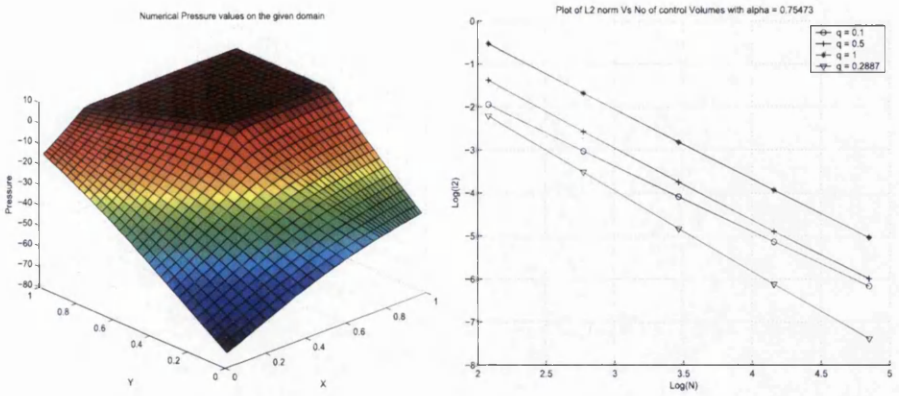

(a) (b)

Figure 5.24: CASE 5: (a) Numerical Pressure solution. (b) Numerical Pressure convergence with variable quadrature.

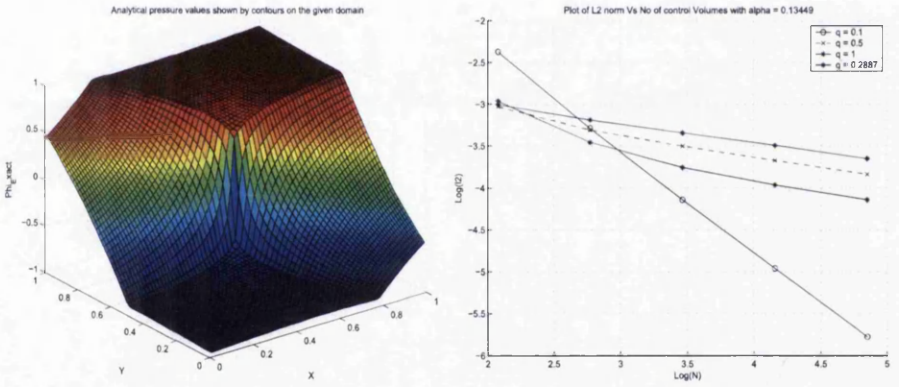

(a) (b)

Figure 5.25: CASE 6: (a) Numerical pressure on the given domain. (b) Convergence of Numerical pressure for different quadrature points.

$$\begin{aligned} \alpha &= 0.75472745, \\ a_1 &= 1.0, \qquad\qquad b_1 = 1.00995049, \\ a_2 &= 100.980198, \qquad\qquad b_2 = 1.99990197. \end{aligned} \tag{5.47}$$

For this test case numerical convergence of pressure was obtained to be the order of $h^{1.523}$, for quadrature point $q = 0.1$ on the grid aligned along the discontinuity. The pressure convergence for different quadrature point is shown in figure 5.24. The convergence for velocity was found to be of the order of $h^{0.75}$. On using the gauss quadrature point $q = 0.2887$ the convergence rate of pressure was found to be of the order of $h^{1.87}$. It was found that gauss quadrature points sometimes perform better in the case of smoother problems.

CASE 6:

Here the analytical solution is given by equation 5.44 and the domain discontinuity is along the line $2\pi/3$ as shown in figure 5.15(d) with the permeability tensor $\mathbf{K_i} = k_i\mathbf{I}$ where k_i is a scalar, for $1, ..., 4$, taking values $k_1 = 100, k_3 = k_1$ and $k_2 = 1, k_4 = k_1$. The grids used to test this case were aligned along the discontinuity. The coefficients that describe the analytical solution are given by

$$\begin{aligned}
\alpha &= 0.13448835, \\
a_1 &= 1.0, & b_1 &= 0.14177447, \\
a_2 &= 4.90138222, & b_2 &= -13.3407815, \\
a_3 &= -0.85392910, & b_3 &= -0.53935618, \\
a_4 &= -9.94074425, & b_4 &= 10.1578346.
\end{aligned} \tag{5.48}$$

The plots in figure 5.25(a) and figure 5.25(b) shows the numerical pressure solution and pressure convergence respectively for this test case. The pressure convergence for this test case using the grid aligned along the discontinuity was found to be of the order of $h^{1.23}$ for quadrature $q = 0.1$. The reported convergence of pressure for this test case in [82] was of the order of $h^{0.24}$. This result again demonstrates that a significant improvement in convergence is obtained by exploiting the family of schemes

and using the quadrature point $q = 0.1$. This case is not as smooth as the previous one and on using gauss quadrature point $q = 0.2887$ the convergence of pressure for this case was found to be of the order of $h^{0.43}$ which is less than the convergence rate found for q =*0.1*.

CASE 7:

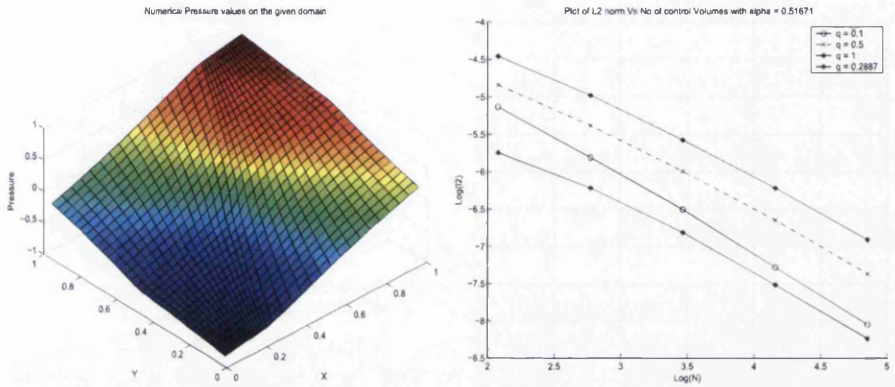

(a) (b)

Figure 5.26: CASE 7: (a) Numerical Pressure solution. (b)Numerical Convergence of Pressure with variable quadrature points.

Here the analytical solution for pressure is also given by equation 5.44 and the domain discontinuity is along the line $\pi/3$ as shown in figure 5.15(b) with the permeability tensor $\mathbf{K_i} = k_i\mathbf{I}$, where k_i is a scalar, for $1, ..., 4$, taking values $k_1 = 6, k_3 = k_1$ and $k_2 = 1, k_4 = k_1$. The grids used to test this case were aligned along the disconti-

nuity. The coefficients that describe the analytical solution are given by

$$\begin{aligned}
\alpha &= 0.51671199, \\
a_1 &= 1.0, & b_1 &= 0.27735010, \\
a_2 &= 1.71428571, & b_2 &= -0.91129318, \\
a_3 &= 0.32944606, & b_3 &= -0.98406726, \\
a_4 &= -0.820074971, & b_4 &= -1.75974652.
\end{aligned} \tag{5.49}$$

The plots in figure 5.26(a) and figure 5.26(b) shows the numerical pressure solution and pressure convergence respectively for this test case. The pressure convergence for this test case with the grid aligned along the discontinuity was of the order of $h^{1.051}$ for quadrature $q = 0.1$ and the velocity convergence was found to be of the order of $h^{0.52}$.

A series of other numerical examples were also tested on Cartesian and zigzag grids with different values of α, a_i and b_i over the domains shown in figure 5.15(b),5.15(c) and 5.15(d). All show the same trend, i.e. for quadrature point $q = 0.1$ convergence results are the best compared to other quadrature points.

5.5.2 Convergence results on unstructured grids

In this section convergence rates for the family of flux-continuous schemes is presented for tests performed on unstructured grids. Numerical convergence for the family of schemes on unstructured grids was also presented by the author in [5, 7]. The formulation of the family of schemes on unstructured grids is cell-vertex based [5, 7] (as explained in section 5.3.5),therefore for cases with internal discontinuities, boundary aligned grids (BAG)[5, 52]are used for numerical convergence (for details on BAG see appendix A). The convergence is measured in discrete L_2 norm as shown in equation 5.40,5.41 for both pressure and normal velocities.

CASE 8:

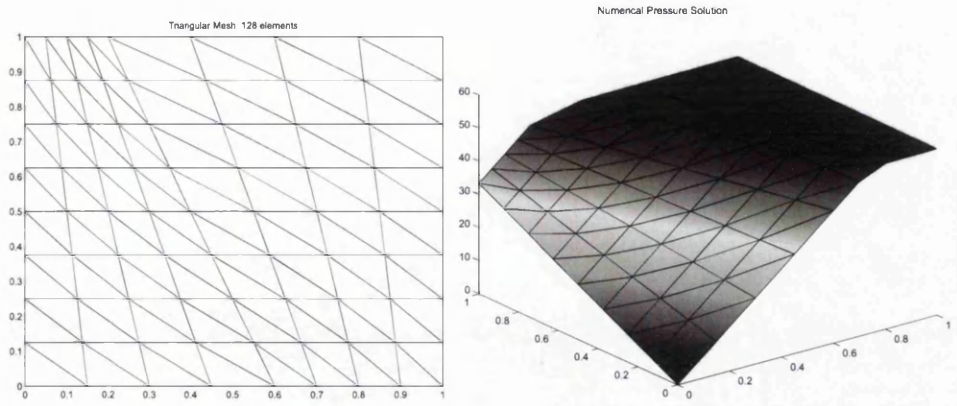

(a) (b)

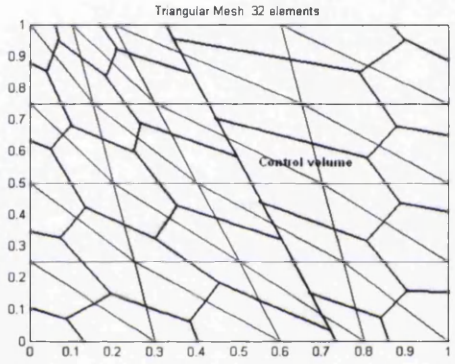

(c)

Figure 5.27: CASE 8:(a) Unstructured Grid. (b) Exact Numerical Solution. (c)Control-volume aligned triangular grid.

This test case is taken from Edwards and Rogers [3]. For this case the permeability is discontinuous with a domain discontinuity similar to the one shown in CASE 1 and is given along the line $x + y/2 = 3/4$. The grid used for solving the unstructured case is control-volume boundary aligned as shown in figure 5.27(c). The pressure field is piecewise linear and is given by

$$\phi(x,y) = \begin{cases} 200/3(x+y/2), & x+y/2 < 3/4, \\ 2/3(x+y/2)+99/2, & x+y/2 \geq 3/4, \end{cases} \tag{5.50}$$

A full discontinuous permeability tensor is defined as

$$K = \begin{cases} \begin{pmatrix} 1 & -1/4 \\ -1/4 & 1/2 \end{pmatrix}, & x+y/3 < 3/4, \\ \begin{pmatrix} 100 & -100/4 \\ -100/4 & 100/2 \end{pmatrix}, & x+y/2 \geq 3/4, \end{cases}$$

On solving this problem on a unstructured grid with 128 elements shown in figure 5.27(a) the exact solution shown in figure 5.27(b) was obtained using the physical space formulation for all quadrature points. This verifies that the family of flux-continuous schemes is equally applicable to unstructured grids and is exact for linear (or piecewise linear) problems.

The rest of the test cases are presented on smooth and rough unstructured grids as shown in figure 5.28. Rough grids are formed by introducing an $O(h)$ random perturbation in smooth grids. The grid refinement levels for L_2 norm calculation are from 16x16 to 128x128.

CASE 9:

In this test case the analytical solution is given by

$$\phi(x,y) = cosh(\pi x)cosh(\pi y) \tag{5.51}$$

on a square domain [0,1]x[0,1] with homogeneous permeability tensor. The Convergence of velocity and pressure was found to be of the order of $O(h^{1.5})$ and $O(h^2)$ respectively (figure 5.29) using smooth grid as shown in figure 5.28(a). Convergence of velocity was found to be order of $O(h^1)$ on rough grids (figure 5.28(b)), shown in figure 5.29. Pressure and velocity convergence rates (for different quadrature points)

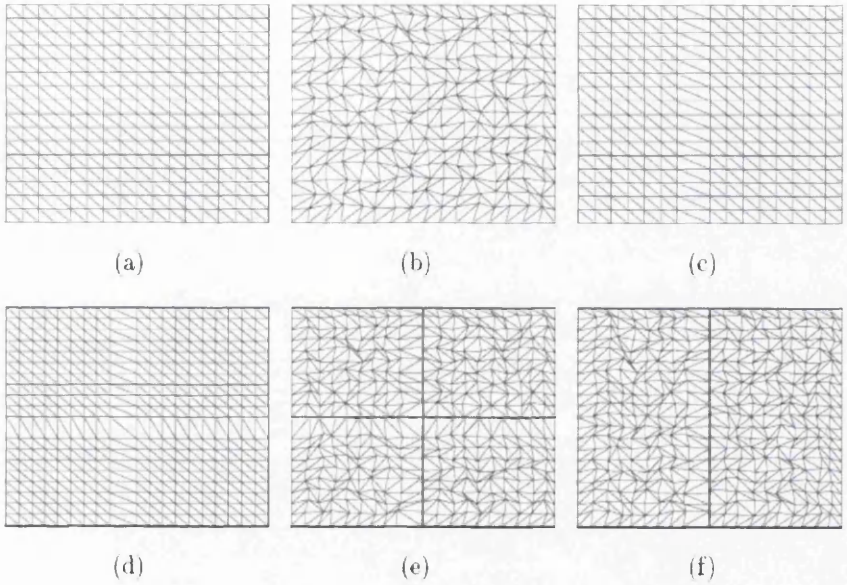

Figure 5.28: (a) Regular Triangular mesh. (b) Perturb Triangular mesh. (c) Control-volume aligned Triangular mesh for discontinuity at x = 0.5. (d) Control-volume aligned Triangular mesh for discontinuity at x = 0.5 and y = 0.5. (e) Control-volume aligned perturbed mesh. (f) Control-volume aligned perturbed mesh.

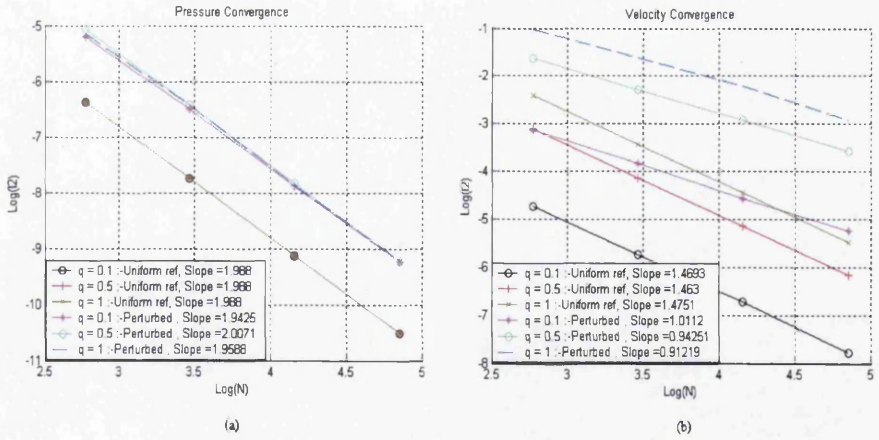

Figure 5.29: CASE 9: (a) Pressure convergence. (b) Velocity Convergence

Quadrature q	ϕ_h Convergence	f_h Convergence
$q = 0.1$	$O(h^{1.988})$	$O(h^{1.469})$
$q = 0.5$	$O(h^{1.988})$	$O(h^{1.463})$
$q = 1$	$O(h^{1.988})$	$O(h^{1.475})$

Table 5.6: Numerical Convergence rates for Pressure and Velocity on smooth grids : CASE 9

Quadrature q	ϕ_h Convergence	f_h Convergence
$q = 0.1$	$O(h^{1.943})$	$O(h^{1.011})$
$q = 0.5$	$O(h^{2.007})$	$O(h^{0.943})$
$q = 1$	$O(h^{1.958})$	$O(h^{0.912})$

Table 5.7: Numerical Convergence rates for Pressure and Velocity on rough grids : CASE 9

for this test case are also shown in table 5.6 and 5.7 respectively for smooth and rough grids.

CASE 10:

This test case is similar to CASE 2 presented before, this case is tested on unstructured grids shown in figure 5.28(c) and 5.28(f). The best numerical convergence of pressure and velocity for uniform triangular grids (shown in figure 5.28(c)) was found to be $O(h^{3.073})$ and $O(h^{1.95})$ respectively for quadrature q = 0.1, figure 5.30. However this is a non-uniform refinement with h reduced significantly at the boundary due to the boundary aligned grid. On randomly perturbed grid (shown in figure 5.28(f)) numerical convergence of pressure and velocity falls to $O(h^{1.33})$ and $O(h^{0.97})$ respectively for quadrature q = 0.1,figure 5.30. The convergence rates in tabular form are indicated in table 5.8 and 5.9 for smooth and rough grids respectively.

CASE 11:

The following examples test the numerical convergence of the unstructured scheme for the previously defined range of quadrature points applied to a challenging examples involving a corner point singularity in the field (taken from [41, 82]. The test

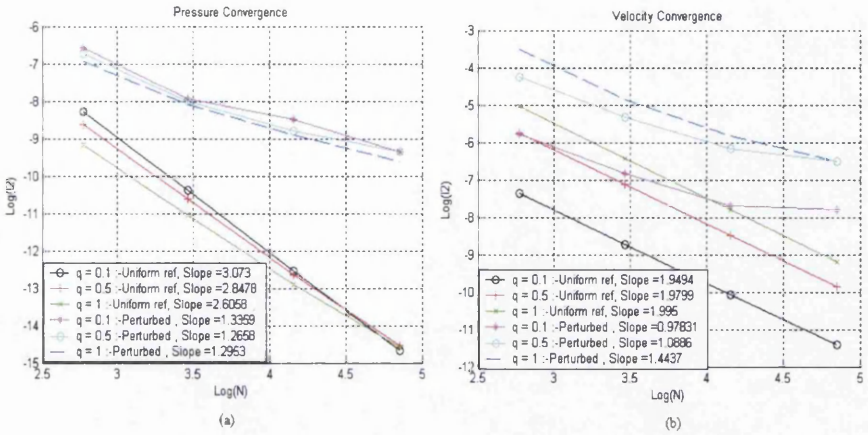

Figure 5.30: CASE 10: (a) Pressure convergence. (b) Velocity Convergence

Quadrature q	ϕ_h Convergence	f_h Convergence
$q = 0.1$	$O(h^{3.073})$	$O(h^{1.949})$
$q = 0.5$	$O(h^{2.487})$	$O(h^{1.979})$
$q = 1$	$O(h^{2.605})$	$O(h^{1.995})$

Table 5.8: Numerical Convergence rates for Pressure and Velocity on smooth grids : CASE 10

Quadrature q	ϕ_h Convergence	f_h Convergence
$q = 0.1$	$O(h^{1.335})$	$O(h^{0.978})$
$q = 0.5$	$O(h^{1.265})$	$O(h^{1.088})$
$q = 1$	$O(h^{1.295})$	$O(h^{1.443})$

Table 5.9: Numerical Convergence rates for Pressure and Velocity on rough grids : CASE 10

case is similar to CASE 3 presented on structured quads before. The square domain is sub-divided into four sub-domains and permeability tensor is discontinuous across each sub-domain boundary. The analytical solution of pressure is given by equation 5.44. The difference between the problems is in terms of the strength of coefficients and permeability tensor. For case with $\alpha = 0.5354$ best numerical convergence for

pressure and velocity on uniform triangular grids (shown in figure 5.28(d)) was found to be of the order $O(h^{2\alpha})$respectively for quadrature $q = 0.1$, figure 5.31(a). The numerical convergence falls to an order less than $O(h^{2\alpha})$ for perturbed gird (shown in figure 5.28(e)) with best convergence is achieved for quadrature q = 0.1, figure 5.31(b). We found that for decreasing value of parameter α the numerical convergence of pressure falls and, for cases with strong discontinuity and smaller value of parameter α, numerical velocity start to show diverging behavior. But in general better convergence is obtained by using quadrature q = 0.1 which is consistent with the results presented on structured quads [5]. This result is also consistent with an earlier observation regarding these schemes being more sensitive to cross-flow for $q < 1$ [20]. The convergence results are also shown in table 5.10 and 5.11 for smooth and rough grids respectively.

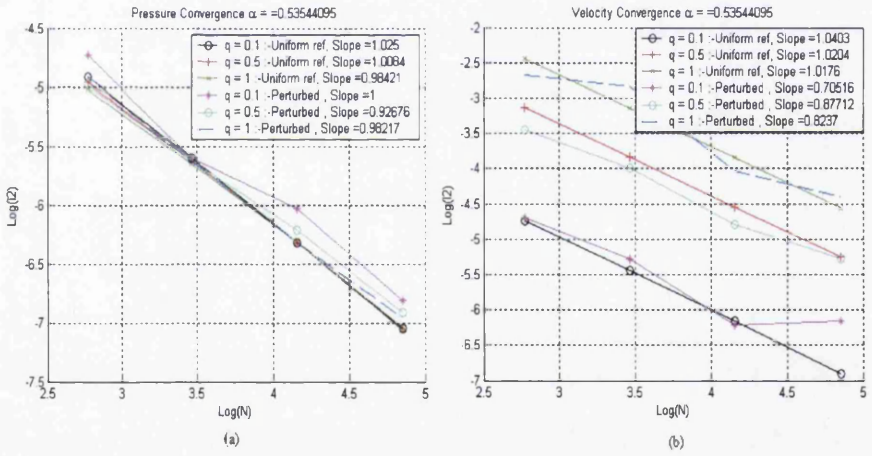

Figure 5.31: CASE 11: (a) Pressure convergence. (b) Velocity Convergence

CASE 12:

Now, we present a test case on domains involving faults. In this test case a square domain with layered permeability field with faults is chosen as shown in figure 5.32(a). Boundary conditions are chosen such that pressure is specified at the top and bottom

Quadrature q	ϕ_h Convergence	f_h Convergence
$q = 0.1$	$O(h^{1.025})$	$O(h^{1.040})$
$q = 0.5$	$O(h^{1.00})$	$O(h^{1.020})$
$q = 1$	$O(h^{0.982})$	$O(h^{1.018})$

Table 5.10: Numerical Convergence rates for Pressure and Velocity on smooth grids : CASE 11

Quadrature q	ϕ_h Convergence	f_h Convergence
$q = 0.1$	$O(h^{1})$	$O(h^{0.705})$
$q = 0.5$	$O(h^{0.927})$	$O(h^{0.877})$
$q = 1$	$O(h^{0.983})$	$O(h^{0.824})$

Table 5.11: Numerical Convergence rates for Pressure and Velocity on rough grids : CASE 11

boundary of the domain. No-flow conditions are imposed on left and right boundary of the domain.

Initially the domain is mapped with a primal quad mesh as shown in figure 5.32(b). Now a secondary mesh is created by joining the cell-centres of the quadrilaterals to cell edge mid-points, figure 5.32(c). Now the problem is solved on the secondary grid using cell-vertex formulation of the scheme [5] with primal grid forming the boundary aligned control-volumes for the secondary grid. The numerical result for this flow problem is shown in figure 5.33(b).

This test case demonstrates the capability of the family of schemes to be applicable on domains involving faults. It also shows the benefits of cell-vertex formulation.

5.5.3 Summary - 2D Results

The families of *physical* space flux-continuous schemes are shown to be exact on structured and unstructured grids (for all quadrature points) for problems where pressure is piecewise linear.

More generally, for the cases involving an interior field singularity where pressure

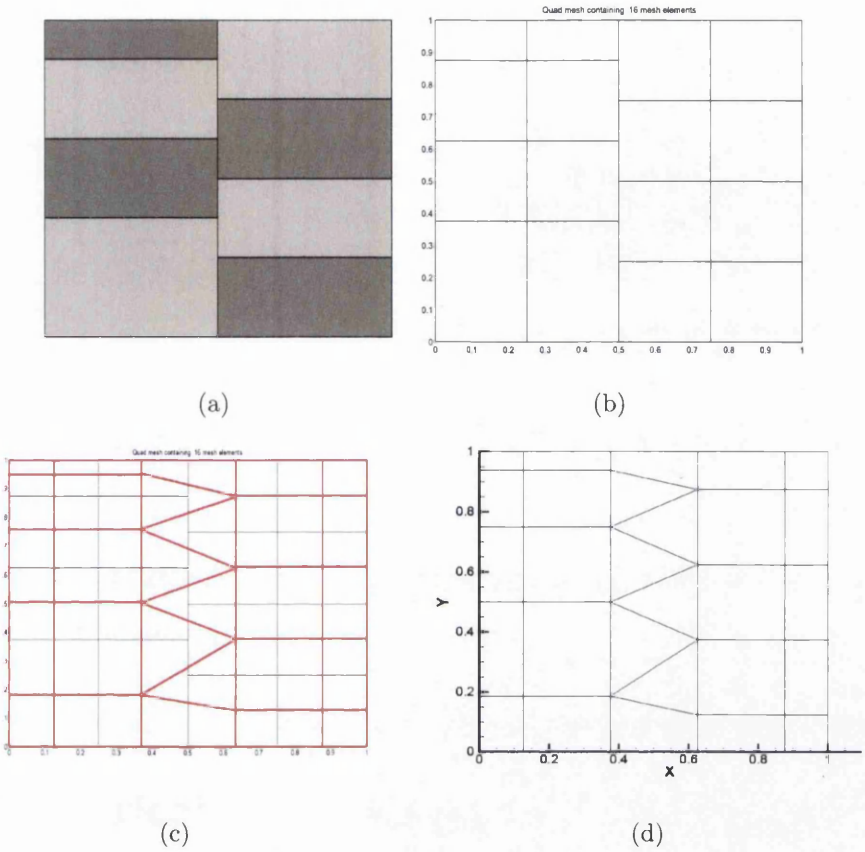

Figure 5.32: CASE 12: (a) Layer permeability in a domain with fault. (b) Quad mesh mapping faulted domain. (c) Transformation mesh formed by joining cell-centres to cell edge mid-points. (b)Transformed hybrid mesh.

is expressed in polar form as a function of α it was found that convergence rate for pressure and velocity decreases with decreasing α. The numerical experiments show that there is a certain inverse proportionality between convergence rate and roughness of the coefficients, smoother coefficients tend to yield better convergence, as the coefficient of roughness increases the convergence rate decreases. However, from the convergence study it is observed that quadrature point $q = 0.1$ appears to be optimal and results in improved convergence compared to other quadrature points tested. In particular significant improvement in convergence rates are obtained for

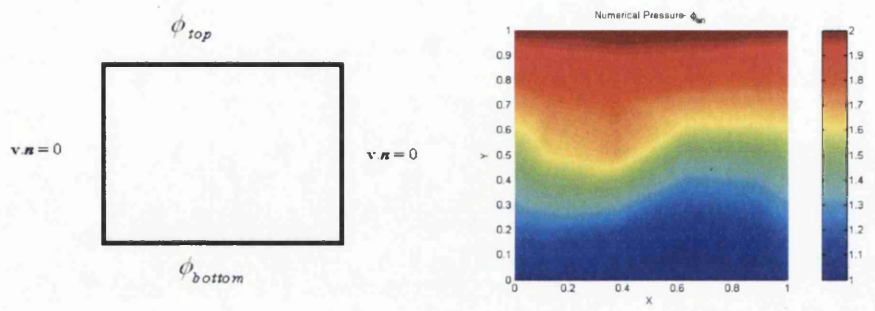

(a) (b)

Figure 5.33: CASE 12: (a) Specified boundary condition. (b)Numerical solution.

$q = 0.1$ compared to standard MPFA ($q = 1$). Similar behavior was also observed in one of the earlier papers by Edwards [20], where superconvergence was observed for $q < 1$.

5.6 Numerical Convergence on 3D Grids

In this section convergence study results are presented for the family of schemes for a range of quadrature points ($0 < q \leq 1$) . Similar convergence tests were also presented for 3-D formulation of the family of schemes by Pal and Edwards in [25]. The convergence rates are measured by discrete L_2 norms for both pressures and normal velocities,

$$\begin{aligned} \| \phi_h - \phi \| &= \left(\sum_i V_i (\phi_{h,i} - \phi_i)^2 \right)^{1/2} \\ \| f_h - f \| &= \left(\sum_j \frac{(V_{j+} + V_{j-})}{4} (f_{h,j} - f_j)^2) \right)^{1/2} \end{aligned} \tag{5.52}$$

Here f_h is the discrete flux and ϕ_h refers to the discrete solution. is the volume of the cell i and $V_{\pm}$ are the volumes of the cell separated by edge j. The simulation

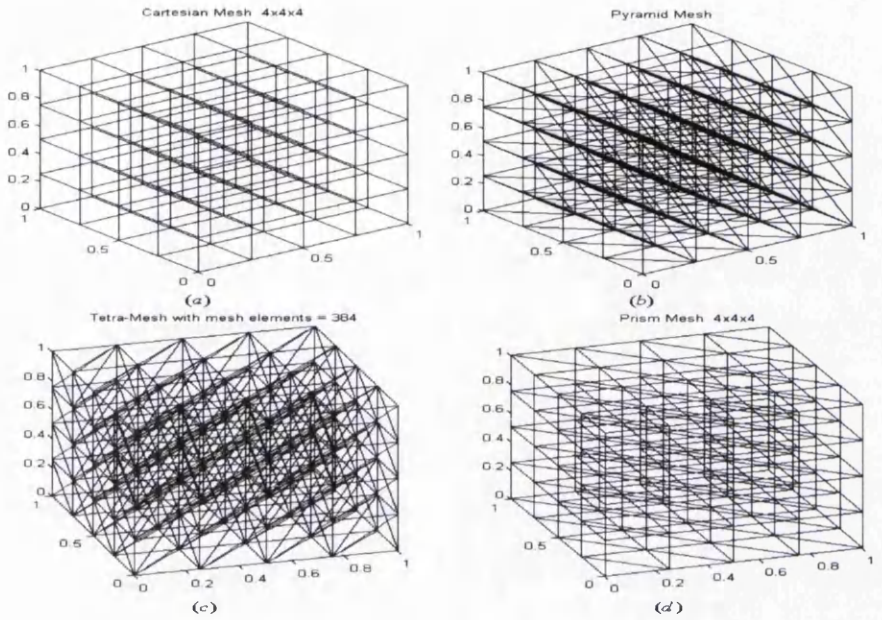

Figure 5.34: (a) Hexahedra element mesh. (b) Pyramid element mesh. (c) Tetrahedra element mesh. (d) Prism element mesh

domain is [0,1]x[0,1]x[0,1] and hence the total volume of simulated domain in all the test cases is unity.

The 3-D formulation described here is cell-vertex based as for unstructured grids, therefore cases with internal discontinuities requires boundary aligned grids [5, 7, 52] for testing numerical convergence (see appendix A). The convergence test is carried out using different types of grids shown in figure 5.34 and 5.35.

CASE 1:

First we test the convergence of the numerical solution where the analytical solution is given by $\phi(x, y, z) = x + y + z + 1$ on the domain [0,1]x[0,1]x[0,1] with homogeneous permeability tensor $\mathbf{K} = \mathbf{I}$. Dirichlet conditions boundary conditions are implemented by specifying solution at the boundary nodes. The numerical solution was found to be exact for pressure (shown in figure 5.36) and velocity for all the grids shown in figure 5.34 and 5.35.

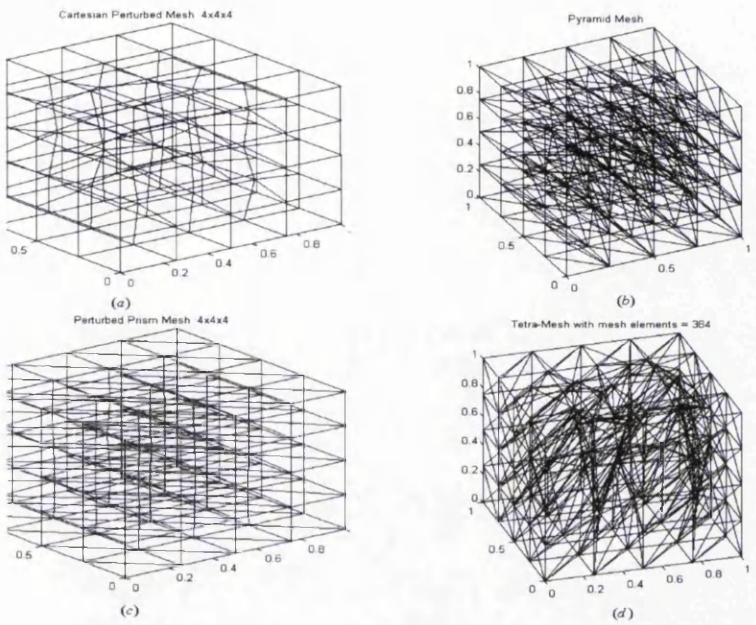

Figure 5.35: (a) Hexahedra element perturbed mesh. (b) Perturbed pyramid element mesh. (c) Perturbed prism element mesh. (d) Perturbed tetrahedral element mesh.

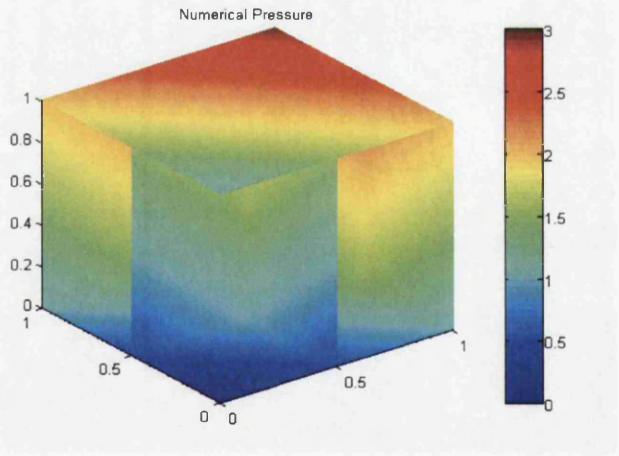

Figure 5.36: Numerical Pressure solution shown in slice: 3D-Case 1.

CASE 2:

This test case is taken from [125] here the exact pressure solution is given as:

$$\phi(x, y, z) = sin(\sqrt{2}\pi x)sinh(\pi y)sinh(\pi z) \tag{5.53}$$

and the medium is chosen to be isotropic and homogeneous. Convergence is considered for both pressure and normal velocity. Dirichlet boundary conditions are prescribed via exact solution. The numerical pressure solution is shown in figure 5.37.

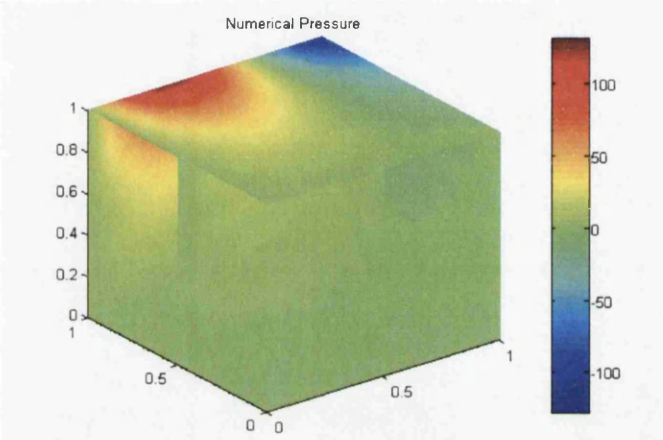

Figure 5.37: Numerical Pressure solution shown in slice: 3D-Case 2.

Convergence tests were performed using the uniform grids shown in figure 5.34. In general Convergence of pressure is found to be of $O(h^2)$, figure 5.38. Super convergence in pressure with $O(h^4)$ was seen for quadrature q = 0.5 in case of a hexahedral mesh, figure 5.38(a). This behavior illustrating increased accuracy (super convergence) is consistent with the property reported in [3] for constant homogeneous tensor. Convergence of velocity was also found to be of $O(h^2)$ as expected.

CASE 3:

This case involves the same problem as case 2, now using slightly perturbed grids as shown in figure 5.35. The convergence of velocity and pressure for all quadrature points for this case is shown in figure 5.39 and 5.40. The convergence of pressure was found to be of $O(h^2)$ and velocity convergence was found to drop to $O(h^1)$ for $q = 0.1$.

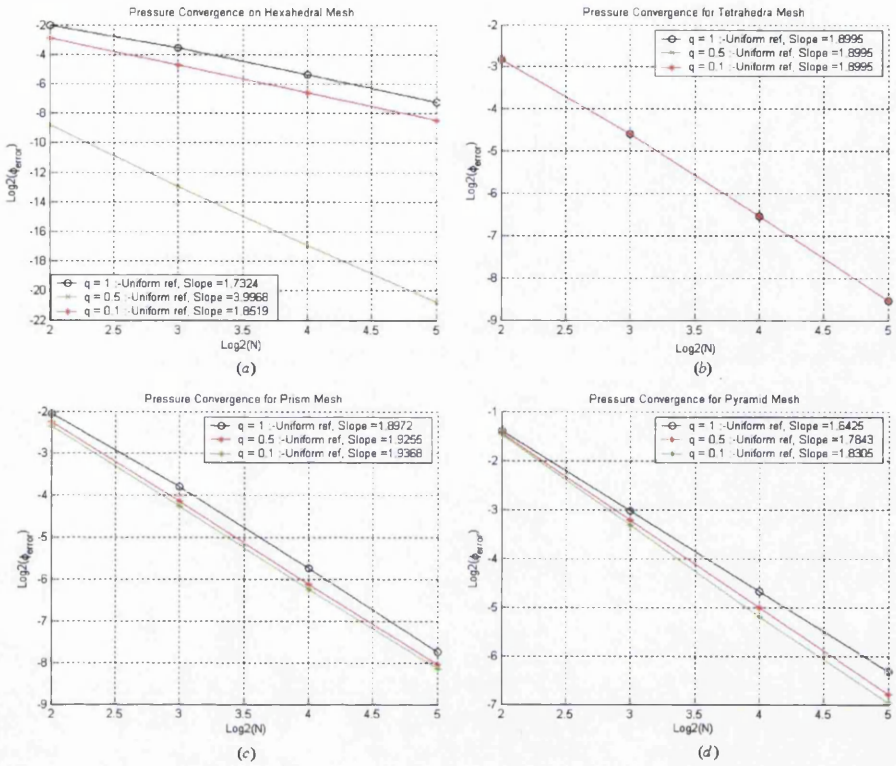

Figure 5.38: 3D-CASE 2: (a) Pressure Convergence on Hexahedral Mesh. (b) Velocity Convergence on Tetrahedral mesh. (c) Pressure Convergence on Prism Mesh. (d) Velocity Convergence on Pyramid Mesh.

In general convergence in pressure was found to improve with use of quadrature $q = 0.1$ and velocity convergence was found best for $q = 1$, figure 5.39.

CASE 4:

This test case was first presented in [25]. This case involves a discontinuity in the medium where the medium is divided into two subdomains at x = 0.5. The analytical solution for pressure in the two subdomains is given by:

$$\phi_L = (2x-1)^2 + 5(2x-1)y + 5(2x-1)z \qquad 0.0 \leq x < 0.5 \quad (5.54)$$

$$\phi_R = (2x-1)^2 + (2x-1)y + (2x-1)z \qquad 0.5 \leq x \leq 1.0$$

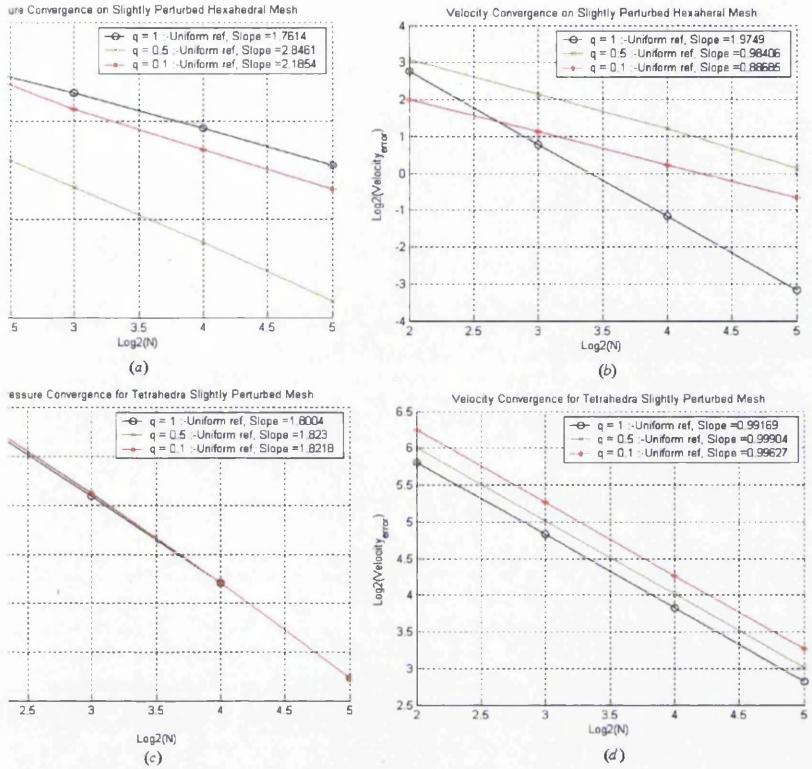

Figure 5.39: 3D-CASE 3: (a) Pressure Convergence on Perturbed Hexahedral Mesh. (b) Velocity Convergence on Perturbed Hexahedral mesh. (c) Pressure Convergence on Perturbed Tetrahedral Mesh. (d) Velocity Convergence on Perturbed Tetrahedral Mesh.

The permeability tensor is given as:

$$K_L = \begin{pmatrix} 1 & 0 & 0 \\ 0 & 1 & 0 \\ 0 & 0 & 1 \end{pmatrix} \qquad 0.0 \leq x < 0.5 \tag{5.55}$$

$$K_R = \begin{pmatrix} 5 & 4 & 4 \\ 4 & 5 & 4 \\ 4 & 4 & 5 \end{pmatrix} \qquad 0.5 \leq x \leq 1.0$$

This problem is tested on a hexahedral and pyramid element boundary aligned

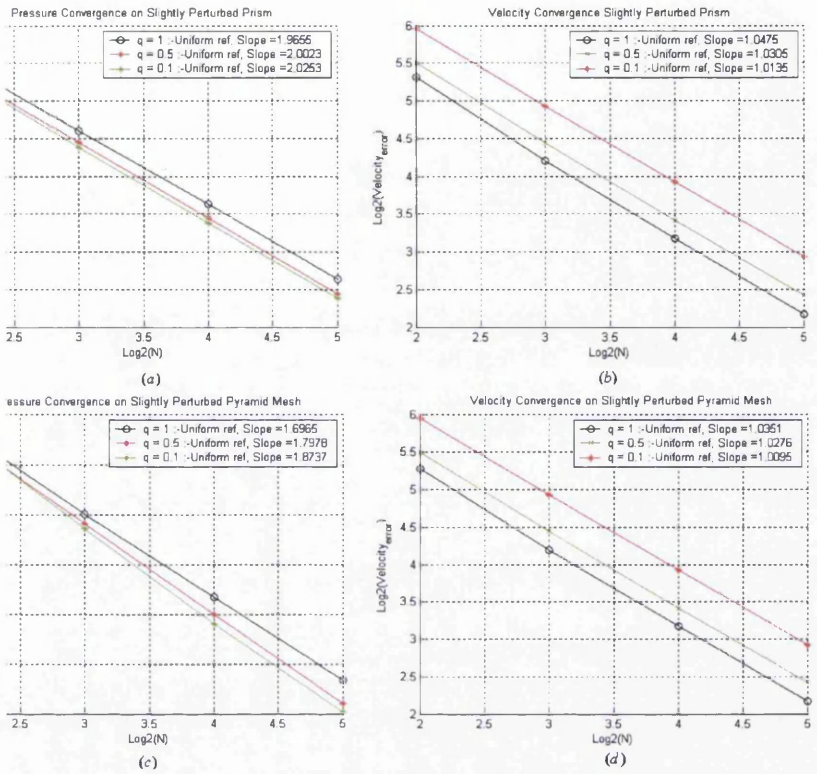

Figure 5.40: 3D-CASE 3: (a) Pressure Convergence on Perturbed Prism Mesh. (b) Velocity Convergence on Perturbed Prism mesh. (c) Pressure Convergence on Perturbed Pyramid Mesh. (d) Velocity Convergence on Perturbed Pyramid Mesh.

grid where the domain discontinuity is aligned with the control-volume [5, 7, 52]. The convergence of numerical pressure and velocity for BAG grid with hexahedral element is shown in figure 5.41. The convergence of numerical pressure and velocity for BAG grid with pyramid elements is shown in figure 5.42. The numerical pressure solution is shown in figure 5.43.

In both cases (Hexahedral and Pyramid BAG's) the convergence of pressure was found to be of order slightly greater than $O(h)$ with better convergence for q = 0.1. The numerical convergence of velocity was found to be close to $O(h)$.

CASE 5:

This case is taken from [42], the domain is a box [0,1]x[0,1]x[0,1]. The coefficient

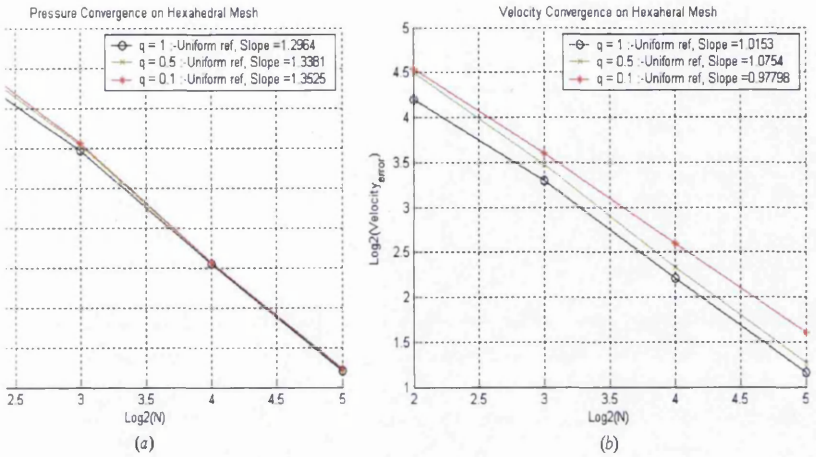

Figure 5.41: 3D-CASE 4: (a) Pressure Convergence on Boundary Aligned Hex Mesh. (b) Velocity Convergence on Boundary Aligned Hex Mesh.

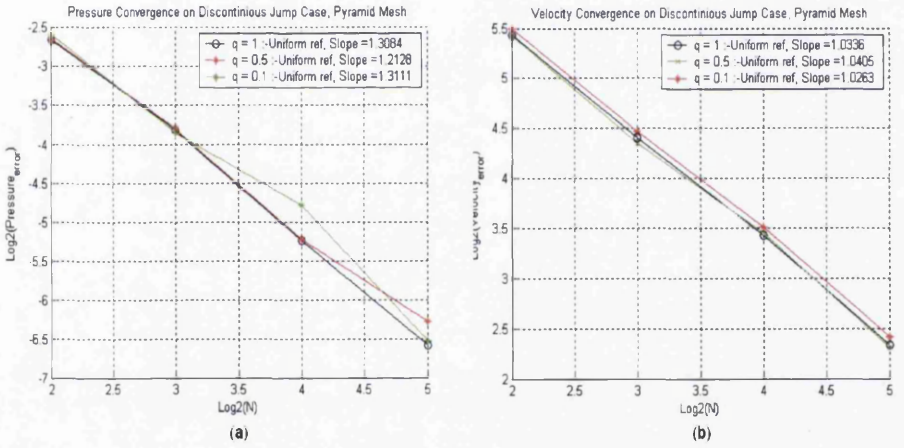

Figure 5.42: 3D-CASE 4: (a) Pressure Convergence on Boundary Aligned Pyramid Mesh. (b) Velocity Convergence on Boundary Aligned Pyramid Mesh.

tensor $\mathbf{K} = \mathbf{I}$. Dirichlet boundary conditions are imposed using the exact pressure solution given as:

$$\phi(x, y, z) = exp(-x^2 - y^2 - z^2) \tag{5.56}$$

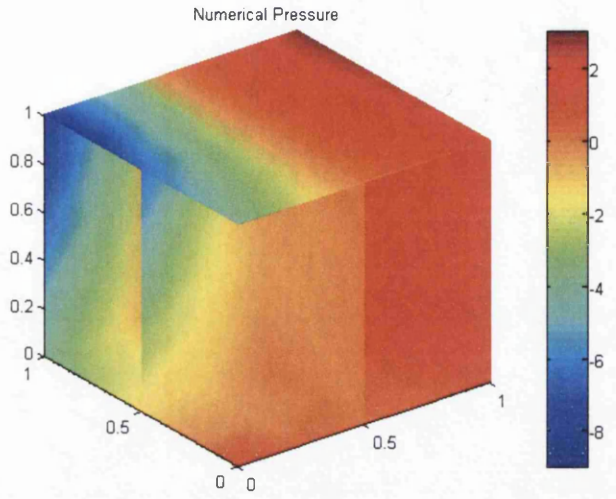

Figure 5.43: 3D-CASE 4: Numerical Pressure shown in slice on a boundary aligned Hex Mesh.

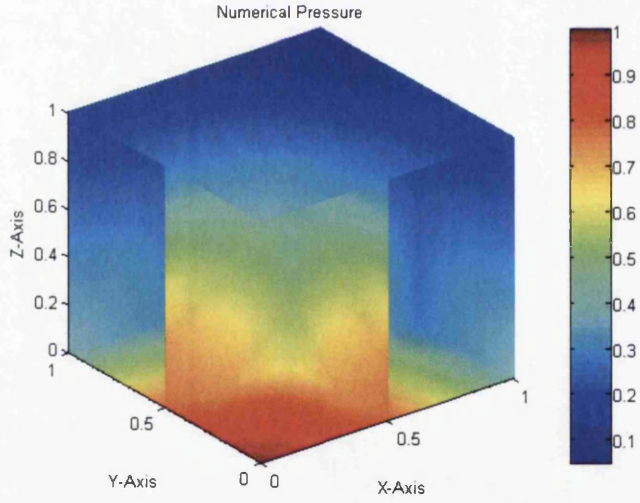

Figure 5.44: 3D-CASE 5:Numerical Pressure solution shown in slice on Tetrahedral Mesh.

The numerical solution is obtained on the uniform hexahedral mesh of figure 5.34(a). The numerical solution is shown in figure 5.44. The numerical convergence for pres-

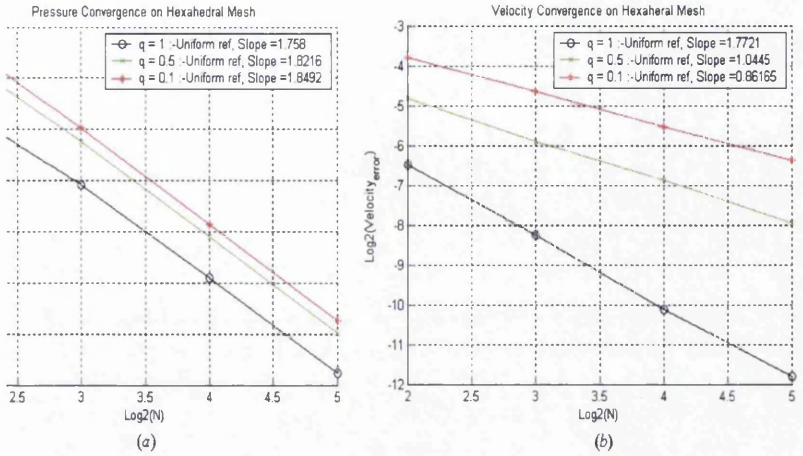

Figure 5.45: 3D-CASE 5:(a) Convergence of Numerical Pressure. (b) Convergence of Velocity.

sure and velocity for this case using hexahedral mesh is shown in figure 5.45. The convergence of pressure was found to be close to order $O(h^2)$. The convergence of velocity is also found to be of order $O(h^2)$ for q = 1 whereas for other quadrature points convergence of velocity falls to $O(h)$.

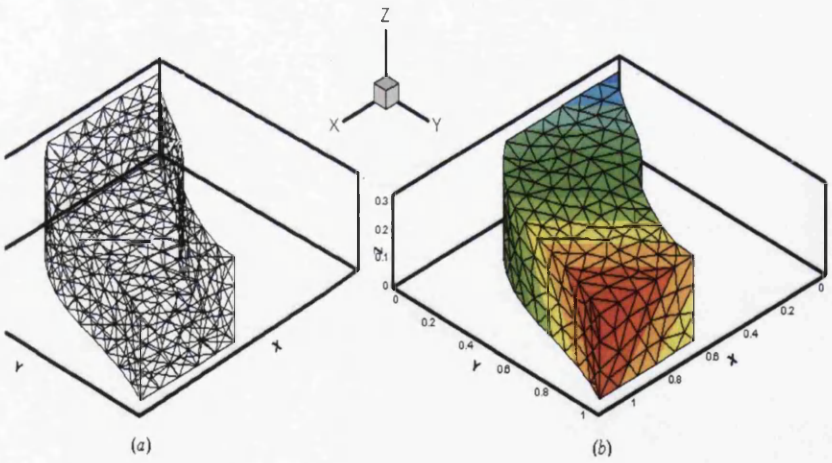

Figure 5.46: 3D-CASE 6:(a) Domain meshed with tetrahedral elements. (b) Numerical Pressure Solution.

CASE 6:

In order to verify the validity of the code on an irregular domain, a linear pressure field with isotropic permeability tensor is used to define the test case. The irregular domain is meshed with tetrahedral elements as shown in figure 5.46 (a). Exact values of pressure and velocity are obtained for all quadrature points. The numerical pressure solution is shown in figure 5.46 (b).

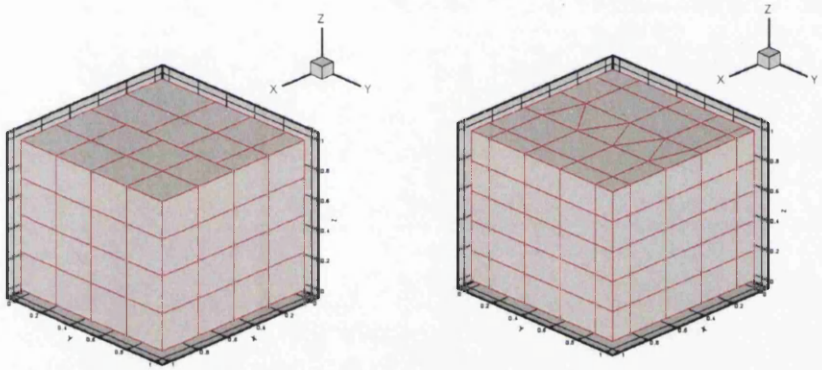

(a) (b)

Figure 5.47: 3D-CASE 7: (a) Hex mesh mapping faulted domain. (b) Transformed mesh formed by joining cell-centres to cell edge mid-points.

CASE 7:

Finally, we present a test case on domains involving faults, in this test case a cubical domain [0-1, 0-1, 0-1] with layered permeability field with faults is chosen, similar to the 2D test case (CASE 12) as shown in figure 5.32(a). Similar boundary conditions are are implemented with the pressure being specified at (x-z) face of the domain for (y = 0) and (y = 1). No-flow conditions are imposed on the other boundaries of the cubical domain.

To obtain the numerical solution, approach used here is similar to the one used for 2D test case (CASE 12). Initially the cubical domain is mapped with a primal mesh consisting of hexahedral elements, figure 5.47(a). Now a secondary mesh is created

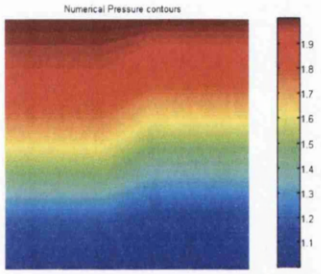

Figure 5.48: 3D-CASE 7: (a) Numerical Solution shown as a slice at z = 0.5.

by joining the cell-centres of the hexahedra to cell edge mid-points resulting in a control-volume boundary aligned mesh consisting of hexahedra and prims elements, figure 5.37(b). Now the problem is solved on the secondary grid using cell-vertex formulation of the scheme [5] with primal grid forming the boundary aligned control-volumes for the secondary grid. The numerical pressure solution is shown as a slice at z = 0.5 for this flow problem in figure 5.48. The numerical pressure solution resembles the numerical solution obtained for 2D case (CASE 12), figure 5.33(b).

This test case demonstrates the capability of the family of schemes to be applicable on domains involving faults in 3D with use of mixed grids (hexahedra and prims elements). The test case also demonstrates the benefit of formulating family of schemes on different element types in 3D, thereby giving flexibility in application of the schemes. Last but not the least this test case also shows the benefits of cell-vertex formulation.

5.6.1 Summary 3-D Results

The family of flux-continuous finite-volume schemes is presented for different element types including Hexahedra, Prisms, Tetrahedra and Pyramid elements. The scheme is found to be exact for all quadrature points q, for cases where pressure is linear and the medium is isotropic and homogeneous. Use of quadrature parame-

terization is explored for 3D grids. Benefits of using different quadrature types are also noted with improved convergence behavior in cases including discontinuous coefficients. Super convergence is also observed for one of the test cases with quadrature $q = 0.5$. Use of quadrature $q = 0.1$ in 3D shows improved convergence behavior consistent with that observed previously in 2-D [5].

Chapter 6

Positive Definite Pressure Equation Discretization

6.1 Introduction

As stated in the previous chapter, formulation of the family of flux-continuous finite-volume schemes in *physical* space leads to a discretization matrix which is non-symmetric in the general case for both quadrilateral grids and triangular grids. However, an alternative formulations for the family of schemes that yield a symmetric positive definite (SPD) discrete matrix have been derived in *transform* space [3]. Where, a local piece-wise constant general-tensor (T) approximation is introduced over the cell or control-volume [3], [56] for structured grids.

Here, we present another family of schemes which are formed when introducing piece-wise constant general-tensor approximations over the subcells of each control-volume. These schemes were initially presented in [4, 22, 23], where the schemes were developed for structured and unstructured grids and were shown to be SPD for any grid. These formulations achieve SPD discretization by introduction of additional approximation in geometry. Further details of the material in this chapter are given in [24, 67].

This chapter presents a convergence study of the locally conservative sub-cell based flux-continuous formulations with focus on both, the effect of the local sub-cell tensor approximation and the effect of different quadrature rules [5]. A comparison of the sub-cell family of flux-continuous schemes, with *physical* and control-volume *transform* space formulations of the family schemes is also presented, with the help of numerical convergence tests. In this study the sub-cell schemes are formulated with respect to cell-centered flow and rock variables where control-volumes are the primal quadrilateral grid cells. The base sub-cell schemes yield a discretization matrix which is symmetric positive definite. The relationship between the new formulations and earlier flux continuous schemes is given.

This chapter is organized as follows: Section 6.2 discusses *physical* space formulation of the scheme and loss of symmetry for the *physical* space formulation in general case. General positive definite conditions are summarized in section 6.3. Subcell tensor approximations are presented in section 6.4. The subcell family of flux-continuous schemes is presented in section 6.5. A comparison between *physical*, *transform* and *subcell transform* space formulations of the family of scheme is presented in section 6.6, with the help of numerical convergence tests for a range of quadrature points. A summary follows in section 6.7.

6.2 Loss of Symmetry in *Physical* Space Formulation

Following the discussion from previous chapter, for a general quadrilateral cell of arbitrary distortion the local variation in geometry will mean that the local general tensor T will vary according to local spatial position in the cell. Referring again to the example cell in figure 5.7(a) in general

$$T_{12}|_W^1 \neq T_{12}|_S^1 \tag{6.1}$$

which is the source of loss of symmetry in the local subcell flux matrix [22, 67] and consequent loss in the discrete matrix of the *physical* space formulation. The effect on discretization is discussed below.

6.2.1 Physical-Space Flux: Inverse Tensor Form

In this section, the physical space flux is now derived in an alternative form involving potential differences between nodes [6, 4] and follow the analysis presented in [67]. We return to the physical space flux of equation 5.17 expressed in terms of potential differences between interface pressures and nodal pressures, for any quadrature point on the interface, and reformulate the flux continuity conditions in terms of the subcell tensors as

$$
\begin{aligned}
(T^1)^{-1}\begin{pmatrix} F_S \\ F_W \end{pmatrix} &= -\begin{pmatrix} \phi_S - \phi_1 \\ \phi_W - \phi_1 \end{pmatrix}, \qquad (T^2)^{-1}\begin{pmatrix} F_S \\ F_E \end{pmatrix} = -\begin{pmatrix} \phi_2 - \phi_S \\ \phi_E - \phi_2 \end{pmatrix}, \\
(T^3)^{-1}\begin{pmatrix} F_N \\ F_E \end{pmatrix} &= -\begin{pmatrix} \phi_3 - \phi_N \\ \phi_3 - \phi_E \end{pmatrix}, \qquad (T^4)^{-1}\begin{pmatrix} F_N \\ F_W \end{pmatrix} = -\begin{pmatrix} \phi_N - \phi_4 \\ \phi_4 - \phi_W \end{pmatrix}
\end{aligned} \tag{6.2}
$$

where fluxes are grouped according to subcell numbers (general-tensor superfixes) that are in common and equation 6.2 is an equivalent form of equation 5.17. The physical space tensor approximations belonging to each subcell are given below

$$
\begin{aligned}
T^1 &= \begin{pmatrix} T_{11}|_S^1 & T_{12}|_S^1 \\ T_{12}|_W^1 & T_{22}|_W^1 \end{pmatrix}, \qquad T^2 = \begin{pmatrix} T_{11}|_S^2 & T_{12}|_S^2 \\ T_{12}|_E^2 & T_{22}|_E^2 \end{pmatrix} \\
T^3 &= \begin{pmatrix} T_{11}|_N^3 & T_{12}|_N^3 \\ T_{12}|_E^3 & T_{22}|_E^3 \end{pmatrix}, \qquad T^4 = \begin{pmatrix} T_{11}|_N^4 & T_{12}|_N^4 \\ T_{12}|_W^4 & T_{22}|_W^4 \end{pmatrix}
\end{aligned} \tag{6.3}
$$

It is important to note that the tensor approximations resulting from physical space resolution are not generally symmetric unless the cell is a square, rectangle or a parallelogram. With $T_{12}^1 = T_{12}|_S^1$ and $T_{21}^1 = T_{12}|_W^1$ then by equation 6.1 $T_{12}^1 \neq T_{21}^1$ in the general case. Thus the inverses of the discrete tensors in equation 6.2 are

not symmetric in the general case. Denoting the inverse of the general-tensor by $\widetilde{T} = (T)^{-1}$ and adding pairs of equations operating on common fluxes, e.g., adding the top rows of the first pair of equation sets in equation 6.2 yields

$$(\widetilde{T}^1_{11} + \widetilde{T}^2_{11})F_S + \widetilde{T}^2_{12}F_E + \widetilde{T}^1_{12}F_W = -(\phi_2 - \phi_s + \phi_s - \phi_1) = -(\phi_2 - \phi_1) \tag{6.4}$$

which eliminates the unknown interface pressure directly. Gathering the other flux pairs and expanding in a similar fashion leads to a system of equations that expresses the fluxes directly in terms of potential differences viz

$$A\mathbf{F} = -\Delta\phi_{\mathbf{v}} \tag{6.5}$$

where

$$\mathbf{F} = (F_S, F_E, F_N, F_W)^T, \qquad \Delta\phi_{\mathbf{v}} = (\phi_{21}, \phi_{32}, \phi_{34}, \phi_{41})^T \tag{6.6}$$

and the flux coefficient matrix is given by

$$A = \begin{pmatrix} \widetilde{T}^1_{11} + \widetilde{T}^2_{11} & \widetilde{T}^2_{12} & 0 & \widetilde{T}^1_{12} \\ \widetilde{T}^2_{21} & \widetilde{T}^2_{22} + \widetilde{T}^3_{22} & \widetilde{T}^3_{21} & 0 \\ 0 & \widetilde{T}^3_{12} & \widetilde{T}^4_{11} + \widetilde{T}^3_{11} & \widetilde{T}^4_{12} \\ \widetilde{T}^1_{21} & 0 & \widetilde{T}^4_{21} & \widetilde{T}^1_{22} + \widetilde{T}^4_{22} \end{pmatrix} \tag{6.7}$$

The dual-cell flux matrix entries are equal to elements of the general tensor inverse corresponding to each subcell component of control-volume. This form of the physical space scheme shows that

a) the flux can be written as a linear combination of pressure differences where

$$\mathbf{F} = -A^{-1}\Delta\phi_{\mathbf{v}} \tag{6.8}$$

and therefore demonstrates consistency for a constant pressure field for any quadrature point q.

b) the physical-space flux matrix is not generally symmetric.

c) the introduction of a symmetric tensor approximation will lead to a symmetric flux

matrix and an SPD discrete system [4].

d) a connection between the physical space scheme and the mixed finite element method can be made [4, 24].

The fluxes of equation 6.5 embody the full tensor generalization of the harmonic mean. This is seen by considering the case of a diagonal tensor. In this case at each interface equation 6.4 reduces to

$$-\frac{1}{2}(\frac{h}{K_r}+\frac{h}{K_l})F=(\phi_r-\phi_l) \tag{6.9}$$

Where for a given interface l and r denotes the respective left and right hand side control-volumes. Rearranging equation 6.9 leads directly to the well-known 2-point flux approximation with harmonic mean coefficient.

For the base scheme $q = 1$, the positions of interface pressures from adjacent dual-cells will coincide. While each interface pressure is continuous in the direction normal to the control-volume face by construction, the interface pressures can be discontinuous in the tangential direction (to the interface), i.e. between adjacent dual-cells when a full-tensor is present. This crucial step leads to the system being locally coupled. Conversely, had the interface pressures been continuous tangentially as well as in the normal direction, the system would be globally coupled. Following Russell and Wheeler [26], this key observation has been extended to full tensors in [4, 24, 67] to unlock the relationship between the physical space MPFA schemes and the mixed finite element method.

6.3 Positive Definite Physical Space Family of Schemes

Following the positive definite analysis presented in [67], it can be stated that a (not necessarily symmetric) matrix M_G is positive definite, if for any non-zero vector Φ_G

$$\Phi_G^T M_G \Phi_G > 0 \tag{6.10}$$

The analysis presented in [67] shows that the schemes are positive definite if the symmetric part of the discrete tensor $\mathbf{T}$, i.e. $\frac{1}{2}(\mathbf{T} + \mathbf{T}^t)$ (superfix t is transpose) is positive definite.

Note that this result does not require that the tensor actually be symmetric and therefore applies for all quadrature points q and thus the whole family of both physical space and transform space schemes, provided that the local discrete tensor is elliptic and holds for each subcell energy contribution. A symmetric positive definite (SPD) scheme will result if each discrete subcell tensor is symmetric ($T_{12}^i = T_{21}^i$) and elliptic ${T_{12}^i}^2 \leq (T_{11}^i T_{22}^i)$, as constructed in the next sections. The SPD result will then follow from the above since the flux matrix equation 6.7 will then be symmetric, leading to a symmetric global matrix [4] and ellipticity ensures that equation 6.10 is positive. These results also hold for triangles, the cell vertex formulation is treated in [4, 7, 25] and cell-centred formulation in [126].

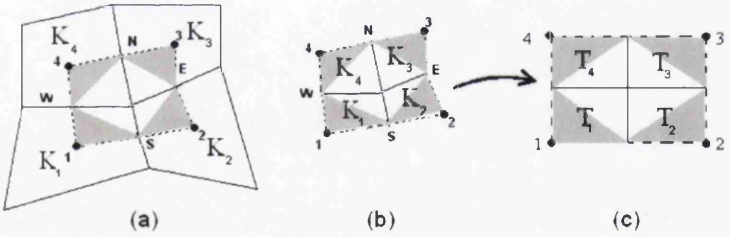

Figure 6.1: (a)Physical-space Quads and Piece-wise constant Tensor (*quadrature point q = 1*) (b) Piece-wise constant Tensor over subcells. (c) Sub-cell Transformation to Piece-wise constant General Tensor per subcell.

6.4 Symmetric Positive Definite Tensor Approximation

Loss of symmetry in the general tensor occurs in the physical space approximation due to the variation in general tensor over the control-volume faces, as discussed in the above section. An SPD formulation is favored theoretically for proving convergence and practically for using simpler more robust solvers. A symmetric positive definite (SPD) flux-continuous scheme is obtained if each pair of sub-cell fluxes are defined with respect to the *same* piece-wise constant *symmetric* general tensor per sub-cell [4], figure 6.1 where local numbering refers to the subcells of the control-volume.

This approximation has been shown to lead to a symmetric flux matrix and a symmetric positive definite discretization matrix [4]. A symmetric positive definite discrete general tensor is a fundamental condition for obtaining a symmetric positive discrete matrix. Also use of a *unique* local SPD tensor in defining local sub-cell fluxes mirrors an analytic flux property in the discrete approximation.

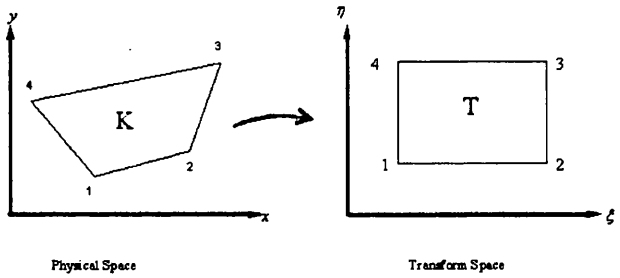

Figure 6.2: Control-volume Cell-wise Transformation.

The first flux continuous schemes that have been shown to be SPD for quadrilateral meshes, were obtained by using a *transform* space formulation at the cell level where a mean piece-wise constant general-tensor approximation is used over each cell (control-volume), figure 6.2, and the general-tensor is approximated at the cell-center [3, 53]. However, an SPD formulation is obtained at the expense of an additional ap-

proximation in geometry, compared to the physical space formulation which maintains exact geometry and is therefore more accurate.

While both formulations (cell level and subcell level) ensure that the discrete matrix is SPD, the subcell formulation first proposed by Edwards [4], [22], [23] has important advantages over the cell-wise *transform* space formulation proposed in [3, 53]. By definition a piecewise constant subcell tensor is a superior approximation of the tensor due to allowing a finer scale variation in the tensor geometry, precisely on the sub-scale, resulting in four discrete values compared to a single value at the cell level, for a given quadrilateral cell. This has important convergence implications and the practical outcome in terms of convergence rates is presented in the results section. Secondly, unlike the cell-wise approximation, the subcell scheme generalises to unstructured grids as in [4],[22], [23], allowing any grid combination of quadrilateral and /or triangular cells. In all cases the sub-cell flux continuous schemes are symmetric positive definite for any grid type.

One of the key issues in this new formulation is the identification of the appropriate approximation of general-tensor T^k, for each subcell $k = (1, .., 4)$.

In principle there are an infinite number of possibilities depending upon the point chosen to evaluate the tensor inside the subcell. In each of the following subcell tensor approximations the local piecewise constant tensors restore ellipticity and symmetry, e.g. instead of equation 6.1 we now have

$$T_{12}|_W^1 = T_{12}|_S^1 = T_{12}|^1 \tag{6.11}$$

Different possible general-tensor approximations have already been presented for triangles and quadrilaterals in [22, 23]. Here we consider three of the many possible approximations for quadrilateral grids.

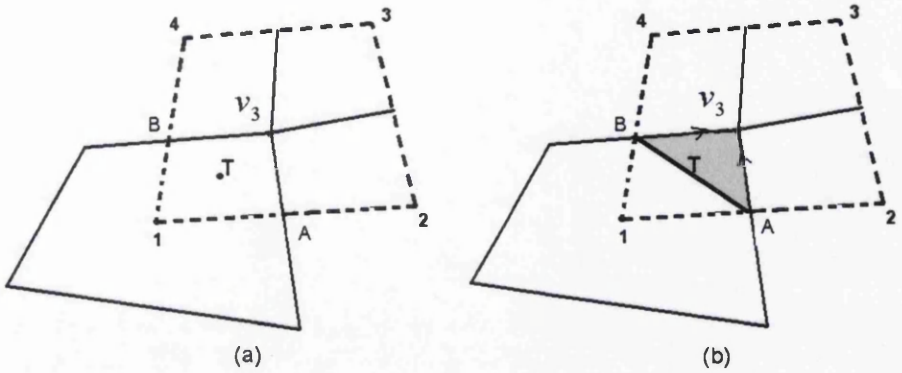

Figure 6.3: (a)Control-volume sub-cell Centre Tensor ($\xi = 0.5, \eta = 0.5$). (b) Control-volume Sub-cell face Tensor ($\xi = 1, \eta = 1$). *Quadrilateral primal grid Cell (solid line) Dual-Cell (dashed line) , Subcell (1,E,M,W).* Subcell transform coordinate system origin ($\xi = \eta = 0$) corresponds to primal grid Quadrilateral mid-point.

6.4.1 Positive Definite - Simple Average

The first definition is defined by a simple average of the cross terms with

$$\hat{T}_{12}|^1 = \frac{1}{2}(T_{12}|^1_W + T_{12}|^1_S) \tag{6.12}$$

this has the effect of replacing the local tensor T^j by

$$\frac{1}{2}(T^j + (T^j)^t) \tag{6.13}$$

(where superfix t denotes transpose) which is one of a number of approximations motivated by the general definition of a positive definite matrix (i.e. $\frac{1}{2}(A^j + (A^j)^t)$) when the matrix is non-symmetric. While equation 6.12 symmetrizes the tensor for any quadrature q, convergence is at best poor.

6.4.2 Local Mapping - Subcell Centre Tensor

The second definition, following [22, 23, 67], is a local mean general-tensor, for each local sub-quadrilateral of every primal quadrilateral cell. In this case each sub-quadrilateral is in effect mapped to a unit cell via a bilinear transformation given

as

$$\mathbf{r} = \mathbf{r}_1(1-\xi)(1-\eta) + \mathbf{r}_2\xi(1-\eta) + \mathbf{r}_3\xi\eta + \mathbf{r}_4(1-\eta)\xi \tag{6.14}$$

where $\mathbf{r}$ is the position vector of an arbitrary point in the subcell, $\mathbf{r}_i$ is the position vector of the sub-cell corner coordinates and (ξ, η) are the local unit transformed cell coordinates figure 6.3(a). In this definition [22] we choose $(\xi = 0.5, \eta = 0.5)$ corresponding to the mean subcell centre value.

6.4.3 Control-volume Face Tensor

In the third definition [22, 23, 67], the piece-wise constant tensor is defined with respect to the subcell control-volume face geometry, figure 6.3(b). The local general tensor is built in a coordinate system directly aligned with the two control-volume faces, so that the surface normal vectors are naturally incorporated within the formulation. This formulation is most closely associated with the physical space control-volume sub-faces and the approximation corresponds to $(\xi = 1, \eta = 1)$, equation 6.14. Thus the tensor is defined by the geometry of the triangle defined by the two parent control-volume *sub faces* i.e. the two faces of the subcell as indicated in figure 6.3(b). This approximation is robust provided that no pair of control-volume sub-cell faces are parallel. If parallel sub-faces are detected the above sub-cell centre tensor approximation is used.

It is anticipated that this approximation will be the most successful, since by definition it is based entirely on control-volume face geometry.

6.5 Family of Subcell Schemes and Symmetric Positive Definite Approximation

The family of subcell tensor schemes is readily defined by returning to the physical space formulation of the family of schemes (section 4.3.3) and replacing the physical

space tensors of equation 6.3 with the piecewise constant symmetric positive definite subcell tensors defined in the previous section, where

$$\hat{T^1} = \begin{pmatrix} \hat{T}_{11}|^1 & \hat{T}_{12}|^1 \\ \hat{T}_{12}|^1 & \hat{T}_{22}|^1 \end{pmatrix}, \qquad \hat{T^2} = \begin{pmatrix} \hat{T}_{11}|^2 & \hat{T}_{12}|^2 \\ \hat{T}_{12}|^2 & \hat{T}_{22}|^2 \end{pmatrix}$$
$$\hat{T^3} = \begin{pmatrix} \hat{T}_{11}|^3 & \hat{T}_{12}|^3 \\ \hat{T}_{12}|^3 & \hat{T}_{22}|^3 \end{pmatrix}, \qquad \hat{T^4} = \begin{pmatrix} \hat{T}_{11}|^4 & \hat{T}_{12}|^4 \\ \hat{T}_{12}|^4 & \hat{T}_{22}|^4 \end{pmatrix} \tag{6.15}$$

and the tensor superfix corresponds to the local number of the subcell in the dual-cell. The subcell schemes follow directly, using equation 6.15 in equations 5.15 - 5.19 now formed with respect to each local subcell transform space where

$$\phi_\xi = J(\phi,\eta)/J(\xi,\eta), \qquad \phi_\eta = J(\xi,\phi)/J(\xi,\eta) \tag{6.16}$$

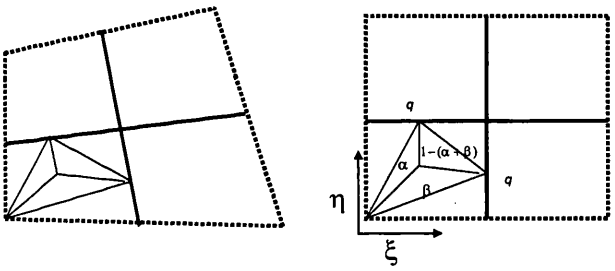

Figure 6.4: Subcell Transform Space and General Quadrature Point q

where $J(\xi,\eta) = \xi_\alpha\eta_\beta - \xi_\beta\eta_\alpha$ and (α,β) are area coordinates of the pressure sub-triangle in subcell transform space, figure 6.4. The range of quadrature points correspond to the interface pressure points as before and now define a family of schemes in sub-cell transform space.

6.5.1 Subcell Tensor SPD Flux

In [4] it is shown that for the base member of the family of subcell schemes, using quadrature $q = 1$ yields a symmetric positive definite discretization matrix for quadri-

lateral and triangle meshes. The base (SPD) scheme flux is derived directly below in cell centred form. Using (one-sided) control-volume face mid-point quadrature ($q = 1$), (figure 5.7(c)) and repeating the steps of equations 6.2 - 6.7 with equation 6.3 replaced by equation 6.15 with a piecewise constant symmetric tensor per subcell, the flux is given by

$$A\mathbf{F} = -\Delta\phi_{\mathbf{v}} \tag{6.17}$$

where

$$\mathbf{F} = (F_S, F_E, F_N, F_W)^T, \qquad \Delta\phi_{\mathbf{v}} = (\phi_{21}, \phi_{32}, \phi_{34}, \phi_{41})^T \tag{6.18}$$

and in this case the flux coefficient matrix is *symmetric*, with

$$A = \begin{pmatrix} \hat{T}^1_{11} + \hat{T}^2_{11} & \hat{T}^2_{12} & 0 & \hat{T}^1_{12} \\ \hat{T}^2_{12} & \hat{T}^2_{22} + \hat{T}^3_{22} & \hat{T}^3_{12} & 0 \\ 0 & \hat{T}^3_{12} & \hat{T}^4_{11} + \hat{T}^3_{11} & \hat{T}^4_{12} \\ \hat{T}^1_{12} & 0 & \hat{T}^4_{12} & \hat{T}^1_{22} + \hat{T}^4_{22} \end{pmatrix} \tag{6.19}$$

The dual-cell flux matrix entries are now comprised of elements of the inverse of the subcell tensors corresponding to each subcell component of control-volume. Symmetry of the flux matrix equation 6.19 follows from the symmetry of the subcell tensors. In contrast compare the physical-space flux matrix of equation 6.7 with the subcell tensor flux matrix equation 6.19. Symmetry of the flux matrix equation 6.19 leads to a symmetric discretization matrix together with positive definiteness [4].

The subcell fluxes of equations 6.5,6.17 embody the full tensor generalization of the harmonic mean. If the tensor is locally diagonal the interface equations reduce to the form of equation 6.9 or

$$F = -\frac{2K_lK_r(\phi_r - \phi_l)}{h(K_l + K_r)} \tag{6.20}$$

recovering the well-known 2-point flux approximation with harmonic mean coefficient.

6.6 Numerical Results

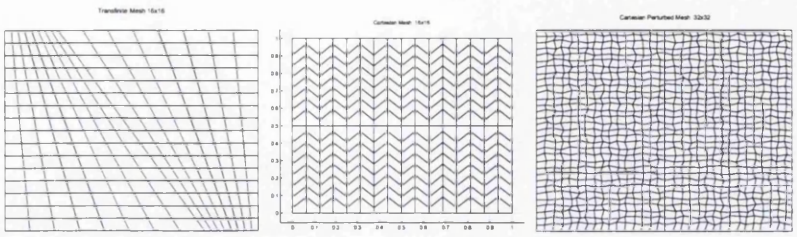

Figure 6.5: (a) Transfinite mesh aligned along $\theta = 2\pi/3$ discontinuity. (b) Zig-Zag grid honoring internal discontinuity along X and Y axis. (c) Cartesian Perturbed Grid honoring discontinuity.

In this section we present a study of the effect of subcell tensor approximation, where the tensor is calculated using control-volume face geometry (figure 6.3) and quadrature point on convergence of the subcell scheme formulation. A comparison is made between the subcell formulation, physical space formulation and the cell-wise transformed control-volume scheme. A positive-definite test of the physical space and subcell transform space tensors is also conducted for each q considered in the convergence study (except for subcell transform space $q = 1$, which is SPD). For all grids the discrete physical space and subcell transform space tensors are found to be positive-definite for $q = 0.5$ and $q = 1$. We note that the numerical convergence study of the family of flux continuous schemes in *physical* space (presented in previous chapter) has shown that quadrature point $q = 0.1$ yields improved convergence when compared to other quadrature points [5].

6.6.1 Convergence Results

A convergence study is presented for the subcell schemes using the subcell tensor approximations described above and range of quadrature points $q = 0.1, 0.5$ and 1. The subcell schemes are tested on the grids shown in figure 6.5.

Pressure and velocity convergence are measured using the L_2 error *norm* where

$$L_2 = \left(\frac{\sum_i (A_i (p_i^{analytical} - p_i^{numerical})^2)}{\sum_i A_i} \right)^{1/2} \tag{6.21}$$

and A_i is the area of the grid cell i. The grid refinement levels used for the L_2 *norm* calculation are 4x4, 8x8, 16x16,32x32 and 64x64 for all test cases.

CASE 1: The first test example involves uniform flow over a rectangular domain. The pressure field is linear and varies as

$$\phi(x, y) = x + y - 1/2 \tag{6.22}$$

The diagonal permeability tensor $\mathbf{K} = c\mathbf{I}$, where c = 10. The numerical solution of equation 6.22 is obtained on a grid aligned with an interior boundary oriented at $2\pi/3$ from the horizontal line as shown in figure 6.5 (a). The numerical pressure and

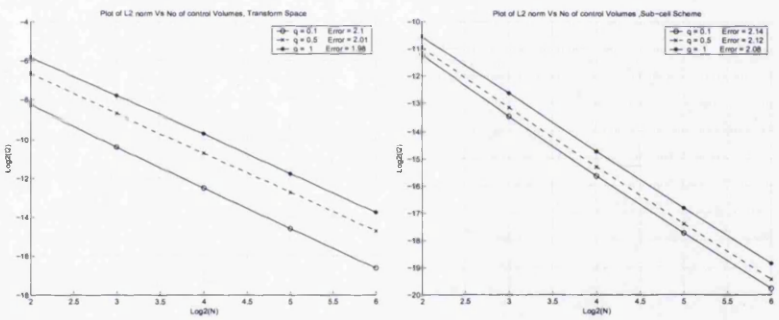

Figure 6.6: CASE 1: (a) Plot of L2 error norm for pressure, Cell-wise Transform Space. (b) Plot of L2 error norm for pressure, Sub-cell Scheme.

velocity were found to be exact for all quadrature points when using the *physical* space scheme as control-volume geometry is exactly represented and the numerical approximation and exact solution are both piecewise linear. Since the tensor fields are found to be positive definite for this case (so that discrete operator M_G is positive definite and the inverse exists) the exact solution property can be deduced from the discrete error equation $M_G e_h = 0$ where solution error $e_h = \phi(x, y) - \phi_h$ (difference

between exact and discrete solutions). For the cell-wise transform space scheme, convergence of the numerical solution is found to be of the order $O(h^2)$ for pressure and velocity [3, 5, 127].

On solving the problem with the subcell scheme, numerical convergence of pressure and velocity was found to be of order slightly greater than $O(h^2)$ for all quadrature points. The errors obtained in numerical pressure and velocity are found to be much less when using the subcell formulation compared to the cell-wise formulation, figure 6.6. This is consistent with using the superior tensor approximation provided by the subcell scheme.

CASE 2: Next we test an example on a similar grid to that of the previous example, involving a smooth reference solution on a homogeneous medium. The analytical solution of pressure is given by

$$\phi(x, y) = sin(\pi x)sinh(\pi y) \tag{6.23}$$

The permeability tensor is diagonal and is given by $\mathbf{K} = c\mathbf{I}$ where $c = 1000$. Dirichlet

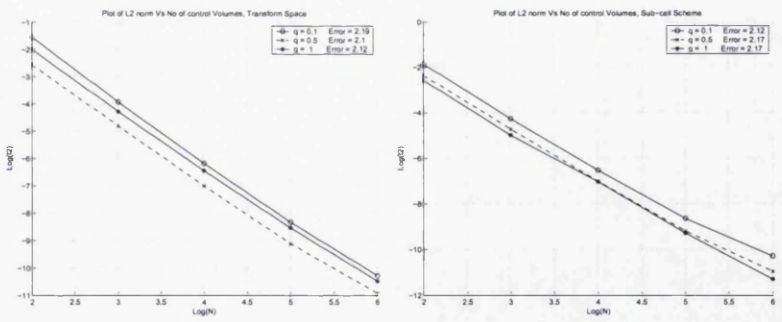

Figure 6.7: CASE 2: (a) Plot of L2 error norm for pressure, Transform Space. (b) Plot of L2 error norm for pressure, Sub-cell Scheme.

boundary conditions are applied on the boundary on a square domain. The order of convergence of pressure and velocity is found to be close to $O(h^2)$ for the cell-wise control-volume transform space formulation. Whereas, for the subcell scheme

formulation the order of convergence for pressure and velocity is found to be greater than $O(h^2)$ for all quadrature points. As in the previous test case, the errors are found to be less for the subcell scheme formulation for all quadrature points compared to the cell-wise formulation, see figure 6.7.

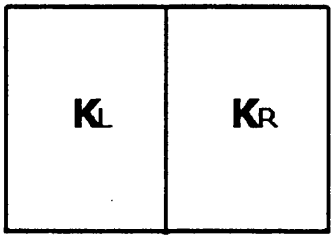

Figure 6.8: Discontinuous Tensor field

CASE 3: The third numerical example ([3]) involves solving the problem with quadratic pressure, where the exact solution given by equation 6.24 below. This example involves a discontinuous jump in permeability and is therefore more challenging than the previous examples. The domain shown in figure 6.8 has a permeability discontinuity at $x = 0.5$ and the permeability tensor is quite distinct in the two subdomains. This numerical example was also presented in previous chapter, where the details of coefficients of equation 6.24 can be found.

$$\phi(x,y) = \begin{cases} c_l x^2 + d_l y^2, & x < 1/2, \\ a_r + b_r x + c_r x^2 + d_r y^2, & x \geq 1/2, \end{cases} \tag{6.24}$$

$$K = \begin{cases} \begin{pmatrix} 50 & 0 \\ 0 & 1 \end{pmatrix}, & x < 1/2, \\ \begin{pmatrix} 1 & 0 \\ 0 & 10 \end{pmatrix}, & x \geq 1/2, \end{cases} \tag{6.25}$$

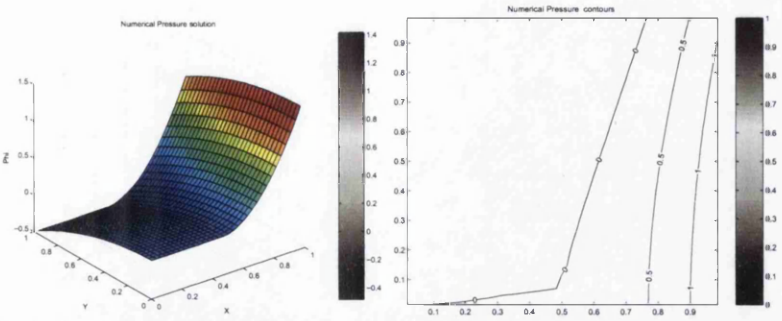

Figure 6.9: CASE 3: (a)Numerical pressure solution using Sub-cell Scheme. (b) Numerical Pressure contours.

Quadrature	q=0.1	q=0.5	q=1
Physical space scheme	$O(h^{1.35})$	$O(h^{1.35})$	$O(h^{1.33})$
Subcell transform space scheme	$O(h^{0.955})$	$O(h^{0.941})$	$O(h^{0.912})$
Cell-wise transform space scheme	$O(h^{0.322})$	$O(h^{0.848})$	$O(h^{0.626})$

Table 6.1: CASE 3: Pressure convergence with variable quadrature q

The above numerical example has been tested previously [3, 5] and a $O(h^2)$ convergence for pressure and close to $O(h^2)$ convergence for velocity has been obtained for the CVD scheme in physical space. Here we test this example on a domain shown in figure 6.8 using cartesian perturbed grids honoring discontinuity as shown in figure 6.5(c). The numerical solution of the pressure is shown along with the pressure contours in figure 6.9. Comparison of numerical convergence results for physical space scheme, subcell transform space scheme and cell-wise transform space scheme are shown in tables 7.1,7.2. Plots of the numerical convergence of pressure and velocity

Quadrature	q=0.1	q=0.5	q=1
Physical space scheme	$O(h^1)$	$O(h^1)$	$O(h^{0.989})$
Subcell transform space scheme	$O(h^{0.231})$	$O(h^{0.227})$	$O(h^{0.256})$
Cell-wise transform space scheme	$O(h^{0.167})$	$O(h^{0.0873})$	$O(h^{0.0943})$

Table 6.2: CASE 3: Velocity convergence with variable quadrature q

for cellwise transform space scheme is shown in figure 6.10. Plots of the numerical pressure and velocity convergence for subcell transform space and physical space schemes are shown in figure 6.11, 6.12 respectively. Convergence rates of pressure and velocity convergence are found to improve when using the subcell scheme which results in reduced computational error compared to the cell-wise formulation.

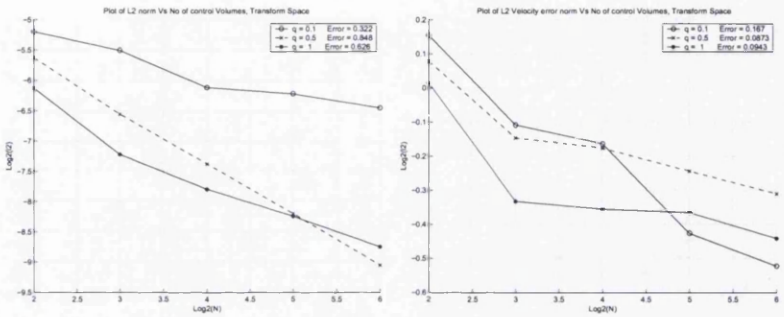

Figure 6.10: CASE 3: (a) Pressure Convergence for cell-wise Transform Space formulation. (b) Velocity Convergence for cell-wise Transform Space formulation.

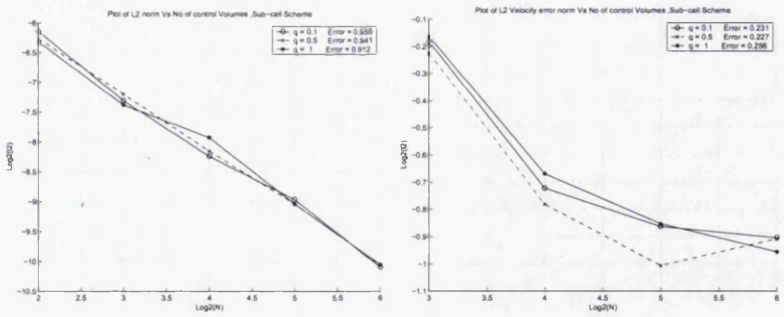

Figure 6.11: CASE 3: (a)Pressure convergence for Sub-cell Scheme formulation. (b) Velocity convergence for Sub-cell Scheme formulation.

CASE 4: The following numerical examples test the numerical convergence of the sub-cell scheme for the previously defined range of quadrature points applied to challenging examples involving a corner point singularity in the field (taken form

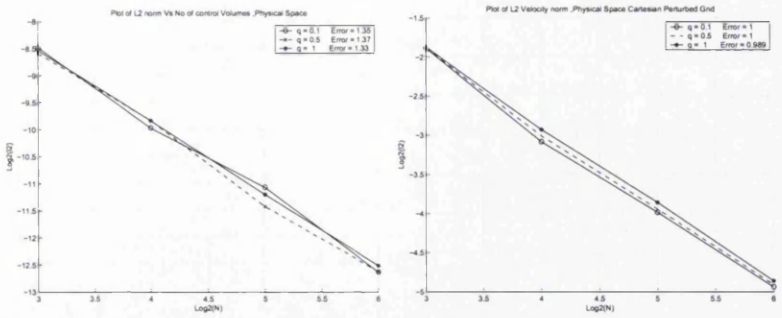

Figure 6.12: CASE 3: (a)Pressure convergence for Physical Space formulation. (b) Velocity convergence for Physical Space formulation.

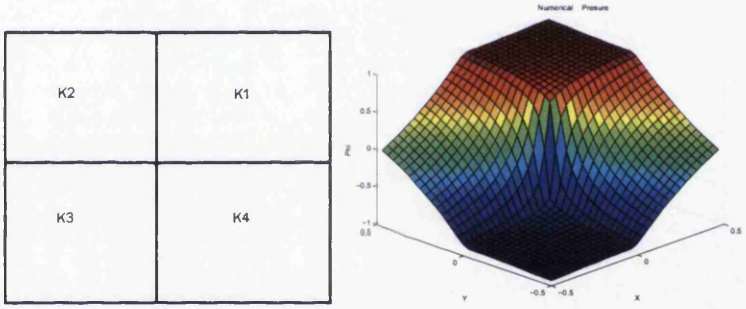

Figure 6.13: CASE 4: (a)Subdomain with discontinuity along $\theta = \pi/2$. (b) Numerical Pressure solution on the domain.

[42, 82]). The domain is divided into four sub-domains and the permeability tensor is discontinuous across each subdomain boundary as shown in figure 6.13(a). The numerical solutions are computed on zig-zag grids honoring the discontinuities shown in figure 6.5 (b). The exact pressure solution is given by

$$\phi(r, \theta) = r^{\alpha}(a_i sin(\alpha\theta) + b_i cos(\alpha\theta)) \tag{6.26}$$

The difference between problems is in terms of strength of the coefficients and permeability tensor, which also determines the level of difficulty in each case. We will start with smoother case with higher value of the parameter α and gradually moving

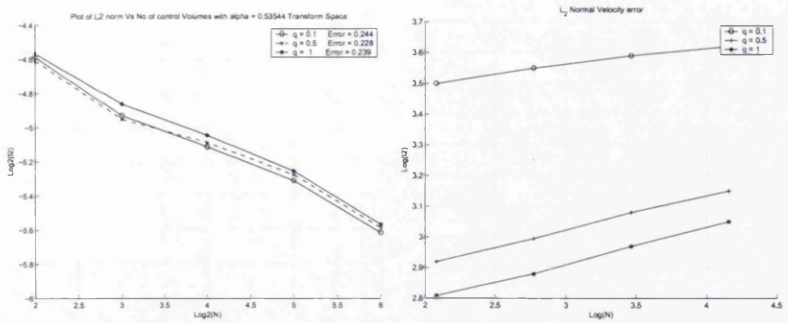

Figure 6.14: SUBCASE 4.1:(a)Pressure convergence for cell-wise Transform space formulation. (b) Velocity convergence for cell-wise Transform space formulation.

to more tougher cases with smaller values of the parameter α.

Quadrature	q=0.1	q=0.5	q=1
Physical space scheme	$O(h^{1.09})$	$O(h^{1.1})$	$O(h^{1.04})$
Subcell transform space scheme	$O(h^{0.781})$	$O(h^{0.806})$	$O(h^{0.910})$
Cell-wise transform space scheme	$O(h^{0.244})$	$O(h^{0.228})$	$O(h^{0.239})$

Table 6.3: SUBCASE 4.1: Pressure convergence with variable quadrature q

SUBCASE 4.1: For the first test example we choose $\alpha = 0.53544095$ (where the other coefficients can be found in [5]), the numerical pressure solution for physical space scheme is shown in figure 6.13(b). Plots of numerical pressure and velocity convergence for the cell-wise transform space control-volume formulation are shown in figure 6.14. Plots of numerical pressure convergence of velocity and pressure for subcell transform space scheme and physical space scheme are shown in figure 6.15.

Quadrature	q=0.1	q=0.5	q=1
Physical space scheme	$O(h^{0.235})$	$O(h^{0.193})$	$O(h^{0.180})$
Subcell transform space scheme	$O(h^{0.205})$	$O(h^{0.186})$	$O(h^{0.175})$
Cell-wise transform space scheme	$O(h^{0.143})$	$O(h^{0.129})$	$O(h^{0.124})$

Table 6.4: SUBCASE 4.1: Velocity convergence with variable quadrature q

And Comparison of numerical convergence results for physical space scheme, subcell transform space scheme and cell-wise transform space scheme are shown in tables 6.3,6.4. Again, errors in pressure and velocity are much less in the case of the subcell scheme compared to the cell-wise transform space formulation.

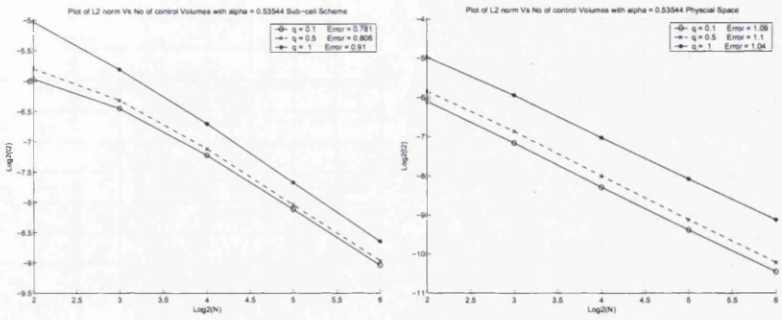

Figure 6.15: SUBCASE 4.1: (a)Pressure convergence for Sub-cell scheme formulation. (b) Pressure convergence for Physical Space formulation.

SUBCASE 4.2: Next we test a numerical example for $\alpha = 0.28009739$. In this case the numerical convergence of pressure for the cell-wise transform space formulation is found to be of the order of $h^{0.502}$ for $q = 0.1$ as shown in figure 6.16(a) and velocities are found to be diverging. For the sub-cell scheme the numerical convergence of pressure is found to be of the order of $O(h^{0.584})$ for $q = 0.1$(figure 6.16(b)) and velocities are diverging. The numerical convergence of pressure for Physical space formulation is shown in figure 6.16(c). Again subcell scheme pressure errors are much less than that of the cell-wise scheme and are quite comparable to physical space pressure convergence results, also, $q = 0.1$ yields the best overall performance.

SUBCASE 4.3: This test case is less smoother compared to previous two test cases because of smaller value of the parameter α. For this test example the parameter $\alpha = 0.1269020697$. The numerical convergence of pressure for the cell-wise transform space formulation is found to be of the order of $O(h^{0.583})$ for $q = 0.1$ as shown in figure 6.17(a) and velocities are found to be diverging.

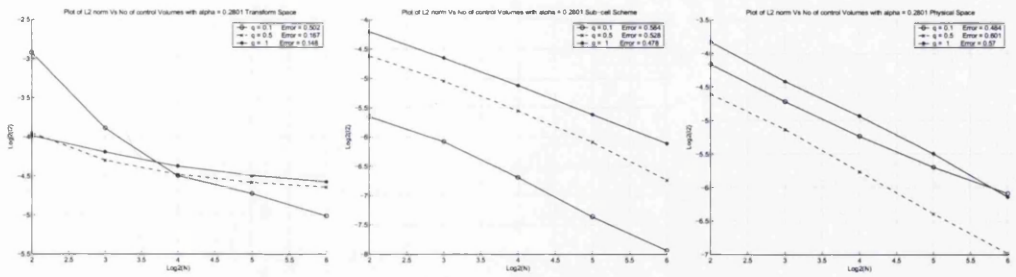

Figure 6.16: SUBCASE 4.2: (a)Pressure convergence for Transform space formulation. (b) Pressure convergence for Sub-cell Scheme formulation. (c) Pressure Convergence Physical Space.

For the subcell scheme the numerical convergence of pressure is found to be of the order of $O(h^{0.625})$ for $q = 0.1$(figure 6.17(b)) and velocities are found to be diverging. The numerical pressure convergence for physical space formulation is found to be of the order of $O(h^{1.04})$ for $q = 0.1$ whereas, numerical velocities are found to be diverging [5, 82]. However, as in the previous cases pressure errors in case of sub-cell scheme formulation are much less than the cell-wise scheme.

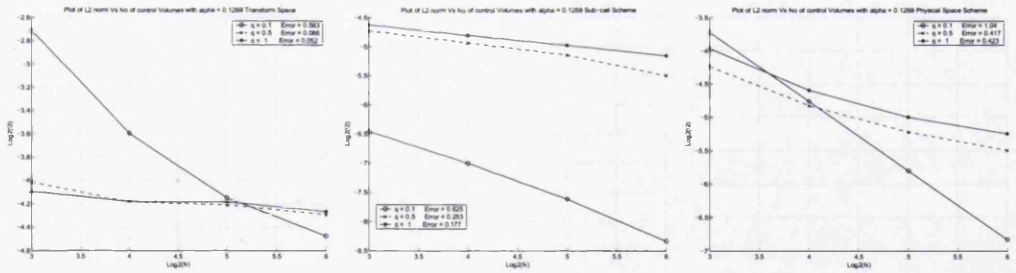

Figure 6.17: SUBCASE 4.3: (a)Pressure convergence for Transform space formulation. (b) Pressure convergence for Sub-cell Scheme formulation. (c) Pressure convergence for Physical Space Scheme formulation.

SUBCASE 4.4:

Finally, we take a test case where $\alpha = 0.13448835$ and the domain discontinuity

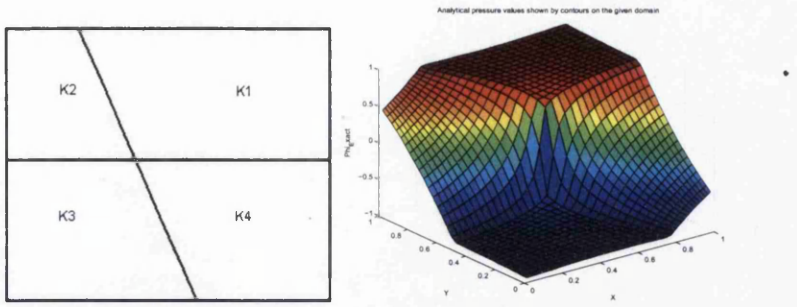

Figure 6.18: SUBCASE 4.4: (a)Subdomain with discontinuity along $\theta = 2\pi/3$. (b) Numerical Pressure solution.

is along the line $2\pi/3$ as shown in figure 6.18(a). The numerical solution is obtained using grid aligned with an interior boundary oriented at $2\pi/3$ from the horizontal line as shown in figure 6.5(a)(further detail regarding strength of coefficients for this test case can be found in [5]). For this test case numerical solution is shown in figure 6.18(b). The numerical pressure convergence for Physical space formulation is shown in figure 6.19(a) and pressure convergence for sub-cell scheme formulation is shown in 6.19(b). The numerical velocities are found to be diverging as also noted in [5, 82]. It can be seen that for this particular test case super-convergence is obtained for $q = 0.1$ for both physical and sub-cell scheme formulations. Also, the convergence rates are quite comparable. The q-family is able to sense cross flow for $q < 1$ [20].

Superior performance of the sub-cell scheme compared to cell-wise transform space is also obtained for stronger values of α, where sub-cell errors are found to be significantly smaller. Velocities are found to be diverging in these later cases for physical and transform space. We note that the rate of pressure convergence has exponent less than one, since velocity is proportional to pressure gradient, velocity errors may loose an order in convergence, which implies a negative rate.

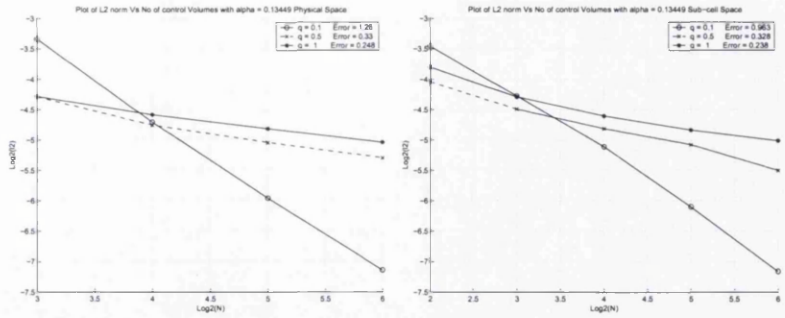

Figure 6.19: SUBCASE 4.4: (a)Pressure Convergence Physical Space scheme. (b) Pressure Convergence Sub-cell Scheme.

6.7 Summary

A symmetric positive definite general-tensor formulation is presented. A new family of flux continuous schemes are defined by the introduction of piecewise constant subcell general-tensor approximations within the formulation. The physical-space fluxes are shown to be non-symmetric for general quadrilateral cells and can consequently lead to non-symmetric discretization schemes.

The effect of subcell tensor approximation and quadrature point on convergence is presented and compared with the cell-wise transformed control-volume scheme. The subcell scheme uses a finer scale representation of the cell geometry compared to the cell-wise transform scheme and is found to have the better overall convergence performance for the cases tested. In particular the control-volume face subcell tensor approximation yields the best results. For the SPD schemes quadrature point $q = 0.1$ is found to be the most beneficial for the subcell schemes.

Note that while symmetry is restored for general quadrilateral grids by the subcell schemes together with SPD discretization for $q = 1$, the piecewise constant subcell tensor still involves an additional approximation in geometry. Consequently the sub-

cell methods cannot generally retain the accuracy of the physical space schemes, but can improve performance when compared with the cell-wise tensor schemes.

The physical space schemes maintain exact geometry of the control-volumes but loose the ability to retain symmetry of the discretization for general quadrilateral grids.

Chapter 7

Monotonicity Issues

7.1 Introduction

Monotonicity behavior of the family of flux-continuous schemes has been in question since its early formulation. Conditions for a symmetric positive definite matrix are given in [3, 4]. Conditions for when the family of schemes yield an M-matrix are are presented in [2, 9, 3], where it is shown that the discretization matrices obtained in the case of a full tensor are conditionally diagonally dominant with negative off-diagonals and M-matrices are only obtained for a limited range of full tensors. For high anisotropic ratios with grid skewness the resulting discrete matrix for these schemes is found to be non-monotonic (as with more standard methods) and the numerical solution consequently exhibits spurious oscillations.

The aim of this chapter is to address the monotonicity issues relating to the family of schemes and to obtain a solution to this problem. In this chapter along with discussion of monotonicity issues numerical tests are also performed in 2-D and 3-D. An M-Matrix analysis [3] is used to determine the route towards optimal schemes with respect to monotonicity.

A novel numerical strategy [7, 8] is presented here which involves the use of flux-splitting (introduced in [6]) applied to the family of flux-continuous schemes. Proper-

ties of the flux-splitting schemes for the single-phase pressure equation are presented in [6, 128]. Here it is shown that careful use of flux-splitting can remove the spurious oscillations introduced in the numerical pressure solution by highly anisotropic permeability tensors in porous medium. Previous work aimed at preserving monotonic behavior of the solutions for strong heterogeneity and skew grids is presented in [129]. Conditions for monotonicity have previously been derived in [2, 9, 3] for an M-matrix and in [83, 84] for a monotone matrix. Grid optimization techniques have also been used to improve monotonicity of the discrete system [130]. However, these techniques appear to be limited subject to permeability anisotropy ratio. In contrast, the flux-splitting techniques [7, 8] presented here are easier to implement for both structured and unstructured grids and can handle very strong anisotropic heterogeneity.

This chapter is organized as follows: Section 7.2 summarizes conditions required to obtain a monotonic solution and describes performance of the family of flux-continuous schemes with respect to monotonicity, with the help of numerical examples. Section 7.3 describes the flux splitting technique to solve the discrete system and shows how it can be used to compute a monotonic solution for the family of flux-continuous schemes. Section 7.4 presents numerical examples that demonstrate the use of flux-splitting techniques for preserving monotonicity. Section 7.5 presents the procedure to obtain quasi-monotonic schemes which minimizes oscillations in numerical solution. A summary follows in section 7.6.

7.2 Monotonicity in 2-D and 3-D

The family of flux-continuous schemes results in a discrete matrix which forms 5-9 row entries on structured 2D grids and 7-27 row entries on structured 3D grids. The discrete system can be written as

$$\mathbf{A}\phi = b \tag{7.1}$$

Where $\mathbf{A}$ is the discrete matrix operator, ϕ is the unknown pressure and b is the source term. Ideally the discrete system of equation 7.1 should be *monotone*, and satisfy a *maximum principle* which is analogous to that of the continuous counterpart of the discrete problem and hence ensuring that the numerical solution is free from nonphysical oscillations. The discrete matrix operator $\mathbf{A}$ is *monotone* if and only if $\mathbf{A}$ is non-singular and it obeys the following condition [131]

$$\mathbf{A}^{-1} \geq \mathbf{O} \tag{7.2}$$

where $\mathbf{O}$ is a zero matrix. While a monotone discretization matrix ensures that a non-negative source and boundary data yields a non-negative pressure field, it has not been proven that a monotone discretization matrix will prevent discrete spurious local extrema occurring in the discrete solution of the general tensor pressure equation. A sufficient condition for a maximum principle (which can ensure that no spurious extrema occur in the discrete solution) is that $\mathbf{A}$ is a $\mathbf{M}-$matrix, i.e. monotone matrix (or positive definite) with $a_{i,j} \leq 0$ for $i \neq j$. The following conditions (often easier to verify) also define an $\mathbf{M}-$matrix:

$$\begin{aligned} a_{i,i} &> 0, \forall i \\ a_{i,j} &\leq 0, \forall i, j, i \neq j \\ \Sigma_j a_{i,j} &\geq 0, \forall i \end{aligned} \tag{7.3}$$

In addition $\mathbf{A}$ must either be strictly diagonally dominant,i.e.

$$A_{i,i} > \sum_{j=1, j\neq i}^{n} \mid A_{i,j} \mid, \quad i = 1, 2, ..., n \tag{7.4}$$

or else $\mathbf{A}$ must be irreducible and

$$A_{i,i} \geq \sum_{j=1, j\neq i}^{n} \mid A_{i,j} \mid, \quad i = 1, 2, ..., n \tag{7.5}$$

with strict inequality for at least one row. The conditions (derived in [3, 9]) for nine-node schemes to have an M-Matrix are

$$min(T_{11}, T_{22}) \geq \eta(T_{11} + T_{22}) \geq \mid T_{12} \mid \tag{7.6}$$

where η is a function of quadrature point [3]. T_{ij} are the general tensor coefficients. One of the essential conditions here is that $T_{12} \leq min(T_{11}, T_{22})$, which is particularly limiting on the range of tensors that are applicable since this condition is only *sufficient* for ellipticity $T_{12}^2 \leq T_{11}T_{22}$, so that in the general case these schemes do not possess M-Matrices.

It has been previously noted in [7, 8, 83, 25] that the 2D 9-point formulation and 3-D 27-point formulation suffers from loss of monotonicity and hence violation of the maximum principle resulting in spurious oscillations in the numerical pressure field, when applied to a medium with high full-tensor anisotropy. However, it will be shown in the next section that solving such problems by the Flux-splitting technique [6] with a locally imposed maximum principle yields numerical pressure solutions that are free of spurious oscillations [7].

We will now present numerical examples which demonstrate the loss of monotonicity and violation of maximum principle when using the finite volume formulation in 2-D and 3-D(note that standard schemes also fail on this example). In these examples a point source is introduced at the centre of the domain (Square [0,1]x[0,1] in 2-D and Cube [0,1]x[0,1]x[0,1] in 3-D) with orthogonal Cartesian grid in 2-D and Hexahedral grid in 3-D and zero Dirichlet pressure holds elsewhere on the boundary. Two different (isotropic and anisotropic) permeability tensor fields are tested and the results are shown for 2-D and 3-D formulation of the scheme in figure 7.1 and 7.3 respectively. It can be seen from figure 7.1(a) and 7.3(a) that the numerical pressure solution in the first case (isotropic) has a maximum principle. In the second case (with anisotropy ratio of 1:1000,with grid *non-aligned* with the principal axes leading to a full-tensor

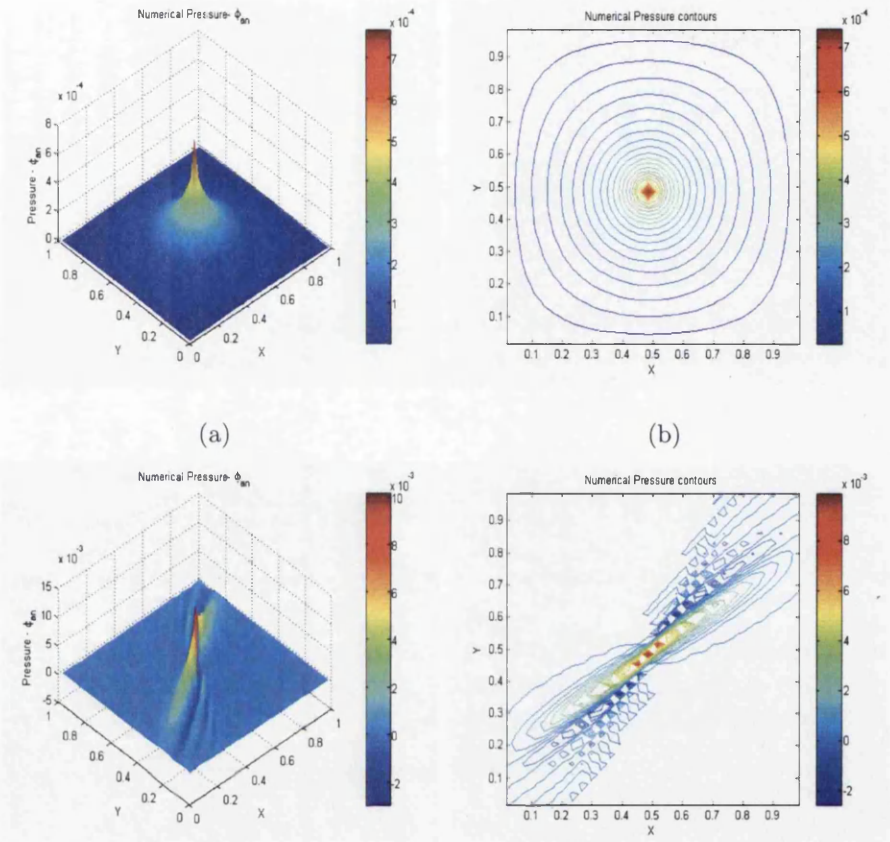

Figure 7.1: (a) 2-D Numerical pressure solution with isotropic permeability tensor. (b) 2-D Numerical pressure contours for isotropic tensor.(c) 2-D Numerical pressure solution with anisotropy ratio 1:1000 and angles between grid and principal permeability axes = 30 degrees.(d) 2-D Numerical pressure contours for anisotropy tensor.

(see Appendix B) $\begin{pmatrix} 250.75 & 432.58 \\ 432.58 & 750.25 \end{pmatrix}$, figure 7.2) the tensor field violates equation 7.6 with $\{min(750.25, 250.75) \ngeq 432.58\}$ and the numerical pressure solution shown in figure 7.1(b) and 7.3(b) clearly violates the maximum principle resulting in spurious oscillations including some negative pressure values, hence equation 7.2 is not valid in this case. The spurious oscillations in pressure do not disappear even with mesh refinement. A similar test in 2-D with Green's function was presented in [83].

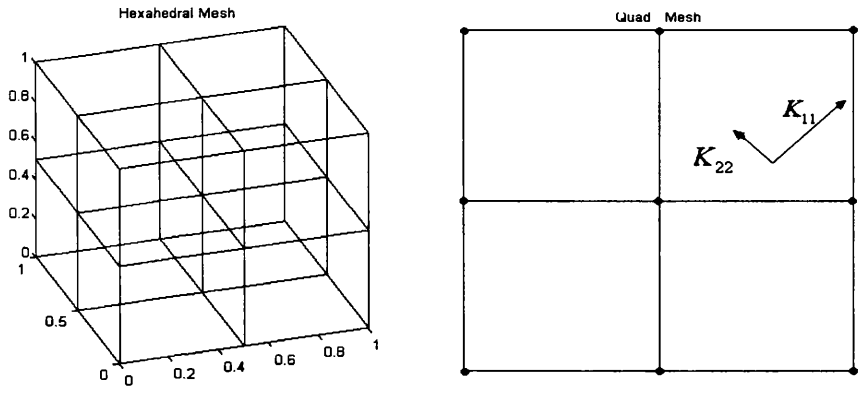

(a) (b)

Figure 7.2: (a)Hexahedral Mesh. (b) Quad Mesh corresponding to Hexahedral Mesh with Discretization Stencil in 2D and Permeability Anisotropy Direction.

The violation of the maximum principle by the family of flux-continuous finite-volume schemes and standard CVFE for high anisotropy ratios presents a major challenge for numerical approximation of elliptic PDE's.

7.3 Flux-Splitting Technique

Flux-splitting for the family of flux-continuous finite volume schemes is presented in [6], where unconditional stability is proven for constant coefficients and its benefits were discussed with respect to computational efficiency. Further properties of flux-splitting discretization are also given in [6] where flux-splitting is defined so as to maintain local conservation at any iterative level, so that non-converged solutions are still locally conservative. A further study of iterative performance of flux-splitting is presented in [128]. In this section a brief overview of flux-splitting is presented and a modification is given to obtain monotonic solutions for cases with high anisotropy ratio. Following [6] fluxes are cast in the form of a leading two-point flux corresponding to the diagonal tensor together with cross-flow terms. The flux is now split so as to

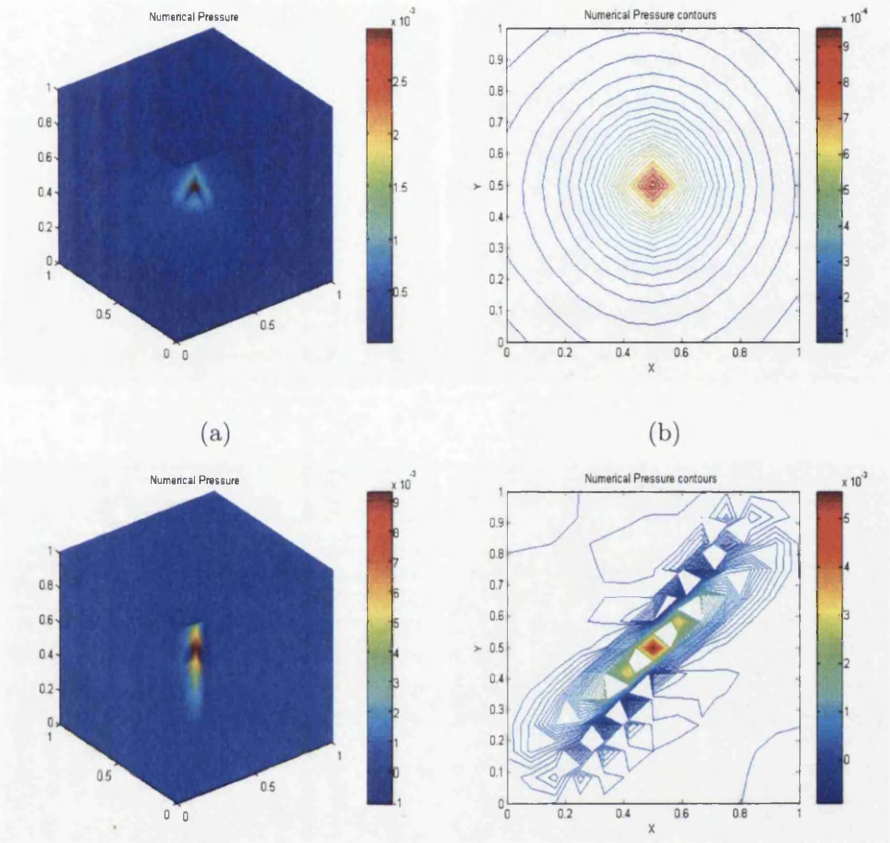

(a) (b)

(c) (d)

Figure 7.3: (a) 3-D Numerical pressure solution with isotropic permeability tensor. (b) 3-D Numerical pressure contours for isotropic tensor shown as slice at z = 0.5.(c) 3-D Numerical pressure solution with anisotropy ratio 1:1000 and angles between grid and principal permeability axes = 30 degrees.(d) 3-D Numerical pressure contours for anisotropy tensor shown as slice at z = 0.5.

generate a semi-implicit scheme that retains an implicit approximation of the diagonal tensor contribution and employs an explicit approximation of all flux cross-flow terms, thereby retaining standard diagonal tensor Jacobian inversion, and preserves existing simulator code design and efficiency.

7.3.1 Splitting at Matrix Level

First we consider splitting at matrix level. Let the fully implicit nine-point discretization matrix be denoted by $A^{(9)}$ and the discrete solution by ϕ_h. Now the matrix $A^{(9)}$ can be decomposed into a leading pentadiagonal matrix $A^{(5)}$ and a residual matrix $A^{(9-5)}$ where

$$A^{(9)} = A^{(5)} + A^{(9-5)} \tag{7.7}$$

the respective split matrices are denoted symbolically by

$$A^{(5)} = \begin{pmatrix} 0 & A^{(9)}_{i,j+1} & 0 \\ A^{(9)}_{i-1,j} & A^{(9)}_{i,j} & A^{(9)}_{i+1,j} \\ 0 & A^{(9)}_{i,j-1} & 0 \end{pmatrix} \tag{7.8}$$

$$A^{(9-5)} = \begin{pmatrix} A^{(9)}_{i-1,j+1} & 0 & A^{(9)}_{i+1,j+1} \\ 0 & 0 & 0 \\ A^{(9)}_{i-1,j-1} & 0 & A^{(9)}_{i+1,j-1} \end{pmatrix} \tag{7.9}$$

Solver strategy can then be defined using a semi-implicit schemes of the form

$$A^{(5)}\phi^{k+1} + A^{(9-5)}\phi^{k} = b \tag{7.10}$$

Another, matrix level splitting can be obtained by splitting the nine-point discretization matrix $A^{(9)}$ into a leading $A^{(9+)}$ matrix and a residual $A^{(9-)}$ matrix. Where $A^{(9+)}$ matrix holds all the positive entries and $A^{(9-)}$ holds all the negative entries. This also give rise to a semi-implicit schemes of the form

$$A^{(9+)}\phi^{k+1} + A^{(9-)}\phi^{k} = b \tag{7.11}$$

Similarly, there can be many other forms of matrix splitting but we are restricting our study to these two types of matrix splitting.

7.3.2 Splitting at Flux level

The splitting is illustrated as follows: Let $\mathbf{A}$ denote the Jacobian matrix for the nine-point flux-continuous system of equations, and $\mathbf{B}$ denote the Jacobian matrix for the classical two-point system of equation. The basic principle behind flux splitting is to express the nine-point flux in terms of two-point flux evaluated at (iterate or time) level $(k+1)$ and a remainder term at level k, written as:

$$\mathbf{F^S} = \mathbf{F^{TP^{k+1}}} + (\mathbf{F^k} - \mathbf{F^{TP^k}}) \tag{7.12}$$

where $\mathbf{F^S}$ is the consistent split-flux, and on a structured grid $\mathbf{F}$ is a 9-point operator in this case and $\mathbf{F^{TP}}$ is 2-point flux. First we rewrite the original discrete system of equations (Eq. 9.2) as:

$$\mathbf{B}\phi + (\mathbf{A} - \mathbf{B})\phi = b \tag{7.13}$$

where

$$B^{(5)} = \begin{pmatrix} 0 & B^{(5)}_{i,j+1} & 0 \\ B^{(5)}_{i-1,j} & B^{(9)}_{i,j} & B^{(5)}_{i+1,j} \\ 0 & B^{(5)}_{i,j-1} & 0 \end{pmatrix} \tag{7.14}$$

results from the 2-point flux and

$$A^{(9)} - B^{(5)} = \begin{pmatrix} X^{(9)}_{i-1,j+1} & X^{(9)}_{i,j+1} & X^{(9)}_{i+11,j+1} \\ X^{(9)}_{i-1,j} & X^{(9)}_{i,j} & X^{(9)}_{i+1,j} \\ X^{(9)}_{i-1,j-1} & X^{(9)}_{i,j-1} & X^{(9)}_{i+1,j-1} \end{pmatrix} \tag{7.15}$$

then the flux-split iteration is defined by:

$$\mathbf{B}\phi^{k+1} = (\mathbf{B} - \mathbf{A})\phi^k + b \tag{7.16}$$

The above equation results in the following iterative method:

$$\phi^{k+1} = (\mathbf{I} - \mathbf{B^{-1}A})\phi^k + \mathbf{B^{-1}}b \tag{7.17}$$

The iteration is stable if $\|(\mathbf{I} - \mathbf{B}^{-1}\mathbf{A})\| \leq 1$ and L_2 stability for a constant full-tensor is proven in [6]. The above iteration scheme converges with a specified tolerance. These flux-splitting formulations are equally applicable to both structured and unstructured control volume distributed formulations.

7.4 Numerical Experiments with Flux-Splitting

In this section some numerical results are presented with application of flux-splitting to the family of flux-continuous finite volume schemes. The matrix splitting methods presented in section 7.3.1 have also been tested but the flux splitting scheme is found to yield the best performance (with fewer iterations) and is therefore used here. Flux-splitting techniques are also equally applicable to structured and unstructured grids.

7.4.1 Flux-splitting on structured grids

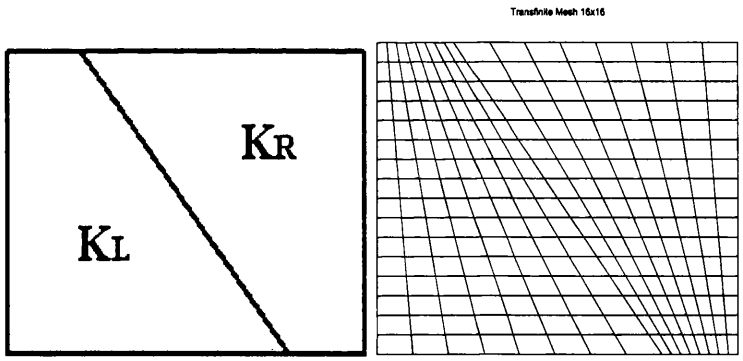

(a) (b)

Figure 7.4: (a) Medium Discontinuity. (b) Mesh aligned along the discontinuity.

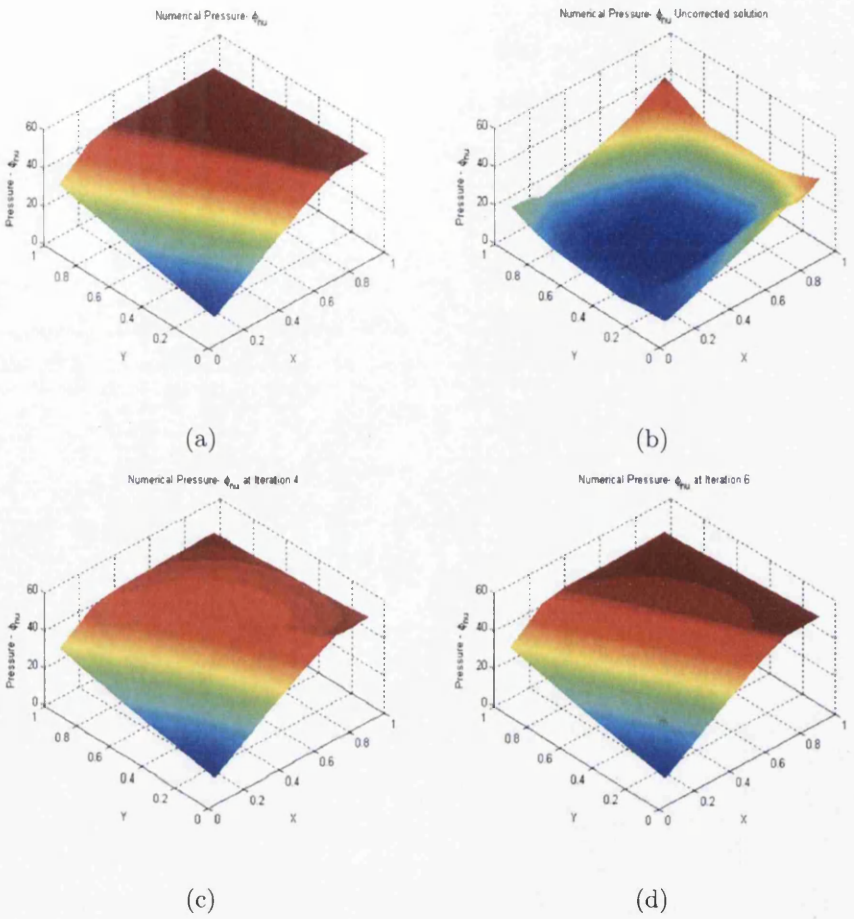

Figure 7.5: (a)Finally converged flux-split solution. (b) Uncorrected Solution. (c) Flux-split solution after 4^{th} iteration. (d) Flux-split solution after 6^{th} iteration.

Linear Discontinuous Pressure Solution

First, we test the flux-splitting technique on a piecewise linear case where the exact solution is well known and monotonic. This example involves uniform flow over a rectangular domain. The medium is divided in two parts as shown in the figure 7.4(a). The grid aligned along the discontinuity was used to obtain the numerical solution as shown in figure 7.4(b). The permeability field is discontinuous and permeability ratio is 1/100 across the discontinuity. The analytical pressure is piece-wise linear and is given by

$$\phi(x,y) = \begin{cases} 200/3(x+y/2), & x+y/2 < 3/4, \\ 2/3(x+y/2)+99/2, & x+y/2 \geq 3/4, \end{cases} \tag{7.18}$$

A full discontinuous permeability tensor is defined as

$$K = \begin{cases} \begin{pmatrix} 1 & -1/4 \\ -1/4 & 1/2 \end{pmatrix}, & x+y/3 < 3/4, \\ \begin{pmatrix} 100 & -100/4 \\ -100/4 & 100/2 \end{pmatrix}, & x+y/2 \geq 3/4, \end{cases}$$

The flux-splitting technique presented in section 7.3.2 is used to obtain the numerical solution, figure 7.5. The numerical solution after 6^{th} iteration is obtained with $O(h^3)$ error compared to the numerically converged solution, shown in figure 7.5(c) and figure 7.5(d).

Non-smooth Anisotropic Solution with Point Source at Centre

Next, we apply the method to a Green's function on a Cartesian grid, using the flux-splitting technique to obtain a monotonic solution for a case with high anisotropic ratio. The problem in consideration has a anisotropy ratio of 1/1000, with angle between grid and principal permeability axes of $\pi/6$ leading to a full tensor(see Appendix B) and thus violates equation 7.6. As with the direct discrete solution, the final converged solution is non-monotonic as shown in figure 7.6(a) because of high anisotropy and oscillations in numerical solution can be seen clearly in figure 7.6(b). Here we introduce a slightly modified iteration strategy for flux-splitting technique compared to that presented in section 7.3.2. The algorithm for which is described as follows: In order to obtain a monotonic solution, as the iteration proceeds k^{th} iterate is stored and solution at iteration $k+1$ is computed and a test for local extrema is conducted, away from sources and sinks, if for all nodes j connected to node i

$$min_j\{\phi_j\} \leq \phi_i \leq max_j\{\phi_j\} \tag{7.19}$$

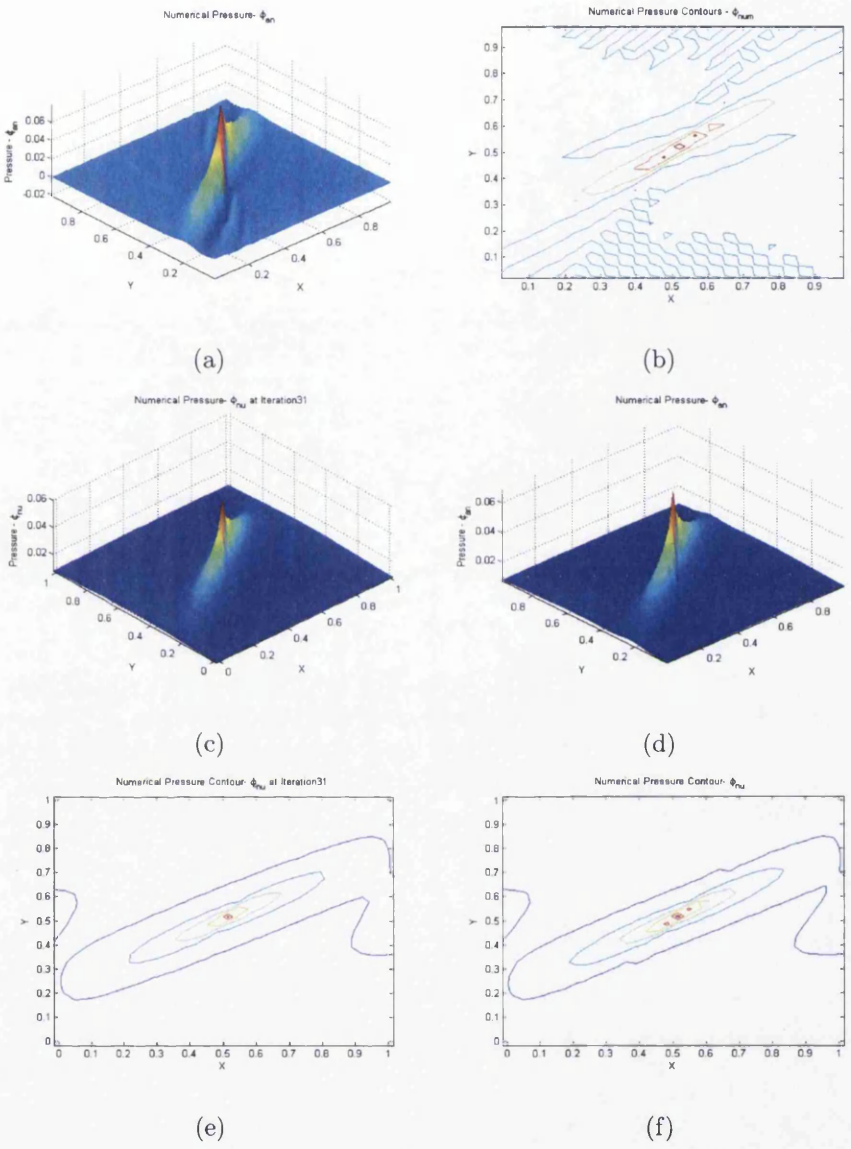

Figure 7.6: (a)Converged Solution of a Green's Function on anisotropic medium with anisotropic ratio of 1/1000, angle between grid and principal permeability axes $\pi/6$. (b)Numerical solution contours showing the oscillations. (c) Flux-split solution after 31^{st} iteration. (d) Finally converged flux-split solution. (e) Oscillation free flux-split solution contours after 31^{st} iteration. (f) Oscillation free flux-split solution contours of finally converged solution.

the iteration proceeds and the solution at the k^{th} iteration is overwritten with the solution obtained after the $k+1$ iteration. If the test fails (equation 7.19) numerical solution at $k+1$ iteration is replaced by the value stored at k^{th} iterate for each node that fails equation 7.19. The iteration proceeds until the desired tolerance criteria is met. Thus the solution process is in effect non-linear. Using this iteration strategy the finally converged solution thus obtained is free of any numerical oscillations. The numerical results after the 31^{st} iteration and finally converged solution are presented for this case in figure 7.6(c) and 7.6(d) respectively. These non-converged solutions are monotonic and free from spurious oscillations as shown in solution contours (figure 7.6(d),7.6(e)) compared to the non-monotonic converged solution in figure 7.6(a).

Numerical convergence rates are computed for this non-smooth anisotropic solution, for different quadrature points q. The discrete L_2 norm is used to evaluate approximation errors. The fine grid discrete solution is used as the reference solution for the convergence test, figure 7.7. The numerical pressure convergence rates are shown in figure 7.8. The numerical values of convergence rates is also presented in table 7.1.

Quadrature	q=0.1	q=0.5	q=1
Flux-Splitting Scheme	$O(h^{0.200})$	$O(h^{0.191})$	$O(h^{0.185})$

Table 7.1: Non-smooth Anisotropic Solution with Point Source at Centre: Pressure convergence with variable quadrature q

Non-smooth Anisotropic Solution with Source at Corner

Next, we present an example with a point source located at the corner of a square domain with orthogonal grid and zero Dirichlet pressure holds elsewhere on the boundary. Two different permeability tensor fields are tested and the results are shown in figure 7.9. It can be seen from figure 7.9(a) that the numerical pressure solution in the first case (isotropic) has a maximum principle. In the second case (with high anisotropy ratio 1:1000, with grid *non-aligned* with the principal axes leading to a

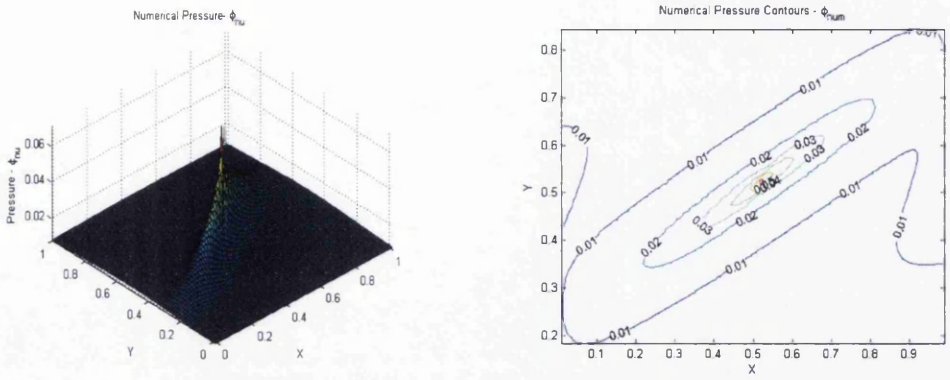

(a) (b)

Figure 7.7: (a) Oscillation free Non-smooth anisotropic flux-split solution with point source at centre on a fine grid. (b) Numerical Pressure Contours.

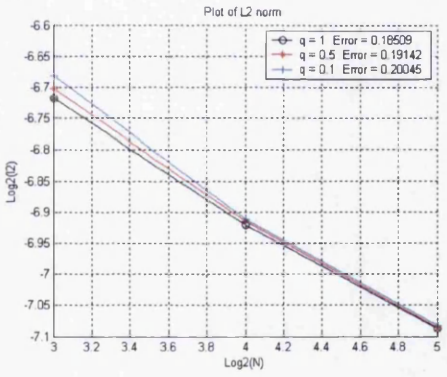

Figure 7.8: Numerical Pressure Convergence Rates for $q = 0.1, 0.5$ and 1.

full-tensor) the tensor field violates 7.6 with $\{min(750.25, 250.75) \ngeq 432.58\}$ and the numerical pressure solution shown in figure 7.9(c) clearly violates the maximum principle resulting in spurious oscillations with negative pressure, hence equation 7.2 is not valid in this case. The spurious oscillations in pressure do not disappear even with mesh refinement. Now, on applying the flux-splitting technique on this problem, following the similar procedure as described for previous test case, the results

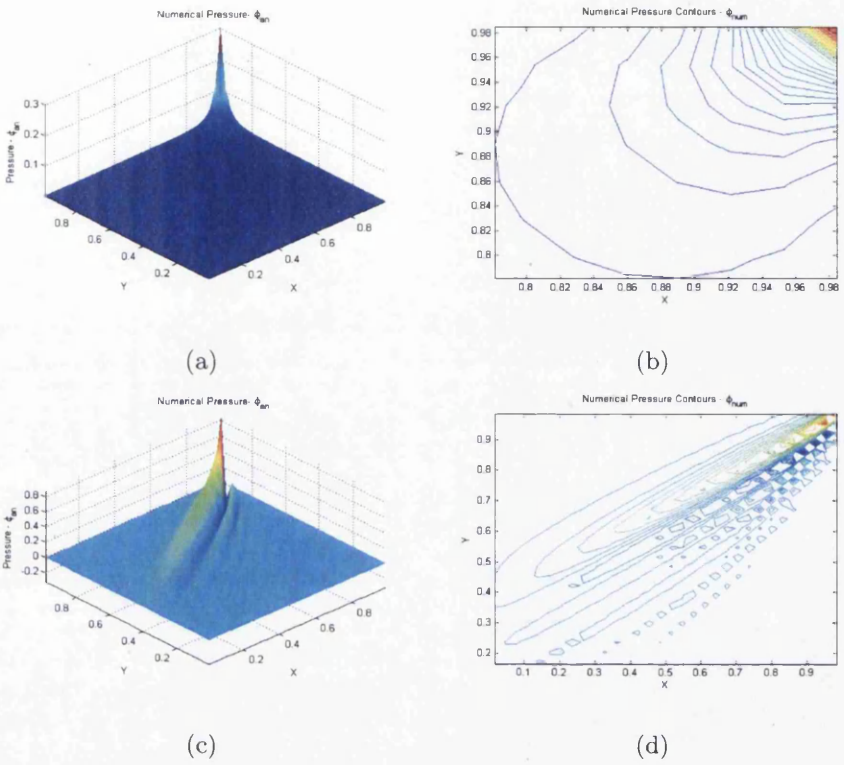

Figure 7.9: (a)Numerical solution for point source with homogeneous diagonal permeability tensor. (b)Numerical solution contours for the source homogeneous diagonal permeability tensor. (c) Numerical solution for point source with high anisotropic medium with anisotropic ratio of 1/1000, angle between grid and principal permeability axes $\pi/6$. (d)Numerical solution contours showing the oscillations.

obtained after 31^{st} iteration and the finally converged solution are shown in figure 7.10(a) and 7.10(b). It can be seen from the contour plots shown in figure 7.10(c) and 7.10(d) that the numerical solutions obtained are free of spurious oscillations and satisfy a general monotonicity condition.

Similar to the previous test case, numerical convergence rates are also computed for this non-smooth anisotropic solution. The discrete L_2 norm is used to evaluate approximation errors. Again, as for this test case exact solution is unknown, we replace it with the discrete solution computed on a very fine mesh, figure 7.11. The numerical pressure convergence rates are shown in figure 7.12. The numerical values

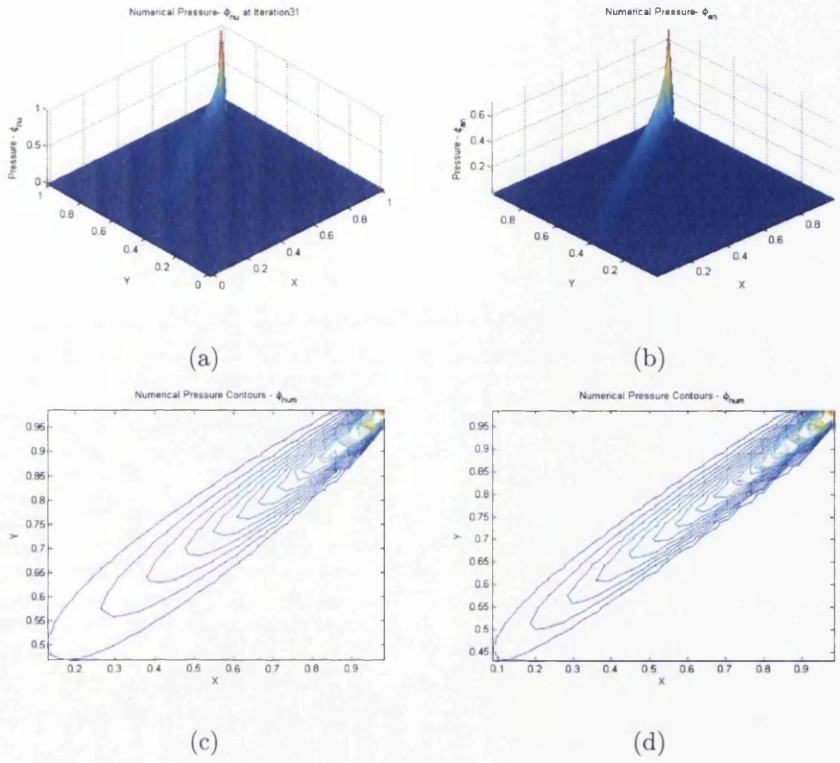

Figure 7.10: (a)Flux-split solution after 31^{st} iteration. (b)Finally Converged flux-split solution.(c) Flux-split solution contours after 31^{st} iteration.(d)Contours of finally converged flux-split solution.

of convergence rates is also presented in table 7.2.

Quadrature	q=0.1	q=0.5	q=1
Flux-Splitting Scheme	$O(h^{0.710})$	$O(h^{0.709})$	$O(h^{0.718})$

Table 7.2: Non-smooth Anisotropic Solution with Point Source at Corner: Pressure convergence with variable quadrature q

7.4.2 Unstructured grids

The final test case involves applying the methods to a Green's function as before, now solved on an unstructured grid (figure 7.13(a)). The (direct method) discrete

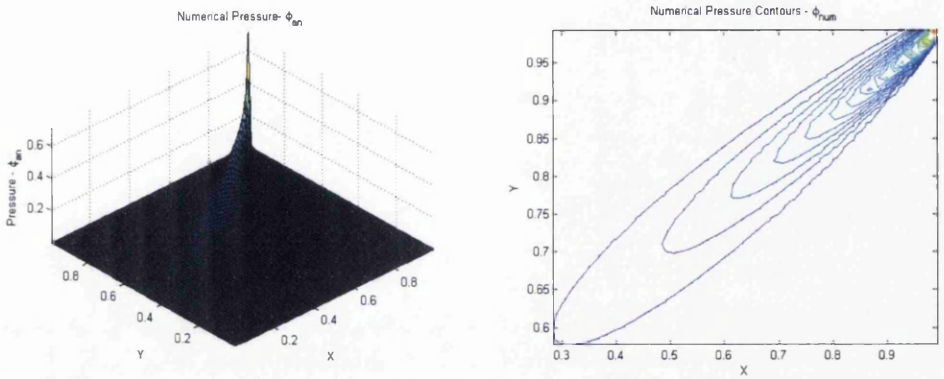

(a) (b)

Figure 7.11: (a) Oscillation free Non-smooth anisotropic flux-split solution with point source at corner on a fine grid. (b) Numerical Pressure Contours.

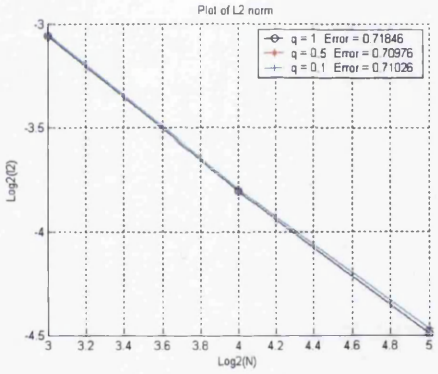

Figure 7.12: Numerical Pressure Convergence Rates for $q = 0.1, 0.5$ and 1.

solution and monotonic-split method solution are shown in figure 7.13(b), 7.13(c) and 7.13(d), which demonstrates the effectiveness of the method on unstructured grids.

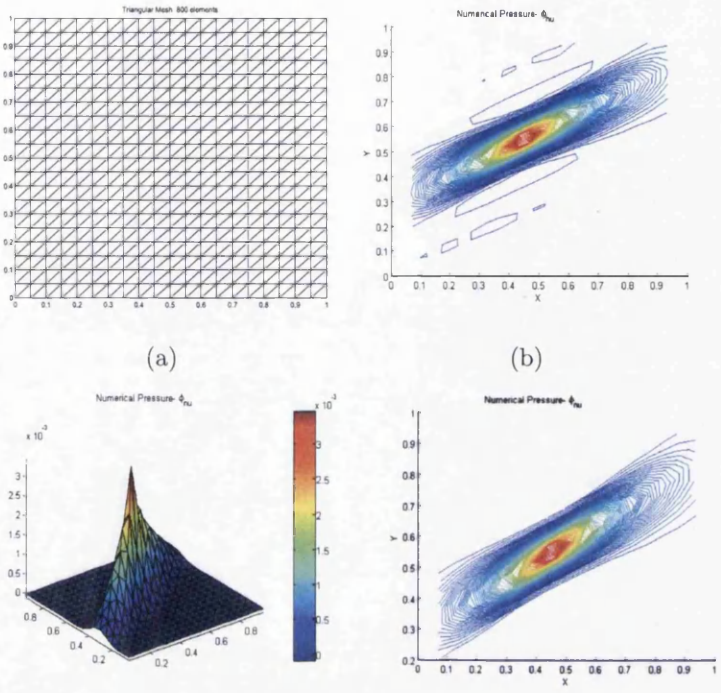

(a) (b)

(c) (d)

Figure 7.13: (a)Unstructured mesh aligned with anisotropy. (b)Oscillatory numerical solution contours.(c)Oscillation free flux-split solution after 14^{th} iteration.(d) Contours of flux-split solution after 14^{th} iteration.

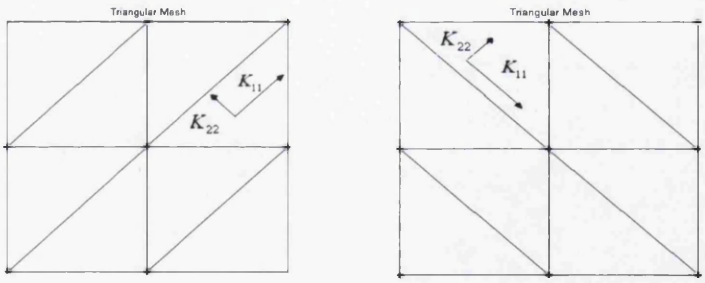

(a) (b)

Figure 7.14: (a) Positive +ve stencil for positive . (b) Negative -ve stencil for negative.

7.5 Quasi-Monotonic Schemes in 2-D and 3-D

In this section we will use equation 7.6 to guide construction of optimal schemes that minimize the occurrence of spurious oscillations in 2 and 3-D. In particular (following [3]) the quadrature point with

$$\eta = \frac{\mid T_{12} \mid}{T_{11} + T_{22}} \tag{7.20}$$

reduces the condition of equation 7.6 for an M-matrix to

$$min(T_{11}, T_{22}) \geq \mid T_{12} \mid \tag{7.21}$$

and following the M-matrix analysis of [3], the 9-point formulation with quadrature defined by equation 7.20 reduces to a 7-point formulation with angular sign dependent stencil, depending upon the sign of, where stencils Figure 7.14(a),7.14(b) are denoted +ve for positive and -ve for negative respectively. The 7-point schemes have M-matrices provided the appropriate angular sign dependent stencil is used and equation 7.21 holds. The angular direction can be chosen locally over the primal quadrilateral element, giving rise to a variable support scheme [10, 25].

The general conditions for a triangular scheme to have an M-matrix were presented in [22] and are precisely the same as equation 7.21. Therefore the M-matrix analysis is used to guide the triangulation to replicate the "7-point" support according to the sign of stencil. Further details of construction of quadrilateral and triangular schemes of variable support to match the local variation in sign of T_{12} in order to gain an M-matrix or minimise oscillations is presented in [10] and will be discussed in next chapter.

We now present results from a series of tests of the 2D and 3D formulation of the family of schemes for monotonicity. The results show that these schemes exhibit loss of monotonicity (but only in a limited sense). The results are consistent with the M-matrix conditions of equation 7.20,7.21.

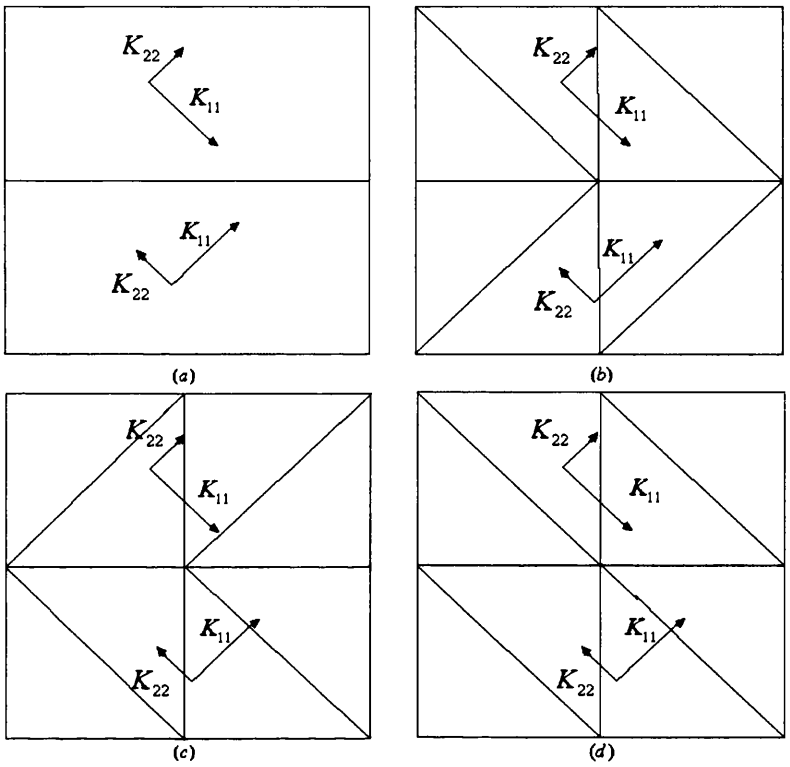

Figure 7.15: (a) Numerical simulation domain with anisotropic permeability. (b) Triangular grid with angular direction of triangulation consistent with direction of anisotropy in both subdomains. (c) Triangular grid with direction of triangulation consistent with anisotropy only in upper subdomain. (d) Triangular grid with direction of triangulation against the direction of anisotropy in both subdomains

Here, we first test a 2-D example with permeability tensor that changes direction in anisotropy halfway across the domain as indicated in figure 7.15(a). A point source is placed in the centre of the [0-1]x[0-1] domain. Three different types of triangulation are compared, with a difference in angular direction in each case, figure 7.15(b-d). Since the scheme on a triangular grid is cell-vertex based, control-volume boundary aligned [5, 7, 52] triangular grids are used to handle the jump in permeability tensor.

From the numerical results shown in figure 7.16-7.18 we conclude that the test case of figure 7.16(a), which has nearest alignment of angular direction with principal

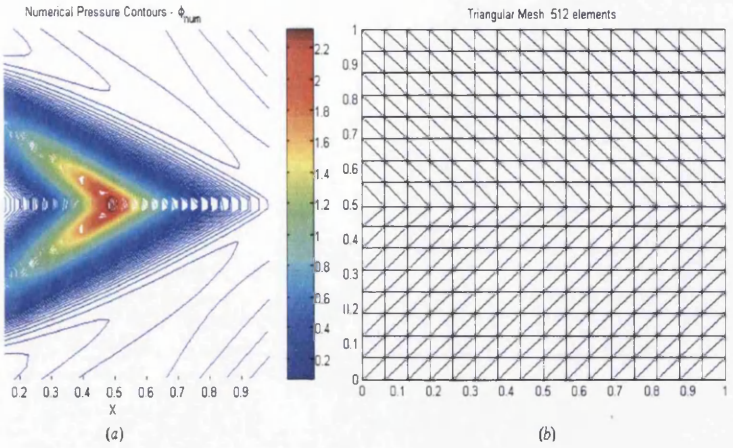

Figure 7.16: (a) Numerical Pressure solution with no pressure oscillations. (b) Triangular grid with direction of triangulation flowing direction of anisotropy in both subdomains.

axes of the permeability tensor (consistent with M-matrix analysis), shows the best pressure solution. In this case the local scheme support varies with consistent angular direction, at the point of change in direction of the permeability principal axes. This example shows that in general, the scheme will require a variable support between 7 to 9 nodes depending on the local permeability field orientation in order to maintain angular consistency with the M-matrix analysis. In contrast, it is seen in figure 7.18 that when the direction of triangulation is in the opposite angular direction to that of the permeability anisotropy, oscillations in numerical pressure solution are more prominent and smearing of the solution increases with departure of angular alignment from the principal axes directions.

We note that a method of minimizing oscillations using grid generation has been presented in [130]. The work of the above section provides fundamental support for this type of approach to grid generation. Indeed the above approach to developing discretization schemes, by maintaining angular consistency between the M-matrix analysis and permeability field orientation also provides a general guiding principle

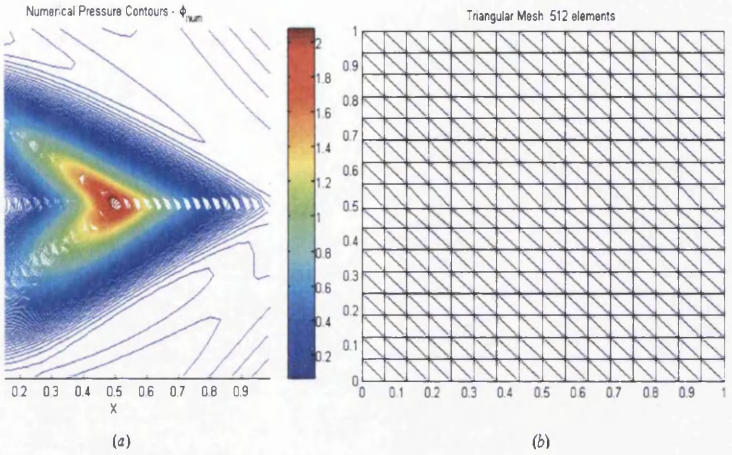

Figure 7.17: (a) Numerical Pressure solution with less dominant pressure oscillations. (b) Triangular grid with direction of triangulation following anisotropy only in upper subdomain.

for unstructured grid generation using any element type.

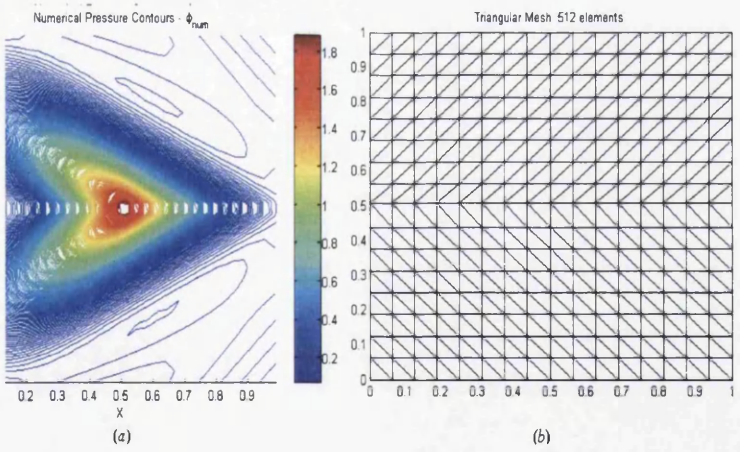

Figure 7.18: (a) Numerical Pressure solution with more prominent oscillations.(b) Triangular grid with direction of triangulation against the direction of anisotropy in both subdomians

Next we test a numerical example involving a Green's function with a point source in 3-D domain. The unit source is located at the centre of the domain. Numerical sim-

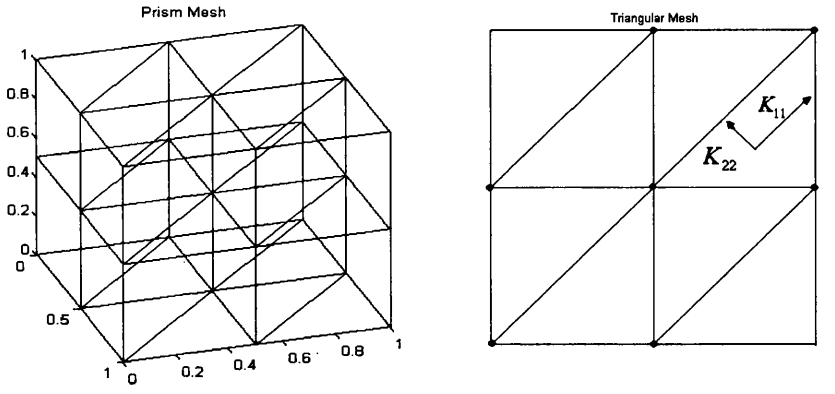

(a) (b)

Figure 7.19: (a)Hexahedral Mesh. (b) Quad Mesh corresponding to Hexahedral Mesh with Discretization Stencil in 2D and Permeability Anisotropy Direction.

ulation is performed using 3-D mesh with prism elements as shown in figure 7.19(a). Two different permeability tensor fields are tested; Isotropic tensor case and a case with underlying permeability tensor having high anisotropy ratio 1:1000 with principal axes at an angle of $\pi/6$ relative to the grid coordinate system leading to a full tensor in the X-Y plane (figure 7.19) that violates equation 7.21. Thus the scheme does not have an M-matrix in this case. Numerical results are shown in figure 7.20. A similar case was tested before for hexahedral mesh in 3-D where severe numerical oscillation were observed for high anisotropy (figure 7.3). In contrast, when prism mesh is used with the same highly anisotropic full permeability tensor the severity of oscillations in the numerical pressure field is much less intense compared to what is seen on the hexahedral mesh, figure 7.20. We note the strong analogy between the 2-D and 3-D meshes for this case. The hexahedral mesh is comprised of a set of planer 2-D quadrilateral meshes and the prism mesh is comprised of a set of planer 2-D triangular meshes (figure 7.19). The behavior of the family of schemes can essentially be understood for this case by looking at the 2-D M-matrix analysis equation 7.6, which shows that a 9-point scheme has more limiting constraints for an M-matrix

than a 7-point scheme, viz equation 7.21. In particular if the resulting 9-point scheme cannot have an M-matrix when a full-tensor is present, whereas the 7-point scheme will permit a full tensor, albeit conditional subject to equation 7.21 [3].

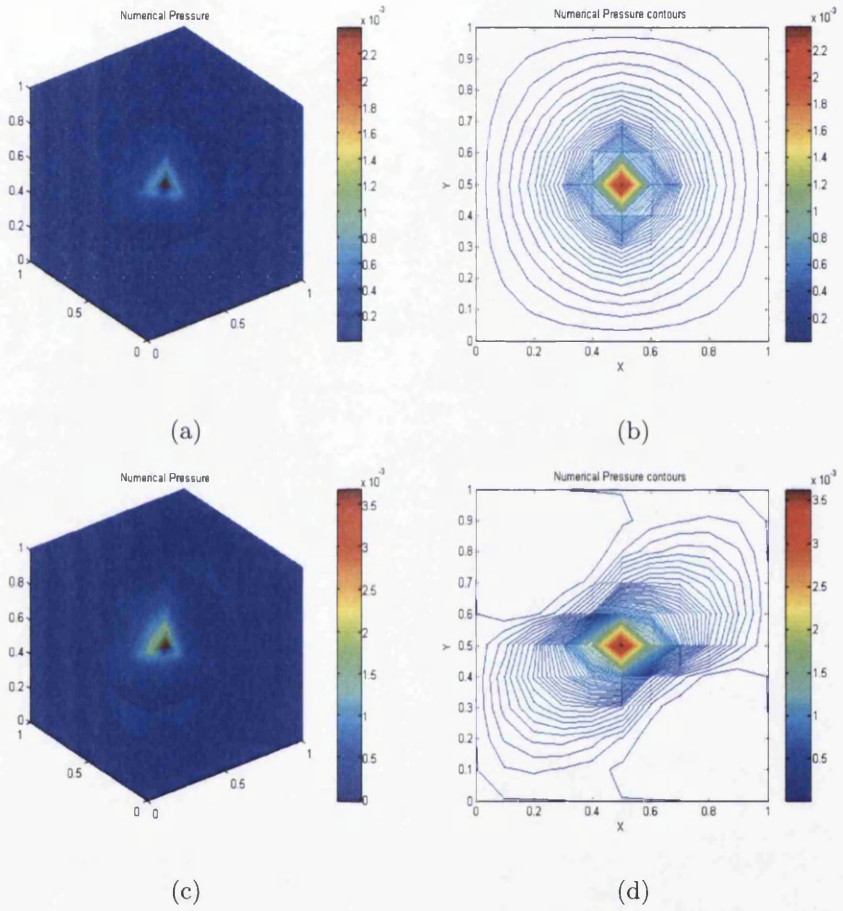

Figure 7.20: (a) Numerical Pressure solution on a uniform prism mesh with isotropic permeability tensor. (b) Numerical Pressure contours for pressure surface in X-Y plane at Z = 0.5. (c) Numerical Pressure solution on a prism mesh with highly anisotropic permeability tensor. (d) Numerical Pressure contours for the pressure surface in X-Y plane at Z = 0.5.

It can be seen in figure 7.19(b) that on a triangulated quadrilateral mesh the discretization stencil reduces to a 7-point scheme compared to 9-point on a quadrilateral mesh (figure 7.2(b)). The reduced 7-point discretization stencil is on a triangular mesh

that "follows" the direction of anisotropy and is angular sign consistent with the M-matrix condition, resulting in improved behavior of the scheme for highly anisotropic permeability tensors. Hence, we can conclude that this behavior of the scheme on the prism grid is due to angular sign alignment of the grid with the direction of anisotropy.

7.6 Summary

In this chapter Monotonicity issues related to the formulation of the family of schemes are explored in 2-D and 3-D. Two different kinds of splitting techniques are presented, which can be broadly classified into *Flux-splitting* and *Matrix-splitting.* The splitting techniques yield monotonic numerical solutions for full-tensor permeability fields with high principal anisotropy ratios. A key component of this solution procedure is in obtaining a predicted monotonic solution computed by the two-point flux approximation, where the resulting M-matrix is used as a driver and the (deferred) correction to the iteration (in this case) is added at each iterative step until a local extrema is detected, in which case the iterative procedure uses the previous value (locally).

The flux-splitting technique is found to be most efficient as its convergence to final solution is faster compared to other splitting techniques. Flux-splitting also maintains local conservation at any level of iteration. These splitting techniques are equally applicable to structured and unstructured grids in two and three dimensions. Splitting techniques may be more suitable for obtaining monotonic numerical solutions when compared to grid optimization, which appear to be applied at lower anisotropy ratio. The splitting technique is used here for anisotropy ratios of 1/1000 and higher.

For cases where an M-matrix can not be obtained, M-matrix analysis [3] is used to develop discretization methods of variable support with minimum spurious oscillations for full-tensor problems with high anisotropy in 2-D and 3-D.

Maintaining angular consistency between the M-matrix analysis and permeability

field orientation provides a general guiding principle for developing discretization schemes and grid generation that minimize spurious oscillations.

Chapter 8

Quasi-Monotonic Variable Support (q_1, q_2) Families of Schemes

8.1 Introduction

The focus of this chapter is on seeking the most robust approximation with respect to monotonicity. A general (two parameter) double (q_1, q_2)-family of flux-continuous schemes is presented [10]. M-matrix analysis for double families presented in [10] exposes the limits on the schemes for ensuring monotonic solutions in the case of full tensors. The generality of the double family analysis establishes a key result; that a locally conservative scheme cannot posses an unconditional M-matrix in the case of an arbitrary elliptic full-tensor. The analysis presented in [10] is used to determine the upper limits for obtaining monotonic solutions and to aid the design of schemes that minimize the occurrence of solutions with spurious oscillations in the general case.

This chapter is organized as follows: A summary of the formulation of the double-family of flux-continuous finite volume schemes, with discretization in physical space is presented in section 8.2. Section 8.3 summarizes the conditions required to obtain a monotonic solution and describes performance of the family of flux-continuous

schemes with respect to monotonicity. Section 8.4 presents numerical examples that demonstrate the benefits of using double family of flux continuous schemes for preserving monotonicity. Finally, a summary is presented in section 8.5.

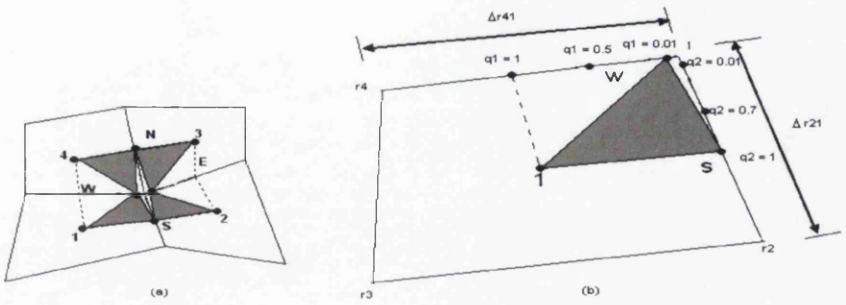

Figure 8.1: (a) Points of Flux-Continuity (N,S,E,W) on sub-cell faces of a *dual-cell* (b) Quadrature points on a sub-cell faces *q1,q2*

8.2 (q1,q2) Families of CVD(MPFA) Schemes - Double Quadrature Parameterization

The formulation and analysis of the double (q_1, q_2)-family of scheme presented in [10] is summarized below. A general guideline for construction of the double (q_1, q_2)-family of flux-continuous schemes on lines similar to the construction of q-family of schemes is presented and the difference between two formulations are highlighted. A detailed formulation of the double (q_1, q_2)-family of flux-continuous schemes is presented in [10].

The double (q_1, q_2)-family of flux continuous schemes is formed when imposing normal flux and pressure continuity conditions on the *sub-faces* where the four shaded triangles meet, at the four positions (N, S, E, W), in (or on the perimeter of) the dual cell figure 8.1(a), as in construction of the q-family. On each *sub-face* the point of continuity is parameterized with respect to the subcell face by the variable $\mathbf{q} = (q_1, q_2)$

depending on the subface, where referring to figure 8.1(b) $(0 < q_1, q_2 \leq 1]$. For a given subcell, the points of continuity can lie anywhere in the intervals $(0 < q_1, q_2 \leq 1]$ on the two faces of each subcell inside a dual cell, that coincide with the control-volume *sub-faces*, and the values of (q_1, q_2) define the local quadrature points and hence the double family of flux-continuous finite-volume schemes.

The parametric variation in $\mathbf{q} = (q_1, q_2)$ is illustrated further using the sub-cell example of figure 8.1(b), with sub-cell containing sub-triangle $(1, S, W)$. Let $\mathbf{r}_1 = (x_1, y_1)$ denote the coordinates of the cell-centre and $\mathbf{r}_S = (x_S, y_S)$,$\mathbf{r}_W = (x_W, y_W)$ denote the local continuity coordinates. Then it is understood that the continuity position is a function of $\mathbf{q}$ with $\mathbf{r}_S(q_1, q_2)$ and $\mathbf{r}_W(q_1, q_2)$. Different values of quadrature point are illustrated in figure 8.1(b).

Now, similar to the q-family of scheme cell face pressures $\phi_N, \phi_E, \phi_S, \phi_W$ are introduced at N, S, E, W locations. Pressure sub-triangles are defined with local triangular support imposed within each quarter (sub-cell) of the *dual-cell* as shown in figure 8.1(a). Pressure ϕ, in local cell coordinates, is piecewise linear over each triangle. Piecewise constant Darcy fluxes are now constructed on each of the pressure sub-triangles belonging to the sub-cells of the *dual-cell* as shown in figure 8.1(a). The local linear pressure ϕ, is expanded in sub-triangle coordinates. The Darcy flux approximation for sub-triangle $(1, S, W)$ is given below.

$$\begin{pmatrix} \phi_\xi \\ \phi_\eta \end{pmatrix} = \begin{pmatrix} \phi_S - \phi_1 \\ \phi_W - \phi_1 \end{pmatrix} \tag{8.1}$$

and

$$\begin{pmatrix} x_\xi(\mathbf{q}) \\ x_\eta(\mathbf{q}) \end{pmatrix} = \begin{pmatrix} x_S(\mathbf{q}) - x_1 \\ x_W(\mathbf{q}) - x_1 \end{pmatrix}, \begin{pmatrix} y_\xi(\mathbf{q}) \\ y_\eta(\mathbf{q}) \end{pmatrix} = \begin{pmatrix} y_S(\mathbf{q}) - y_1 \\ y_w(\mathbf{q}) - y_1 \end{pmatrix} \tag{8.2}$$

Using equations 8.1,8.2 the discrete Darcy velocity is defined as

$$v_h = -\mathbf{K}\nabla\phi_h = -\mathbf{K}\mathbf{G}(\mathbf{q}) \begin{pmatrix} \phi_\xi \\ \phi_\eta \end{pmatrix} \tag{8.3}$$

Where K is the local permeability tensor of cell 1 and dependency of $\nabla\phi_h$ on quadrature point arises through

$$\mathbf{G}(\mathbf{q})\begin{pmatrix}\phi_\xi\\ \phi_\eta\end{pmatrix}=\begin{pmatrix}y_\eta(\mathbf{q}) & -y_\xi(\mathbf{q})\\ -x_\eta(\mathbf{q}) & x_\xi(\mathbf{q})\end{pmatrix}\frac{1}{J(\mathbf{q})}\begin{pmatrix}\phi_S-\phi_1\\ \phi_W-\phi_1\end{pmatrix} \tag{8.4}$$

where approximate $\mathbf{r}_\xi(\mathbf{q})$ and $\mathbf{r}_\eta(\mathbf{q})$are defined by equation 8.2. The normal flux at the left hand side of S(figure 8.1(a)) is resolved along the outward normal vector $dL_S=(\Delta y_{r_3,S},-\Delta x_{r_3,S})=\frac{1}{2}(\Delta y_{32},-\Delta x_{32})$ (figure 8.1(b) and is expressed in terms of the general tensor $T=T(\mathbf{q})$ as

$$F_S^1=v_h\cdot dL_S=-(T_{11}^1\phi_\xi+T_{12}^1\phi_\eta)|_S^1 \tag{8.5}$$

where it is understood that the resulting coefficients of $-(\phi_\xi,\phi_\eta)|_S^1$ denoted by $T_{11}|_S^1$ and $T_{12}|_S^2$ are sub-cell (physical-space) approximations of the general tensor components (equation 8.5) at the left hand face at S, and are functions of $\mathbf{q}$. A similar expression for flux is obtained at the right hand side of S from cell 2(figure 8.1(a). Similarly sub-cell fluxes are resolved on the two sides of the other faces at W,N and E. Flux continuity is then imposed across the four cell interfaces at the four positions N,S,E and W (figure 8.1(a) which are specified according to quadrature point $\mathbf{q}$. The rest of the formulation follows directly from chapter 5. The details of the discrete double family scheme coefficients and the M-matrix analysis are presented in [10].

8.3 CVFE - Double Families and Monotonicity

In the above section we have presented general families of flux-continuous locally conservative finite-volume schemes. For constant permeability coefficients these schemes can be mapped onto a more transparent control-volume finite element CVFE nine-point framework for general schemes presented in [9]. Such a "mapping" was demonstrated in [3] for the family of general tensor schemes as a function of q. The

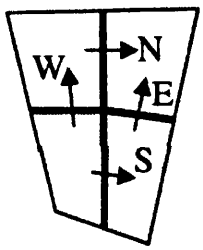

Figure 8.2: Dual-Cell flux approximation

mapping facilitated the first M-matrix analysis of the CVD(MPFA) methods, presented in [2, 3].

In this section we summarize the general *double family* of CVFE schemes presented in [10]. The double family embodies *all* possible locally constant coefficient 9-point schemes and their subordinate 7-point schemes, as indicated in [3] for the single family. The double family of CVFE fluxes is defined over a primal grid cell if a cell-vertex formulation is employed and is defined over the primal dual-cell if a cell-centred formulation is employed. The CVFE fluxes are derived from a bilinear approximation of pressure over the cell parameterized by $(0 \leq \xi \leq 1), (0 \leq \eta \leq 1)$.

For example, control-volume face flux F_S is defined at a point on the subcell control-volume subface ,figure 8.2, where $\xi_S = 1/2$. Similarly F_W is defined on the adjoining control-volume subface ,figure 8.2, where $\eta_W = 1/2$ so that

$$\begin{aligned} F_S &= -\frac{1}{2}(T_{11}((\phi_2 - \phi_1)(1-\eta) + (\phi_3 - \phi_4)\eta) + T_{12}((\phi_4 - \phi_1)(1/2) + (\phi_3 - \phi_2)1/2), \\ F_W &= -\frac{1}{2}(T_{12}((\phi_2 - \phi_1)(1/2) + (\phi_3 - \phi_4)1/2) + T_{22}((\phi_4 - \phi_1)(1-\xi) + (\phi_3 - \phi_2)\xi)) \end{aligned} \tag{8.5}$$

and the S, N fluxes are defined for $(0 \leq \xi < 1/2), (0 \leq \eta < 1/2)$.

8.3.1 Flux-continuity and Local Conservation

We note that CVFE schemes are locally conservative, but not flux continuous; A flux-continuous finite-volume scheme is locally conservative however the converse is not necessarily true and CVFE is a case in point. Of course CVFE is (trivially flux continuous over the control-volume faces [9], but in the CVFE formulation key flux continuity is lacking across the interior interfaces across which the permeability can be discontinuous in the general case.

8.3.2 CVD(MPFA) and CVFE

The key results of the analysis, presented in [10] include a mapping between the coefficients of the CVD(MPFA) double family scheme and the CVFE double family for a spatially constant full-tensor field. The M-matrix analysis of the CVFE double family presented in [10] establishes bounds on the CVFE double family coefficients, which are then used via the mapping to establish the corresponding bounds for the flux-continuous CVD double family coefficients.

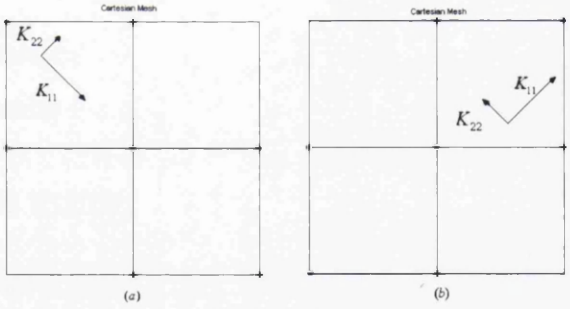

Figure 8.3: (a) -ve stencil(b)+ve stencil

8.3.3 Variable Support Reduction

As noted in [3], if we choose the default (double family) quadrature points with

$$\xi = \eta = \mid T_{12} \mid /(T_{11} + T_{22}) \tag{8.7}$$

then an M-matrix is obtained subject to a sufficient condition for ellipticity, i.e.

$$\mid T_{12} \mid \leq min(T_{11}, T_{22}) \tag{8.8}$$

In general the choice of quadrature defined by equation 8.7 yields a scheme that will select a variable support, which depending upon the local tensor and orientation (figure 8.3) can be between a nine point scheme to a seven point scheme (on a structured grid) and maintain an M-matrix provided equation 8.8 holds. Families of reduced support schemes are also obtained if we exploit the double families of schemes.

All of these schemes give rise to M-matrices provided equation 8.8 is satisfied, further details are given in [10].

8.4 Numerical Results

In this section numerical tests of the reduced support schemes are presented, with specific quadrature points for the double families of schemes.

CASE 1: PLANAR FIELD

The first case involves the a uniform anisotropic domain with a Green's function (point source) in the middle of the domain and with Dirichlet zero pressure conditions imposed on the boundary.

The full-tensor is given by

$$\mathbf{K} = [1, 0.99, 0.99, 1] \tag{8.9}$$

In the first case using the 9-point scheme with $q_1 = q_2 = q = 1$ (with high anisotropy ratio, with grid *non-aligned* with the principal axes leading to a full-tensor) the tensor

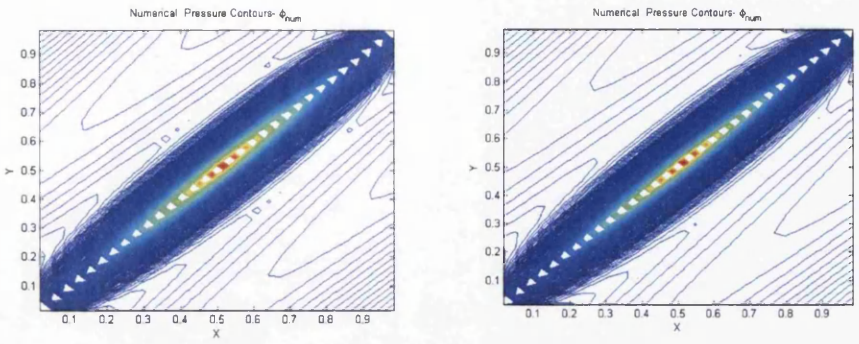

Figure 8.4: (a) Numerical Pressure Contours with visible spurious oscillations $q_1 = q_2 = q = 1$(b) Oscillation free Numerical Pressure Contours. $q_1 = q_2 = q = 0.01$

field violates equation 8.8. The numerical pressure solution shown in figure 8.4(a) with visible spurious oscillations. Clear violation of the maximum principle resulting in spurious oscillations.

In the second case using the 9-point scheme with $q_1 = q_2 = q = 0.01$ deduced from equation 8.7 which ensures that the nine-point scheme will reduce to a seven-point scheme with an M-matrix with off-diagonal terms equal to zero. The scheme and computed numerical pressure solution have a maximum principle figure 8.4(b).

CASE 2: V FIELD

In the next case, we test a 2-D example with a permeability tensor that changes direction in anisotropy halfway across the domain going from $\mathbf{K} = [1, 0.99, 0.99, 1]$ to $\mathbf{K} = [1, -0.99, -0.99, 1]$ as indicated in figure 8.5. A point source is placed in the centre of the [0-1]x[0-1] domain and Dirichlet conditions apply as before. Note that this test case involves a discontinuous jump in permeability tensor, so that the M-matrix conditions are tested under variable coefficient conditions.

Results with $q_1 = q_2 = q = 1$ are shown in figure 8.6(a) with visible spurious

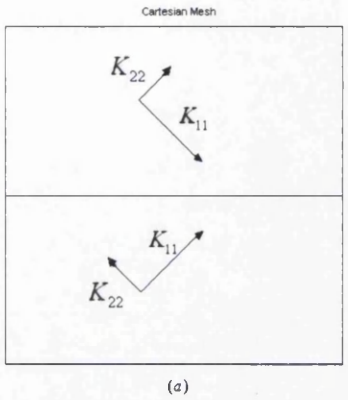

Figure 8.5: (a) Change in direction of anisotropy in Permeability Tensor at $y = 0.5$

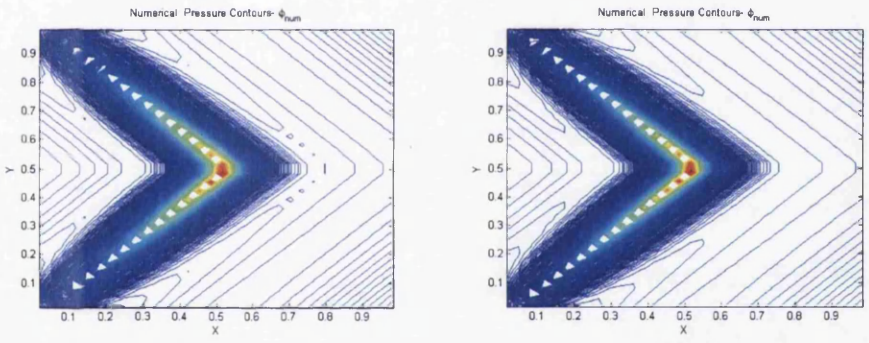

Figure 8.6: (a) Numerical pressure contours with visible spurious oscillations $q_1 = q_2 = q = 1$. (b) Numerical pressure contours with no spurious oscillations $q_1 = q_2 = q = 0.01$.

oscillations. In the second case using the reduced support scheme with $q_1 = q_2 = q = 0.01$ deduced from equation 8.7 yields the results in figure 8.6(b) , also results using the double family with $q_1 = 0.005025125, q_2 = 1$ are shown in figure 8.7. In these cases the M-matrix conditions are satisfied. Further test cases comparing single family, double family and reduced 7-point support are presented in [10].

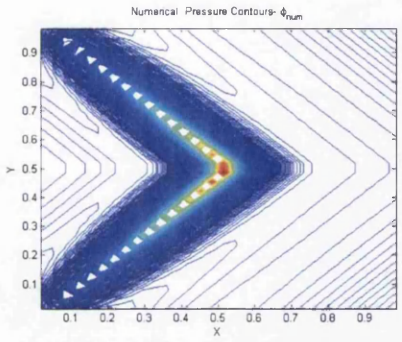

Figure 8.7: (a) Oscillation free Numerical Pressure Contours for double family $q_1 = 0.005025125, q_2 = 1$

8.5 Summary

A general (two parameter) double (q_1, q_2)-family of flux-continuous locally conservative schemes is presented. The generality of the double family analysis establishes a key result; Any locally conservative scheme on or within a 9-point stencil applied to a locally constant full-tensor field can only have a *conditional* M-matrix consistent with the earlier analysis of [3]. The conditions are expressed in terms of limits on the size of the cross terms, which are only sufficient for ellipticity, and on the angular directional support for the upper limit of the family of schemes.

The M-matrix analysis [10] determines the upper limit for obtaining monotonic solutions and to aid the design of schemes that minimize the occurrence of solutions with spurious oscillations in the general case.

The analysis also shows that for weaker cross terms with lower anisotropy ratio there exists a range of M-matrix nine point schemes and therefore the families of schemes enhance the M-matrix conditions.

When the limit on the full-tensor cross terms are exceeded the angular condition resulting from the analysis is used as a guide to construct quasi-monotonic schemes. This results in schemes of locally directional support that vary according to the local

orientation of the tensor field. The variable support schemes are able to compute pressure fields with minimal oscillations and much improved resolution compared to schemes relying on fixed quadrature rules.

Chapter 9

Use of Quadrature Point in Upscaling

9.1 Introduction

Subsurface reservoirs generally have a complex description in terms of both geometry and geology. Typical reservoir grid block sizes are of the order of tens of meters, while rock properties are measured below the centimeter scale. This poses a continuing challenge to modelling and simulation of reservoirs since fine-scale effects often have a profound impact on flow patterns on larger scales. Resolving all pertinent scales and their interaction is therefore imperative to give reliable qualitative and quantitative simulation results. Consequently, averaging or homogenization techniques are needed to scale up the fine scale grid information to resolve the flow on a coarse grid. The representation of fine grid properties on a coarse grid scale is obtained via the principle of upscaling. Upscaling has been a standard procedure in reservoir simulation for nearly four decades, most upscaling techniques are based on some kind of local averaging procedure in which effective properties in each grid-block are calculated solely from properties within the grid block. Different flow patterns may call for different upscaling procedures, it is generally acknowledged that global

effects must also be taken into consideration while using a upscaling technique in order to obtain robust coarse-scale simulation model.

The type of the upscaling technique employed plays a key role in retaining fine scale geological information within grid blocks for practical size. More general methods of upscaling involve local fine scale flow simulations over the domains defined by coarse grid blocks. These methods are subjected to specific boundary conditions and require the use of appropriate discretization schemes. The main quantity computed in single phase upscaling is called as equivalent permeability and is denoted by $\mathbf{K}^*$.

In this work the family of flux-continuous schemes is used for computing upscaling simulations and the performance of different quadrature points in upscaling is measured with respect to equivalent permeability $\mathbf{K}^*$. The refinement studies presented involve:

(i) A pure refinement study showing only the effect of increased grid resolution on upscaled permeability, compared to that obtained directly from the fine scale solution.

(ii) A self consistent comparison where a classical mathematical convergence test is performed. The same coarse scale underlying permeability map is preserved on all grid levels including the fine scale reference solution.

(iii) A consistent comparison of upscaled permeability where each grid level has its own NxN permeability map.

The literature on upscaling procedures is extensive [33, 132, 133], ranging from renormalization techniques, e.g., [20, 30],via local simulation techniques [33, 32], to multiscale methods [37, 86, 35, 34, 134]. A review of different upscaling techniques is also presented in [40]. Several attempts have been made to analyze the upscaling techniques, but so far there is generally no theory or framework for assessing the quality of an upscaling procedure. The quality of upscaling techniques is usually

assessed by comparing upscaled production characteristics with those obtained from a reference solution computed on an underlying fine grid.

This chapter is organized as follows: Section 9.2 gives a brief description of the upscaling problem encountered in reservoir simulation. Section 9.3 presents an overview of the upscaling procedure used in this work. Section 9.4 describes the implementation of the boundary conditions for upscaling procedure. Upscaling results using the different kinds of upscaling procedure used here are presented in section 9.5. Summary follows in section 9.6.

9.2 Problem Description

The process of upscaling permeability from the pressure equation 3.5 is often termed as single-phase upscaling. Most of the single-phase upscaling techniques seek homogeneous block permeabilities that reproduce the same total flow through each coarse grid-block as one would get if the pressure equation was solved on the underlying fine grid with correct fine-scale heterogeneous structures. However, to design upscaling techniques that preserve averaged fine-scale flow-rates is in general nontrivial because the heterogeneities at all scale have a significant effect on the large-scale flow pattern. A proper coarse-scale model must therefore capture the impact of heterogeneous structures at all scales that is not solved by the coarse grid. Hence, the intent here is to replace equation 3.5 on fine scale with a equivalent coarse scale equation characterized by an effective permeability tensor defined as $\mathbf{K}^*$ which varies on a coarse scale i.e

$$\nabla \cdot (-\mathbf{K}^*(X,Y) \cdot \nabla\phi) = 0 \tag{9.1}$$

This equation sates that the net flow-rate is related to the average pressure gradient through a upscaled Darcy law.

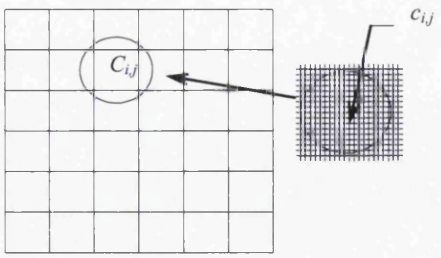

Figure 9.1: Permeability tensor on each fine-scale cell $c_{i,j}$ upscaled over each coarse-scale cell $C_{i,j}$.

9.3 Upscaling Procedure

In upscaling rock properties from fine scale diagonal tensor simulations to grid block scale, the permeability tensor of a porous medium, specified on each fine scale cell $c_{i,j}$ is upscaled or homogenized over each coarse-scale or computational cell $C_{i,j}$ containing the fine cells $c_{i,j}$, figure 9.1.

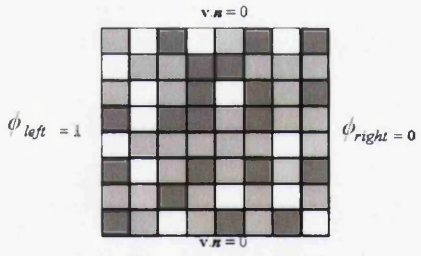

Figure 9.2: Fine scale permeability with standard boundary conditions.

The standard upscaling procedure for a grid cell or grid block involves solving a local flow problem over the cell subject to a global pressure gradient imposed across the cell in the x-direction with no-flow boundary conditions applied on the top and bottom walls of the cell as shown in figure 9.2. This upscaling procedure gives us an effective diagonal permeability tensor. Using the above pressure and velocity boundary condition upscaled permeability $\mathbf{K}^*$ determined by global mass conservation

conditions

$$-K_{11}^{*}\frac{(\phi_{right}-\phi_{left})L_y}{L_x}=-\sum_{i=1}^{ny}\frac{(\phi_{i+1,j}-\phi_{i,j})K_{i+1/2,j}\Delta y}{\Delta x} \tag{9.2}$$

The boundary conditions can then be interchanged between x and y to find the upscaled permeability in other direction

$$-K_{22}^{*}\frac{(\phi_{top}-\phi_{bottom})L_x}{L_y}=-\sum_{j=1}^{nx}\frac{(\phi_{i,j+1}-\phi_{i,j})K_{i,j+1/2}\Delta x}{\Delta y} \tag{9.3}$$

The equation 9.2 gives the equivalent permeability in x-direction $\mathbf{K_{11}^{*}}$, and the equation 9.3 gives the equivalent permeability in y-direction $\mathbf{K_{22}^{*}}$. Due to specification of no-flow ($V \cdot \mathbf{n} = 0$) top and bottom boundary condition and vice-versa there is no cross-flow over the domain and hence the equivalent permeability tensor is diagonal and the cross-terms $\mathbf{K_{12}^{*}}, \mathbf{K_{21}^{*}}$ are equal to zero. The standard no flow condition boundary condition for upscaling is consistent with the harmonic average approximation when a one dimensional permeability field is present. Another popular option is to choose periodic boundary conditions. That is, one assumes that each grid block is a periodic cell in a periodic medium and imposes full correspondence between the pressure and velocities at opposite sides of the block. For a complete overview of existing upscaling techniques that are applied in reservoir simulation one can refer to [33, 132, 133, 20, 30, 32, 37, 12, 40].

9.4 Implementation of Boundary Conditions

Consistent with the cell-centered definition of the scheme, the grid is extended by one cell in each direction i.e if the original grid was 32x32 the extended grid will be 34x34. At the center of each exterior cell (left-right or top-bottom) a constant pressure is imposed. Note that flux integration is now a function of quadrature point q. At boundaries the exterior cell permeability values are set equal to their adjacent cell values. For zero normal flow conditions corner permeability values are set equal

3	3	4	4
3	3	4	4
1	1	2	2
1	1	2	2

(a)

3	0	0	4
3	3	4	4
1	1	2	2
1	0	0	2

(b)

Figure 9.3: (a) Permeability for Linear Interpolation boundary. (b) Permeability for No flow boundary.

to the adjacent cell values as shown for the 2x2 grid in figure 9.3(a). Since no-flow boundary conditions are implemented, the permeability values at the corresponding cell-center points is set to zero, figure 9.3(b).

9.5 Upscaling Results

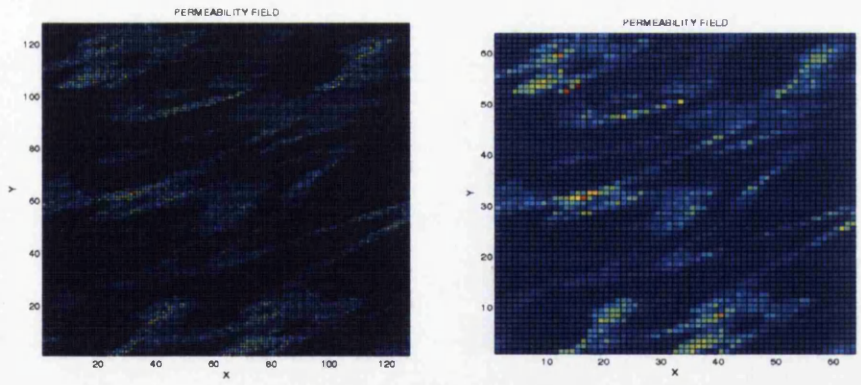

(a) (b)

Figure 9.4: (a)Typical fine scale permeability distribution on 128x128 mesh. (b) Upscaled permeability on a 64x64 mesh.

In this section the upscaling results are presented. A series of data-sets are taken as slices from the SPE10 permeability data-set for upscaling [135]. A typical perme-

ability distribution on a fine mesh along with upscaled permeability on a coarse mesh is shown in figure 9.4. Although, the family of family of flux-continuous finite volume schemes can be used for upscaling both diagonal or full permeability tensor. Whereas here, the family of schemes is used to upscale only diagonal permeability tensor cases. The results are presented for three different types of upscaling refinement strategy subject to the same boundary conditions. Different cartesian meshes are used in obtaining the upscaling results, with the finest mesh of 128x128 grid resolution and the coarsest mesh of 4x4 grid resolution.

9.5.1 1.0 Refinement Study with Renormalized Permeability

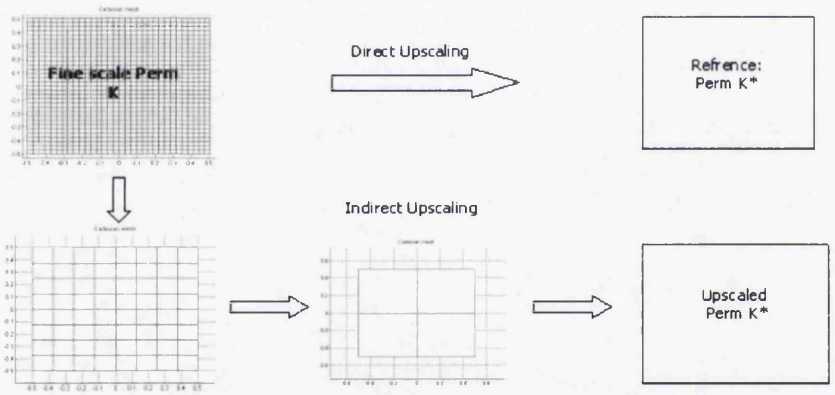

(a)

Figure 9.5: (a) Refinement with Renormalized Permeability, e.g. upscale 128x128 => 64x64, this upscaled permeability field (64x64) is then used in next upscaling step.

In this refinement comparison, the local permeability is upscaled to the next course grid level hierarchically, so that permeability values are renormalized to each courser level. Results showing the effect of different grid levels on upscaled permeability, compared to that obtained directly from the fine scale solution are presented, figure 9.5. The effect of using different quadrature points (i.e. different q) on upscaling is

analyzed. The upscaled values of equivalent permeability $\mathbf{K}^*_{11}$ and $\mathbf{K}^*_{22}$ with variable quadrature is shown in table 9.1 and table 9.2. Referring to the tables, upscaling with quadrature $q = 0.1$ gives the best results compared to other quadrature points.

	Quadrature	q=0.1	q=0.5	q=1
DataSet 1	Reference	65.5576	61.4317	58.9494
	Upscaled	44.9324	43.6320	42.8440
DataSet 2	Reference	42.5595	40.4588	39.1664
	Upscaled	32.7892	31.7659	31.1485
DataSet 3	Reference	94.4637	78.1605	70.2935
	Upscaled	58.5310	51.9994	48.4086

Table 9.1: Reference and Upscaled permeability $\mathbf{K}^*_{11}$ for *Data-Set 1,2 and 3* with variable quadrature q: Refinement with Renormalized Permeability.

	Quadrature	q=0.1	q=0.5	q=1
DataSet 1	Reference	42.5595	40.4588	39.1664
	Upscaled	32.7892	31.7659	31.1485
DataSet 2	Reference	23.8880	22.5757	21.8116
	Upscaled	20.1288	19.2585	18.7463
DataSet 3	Reference	21.9042	18.7096	17.3311
	Upscaled	19.9642	17.3430	16.1758

Table 9.2: Reference and Upscaled permeability $\mathbf{K}^*_{22}$ for *Data-Set 1,2 and 3* with variable quadrature q: Refinement with Renormalized Permeability.

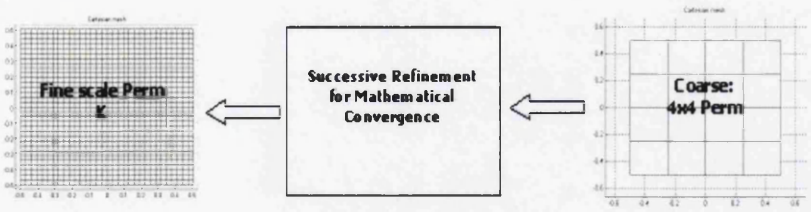

(a)

Figure 9.6: (a) Consistent Problem Invariant Convergence Test.

9.5.2 2.0 Refinement Study with Invariant Permeability Distribution

In this case the permeability distribution is the same for all grid levels including the fine scale reference solution, enabling a classical consistent mathematical convergence test to be performed, figure 9.6. Effects of different quadrature points on the convergence of upscaled permeability tensor is explored. Convergence results for upscaled permeability tensor $\mathbf{K}^*_{11}$ and $\mathbf{K}^*_{22}$ are shown in figure 9.7. Here, again it can be noted that quadrature *q= 0.1* performs better than the other quadrature point values.

9.5.3 Reservoir Field Refinement Study

This case involves a reservoir field refinement study, where cell values for each grid level have permeability defined by upscaling directly from the fine scale permeability field as in standard simulation practice. Each grid level is then simulated following the standard boundary condition procedure and an equivalent permeability tensor is deduced and compared with the reference solution obtained from upscaling the global fine scale permeability field, figure 9.8. The upscaled permeability values $\mathbf{K}^*_{11}$ and $\mathbf{K}^*_{22}$ for *data-sets 1, 2 and 3* are shown in tables 9.3,9.4, 9.5,9.6,9.7 and 9.8 respectively. The results show (as in the previous tests) that *q= 0.1* provides the best overall performance.

9.6 Summary

A study of a locally conservative family of flux-continuous schemes applied to upscaling is presented. Equivalent permeability is then used as a measure of scheme performance. Convergence tests are performed; (i) comparing equivalent permeability convergence with grid refinement and renormalized permeability. (ii) a self consistent

Quadrature	q=0.1	q=0.5	q=1
Reference(128x128)	65.5576	61.4317	58.9494
Upscaled(64x64)	63.5480	59.6080	52.4568
Upscaled(32x32)	60.0459	52.1773	47.4611
Upscaled(16x16)	59.2855	52.0012	47.8408
Upscaled(8x8)	59.2298	52.4006	48.5089
Upscaled(4x4)	55.4194	50.5745	47.6116

Table 9.3: Reference and Upscaled permeability $\mathbf{K}^*_{11}$ for *Data-Set 1* with variable quadrature q: Reservoir Field Refinement Study.

Quadrature	q=0.1	q=0.5	q=1
Reference(128x128)	42.5595	40.4588	39.1664
Upscaled(64x64)	38.8468	35.6740	32.7899
Upscaled(32x32)	28.3519	24.7645	22.8728
Upscaled(16x16)	27.2980	24.0491	22.3203
Upscaled(8x8)	26.8884	23.9251	22.2696
Upscaled(4x4)	24.8003	22.8183	21.6604

Table 9.4: Reference and Upscaled permeability $\mathbf{K}^*_{22}$ for *Data-Set 1* with variable quadrature q: Reservoir Field Refinement Study.

Quadrature	q=0.1	q=0.5	q=1
Reference(128x128)	56.2280	52.6990	50.5713
Upscaled(64x64)	54.6767	48.7680	43.6740
Upscaled(32x32)	51.7379	45.0948	41.0981
Upscaled(16x16)	52.2747	45.6833	41.9042
Upscaled(8x8)	50.3396	44.4549	41.0701
Upscaled(4x4)	43.3755	39.5181	37.1926

Table 9.5: Reference and Upscaled permeability $\mathbf{K}^*_{11}$ for *Data-Set 2* with variable quadrature q: Reservoir Field Refinement Study.

study where the same (coarse) permeability field is used for each grid level including the reference solution (problem invariant per grid level). (iii) a practical convergence study where each grid level has a permeability field obtained by upscaling directly from the finest grid level. Note that the problem permeability field changes on each

Quadrature	q=0.1	q=0.5	q=1
Reference(128x128)	23.8880	22.5757	21.8116
Upscaled(64x64)	23.4380	21.7867	20.8896
Upscaled(32x32)	23.3436	20.5161	19.0252
Upscaled(16x16)	23.2004	20.4882	19.0578
Upscaled(8x8)	22.9740	20.5094	19.1416
Upscaled(4x4)	20.2055	18.7261	17.8856

Table 9.6: Reference and Upscaled permeability $\mathbf{K}^*_{22}$ for *Data-Set 2* with variable quadrature q: Reservoir Field Refinement Study.

Quadrature	q=0.1	q=0.5	q=1
Reference(128x128)	94.4637	78.1605	70.2935
Upscaled(64x64)	92.0353	68.3512	57.5476
Upscaled(32x32)	91.9651	74.9757	66.9956
Upscaled(16x16)	89.9315	74.5197	67.0022
Upscaled(8x8)	84.7896	70.1481	63.0479
Upscaled(4x4)	76.1334	63.0145	56.6640

Table 9.7: Reference and Upscaled permeability $\mathbf{K}^*_{11}$ for *Data-Set 3* with variable quadrature q: Reservoir Field Refinement Study.

Quadrature	q=0.1	q=0.5	q=1
Reference(128x128)	21.9042	18.7096	17.3311
Upscaled(64x64)	21.2921	17.1401	15.3652
Upscaled(32x32)	21.3842	17.9277	16.3889
Upscaled(16x16)	21.7363	18.4977	17.1098
Upscaled(8x8)	21.1987	18.1143	16.8027
Upscaled(4x4)	17.9895	15.4713	14.4080

Table 9.8: Reference and Upscaled permeability $\mathbf{K}^*_{22}$ for *Data-Set 3* with variable quadrature q: Reservoir Field Refinement Study.

grid level for strategies (i) and (iii). Results are presented for a number of permeability fields. Consistently throughout the study under the different convergence comparisons and quite distinct permeability fields, results show that quadrature $q = 0.1$ improves upscaling when compared to other quadrature points. This is consistent with earlier

results of pressure field convergence tests as presented in [5, 20].

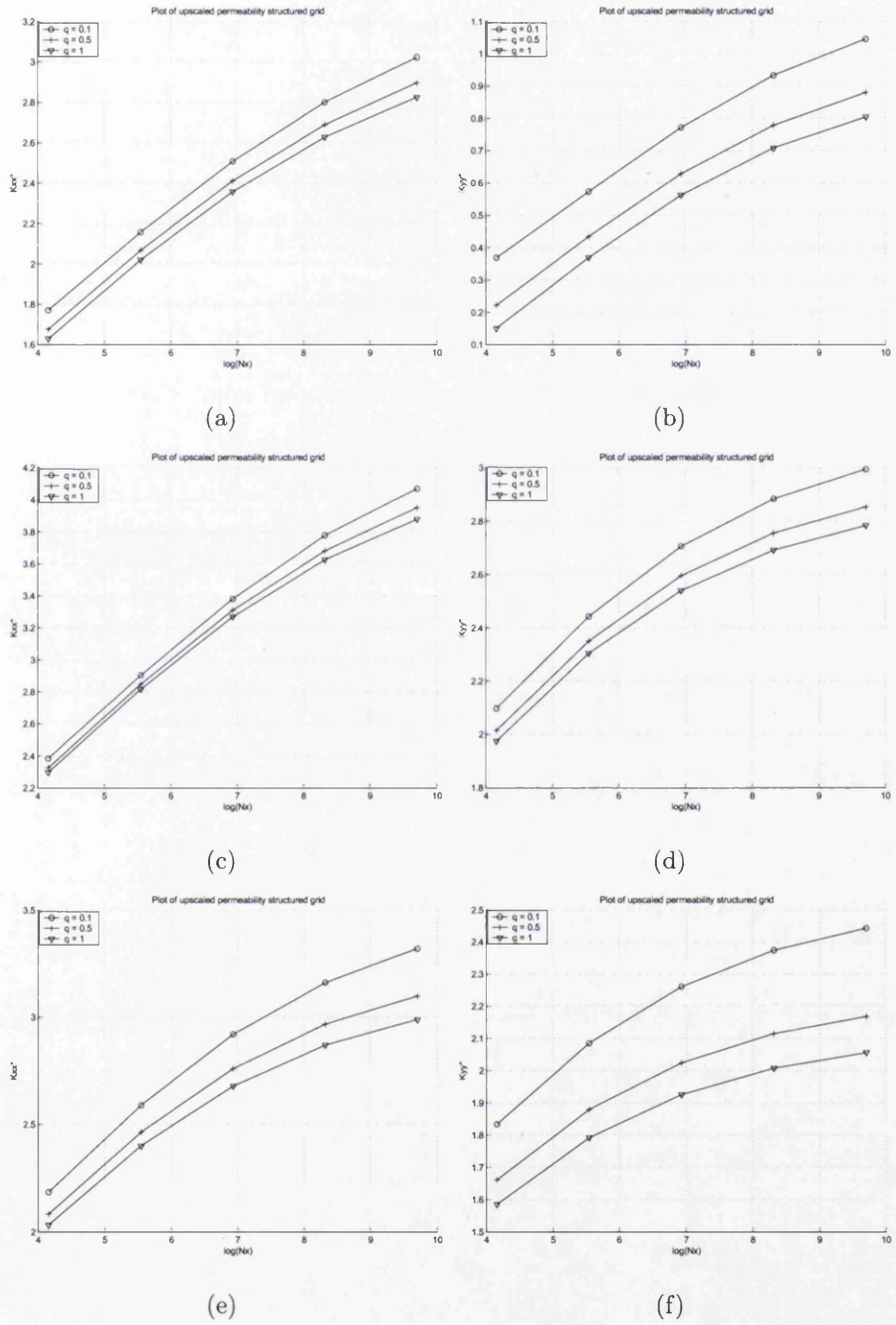

Figure 9.7: Upscaled Permeability Convergence of $\mathbf{K}^*_{xx}$ and $\mathbf{K}^*_{yy}$ for Data-Set 1,2 and 3 respectively with variable quadrature point (q): Consistent Problem Invariant Convergence Test.

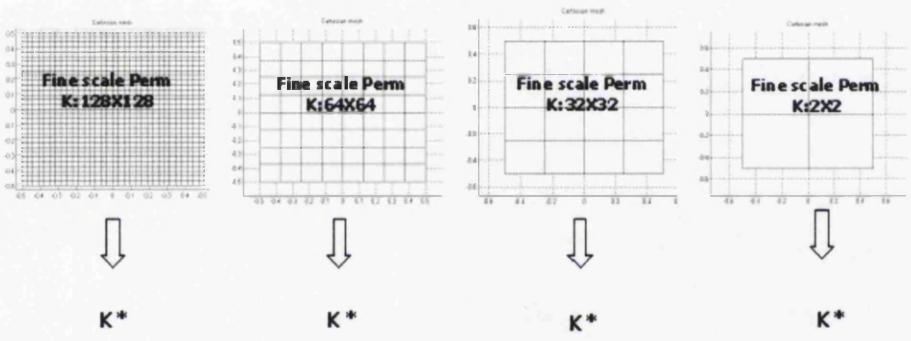

(a)

Figure 9.8: (a) Consistent Upscaling Convergence Test.

Chapter 10

Conclusions and Recommendations

10.1 Conclusions

Locally conservative families of flux-continuous finite-volume schemes have been presented for the physical space formulation in this thesis. The two dimensional formulation of the family of schemes was first introduced by Edwards and Rogers in [2]. The family of schemes are quantified by quadrature parametrization where quadrature defines the point of continuity and hence the family. The family of schemes are applicable to diagonal and full discontinuous tensor coefficients. This thesis presents the complete extension of the family of flux continuous finite-volume schemes CVD (MPFA) to all elements Hexahedra, Prism, Pyramid and Tetrahedral in 3-D and is a major contribution towards unstructured grid flow discretization.

In this thesis CVD(MPFA) schemes are used in an attempt to overcome some of the major limitations of standard schemes when applied to general geologies and geometries. The families of CVD(MPFA) schemes ensure that a consistent locally conservative flux approximation is achieved for grids comprised of any element type and combination allowing maximum flexibility in grid generation.

Numerical convergence test for full tensor problems with discontinuous coefficients show improved convergence behavior with use of quadrature parameterization q. In

general it is observed from the convergence study that quadrature point $q = 0.1$ appears to be optimal and results in improved convergence compared to other quadrature points. In particular significant improvement in convergence rates are obtained for $q = 0.1$ compared to standard MPFA ($q = 1$). This observation is substantiated further by performing a convergence study with respect to a standard upscaling procedure.

In the general case these schemes do not always lead to an M-Matrix. The physical space schemes are non-symmetric for general quadrilateral cells. Hence, a new family of flux-continuous schemes presented in [67] is discussed here for obtaining a symmetric positive definite general-tensor formulation. Whereby symmetry is achieved by introduction of piecewise constant subcell general-tensor approximation within the formulation.

The effect of subcell tensor approximation and quadrature point on convergence is presented and compared with both the physical space schemes and the cell-wise transformed control-volume schemes. The subcell schemes use a finer scale representation of the cell geometry compared to the cell-wise transform scheme and are found to have the best overall convergence performance for the cases tested. In particular the control-volume face subcell tensor approximation yields the best results. The quadrature point $q = 0.1$ is found to be the most beneficial in terms of numerical convergence. It is also found that the subcell scheme numerical convergence is considerably closer to that of the physical space formulation than the cell-wise transform-space scheme.

Monotonicity issues related to the family of schemes are discussed. The flux-splitting technique is applied to the family of schemes and developed to obtain improved monotonic behavior of the schemes when applied to problems with highly anisotropic media. An important component of this solution procedure is to obtain a monotonic solution computed by the two-point flux approximation, where the resulting M-martix is used as a driver and the remainder (deferred) correction to the iteration is added at each iterative step before a local extrema is detected. For cases

where an M-matrix can not be obtained, M-matrix analysis is used to develop specific discretization methods which guarantees minimum spurious oscillations for full-tensor problems with high anisotropy in 2-D and 3-D.

A general double (q_1,q_2)-family of flux-continuous locally conservative schemes is presented. M-matrix analysis is used to determine the upper limit for obtaining monotonic solutions and to aid the construction of schemes that minimize the occurrence of numerical solutions with spurious oscillations in the general case.

Finally, the q-family of schemes is applied to carry out upscaling on slices of SPE10 data-set [135] using different upscaling techniques. A series of convergence tests are performed on different slices of SPE10 permeability data using different quadrature -q. Here again benefits of using quadrature parametrization are highlighted.

10.2 Recommendations for Future Work

The work presented in this thesis is only the beginning for research and development of the family of control-volume distributed flux-continuous schemes (CVD-MPFA q-family of schemes). This work has laid the foundation for numerous further investigations, all of which will hopefully give an even greater insight on this novel and interesting approach with application to subsurface reservoir simulation. Further possible research routes are suggested here:

(i) A quasi monotonic variable support ($q1$,$q2$)-family of schemes is presented here. Further extension of the variable support family of schemes to general unstructured 2D and 3D grids can be carried out. A numerical convergence study should also be carried out for the variable support (q_1, q_2)-family of schemes for 2D and 3D formulation on structured and unstructured grids highlighting the quadrature parametrization and its benight.

(ii) The variable support scheme presented here, in a limiting case, results in a

seven or nine point scheme. Variable support scheme gives improved monotonicity behavior when applied highly heterogeneous anisotropic medium, compared to q-family of nine point schemes. The variable support scheme can also be combined with flux-splitting similar to the single (q)- family of scheme and monotonicity behavior of combined scheme can be investigated for both 2D and 3D formulation.

(iii) Flux-splitting scheme presented here for the single (q)- family of schemes results in improved monotonicity behavior for the schemes. Further, work on flux-splitting with the family of schemes formulation in 3D can be carried out and its effect on monotonicity behavior of the family of schemes in 3D can be investigated.

(iv) Here, the family of schemes formulation has been presented on different types of 2D and 3D grids. Very simple examples of mixed grids in 2D and 3D have been presented in this thesis. Further work can be undertaken where family of schemes can be tested on different types of increasingly complex mixed grids in 2D i.e unstructured grids comprising of quadrilateral and triangular elements. And mixed grids in 3D comprising of different element types e.g., hexahedra, prism, tetrahedra and pyramids.

(v) In this work very simple examples are tested using family of schemes for boundary aligned grids and cases with faults in 2D and 3D. Further work can be done where boundary alignment algorithm can be generalized to more complicated boundaries and further cases with faults and pinch-outs can be tested.

(vi) In this work relatively less emphasis has been put on improving the solver. Simple gaussian elimination has been used for matrix inversion operations. Further research and development can be done in this area by implementing better sparse solvers. Especially, for carrying out numerical convergence study with

more number of cells/elements in 3D. Parallel programming approach can also be looked into for testing increasing complex numerical examples in 3D.

(vii) The upscaling technique presented in this thesis using family of schemes is implemented using no-flow boundary conditions and is limited to 2D. Further work can be done in this direction where upscaling can be carried out implementing periodic boundary conditions and using family of schemes in 3D.

(viii) In this work some interesting examples are presented where cell-vertex and cell-centred approaches are combined to obtain solution for cases involving faults in 2D and 3D. This combined approach appears to be very promising and this area needs further investigation.

List of Symbols

Upper-Case Roman

$\mathbf{A}$	Jacobian matrix of 9-point flux-continuous system of equations
A_L	Matrix of assembled flux-coefficients operating on interface pressures (L-Left)
A_R	Matrix of assembled flux-coefficients operating on vertex pressures (R-Right)
$\mathbf{B}$	Jacobian matrix of 2-point flux-continuous system of equations
B_L	Matrix of assembled flux-coefficients operating on interface pressures (L-Left)
B_R	Matrix of assembled flux-coefficients operating on vertex pressures (R-Right)
$C_{i,j}$	Coarse scale cell (i-row, j-col)
E	Ellipticity of tensor ($E \leq 1$)
E	East direction
$\mathbf{F}$	Flux-coefficient matrix (2D Structured - 4x4, 2D Unstructured - 3x3)
F	Flux in x-coordinate direction
G	Flux in y-coordinate direction
$\mathbf{G}$	Gradient operator
$\mathbf{I}$	Identity matrix
J	Jacobian matrix
$\mathbf{K}$	Permeability tensor (2x2 - 2D, 3x3 - 3D)
$\mathbf{K^*}$	Equivalent permeability tensor (2x2 - 2D, 3x3 - 3D)
L_x	Face length along x-coordinate direction
L_y	Face length along y-coordinate direction
L_2	Error norm
M	Specified source or sink term
M_G	A positive definite matrix of size (nxn)
N	North direction
$\mathbf{O}$	Zero-matrix, matrix with all entries equal zero
Q	Source term
S	South direction
$\mathbf{S}$	Surface of domain Ω
$\mathbf{T}$	Transmissibility tensor (2x2 - 2D, 3x3 - 3D)
$\tilde{\mathbf{T}}$	Transformed tensor (2x2 - 2D, 3x3 - 3D)
$\mathbf{U_h}$	Function space in U
$\mathbf{V_h}$	Function space in V
W	West direction
X	X-coordinate direction
Y	Y-coordinate direction
Z	Z-coordinate direction

Lower-Case Roman

$a_{i,j}$	Element entries of matrix **A** (i-row, j-col)
$c_{i,j}$	Fine scale cell (i-row, j-col)
e_i	Edge mid-point index
e_h	Solution error $\phi - \phi_h$
f	One dimensional scalar flux
f_h	Discrete flux
f_{h_x}	Discrete flux in x-direction
f_{h_y}	Discrete flux in y-direction
f	Subscript used to represent interface of left and right cells
h	Small increment in x or y direction
i	No of cells in x-direction
j	No of cells in y-direction
k	One dimensional permeability
l	Different phases (oil, water, gas)
l	Subscript used to represent left cell
m	Source or sink in 1D
n	Iteration level
$\mathbf{n}$	Outward normal vector
$\hat{\mathbf{n}}$	Outward unit normal vector
$\vec{n_N}$	Outward normal vector at interface N
$\vec{n_S}$	Outward normal vector at interface S
$\vec{n_E}$	Outward normal vector at interface E
$\vec{n_W}$	Outward normal vector at interface W
p	Quadrature value corresponding to q_1
q	Quadrature parametrization
$\mathbf{q}$	Col-vector with values (q_1, q_2) in 2D and (q_1, q_2, q_3) in 3D
$\mathbf{r}$	Parametric variation in x and y coordinate direction
r	Subscript used to represent right cell
t	Superscript used to represent transpose of a matrix
$\mathbf{u}$	Flux in x-direction
$\mathbf{v}$	Flux in y-coordinate direction
x	x-coordinate direction
y	y-coordinate direction
z	z-coordinate direction

Upper-case Greek

Γ	Boundary of domain Ω
Δ_i	Quantity between two different levels of i
Δ_j	Quantity between two different levels of j
$\Delta_\xi F$	Quantity between two different levels of F in ξ-coordinate
$\Delta_\eta G$	Quantity between two different levels of G in ηcoordinate
$\Delta_\phi F$	Quantity between two different levels of ϕ
$\nabla\phi$	Gradient of pressure ϕ
∇v	Gradient of velocity **v**
∇z	Gradient of depth **z**
Φ	Vector of pressure ϕ
Φ_F	Vector of interface pressure ϕ_f
Φ_V	Vector of vertex pressure ϕ_v
Ω	Any problem domain

Lower-case Greek

ϕ	Discrete pressure values
ϕ_x	Derivative of pressure in x-coordinate direction
ϕ_y	Derivative of pressure in y-coordinate direction
ϕ_z	Derivative of pressure in z-coordinate direction
ϕ_l	Discrete pressure value in left cell
ϕ_r	Discrete pressure value in right cell
ϕ_f	Discrete interface pressure value
(ξ, η)	Transformed coordinates $0 \leq (\xi, \eta) \leq 1$
θ	Angle in degrees
ψ	Test function in L_2 space
φ	Test function in $H(div)$ space
(α, β)	Area coordinates
σ	Value which is function of (p,q)
μ	Viscosity of fluid
Π	pi with value in degrees = 180 degrees

Symbols

min	Minimum
max	Maximum
$Physical$	Physical Space
$Transform$	Transform Space
∂_i	Partial derivative with respect to i,j,..
∇	Gradient operator
∇^T	Divergence operator
∇^2	Laplacian operator

Abbreviations

CVD	Control Volume Distributed
DG	Discontinuous Galerkin
FDM	Finite Difference Method
FEM	Finite Element Method
FVM	Finite Volume Method
MFEM	Mixed Finite Element Method
MPFA	Multi Point Flux Approximation
NP	Nine Point
SPD	Symmetric Positive Definite
SPE	Society of Petroleum Engineers
TPFA	Two Point Flux Approximation
TP	Two Point

Bibliography

[1] Edwards M.G. and Rogers C.F. Multigrid and renormalization for reservoir simulation. *Multigrids Methods, Eds: Hemker and Wesseling (Birkhauser, Basel,1993)*, (1):190–200, 1993.

[2] Edwards M.G. and Rogers C.F. A flux continuous scheme for the full tensor pressure equation. *Proceedings: 4^{th} European Conference on the Mathematics of Oil Recovery, Norway*, 1994.

[3] Edwards M.G. and Rogers C.F. Finite volume discretization with imposed flux continuity for the general tensor pressure equation. *Comput. Geo.*, (2):259–290, 1998.

[4] Edwards M.G. Unstructured, control-volume distributed, full tensor finite volume schemes with flow based grids. *Comput. Geo.*, (6):433–452, 2002.

[5] Pal M. Edwards M.G. and Lamb A.R. Convergence study of a family of flux continuous, finite volume schemes for the general tensor pressure equation. *Int.J.Numer.Methods in Fluids*, 51:1177–1203, 2006.

[6] Edwards M.G. M-matrix flux splitting for general full tensor discretization operator on structured and unstructured grids. *J. Comput. Phys.*, (160):1–28, 2000.

[7] Pal M. and Edwards M.G. Family of flux-continuous finite-volume schemes

with improved monotonicity. *Proceedings of the 10th European Conference on the Mathematics of Oil Recovery,Amesterdam, The Netherlands*, 2006.

[8] Pal M. and Edwards M.G. Flux-splitting schemes for improved montonicity of discrete solution of elliptic equation with highly anisotropic coefficients. *In Proceedings, ECOMASS CFD-2006 Conference, Egmond aan Zee, The Netherlands*, 2006.

[9] Edwards M.G. Symmetric, flux-continuous positive definite approximation of elliptic full tensor pressure equation in local conservation form. *SPE 291471, 13^{th} SPE Reservoir Simulation Symposium, San Antonio, Texas,USA*, pages 553–562, 1995.

[10] Edwards M.G. Pal M. and Zheng H. Quasi-montonic variable support (q1,q2) families of continuous darcy-flux cvd(mpfa) finite volume schemes. *Preprint*, 2006.

[11] Edwards M.G. and Zheng H. A quasi-montonic family of continuous darcy-flux cvd(mpfa) finite volume schemes with full pressure support. *Preprint*, 2007.

[12] Pal M. and Edwards M.G. Effective upscaling using a family of flux-continuous, finite-volume schemes for the pressure equation. *In Proceedings, ACME 06 Conference, Queens University Belfast,Northern Ireland-UK*, pages 127–130, 2006.

[13] Scientific Software Corporation GS Contract No. 14-08-0001-13926. *Reservoir Simulation Manual.* National Technical Information Service U.S.Department Of Commerce, Springfield, VA.22161, 1975.

[14] Aziz K. and Settari A. *Petroleum Reservoir Simulation.* Applied Science Publishers, London, 1979.

[15] Peaceman D.W. A personal retrospection of reservoir simulation. *Proceedings of the first and second international forum on reservoir simulation, Alpbach, Austria, Sept. 12-16, 1988 and Sept. 4-8, 1989.*, 1988-89.

[16] Wycoff R.D. Botset H.G. and Muskat M. The mechanics of porous flow applied to water-flooding problems. *Transaction of the AIME*, (103):219–249, 1933.

[17] Muskat M. and Wycoff R.D. An approximate theory of water-coning in oil production. *Transaction of the AIME*, (114):144–163, 1935.

[18] Darcy H. Les fontaines publiques de la ville de dijon. 1856.

[19] Jacob Bear. *Dynamics of Fluids in Porous Media.* Courier Dover Publications, 1989.

[20] Edwards M.G. Superconvergent renormalization and tensor approximation. 5^{th} *European Conference on Mathematics of Oil Recovery,Leoben-Austria*, pages 445–454, 1996.

[21] Edwards M.G. Cross flow tensor and finite volume approximation with by deferred correction. *Comput. Methods. Appl. Mech. Engrg.*, (151):143–161, 1998.

[22] Edwards M.G. Symmetric positive definite general tensor discretization operator on unstructured and flow based grids. 8^{th} *European Conference on Mathematics of Oil Recovery,Freiberg,Germany*, 2002.

[23] Edwards M.G. Control-volume distributed sub-cell flux schemes for unstructured and flow based grids. *SPE Reservoir Simulation Symposium, Houston, Texas,USA*, 2003.

[24] Edwards M.G. and Pal M. Symmetric positive definite general tensor discretization: A family of sub-cell flux continuous schemes on cell centred quadrilateral grids. *In Proceedings of the 10th European Conference on the Mathematics of Oil Recovery,Amesterdam, The Netherlands*, 2006.

[25] Pal M. and Edwards M.G. Quasi-monotonic continuous darcy-flux approximation for general 3-d grids of any element type. *SPE Reservoir Simulation Symposium, Houston, Texas-USA*, 2007.

[26] Russel T. F. and Wheeler M. F. Finite element and finite difference methods for continuous flows in porous media. *Chapter 2, in the Mathematics of Reservoir Simulation, R.E. Ewing ed, Frontiers in Applied Mathematics SIAM*, pages 35 –106, 1983.

[27] Young L.C. A study of spatial approximation for simulating fluid displacements in petroleum reservoirs. *Comp. Meth. in Appl. Mech. Eng.*, (47):2–46, 1984.

[28] Hornung U. *Homogenization and Porous Media.* Springer-Verlag,NY, 1997.

[29] Jikov V.V. Kozlov S.M and Oleinik O.A. *Homogenization of Differential Operators and Integral Functionals.* Springer-Verlag,NY, 1994.

[30] King P.R. The use of renormalization in calculating effective permeability. *Transport in Porous Media*, 4:37, 1989.

[31] Journel A.G. Deutsch C.V. and Desbarats A.J. Power averaging for block effective permeability. *SPE Californial Regional Meeting,Oaklands,California*, SPE15128, 1986.

[32] Begg S.H. Carter R.R and Dranfield. A critical review of the use of pseudorelative permeabilities for upscaling. *SPE Reservoir Eng.*, 4(4):455–463, 1989.

[33] Durlofsky L.J. Numerical calculation of equivalent grid block permeability tensors for heterogeneous media. *Water Resources Research*, 27:699–708, 1991.

[34] Hou T.Y. and Wu X.H. A multiscale finite element method for elliptic problems in composite material and porous media. *J. Comput. Phys.*, (134):169–189, 1997.

[35] Chen Z. and Hou T.Y. A mixed multiscale finite element method for elliptic problems with oscillating coefficients. *Math. Comp.*, 72:541–576, 2003.

[36] Jenny P. Lee S.H. and Tchelepi H.A. Adaptive multiscale finite volume method for multiphase flow and transport in porous media. *Multiscale Model. Simul.*, 3(1):50–64, 2004.

[37] Arnes J.E. On the use of mixed multiscale finite element method for greater flexibility and increased speed or improved accuracy in reservoir simulation. *Multiscale Model. Simul.*, 2(3):421–439, 2004.

[38] Baker A.A. Gelhar L.W. Gutjahr A.L. and Macmillan J.R. Stochastic analysis of spatial variability in subsurface flows, i. comparision of one-and three-dimensional flows. *Water Resour. Res.*, 14(2):263–271, 1978.

[39] Gelhar L.W. and Axness C.L. Three-dimensional stochastic analysis of macro-dispersion in aquifers. *Water Resour. Res*, (19(1)):161–180, 1983.

[40] Farmer C.L. Upscaling: a review. *International Journal of Numerical Methods in Fluids*, 40:63–78, 2002.

[41] Riviere B. Discontinuous galerkin method for solving the miscible displacement problem in porous media. *Ph.D.thesis, The University of Texas at Austin*, 2000.

[42] Riviere B. Wheeler M.F. and Banas K. Discontinuous glaerkin method applied to a single phase flow in porous media. *Comput.Geo*, (49):337, 2000.

[43] Ewing R.E. Russel T.F. and Wheeler M.F. Simulation of miscible displacement using mixed methods and a modified methods of characterstics. *SPE Reservoir Simulation Symposium, San Francisco*, (SPE 12241), 1983.

[44] Ewing R.E. and Heinemann R.F. Incorporation of mixed finite element in compositional simulation for reduction of numerical dispersion. *SPE Reservoir Simulation Symposium, San Fransisco*, (SPE 12267):341–347, 1983.

[45] Douglas Jr. J. Ewing R.E. and Wheeler M.F. The approximation of the pressure by mixed method in the simulation of miscible discplacement. *A.A.I.R.O Analyse Numerique*, 17:17–33, 1983.

[46] Douglas Jr. J. Ewing R.E. and Wheeler M.F. The approximation of the pressure by mixed method in the simulation of miscible discplacement. *A.A.I.R.O Analyse Numerique*, 17:249–265, 1983.

[47] Ewing R.E. and Wheeler M.F. *Computational Aspects of Mixed Finite Element Methods, Numerical Methods for Scientific Computing (Ed. R.S. Stepleman).* North-Holland,NY.

[48] Durlofsky L.J. A triangle based mixed finite element finite volume technique for modeling two phase flow through porous media. *J.Comput.Phys*, 105:252–226, 1993.

[49] Wheeler M. F. Arbogast T. and I. Yotov. Mixed finite elements for elliptic problems with tensor coefficients as cell centered finite differences. *SIAM J. Numer. Anal.*, 34-2:828, 1997.

[50] M.Shashkov J.M.Hyman and S.Steinberg. The numerical solution of diffusion problems in strongly heterogeneous non-isotropic materials. *J. Comput. Phys*, pages 327 – 344, 1990.

[51] Aavatsmark I. Barkve T. Bøe Ø. and Mannseth T. Discretization on non-orthogonal, curvilinear grids for multiphase flow. *Proceedings of* 4^{th} *European Conference on the Mathematics of Oil Recovery, Norway*, 1994.

[52] Verma S. Phd thesis, stanford university. 1996.

[53] Aavatsmark I. Barkve T. Bøe Ø. and Mannseth T. Discretization on non-orthogonal, quadrilateral grids for inhomogeneous, anisotropic media. *J.Comput.Phys.*, 127:2–14, 1996.

[54] Aavatsmark I. Barkve T. Bøe Ø. and Mannseth T. Discretization on unstructured grids for inhomogeneous, anisotropic media. part i: Derivation of the methods. *SIAM J.Sci.Comput.*, 19:1700–1716, 1998.

[55] Aavatsmark I. Barkve T. Bøe Ø. and Mannseth T. Discretization on unstructured grids for inhomogeneous, anisotropic media. part ii: Discussion and numerical results. *SIAM J.Sci.Comput.*, 19:1717–1736, 1998.

[56] Aavatsmark I. Introduction to multipoint flux approximation for quadrilateral grids. *Comput.Geo*, 6:405–432, 2002.

[57] Celia M.A. Russel T.F. Herrera I. and Ewing R.E. An eulearian-lagrangian localized adjoin method for the advection-diffusion equation. *Advances in Water Resources*, 13(4):187–206, 1990.

[58] Dhale H.K. Ewing R.E. and Russel T.F. Eulerian-lagrangian localized adjoint method for advection-diffusion equation. *Comput. Methods Appl. Mech. Engrg*, 122:223–250, 1995.

[59] Russel T. F. and Celia M. A. An overview of research on eulerian-lagrangian localized adjoint method (ellam). *Advances in Water Resources Research*, (25(8-12)):1215–1231, 2002.

[60] Espedal M.S. and Ewing R.E. Characterstic petrov-galerkin subdomain methods for two-phase imiscible flow. *Computer Methods in Applied Mechanics and Engineering*, (46):113–135, 1987.

[61] Edwards M.G. A higher order godunov scheme coupled with dynamic local grid refinement for flow in a porous medium. *Comput. Methods. Appl. Mech. Engrg*, (131):287 – 308, 1996.

[62] Ewing R.E. and Wang J. Analysis of multilevel decomposition iterative method

for mixed finite element methods. *M^2AN, Math. Modelling and Numer. Anal.*, (28):377–398, 1994.

[63] Ronald H. W. Hoppe and Barbara Wohlmuth. Multilevel iterative solution and adaptive mesh refinement for mixed finite element discretizations. *Applied Numerical Mathematics: Transactions of IMACS*, 23(1):97–117, 1997.

[64] Zhang K. Wu Y.S. Ding C. Pruess K. and Elmroth E. Parallel computing techniques for large-scale reservoir simulation of multi-component and multi-phase fluid flow. *SPE Reservoir Simulation Symposium, Houston - Texas*, (SPE 66343), 2001.

[65] M. F. Wheeler and I. Yotov. Physical and computational domain decomposition for modeling subsurface flows. *Contemp. Math.*, 218:217,228, 1998.

[66] Mishev I. and Nepomnyaschikh S. Domain decomposition methods for reservoir simulation problems. *IMACS Conference on Iterative Methods in Scientific Computation, TAMU, Texas*, 2006.

[67] Edwards M.G. and Pal M. Positive definite q-families of continuous sub-cell darcy-flux cvd(mpfa) finite volume schemes and the mixed finite element method. *To Appear for Publication in IJNMF*, 2007.

[68] Verma S. and Aziz K. Two and three dimensional flexible grids in reservoir simulation. 5^{th} *European Conference on Mathematics of oil Recovery, Leoben, Austria, 3-6 Sept*, 1996.

[69] Aavatsmark I. Barkve T. Bøe Ø. and Mannseth T. Method for discretization on triangular grids for general media. *Third SIAM Conference on Mathematical and Computational Issues in the Geosciences, San Antonio, Feb 8-10*, 1995.

[70] Edwards M.G. Higher-resolution hyperbolic-coupled-elliptic flux continuous cvd

schemes on structured and unstructured grids in 3-d. *International Journal of Numerical Methods in Fluids*, (51):1079–1095, 2006.

[71] Edwards M.G. Higher-resolution hyperbolic-coupled-elliptic flux continuous cvd schemes on structured and unstructured grids in 2-d. *International Journal of Numerical Methods in Fluids*, (51):1059 – 1077, 2006.

[72] Heinemann Z.E. Brand C.W. Munka M. and Chen Y.M. Modeling reservoir geometry with irregular grids. *SPE 18412 Presented at 10th SPE RSS, Houston, Feb.6-8*, 1989.

[73] Heinemann Z.E. Brand C.W. Munka M. and Chen Y.M. Modeling reservoir geometry with irregular grids. *SPERE*, pages 225–232, May 1991.

[74] Yanosik J.L. and McCracken T.A. A nine-point finite-difference reservoir simulation for realistic prediction of adverse mobility ratio displacements. *SPE Journal*, (267):253–262, 1979.

[75] Bertiger W.I. and Padamanabhan L. Finite difference solution to grid orientation problems using impes. *SPE 12250 Reservoir Simulation Symposium,San Francisco*, page 12250, 1983.

[76] Shah P.C. A nine-point finite difference operator for reduction of grid orientation effect. *SPE Reservoir Simulation Symposium*, page 12252, 1983.

[77] Lee S. H. Tchelepi H. and DeChant L. J. Implementation of a flux continuous finite difference method for stratigraphic hexahedron grids. *SPE Reservoir Simulation Symposium, Houston, Texas, USA*, page SPE 51901, 1999.

[78] Lee S. H. Jenny P. and Tchelepi H. A finite volume method with hexahedral multiblock grids for modeling flow in porous media. *Comput.Geo*, 6:353–379, 2002.

[79] Russell T.F. Relationships among some conservative discretization methods. *In: Numerical Treat ment of Multiphase Flows in Porous Media, eds. Z. Chen et al., Lecture Notes in Physics*, (552):267–282, 1992.

[80] Raviart R. A. and Thomas J. M. *Lecture Notes in Mathematics 606.* Springer-Verlag New York, 1977.

[81] Farmer C.L. Heath D.E. and Moody R.O. Global optimization approach to grid generation. *SPE Reservoir Simulation Symposium, Anaheim CA, USA*, pages 341–350, 1991.

[82] Eigestad G.T. and Klausen R.A. On the convergence of the multi-point flux approximation o-method: Numerical experiments for discontinuous permeability. *Numerical Methods for Partial Differential Equations*, (21(6)):1079–1098, 2005.

[83] Nordbotten J.M. and Aavatsmark I. Montonicity conditions for control volume methods on uniform parallelogram grids in homogeneous media. *Compt. Geo.*, 9:61–72, 2005.

[84] Nordbotten J.M. Aavatsmark I. and Eigestad G.T. Monotonicity of control volume methods. *Numerische Mathematik*, 211:006–0060, 2007.

[85] Norman J.C. *Elements of Petroleum Reservoirs.* Henry L. Doherty Series, 1969.

[86] Arnes J.E. Gimse T. and Lie K.-A. *An Introduction to The Numerics of Flow in Porous Media Using Matlab:Geometrical Modeling, Numerical Simulation, and Optimization: Industrial Mathematics at SINTEF.* Springer Verlag.

[87] Bruce G.H. Peaceman D.W. Rachford Jr. H.H. and Rice J.D. Calculation of unsteady state gas flow through porous media. *Trans AIME*, 198:79–92, 1953.

[88] Peaceman D.W. and Rachford Jr. H.H. The numerical solution of parabolic and elliptic differential equations. *SIAM J.*, 3:28–41, 1955.

[89] Douglas Jr. J. Peaceman D.W. and Rachford Jr. H.H. A method for calculating multi-dimensional immiscible displacement. *AIME*, 216:297–308, 1959.

[90] Letkeman J.P. and Ridings R.L. A numerical coning model. *Trans AIME Soc.Petr.Eng.J.*, (10):418–424, 1970.

[91] Price H.S. and Coats K.H. Direct methods in reservoir simulation. *SPE Preprint No. 4278*, 1973.

[92] Leveque R.J. *Finite Volume Methods for Hyperbolic Problems.* Cambridge University Press-London, 2002.

[93] Leveque R.J. *Numerical Methods for Conservation Laws.* Lecture in Mathematics, ETH-Zurich, Birkhauser Verlag,Basel, 2^{nd} edition, 1994.

[94] Zienkiewicz O.C. Origins, milestones and directions of the finite element method - personal view. *Handbook of Numerical Analysis, P.G. Ciarlet and J.L Lions (eds), Elsevier*, (4):7–67, 1996.

[95] Oden J.T. *Finite Elements: an introduction. Handbook of Numerical Analysis, P.G.Ciarlet and J.L.Lions (eds.).* Elsevier, 1996.

[96] Gupta K.K. and Meek J.L. A brief history of the beginning of the finite element method. *Handbook of Numerical Analysis, P.G. Ciarlet and J.L Lions (eds), Elsevier*, (39):3761–3774, 1996.

[97] Zienkiewicz O.C. and Cheung YK. Finite elements in the solution of field problems. *Engineer*, (200):507–510, 1965.

[98] Zienkiewicz O.C. with Cheung YK. *The Finite Element Method in Continuum and Structural Mechanics.* McGraw Hill, 1967.

[99] Strang G. and Fix GJ. *An Analysis of The Finite Element Method.* Prentice Hall, 1973.

[100] Zienkiewicz O.C. and Morgan K. *Finite Elements and Approximation.* Wiley, 1st edition, 1982.

[101] Prevost M. Edwards M.G. and Blunt M.J. Spe 66347 streamlines tracing on curvilinear structured and untructured grids. *SPE RSS, Houston, Texas, Feb*, 2001.

[102] Klausen R.A. On locally conservative numerical methods for elliptic problems; application to reservoir simulation. *PhD Thesis,Centre for Integrated Petroleum Research CIPR, University of Bergen.*, 2003.

[103] Hughes TJR. Franca LP. Harari I. Mallet M. Shakib F. and Spelce T.E. Finite element methods for high-speed: Consistent calculation of boundary flux. *AIAA* 25^{th} *Aerospace Science Meeting, Reno, Nevada, AIAA-87-0556*, 1987.

[104] Hansbo P. Aspects of conservation in finite element flow computations. *Comput. Methods Appl. Mech. Engrg.*, (117):423–437, 1994.

[105] Berger R.C. and Howington S.E. Discrete fluxes and mass balance in finite elements. *Journal of Hydraulic Engineering*, 128-1:87–92, 2002.

[106] Hughes TJR. Wells GN. Conservation properties for the galerkin and stabilised forms of the advection-diffusion and incompressible navier-stokes equaions. *Computer Methods in Applied Mechanics and Engineering*, 194:1141 – 1159, 2005.

[107] Reed W.H. and Hill T.R. Triangular mesh method for solving neutron transport equation. *Technical Report LA-UR-73-479, Los Alamos Scientific Laboratory*, 1973.

[108] La Saint and Raviart. On a finite element method for solving neutron transport equation. *Mathematical Aspects of finite element methods in partial differential*

equations. Etd. Carl de Boor. Proceeding of a Symposium Conducted by the Mathematic Research Centre, Uni. Wisconsin-Madison, 1974.

[109] Cockburn B. Karniadakis G.E. and Shu C-W. (Eds.). *Lecture Notes in Computational Science and Engineering. The Development of Discontinuous Galerkin Methods. Discontinuous Galerkin Method. Theory, Computation and Applications.* Springer, Berlin, 2000.

[110] Brezzi F. and Fortin M. *Mixed and Hybrid Finite Element Methods. Computational Mathematics.* Springer-Verlag, NY, 1991.

[111] Wheeler J.A. Wheeler M.F. Yotov I. Enhanced velocity mixed finite element methods for flow in multiblock domains. *TICAM Report*, pages 1–27, 2001.

[112] Russel T. F. Relationships amongs some conservative discretizations. *Lecture Notes in Physics, Chen, Ewing and Shi (eds.)*, pages 1–16, 1999.

[113] Cai Z. Jones J.E. McCormick S.F and Russell T.F. Control-volume mixed finite element methods. *Comput. Geo.*, (1):289–315, 1997.

[114] Yotov I. Mixed finite element methods for flow in porous media. *PhD Thesis, Rice University*, 1996.

[115] Klausen R.A. and Winther R. Convergence of multipoint flux approximations on quadrilateral grids. *Num. Met. for PDE*, 22-6:1438–1454, 2006.

[116] Godunov S.K. A finite difference method for numerical computation of discontinuous solution of the equation of fluid dynamics. *Math. Sb.*, 47:271 – 290, 1959.

[117] Lax P.D. Weak solution of nonlinear hyperbolic equations and their numerical computation. *Comm. Pure. Appl. Math.*, 7:159–193, 1954.

[118] Lax P.D. and Wendroff B. System of conservation laws. *Comm. Pure. Appl. Math.*, 13:217–237, 1960.

[119] Harten A. Higher resolution schemes for hyperbolic conservation laws. *J. Comput. Physics*, 49(3):357–393, 1983.

[120] Jameson A. and Caughey D.A. A finite volume method for transonic flow calculations. *AIAA Paper*, pages 77 –635, 1977.

[121] Hyman J. M. Knapp R. and Scovel J. C. High order finite volume approximations of differential operators on nonuniform grids. *Physica D*, 60:112–138, 1992.

[122] Versteeg H. K. and Malalasekera W. *An Introduction to Computational Fluid Dynamics: The Finite Volume Method.* Reading, MA: Addison-Wesley, 1995.

[123] Timothy B. and Mario O. *Finite Volume Methods: Foundation and Analysis, Encyclopdeia of Computational Mechanics. Edited by Erwin Stein, Rene' de Borst and Thomas J.R. Hughes.* John Wiley and Sons, 2004.

[124] Becker E. Carey G. and Oden J.T. *Finite Elements an Introduction.* Prentice Hall, VOL 1, 1981.

[125] Aavatsmark I. and Eigestad G.T. Numerical convergence of mpfa-o and u methods on general quadrilateral grids. *International Journal of Numerical Methods in fluids*, 51:939–961, 2006.

[126] Friss H.A Edwards M.G and Mykkeltveit J. Symmetric positive definite flux-continuous full-tensor finite-volume schemes on unstructured cell centered triangular grids. *preprint*, 2006.

[127] Lamb A. R. Convergence study of a family of nine-point flux continuous, finite volume schemes for the general tensor pressure equation. *Masters Thesis, University of Wales, Swansea*, 2004.

[128] Aadland T. Aavatsmark I. and Dahle H.K. Performance of a flux splitting when solving the single-phase pressure equation discretized by mpfa. *Comput.Geo*, 8(4):325–340(16), 2004.

[129] Nordbotten J.M. and Eigestad G.T. Discretization on quadrilateral grids with improved montonicity properties. *J. Comput. Physics*, 203(2):744–760, 2005.

[130] Mlacnik M. J. and Durlofsky L.J. Unstructured grid optimization for improved monotonocity of discrete solutions of elliptic equation with highly anisotropic coefficients. *Submitted to Elsevier Science.*

[131] Axelsson O. *Iterative Solution Methods.* Cambridge University Press, Cambridge, 1994.

[132] Christe M A. Upscaling for reservoir simulation. *JPT J.Pet Tech,48:1004-1010*, 1996.

[133] Renard P and Marsily G.de. Calculating equivalent permeability: a review. *Adv. Water Resour.*, pages 20:253–278, 1997.

[134] Lee S. H. Jenny P. and Tchelepi H. Multi-scale finite volume methods for elliptic problems in subsurface flow simulation. *J.Comput.Phys.*, 187:47–67, 2003.

[135] Christie M A and Blunt M J. Tenth spe comparative solution project: A comparison of upscaling techniques. *SPE*, 2001.

[136] Palagi C. Generation and application of voronoi grid to model flow in heterogeneous reservoirs. *PhD Thesis, Standford University*, 1992.

Appendix A

Grid Construction

The simulation of fluid flow in petroleum reservoirs is performed by discretizing the actual domain into number of subdomains or gridblocks and locally applying the conservation law to each fluid component in the system. Although the physical processes are independent of this fictitious discretization of the domain, the outcome of any flow simulation depends on the grid geometry and the discretization scheme. Some grids are more appropriate to specific simulation problems than others. Construction procedure of some of these grids is described here.

A.1 Delaunay Triangulation

Delaunay triangulation is the most widely used triangulation method in unstructured mesh generation. It is one of the fastest triangulation methods with relatively easier implementation, giving excellent results for most applications. Given a set of nodes Delaunay triangulation forms triangles by the the criterion that no vertex of a triangle lies inside the circum-centre of any other triangle (also known as circle criterion). In 3D triangulation is such that the circum-sphere of any tetrahedron contains no vertex of any other tetrahedron inside it. Delaunay triangles define nearest natural neighbors in the sense that nodes are closer to their mutual circum-centre than

any other nodes. These circum-centres form the vertices of the Voronoi tessellation. Hence, Voronoi polygon surrounding a node is a region that is closer to that node than to any other node in the set.

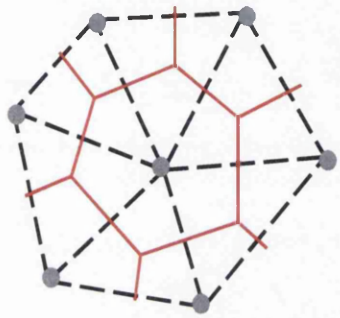

Figure A.1: Voronoi Control-volume surrounding a grid node

A.2 Voronoi Grids

Given a set of grid nodes, Voronoi control-volume/gridblock can be generated using the Voronoi criterion mentioned above. A Voronoi gridblock is defined as the volume associated with each grid node which is nearer to its own grid node than any other grid node. A Voronoi control-volume/gridblock associated with a grid node is shown in figure A.1. Intersection of perpendicular bisector lines (planes in 3D) of the underlying Delaunay mesh of connecting grid nodes defines the boundary of the Voronoi control-volume. Because of the way Voronoi grid geometry is generated, it always gives a convex control-volume/gridblock. The numerical model when permeability field is isotropic is very simple when a Voronoi grid is used to discretize the domain [136]. Geometrical properties are also easier to compute for convex shaped grids [52].

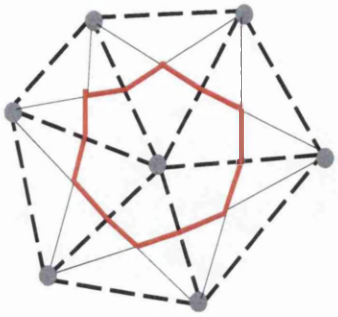

Figure A.2: CVFE grid

A.3 CVFE Grids

A 2D grid is defined to be CVFE type if the control-volume/gridblock boundaries are made from the edge-centres and barycentres of underlying Delaunay triangles. The barycentre of a triangle is the intersection of the line from a vertex to the centre of triangle edge opposite it. In 3D, a CVFE grid is made from the edge-centres, barycentres of triangular faces of the tetrahedra and barycentre of the tetrahedra. For a tetrahedron, the lines from its nodes to the barycentre of the triangular face opposite it intersects at a common point. This point is the barycentre of tetrahedron. A CVFE grid associated with a grid node is shown in figure A.2. CVFE gridblocks are normally not convex unlike Voronoi grids which are always convex, which complicates the calculation of some geometrical properties of the gridblock.

A.4 Control-volume Boundary Aligned Grids

Control-volume boundary aligned grids are formed by aligning the control-volume/grid blocks boundaries with reservoir heterogeneities [5, 7, 52]. To generate a control-volume boundary aligned grid (CV-BAG) the gridblock/control-volume boundaries need to be adapted to the reservoir geometric feature/bed boundaries. A bed boundary is typically defined by a set of points in 2D and is called a ploy line. For each edge

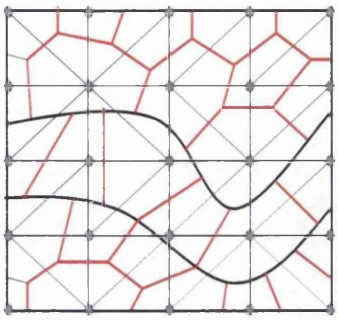

Figure A.3: Control-volume Boundary Aligned Grid (CV-BAG)

of the underlying Delaunay triangles if it is cut by a polyline then the edge midpoint for this edge is modified to be the intersection of the edge and polyline. And the control-volumes are modified to align along the reservoir geometry/bed boundary as shown in figure A.3.

Generating such a grid in 3D is geometrically very complex and requires complex geometrical algorithms and computation. For the purpose of boundary aligned cases tested in this thesis the reservoir bed boundary is defined by straight lines in 2D and by planes in 3D, which can easily be implemented using the procedure defined above.

Appendix B

Permeability Tensors

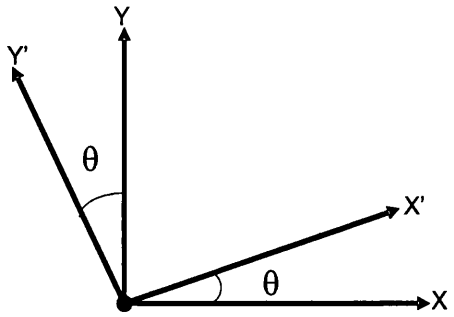

Figure B.1: Cartesian coordinate system X-Y and new coordinate system X'-Y' rotated at an angle θ.

Let the Cartesian coordinate system in 2D be denoted by x, y axes. And in this coordinate system let the velocity for a highly anisotropic diagonal permeability tensor field is given by the equation

$$\mathbf{v} = -\mathbf{K}\nabla\Phi \tag{B.1}$$

where in 2D diagonal anisotropic permeability tensor is give as

$$\mathbf{K} = \begin{pmatrix} K_{11} & 0 \\ 0 & K_{22} \end{pmatrix} \tag{B.2}$$

and the anisotropy ratio is given as K_{11}/K_{22}.

Consider a set of new Cartesian axes x', y' (figure B.1) having the same origin as the old system, and let the position of new axes with respect to the old axes be defined by the direction cosines $c_{x,y}$,i.e., the cosines of the angle (θ) between the new axis x' and the old axis x. Then the permeability tensor in the new system is given by the following equation

$$\mathbf{K}' = \begin{pmatrix} cos(\theta) & -sin(\theta) \\ sin(\theta) & cos(\theta) \end{pmatrix} \begin{pmatrix} K_{11} & 0 \\ 0 & K_{22} \end{pmatrix} \begin{pmatrix} cos(\theta) & sin(\theta) \\ -sin(\theta) & cos(\theta) \end{pmatrix} \tag{B.3}$$

The new permeability tensor field $\mathbf{K}'$ in the system rotated by an angle θ is now a symmetric full tensor with element entries given as [19]:

$$\begin{aligned} K'_{11} &= \frac{K_{11}+K_{22}}{2} + \frac{K_{11}-K_{22}}{2} cos(2\theta) \\ K'_{12} &= -\frac{K_{11}-K_{22}}{2} sin(2\theta) \\ K'_{22} &= \frac{K_{11}+K_{22}}{2} - \frac{K_{11}-K_{22}}{2} cos(2\theta) \end{aligned} \tag{B.4}$$

(B.5)

The axes (x, y) when the off-diagonal entries of the permeability tensor field vanishes are called the principal axes and the element of the diagonal along this axes are called the principal permeabilities. The principal permeabilities are the eigenvalues of the symmetric permeability tensor $(\mathbf{K}')$ in the new axes.

Appendix C

Cell-vertex Formulation

C.1 Construction of the Family of Schemes on Unstructured Triangular Grids

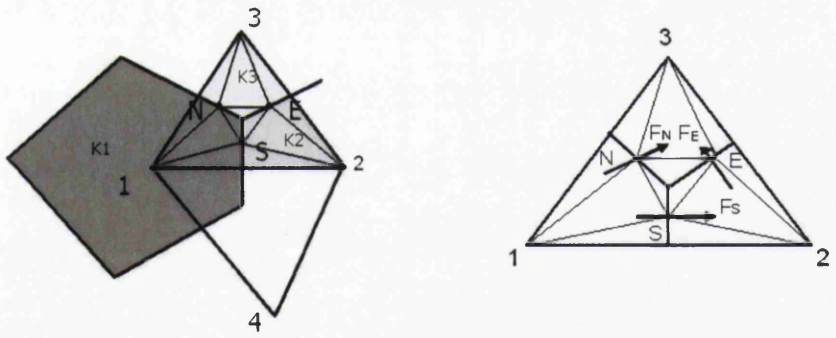

(a) (b)

Figure C.1: (a)Control-volume , Flux and pressure continuity positions at N, S, E shown on a Triangle. Quadrature q = 1/2. (b)Sub-cell triangular basis functions and fluxes at interface.

Here construction of cell-vertex based family of schemes on unstructured grids is described in detail. Figure C.1 shows triangulation of four nodes, voronoi control-

volume (CV) surrounding node 1 and parts of control-volume faces for nodes 2,3 and 4. Since, the formulation considered here is cell-vertex based each control-volume is assigned a permeability tensor e.g., control-volume surrounding node 1 has permeability tensor $\mathbf{K_1}$, similarly control-volumes surrounding nodes 2,3 have permeability tensor $\mathbf{K_2}$ and $\mathbf{K_3}$ respectively. As shown in figure C.1 a triangular pressure support is introduced and continuity of flux and pressure is imposed across control-volume faces at points N,E and S. Where points N,E and S are functions of quadrature parametrization q.

Single phase flow rate across face S is given as:

$$\begin{aligned} f_{1s} &= -\int_s \vec{v_1} \cdot \vec{n_s} dL = -A_S \vec{v_1} \cdot \vec{n_s} \\ &= A_S[v_{1x} n_{xs} + v_{1y} n_{ys}] \end{aligned} \tag{C.1}$$

A positive value of f signifies flow into the control-volume and negative value signifies flow out of the block. Single phase velocity is region 1 is estimated by:

$$\begin{aligned} \vec{v_1} &= -[K_1 \nabla \phi_1] \\ &= -\begin{pmatrix} K_{1_{xx}} & K_{1_{xy}} \\ K_{1_{yx}} & K_{1_{yy}} \end{pmatrix} \begin{pmatrix} \phi_{1x} \\ \phi_{1y} \end{pmatrix} \end{aligned} \tag{C.2}$$

To estimated the potential gradient in equation C.2 we assume potential varies linearly in region 1. Hence we have the equations

$$\begin{aligned} \phi_S &= \phi_1 + (x_S(q) - x_1)\phi_{1x} + (y_S(q) - y_1)\phi_{1y} \\ \phi_N &= \phi_1 + (x_N(q) - x_1)\phi_{1x} + (y_N(q) - y_1)\phi_{1y} \end{aligned} \tag{C.3}$$

Which gives

$$\begin{pmatrix} \phi_{1x} \\ \phi_{1y} \end{pmatrix} = \begin{pmatrix} (x_S(q) - x_1) & (y_S(q) - y_1) \\ (x_N(q) - x_1) & (y_N(q) - y_1) \end{pmatrix}^{-1} \begin{pmatrix} \phi_S - \phi_1 \\ \phi_N - \phi_1 \end{pmatrix}$$
$$= \frac{1}{D_1} \begin{pmatrix} (y_N(q) - x_1) & (y_1 - y_S(q)) \\ (x_1 - x_N(q)) & (x_S(q) - x_1) \end{pmatrix} \begin{pmatrix} \phi_S - \phi_1 \\ \phi_N - \phi_1 \end{pmatrix} \quad \text{(C.4)}$$

where

$$D_1 = x_1(y_S(q) - y_N(q)) + x_S(q)(y_N(q) - y_1) + x_N(q)(y_1 - y_S(q)) \quad \text{(C.5)}$$

Hence we can write equation C.4 as

$$\begin{pmatrix} \phi_{1x} \\ \phi_{1y} \end{pmatrix} = \begin{pmatrix} A_{11}(q) & A_{12}(q) \\ A_{21}(q) & A_{22}(q) \end{pmatrix} \begin{pmatrix} \phi_S - \phi_1 \\ \phi_N - \phi_1 \end{pmatrix} \quad \text{(C.6)}$$

similarly we can write expressions for CV surrounding nodes 2 and 3. For node 2 we have

$$\begin{pmatrix} \phi_{2x} \\ \phi_{2y} \end{pmatrix} = \begin{pmatrix} B_{11}(q) & B_{12}(q) \\ B_{21}(q) & B_{22}(q) \end{pmatrix} \begin{pmatrix} \phi_S - \phi_2 \\ \phi_E - \phi_2 \end{pmatrix} \quad \text{(C.7)}$$

and for CV surrounding node 3 the equation is:

$$\begin{pmatrix} \phi_{3x} \\ \phi_{3y} \end{pmatrix} = \begin{pmatrix} C_{11}(q) & C_{12}(q) \\ C_{21}(q) & C_{22}(q) \end{pmatrix} \begin{pmatrix} \phi_N - \phi_3 \\ \phi_E - \phi_3 \end{pmatrix} \quad \text{(C.8)}$$

It should be noted that the coefficients of the matrices above are functions of quadrature q. As we want fluxes normal to interfaces to mach on either side of points N,E and S. Hence we form three constraint equations, one each at points N,E and S by imposing continuity of fluxes. At S:

$$\vec{v_1} \cdot \vec{n_S} = \vec{v_2} \cdot \vec{n_S} \quad \text{(C.9)}$$

where $\vec{n_S}$ is the outward normal with respect to 1 on the CV face. At N:

$$\vec{v_1} \cdot \vec{n_N} = \vec{v_3} \cdot \vec{n_N} \quad \text{(C.10)}$$

where $\vec{n_N}$ is the outward normal with respect to 1 on the CV face. At E:

$$\vec{v_2} \cdot \vec{n_E} = \vec{v_3} \cdot \vec{n_E} \tag{C.11}$$

where $\vec{n_N}$ is the outward normal with respect to 2 on the CV face. Expanding the continuity equation C.9 we get :

$$(v_{x_1} - v_{x_2})n_{x_S} + (v_{y_1} - v_{y_2})n_{yS} = 0, \tag{C.12}$$

and substituting the terms for velocities we get

$$\begin{aligned}
& n_{x_S}[K_{1_{xx}}(A_{11}(\phi_S - \phi_1) + A_{12}(\phi_N - \phi_1)) \\
& \quad + K_{1_{xy}}(A_{21}(\phi_S - \phi_1) + A_{22}(\phi_N - \phi_1))] \\
& + n_{y_S}[K_{1_{xx}}(A_{11}(\phi_S - \phi_1) + A_{12}(\phi_N - \phi_1)) \\
& \quad + K_{1_{xy}}(A_{21}(\phi_S - \phi_1) + A_{22}(\phi_N - \phi_1))] \\
& = n_{x_S}[K_{2_{xx}}(B_{11}(\phi_S - \phi_2) + B_{12}(\phi_E - \phi_2)) \\
& \quad + K_{2_{xy}}(B_{21}(\phi_S - \phi_2) + B_{22}(\phi_E - \phi_2))] \\
& + n_{y_S}[K_{2_{xx}}(B_{11}(\phi_S - \phi_2) + B_{12}(\phi_E - \phi_2)) \\
& \quad + K_{2_{xy}}(B_{21}(\phi_S - \phi_2) + B_{22}(\phi_E - \phi_2))]
\end{aligned} \tag{C.13}$$

We can now arrange the above equation in terms of the coefficients of $\phi_N, \phi_S, \phi_E, \phi_1$ and ϕ_2. In a similar manner we can use the other two continuity equation C.11, C.12 and then collect the coefficients. Then the three continuity equations C.9 can be cast into following form:

$$\begin{pmatrix} A_{L_{11}} & A_{L_{12}} & A_{L_{13}} \\ A_{L_{21}} & A_{L_{22}} & A_{L_{23}} \\ A_{L_{31}} & A_{L_{32}} & A_{L_{33}} \end{pmatrix} \begin{pmatrix} \phi_S \\ \phi_E \\ \phi_N \end{pmatrix} + \begin{pmatrix} B_{L_{11}} & B_{L_{12}} & B_{L_{13}} \\ B_{L_{21}} & B_{L_{22}} & B_{L_{23}} \\ B_{L_{31}} & B_{L_{32}} & B_{L_{33}} \end{pmatrix} \begin{pmatrix} \phi_1 \\ \phi_2 \\ \phi_3 \end{pmatrix} =$$
$$\begin{pmatrix} A_{R_{11}} & A_{R_{12}} & A_{R_{13}} \\ A_{R_{21}} & A_{R_{22}} & A_{R_{23}} \\ A_{R_{31}} & A_{R_{32}} & A_{R_{33}} \end{pmatrix} \begin{pmatrix} \phi_S \\ \phi_E \\ \phi_N \end{pmatrix} + \begin{pmatrix} B_{R_{11}} & B_{R_{12}} & B_{R_{13}} \\ B_{R_{21}} & B_{R_{22}} & B_{R_{23}} \\ B_{R_{31}} & B_{R_{32}} & B_{R_{33}} \end{pmatrix} \begin{pmatrix} \phi_1 \\ \phi_2 \\ \phi_3 \end{pmatrix} \quad \text{(C.14)}$$

Where the coefficients of the matrix are given as:

$$\begin{aligned} A_{L_{11}} &= n_{x_S} K_{1_{xx}} A_{11} + n_{x_S} K_{1_{xy}} A_{21} \\ A_{L_{12}} &= 0 \\ A_{L_{13}} &= n_{x_S} K_{1_{xx}} A_{12} + n_{x_S} K_{1_{xy}} A_{22} \\ A_{L_{21}} &= 0 \\ A_{L_{22}} &= 0 \\ A_{L_{23}} &= 0 \\ A_{L_{31}} &= n_{y_S} K_{1_{xx}} A_{11} + n_{y_S} K_{1_{xy}} A_{21} \\ A_{L_{32}} &= 0 \\ A_{L_{33}} &= n_{y_S} K_{1_{xx}} A_{12} + n_{y_S} K_{1_{xy}} A_{22} \end{aligned} \quad \text{(C.15)}$$

$$
\begin{aligned}
B_{L_{11}} &= -n_{x_S} K_{1_{xx}} (A_{11} + A_{12}) - n_{x_S} K_{1_{xy}} (A_{11} + A_{12}) \\
B_{L_{12}} &= 0 \\
B_{L_{13}} &= 0 \\
B_{L_{21}} &= -n_{y_S} K_{1_{xx}} (A_{11} + A_{12}) - n_{y_S} K_{1_{xy}} (A_{11} + A_{12}) \\
B_{L_{22}} &= 0 \\
B_{L_{23}} &= 0 \\
B_{L_{31}} &= 0 \\
B_{L_{32}} &= 0 \\
B_{L_{33}} &= 0
\end{aligned}
\tag{C.16}
$$

$$
\begin{aligned}
A_{R_{11}} &= n_{x_S} K_{2_{xx}} B_{11} + n_{x_S} K_{2_{xy}} B_{21} \\
A_{R_{12}} &= n_{x_S} K_{2_{xx}} B_{12} + n_{x_S} K_{2_{xy}} B_{22} \\
A_{R_{13}} &= 0 \\
A_{R_{21}} &= n_{y_S} K_{2_{xx}} B_{11} + n_{y_S} K_{2_{xy}} B_{21} \\
A_{R_{22}} &= n_{y_S} K_{2_{xx}} B_{12} + n_{y_S} K_{2_{xy}} B_{22} \\
A_{R_{23}} &= 0 \\
A_{R_{31}} &= 0 \\
A_{R_{32}} &= 0 \\
A_{R_{33}} &= 0
\end{aligned}
\tag{C.17}
$$

$$
\begin{aligned}
B_{R_{11}} &= 0 \\
B_{R_{12}} &= -n_{x_S} K_{2_{xx}} (B_{11} + B_{12}) - n_{x_S} K_{2_{xy}} (B_{11} + B_{12}) \\
B_{R_{13}} &= 0 \\
B_{R_{21}} &= 0 \\
B_{R_{22}} &= -n_{y_S} K_{2_{xx}} (B_{11} + B_{12}) - n_{y_S} K_{2_{xy}} (B_{11} + B_{12}) \\
B_{R_{23}} &= 0 \\
B_{R_{31}} &= 0 \\
B_{R_{32}} &= 0 \\
B_{R_{33}} &= 0
\end{aligned} \tag{C.18}
$$

Similar expression can be formed for rest of the continuity equation C.10, C.11 and C.12. From equation C.14 interface pressures can be eliminated by expressing interface pressures in terms of cell-vertex pressures as:

$$\Phi_f = (A_L - A_R)^{-1}(B_R - B_L)\Phi v \tag{C.19}$$

where $\Phi_f = [\phi_S, \phi_E, \phi_N]'$ and $\Phi_f = [\phi_1, \phi_2, \phi_3]'$

Once the interface pressures are expressed in terms of cell centred pressures the flux coefficient matrix then can be written as:

$$F = (A_L((A_L - A_R)^{-1}(B_R - B_L)) + B_L)\Phi_v \tag{C.20}$$

Now using similar equations fluxes can be computed for other CV's in the domain and a global assembly can be performed accordingly.

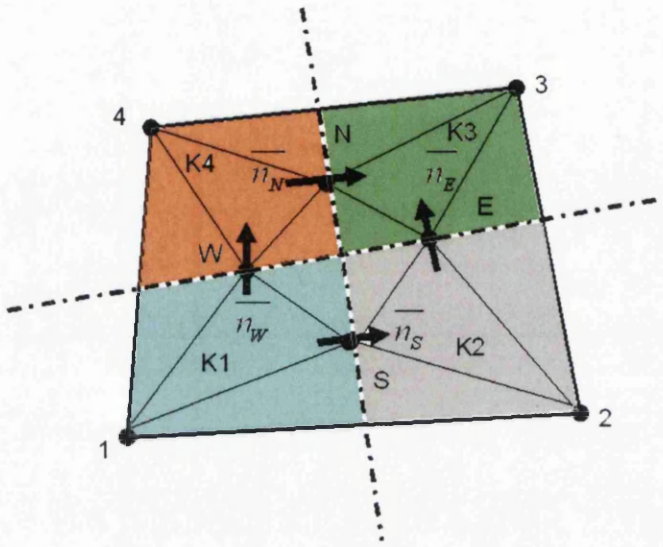

Figure C.2: Control-volume , Flux and pressure continuity positions at N, S, E shown on a Quadrilateral.

C.2 Cell-vertex Formulation on Quadrilateral Grids

This section describes the construction of cell-vertex family of schemes on quadrilateral grids. In cell-vertex based scheme a quadrilateral element contains parts of four homogeneous CVs (with permeability tensor $\mathbf{K_1}, \mathbf{K_2}, \mathbf{K_3}$ and $\mathbf{K_4}$), one surrounding each node and there will be four interfaces of the CVs inside each quadrilateral element, figure C.2. There will thus be four fluxes inside each quadrilateral. An interface pressure is introduced at point N,S,E and W, figure C.2. These interface pressures along with nodal pressures are used to estimate pressure gradient inside each of the CVs in the quadrilateral, which can then be used to compute the velocity at each interface. The velocities are used to estimate fluxes at each interface. Continuity of flux and pressure is imposed at the point N,S,E and W (which are functions of quadrature parametrization q). The single phase flow rate across face S is given as:

Single phase flow rate across face S is given as:

$$\begin{aligned} f_{1s} &= -\int_s \vec{v_1}\cdot\vec{n_s}dL = -A_S\vec{v_1}\cdot\vec{n_s} \\ &= A_S[v_{1x}n_{xs} + v_{1y}n_{ys}] \end{aligned} \tag{C.21}$$

where n_S is the outward normal on the interface S with node 1 considered as an inside point. A positive value of f signifies flow into the block while a negative value signifies flow out of the block. The single phase velocity in region i ($i = 1,..,4$) is given by:

$$\begin{aligned} \vec{v_i} &= -[K_i\nabla\phi_i] \\ &= -\begin{pmatrix} K_{i_{xx}} & K_{i_{xy}} \\ K_{i_{yx}} & K_{i_{yy}} \end{pmatrix}\begin{pmatrix} \phi_{ix} \\ \phi_{iy} \end{pmatrix}, \qquad i = 1,...,4 \end{aligned} \tag{C.22}$$

To estimate the pressure gradient in above equation linear basis functions are introduced in region $1,..,3$ of the quadrilateral element assuming pressure varies linearly. Hence we have the equations:

$$\begin{aligned} \phi_S &= \phi_1 + (x_S(q) - x_1)\phi_{1x} + (y_S(q) - y_1)\phi_{1y} \\ \phi_W &= \phi_1 + (x_W(q) - x_1)\phi_{1x} + (y_W(q) - y_1)\phi_{1y} \end{aligned} \tag{C.23}$$

Which gives

$$\begin{aligned} \begin{pmatrix} \phi_{1x} \\ \phi_{1y} \end{pmatrix} &= \begin{pmatrix} (x_S(q) - x_1) & (y_S(q) - y_1) \\ (x_W(q) - x_1) & (y_W(q) - y_1) \end{pmatrix}^{-1}\begin{pmatrix} \phi_S - \phi_1 \\ \phi_W - \phi_1 \end{pmatrix} \\ &= \frac{1}{D_1}\begin{pmatrix} (y_W(q) - x_1) & (y_1 - y_S(q)) \\ (x_1 - x_W(q)) & (x_S(q) - x_1) \end{pmatrix}\begin{pmatrix} \phi_S - \phi_1 \\ \phi_W - \phi_1 \end{pmatrix} \end{aligned} \tag{C.24}$$

Hence equation C.24 can be written as

$$\begin{pmatrix} \phi_{1x} \\ \phi_{1y} \end{pmatrix} = \begin{pmatrix} A_{11}(q) & A_{12}(q) \\ A_{21}(q) & A_{22}(q) \end{pmatrix}\begin{pmatrix} \phi_S - \phi_1 \\ \phi_W - \phi_1 \end{pmatrix} \tag{C.25}$$

similarly we can write expressions for CVs surrounding nodes 2,3 and 3. For node 2 we have

$$\begin{pmatrix} \phi_{2x} \\ \phi_{2y} \end{pmatrix} = \begin{pmatrix} B_{11}(q) & B_{12}(q) \\ B_{21}(q) & B_{22}(q) \end{pmatrix} \begin{pmatrix} \phi_S - \phi_2 \\ \phi_E - \phi_2 \end{pmatrix} \tag{C.26}$$

,for node 3 we have

$$\begin{pmatrix} \phi_{3x} \\ \phi_{3y} \end{pmatrix} = \begin{pmatrix} C_{11}(q) & C_{12}(q) \\ C_{21}(q) & C_{22}(q) \end{pmatrix} \begin{pmatrix} \phi_W - \phi_3 \\ \phi_N - \phi_3 \end{pmatrix} \tag{C.27}$$

and finally for node 4 we have

$$\begin{pmatrix} \phi_{4x} \\ \phi_{4y} \end{pmatrix} = \begin{pmatrix} D_{11}(q) & D_{12}(q) \\ D_{21}(q) & D_{22}(q) \end{pmatrix} \begin{pmatrix} \phi_E - \phi_4 \\ \phi_N - \phi_4 \end{pmatrix} \tag{C.28}$$

Flow rates across the interfaces are based on the velocities at the points N,S,E and W. As mentioned earlier, velocities normal to interfaces should match at these points on both side of the interface. Hence four continuity equations are formed, one at each of the points. The continuity equations at points N,S,E and W are:

$$\begin{aligned} \vec{v_1} \cdot \vec{n_S} &= \vec{v_2} \cdot \vec{n_S} \\ \vec{v_1} \cdot \vec{n_W} &= \vec{v_3} \cdot \vec{n_W} \\ \vec{v_2} \cdot \vec{n_E} &= \vec{v_3} \cdot \vec{n_E} \\ \vec{v_3} \cdot \vec{n_N} &= \vec{v_4} \cdot \vec{n_N} \end{aligned} \tag{C.29}$$

respectively, where $\vec{n_E}, \vec{n_W}, \vec{n_N}$ and $\vec{n_S}$ are outward normals on face E, W, N and S respectively. Now expanding the equation C.30 and substituting the terms for velocities similar to the formulation on triangles as in section C.1 we obtain expressions like

$$
\begin{aligned}
& n_{x_S}[K_{1_{xx}}(A_{11}(\phi_S-\phi_1)+A_{12}(\phi_N-\phi_1)) \\
& \quad +K_{1_{xy}}(A_{21}(\phi_S-\phi_1)+A_{22}(\phi_N-\phi_1)) \\
& +n_{y_S}[K_{1_{xx}}(A_{11}(\phi_S-\phi_1)+A_{12}(\phi_N-\phi_1)) \\
& \quad +K_{1_{xy}}(A_{21}(\phi_S-\phi_1)+A_{22}(\phi_N-\phi_1))] \\
& = n_{x_S}[K_{2_{xx}}(B_{11}(\phi_S-\phi_2)+B_{12}(\phi_E-\phi_2)) \\
& \quad +K_{2_{xy}}(B_{21}(\phi_S-\phi_2)+B_{22}(\phi_E-\phi_2))] \\
& +n_{y_S}[K_{2_{xx}}(B_{11}(\phi_S-\phi_2)+B_{12}(\phi_E-\phi_2)) \\
& \quad +K_{2_{xy}}(B_{21}(\phi_S-\phi_2)+B_{22}(\phi_E-\phi_2))]
\end{aligned}
\tag{C.30}
$$

similar expression can be obtained for rest of the continuity equations. Following from section C.1 the above equations can now be cast into following form:

$$A_L\Phi_f + B_L\Phi_v = A_R\Phi_f + B_R\Phi_v \tag{C.31}$$

where $\Phi_f = [\phi_N, \phi_S, \phi_E, \phi_W]'$ and $\Phi_v = [\phi_1, \phi_2, \phi_3, \phi_4]'$, and AL, BL, AR, BR are matrices of size 4x4. The coefficients of the matrices are expressed as:

$$
\begin{aligned}
A_{L_{11}} &= n_{x_S} K_{1_{xx}} A_{12} + n_{x_S} K_{1_{xy}} A_{22} \\
A_{L_{12}} &= n_{x_S} K_{1_{xx}} A_{11} + n_{x_S} K_{1_{xy}} A_{21} \\
A_{L_{13}} &= 0 \\
A_{L_{14}} &= 0 \\
A_{L_{21}} &= n_{y_S} K_{1_{xx}} A_{12} + n_{y_S} K_{1_{xy}} A_{22} \\
A_{L_{22}} &= n_{y_S} K_{1_{xx}} A_{11} + n_{y_S} K_{1_{xy}} A_{21} \\
A_{L_{23}} &= 0 \\
A_{L_{24}} &= 0 \\
A_{L_{31}} &= 0 \\
A_{L_{32}} &= 0 \\
A_{L_{33}} &= 0 \\
A_{L_{34}} &= 0 \\
A_{L_{41}} &= 0 \\
A_{L_{42}} &= 0 \\
A_{L_{43}} &= 0 \\
A_{L_{44}} &= 0
\end{aligned}
\tag{C.32}
$$

$$
\begin{aligned}
B_{L_{11}} &= -n_{x_S} K_{1_{xx}} A_{11} - n_{x_S} K_{1_{xy}} A_{21} \\
B_{L_{12}} &= 0 \\
B_{L_{13}} &= 0 \\
B_{L_{14}} &= 0 \\
B_{L_{21}} &= n_{y_S} K_{1_{xx}} A_{11} + n_{y_S} K_{1_{xy}} A_{21} \\
B_{L_{22}} &= 0 \\
B_{L_{23}} &= 0 \\
B_{L_{24}} &= 0 \\
B_{L_{31}} &= 0 \\
B_{L_{32}} &= 0 \\
B_{L_{33}} &= 0 \\
B_{L_{34}} &= 0 \\
B_{L_{41}} &= 0 \\
B_{L_{42}} &= 0 \\
B_{L_{43}} &= 0 \\
B_{L_{44}} &= 0
\end{aligned}
\tag{C.33}
$$

$$
\begin{aligned}
A_{R_{11}} &= 0 \\
A_{R_{12}} &= n_{x_S} K_{2_{xx}} B_{11} + n_{x_S} K_{2_{xy}} B_{21} \\
A_{R_{13}} &= n_{x_S} K_{1_{xx}} B_{12} + n_{x_S} K_{2_{xy}} B_{22} \\
A_{R_{14}} &= 0 \\
A_{R_{21}} &= 0 \\
A_{R_{22}} &= n_{y_S} K_{2_{xx}} B_{11} + n_{y_S} K_{2_{xy}} B_{21} \\
A_{R_{23}} &= n_{y_S} K_{1_{xx}} B_{12} + n_{y_S} K_{2_{xy}} B_{22} \\
A_{R_{24}} &= 0 \\
A_{R_{31}} &= 0 \\
A_{R_{32}} &= 0 \\
A_{R_{33}} &= 0 \\
A_{R_{34}} &= 0 \\
A_{R_{41}} &= 0 \\
A_{R_{42}} &= 0 \\
A_{R_{43}} &= 0 \\
A_{R_{44}} &= 0
\end{aligned}
\tag{C.34}
$$

$$
\begin{aligned}
B_{R_{11}} &= 0 \\
B_{R_{12}} &= -n_{x_S} K_{2_{xx}} B_{11} - n_{x_S} K_{2_{xy}} B_{21} \\
B_{R_{13}} &= 0 \\
B_{R_{14}} &= 0 \\
B_{R_{21}} &= 0 \\
B_{R_{22}} &= n_{y_S} K_{2_{xx}} B_{11} + n_{y_S} K_{2_{xy}} B_{21} \\
B_{R_{23}} &= 0 \\
B_{R_{24}} &= 0 \\
B_{R_{31}} &= 0 \\
B_{R_{32}} &= 0 \\
B_{R_{33}} &= 0 \\
B_{R_{34}} &= 0 \\
B_{R_{41}} &= 0 \\
B_{R_{42}} &= 0 \\
B_{R_{43}} &= 0 \\
B_{R_{44}} &= 0
\end{aligned}
\tag{C.35}
$$

From equation C.31 interface pressures Φ_f can now be eliminated by expressing them in terms of vertex pressures Φ_v.

$$\Phi_f = (A_L - A_R)^{-1}(B_R - B_L)\Phi v \tag{C.36}$$

After eliminating interface pressures the flux coefficient matrix can then be written in a similar manner as:

$$F = (A_L((A_L - A_R)^{-1}(B_R - B_L)) + B_L)\Phi_v \tag{C.37}$$

Once the fluxes are computed using equation C.37 global assembly follows.

C.3 Cell-vertex Formulation on Quadrilateral Grids: Inverse Tensor Form

The flux is now derived in an alternative form involving potential differences between nodes following [6, 4]. We return to the physical space flux of equation C.30 expressed in terms of potential differences between interface pressures and nodal pressures, for any quadrature point on the interface, and reformulate the flux continuity conditions in terms of the subcell tensors as:

$$\begin{aligned}
(T^1)^{-1}\begin{pmatrix} F_S \\ F_W \end{pmatrix} &= -\begin{pmatrix} \phi_S - \phi_1 \\ \phi_W - \phi_1 \end{pmatrix}, \qquad (T^2)^{-1}\begin{pmatrix} F_S \\ F_E \end{pmatrix} = -\begin{pmatrix} \phi_2 - \phi_S \\ \phi_E - \phi_2 \end{pmatrix}, \\
(T^3)^{-1}\begin{pmatrix} F_N \\ F_E \end{pmatrix} &= -\begin{pmatrix} \phi_3 - \phi_N \\ \phi_3 - \phi_E \end{pmatrix}, \qquad (T^4)^{-1}\begin{pmatrix} F_N \\ F_W \end{pmatrix} = -\begin{pmatrix} \phi_N - \phi_4 \\ \phi_4 - \phi_W \end{pmatrix}
\end{aligned} \tag{C.38}$$

where fluxes are grouped according to subcell numbers (denoted by general-tensor superfixes) that are in common and equation C.38 is then an equivalent form of equation C.30. The physical space tensor approximations belonging to each subcell are written as:

$$\begin{aligned}
T^1 &= \begin{pmatrix} T_{11}|_S^1 & T_{12}|_S^1 \\ T_{12}|_W^1 & T_{22}|_W^1 \end{pmatrix}, \qquad T^2 = \begin{pmatrix} T_{11}|_S^2 & T_{12}|_S^2 \\ T_{12}|_E^2 & T_{22}|_E^2 \end{pmatrix} \\
T^3 &= \begin{pmatrix} T_{11}|_N^3 & T_{12}|_N^3 \\ T_{12}|_E^3 & T_{22}|_E^3 \end{pmatrix}, \qquad T^4 = \begin{pmatrix} T_{11}|_N^4 & T_{12}|_N^4 \\ T_{12}|_W^4 & T_{22}|_W^4 \end{pmatrix}
\end{aligned} \tag{C.39}$$

Now denote $T_{12}^1 = T_{12}|_S^1$, $T_{21}^1 = T_{12}|_W^1$ and $T_{12}^1 \neq T_{21}^1$ in the general case. Thus the inverses of the discrete tensors in equation C.39 are not symmetric in the general case. Denoting the inverse of the general-tensor by $\widetilde{T} = (T)^{-1}$ and adding pairs of equations operating on common fluxes, e.g., adding the top rows of the first pair of equation sets in equation C.38 yields

$$(\widetilde{T}_{11}^1 + \widetilde{T}_{11}^2)F_S + \widetilde{T}_{12}^2 F_E + \widetilde{T}_{12}^1 F_W = -(\phi_2 - \phi_s + \phi_s - \phi_1) = -(\phi_2 - \phi_1) \tag{C.40}$$

which eliminates the unknown interface pressure directly. Gathering the other flux pairs and expanding in a similar fashion leads to a system of equations that expresses the fluxes directly in terms of potential differences viz

$$A\mathbf{F} = -\Delta\phi_{\mathbf{v}} \tag{C.41}$$

where

$$\mathbf{F} = (F_S, F_E, F_N, F_W)^T, \qquad \Delta\phi_{\mathbf{v}} = (\phi_{21}, \phi_{32}, \phi_{34}, \phi_{41})^T \tag{C.42}$$

where double suffices of ϕ denote potential differences e.g. $\phi_{21} = \phi_2 - \phi_1$ and the flux coefficient matrix is given by

$$A = \begin{pmatrix} \widetilde{T}^1_{11} + \widetilde{T}^2_{11} & \widetilde{T}^2_{12} & 0 & \widetilde{T}^1_{12} \\ \widetilde{T}^2_{21} & \widetilde{T}^2_{22} + \widetilde{T}^3_{22} & \widetilde{T}^3_{21} & 0 \\ 0 & \widetilde{T}^3_{12} & \widetilde{T}^4_{11} + \widetilde{T}^3_{11} & \widetilde{T}^4_{12} \\ \widetilde{T}^1_{21} & 0 & \widetilde{T}^4_{21} & \widetilde{T}^1_{22} + \widetilde{T}^4_{22} \end{pmatrix} . \tag{C.43}$$

Thus the dual-cell flux matrix entries are comprised of elements of the general tensor inverse corresponding to each subcell component of control-volume.

C.4 Cell-vertex Formulation in 3D

Construction of the cell-vertex family of schemes on general 3D grids is presented in chapter 5. In this section scheme construction is presented for a tetrahedral element, figure C.3. Exactly the same principles as mentioned in chapter 5, section C.1 and section C.2 will be used for construction of the cell-vertex family of schemes on a tetrahedral element. Decomposition of a tetrahedron into homogeneous control-volumes associated with the vertices is shown in figure C.3. It is assumed that properties like permeability tensor inside each control-volume are homogeneous. The permeability tensor may be full, asymmetric and anisotropic.

A tetrahedron will have four homogeneous regions, one surrounding each node and there will be six interfaces inside each tetrahedron. There will thus be six flow

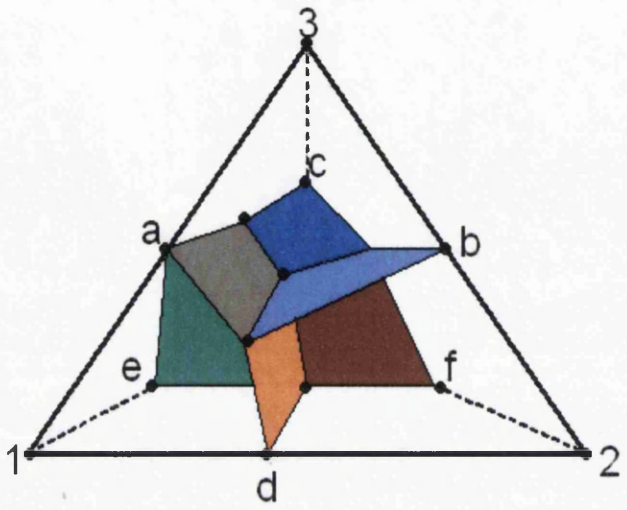

Figure C.3: Control-volume faces, Flux and pressure continuity positions at a, b, c, d, e and f shown on a Tetrahedral element. (*quadrature q = 1)*

terms inside each tetrahedron. An interface pressure is introduced at each interface depending on position of continuity parameterized by quadrature q (just like 2D case presented in section C.1 and C.2). These interface pressures along with cell-vertex pressures are used to estimate pressure gradient inside each of the control-volumes in the tetrahedron which can then be used to estimate velocity at each interface. The velocities are used to estimate the fluxes at each interface. The flux across an interface should be the same when calculated with properties of the control-volumes on either side of the interface. This condition is satisfied by forcing the velocities normal to interface to be same on both sides (pointwise continuity condition, where the point of continuity is determined by quadrature - q).

Single phase flow rate, for a fluid of unit viscosity μ_p and unit formation volume factor B_p, across interface a (i.e the interface on which a lies), based on the velocity in region 1 is

$$\begin{aligned} f_{1a} &= -\int_a \vec{v_1}\cdot\vec{n_a}dA = -A_a\vec{v_1}\cdot\vec{n_a} \\ &= A_a[v_{1x}n_{xa} + v_{1y}n_{ya} + v_{1z}n_{za}], \end{aligned} \tag{C.44}$$

where n_a is the outward normal on the interface a with node 1 considered as an inside point. A positive value of f signifies flow into the block while negative value signifies flow out of the block. Single phase velocity in region $i(\ i = 1,..,4)$ is given by:

$$\begin{aligned} \vec{v_i} &= -[K_i\nabla\phi_i] \\ &= -\begin{pmatrix} K_{i_{xx}} & K_{i_{xy}} & K_{i_{xz}} \\ K_{i_{yx}} & K_{i_{yy}} & K_{i_{yz}} \\ K_{i_{zx}} & K_{i_{zy}} & K_{i_{zz}} \end{pmatrix} \begin{pmatrix} \phi'_{ix} \\ \phi'_{iy} \\ \phi'_{iz} \end{pmatrix}, \qquad i = 1,...,4 \end{aligned} \tag{C.45}$$

To estimate the pressure gradients in the above equations we assume that potential varies linearly in region $1,...4$ of the tetrahedron. And this gives following equations:

$$\begin{aligned} \phi_a &= \phi_1 + (x_a(q) - x_1)\phi_{1x} + (y_a(q) - y_1)\phi_{1y} + (z_a(q) - y_1)\phi_{1z} \\ \phi_b &= \phi_1 + (x_b(q) - x_1)\phi_{1x} + (y_b(q) - y_1)\phi_{1y} + (z_b(q) - y_1)\phi_{1z} \\ \phi_c &= \phi_1 + (x_c(q) - x_1)\phi_{1x} + (y_c(q) - y_1)\phi_{1y} + (z_c(q) - y_1)\phi_{1z} \end{aligned} \tag{C.46}$$

Which gives

$$\begin{pmatrix} \phi_{1x} \\ \phi_{1y} \\ \phi_{1z} \end{pmatrix} = \begin{pmatrix} (x_a(q) - x_1) & (y_a(q) - y_1) & (z_a(q) - z_1) \\ (x_b(q) - x_1) & (y_b(q) - y_1) & (z_b(q) - z_1) \\ (x_c(q) - x_1) & (y_c(q) - y_1) & (z_c(q) - z_1) \end{pmatrix}^{-1} \begin{pmatrix} \phi_a - \phi_1 \\ \phi_b - \phi_1 \\ \phi_c - \phi_1 \end{pmatrix} \tag{C.47}$$

Hence the equation C.47 can be written as

$$\begin{pmatrix} \phi_{1x} \\ \phi_{1y} \\ \phi_{1z} \end{pmatrix} = \begin{pmatrix} A(q)_{x1} & A(q)_{x2} & A(q)_{x3} \\ A(q)_{y1} & A(q)_{y2} & A(q)_{y3} \\ A(q)_{z1} & A(q)_{z2} & A(q)_{z3} \end{pmatrix} \begin{pmatrix} \phi_a - \phi_1 \\ \phi_b - \phi_1 \\ \phi_c - \phi_1 \end{pmatrix} \tag{C.48}$$

In a similar manner expressions for region 2, 3 and 4 are obtained. In region 2 pressure at points a,d and e (which are function of quadrature - q)are expanded about the pressure at node 2, in region 3 pressure at points b,d and f are expanded about node 3 and in region 4 pressure at points c, e and f are expanded about node 4. Using these expression like above the pressure gradient in each of the remaining three regions can be obtained and can be given as:

$$\begin{pmatrix} \phi_{2x} \\ \phi_{2y} \\ \phi_{2z} \end{pmatrix} = \begin{pmatrix} B(q)_{x1} & B(q)_{x2} & B(q)_{x3} \\ B(q)_{y1} & B(q)_{y2} & B(q)_{y3} \\ B(q)_{z1} & B(q)_{z2} & B(q)_{z3} \end{pmatrix} \begin{pmatrix} \phi_a - \phi_2 \\ \phi_d - \phi_2 \\ \phi_e - \phi_2 \end{pmatrix}, \tag{C.49}$$

$$\begin{pmatrix} \phi_{3x} \\ \phi_{3y} \\ \phi_{3z} \end{pmatrix} = \begin{pmatrix} C(q)_{x1} & C(q)_{x2} & C(q)_{x3} \\ C(q)_{y1} & C(q)_{y2} & C(q)_{y3} \\ C(q)_{z1} & C(q)_{z2} & C(q)_{z3} \end{pmatrix} \begin{pmatrix} \phi_b - \phi_3 \\ \phi_d - \phi_3 \\ \phi_f - \phi_3 \end{pmatrix}, \tag{C.50}$$

and

$$\begin{pmatrix} \phi_{4x} \\ \phi_{4y} \\ \phi_{4z} \end{pmatrix} = \begin{pmatrix} D(q)_{x1} & D(q)_{x2} & D(q)_{x3} \\ D(q)_{y1} & D(q)_{y2} & D(q)_{y3} \\ D(q)_{z1} & D(q)_{z2} & D(q)_{z3} \end{pmatrix} \begin{pmatrix} \phi_c - \phi_4 \\ \phi_e - \phi_4 \\ \phi_f - \phi_4 \end{pmatrix}. \tag{C.51}$$

Flow rates across the interfaces are based on the velocities at the points a, b, c, d, e and f. As mentioned earlier, velocities normal to the interface should match at these points on both sides of the interface. Hence six continuity equations are formed, one at each of the points. The continuity equations at points a, b, c, d, e and f are:

$$
\begin{aligned}
\vec{v_1} \cdot \vec{n_a} &= \vec{v_2} \cdot \vec{n_a} \\
\vec{v_1} \cdot \vec{n_b} &= \vec{v_3} \cdot \vec{n_b} \\
\vec{v_1} \cdot \vec{n_c} &= \vec{v_4} \cdot \vec{n_c} \\
\vec{v_2} \cdot \vec{n_d} &= \vec{v_3} \cdot \vec{n_d} \\
\vec{v_2} \cdot \vec{n_e} &= \vec{v_4} \cdot \vec{n_e} \\
\vec{v_3} \cdot \vec{n_f} &= \vec{v_4} \cdot \vec{n_f}
\end{aligned} \tag{C.52}
$$

respectively, where $\vec{n_a}, \vec{n_b}, \vec{n_c}, \vec{n_d}, \vec{n_e}$, and $\vec{n_f}$ are outward normals on face a, b, c, d, e and f respectively. The following variables, for $u = x, y$ and z, are now defined:

$$
\begin{aligned}
F_{ua_i} &= K_{xu_i} n_{x_a} + K_{yu_i} n_{y_a} + K_{zu_i} n_{z_a}; \qquad i = 1, 2, \\
F_{ub_i} &= K_{xu_i} n_{x_b} + K_{yu_i} n_{y_b} + K_{zu_i} n_{z_b}; \qquad i = 1, 3, \\
F_{uc_i} &= K_{xu_i} n_{x_c} + K_{yu_i} n_{y_c} + K_{zu_i} n_{z_c}; \qquad i = 1, 4, \\
F_{ud_i} &= K_{xu_i} n_{x_d} + K_{yu_i} n_{y_d} + K_{zu_i} n_{z_d}; \qquad i = 2, 3, \\
F_{ue_i} &= K_{xu_i} n_{x_e} + K_{yu_i} n_{y_e} + K_{zu_i} n_{z_e}; \qquad i = 2, 4, \\
F_{uf_i} &= K_{xu_i} n_{x_f} + K_{yu_i} n_{y_f} + K_{zu_i} n_{z_f}; \qquad i = 3, 4.
\end{aligned} \tag{C.53}
$$

The expressions for pressure gradients from equations C.48,C.49,C.50 and C.51 are put into the expressions for velocities in equation C.45. The resulting expressions are put into the set of continuity equations C.52. The coefficients of interface pressure and cell vertex pressures are then collected in the continuity equations and following equation (in matrix form) results:

$$
A_L \Phi_f + B_L \Phi_v = A_R \Phi_f + B_R \Phi_v \tag{C.54}
$$

where $\Phi_f = [\phi_a, \phi_b, \phi_c, \phi_d, \phi_e, \phi_f]'$ and $\Phi_v = [\phi_1, \phi_2, \phi_3, \phi_4]'$. From equation C.31 interface pressures Φ_f can now be eliminated by expressing them in terms of vertex

pressures Φ_v. After eliminating interface pressures the flux coefficient matrix can then be written in a similar manner as:

$$F = (A_L((A_L - A_R)^{-1}(B_R - B_L)) + B_L)\Phi_v \tag{C.55}$$

Once the fluxes are computed using equation C.55 global assembly follows.

Author's Publications

1. Mayur Pal and M.G.Edwards, *Convergence study of a family of flux-continuous, finite-volume schemes for the general tensor pressure equation*, 13^{th} International Congress on Finite Element for Flow Problems. Proceedings of FEF05 IACM Special Interest Conference supported by ECCOMAS, University of Wales Swansea, 4-6 April 2005.

2. Mayur Pal, Michael G. Edwards, Anthony R. Lamb, *Convergence study of a family of flux-continuous, finite-volume schemes for the general tensor pressure equation*, International Journal for Numerical Methods in Fluids 2005 - Vol. 51, Issue 9-10, Pages 1177 - 1203,2006.

3. Mayur Pal and M.G.Edwards, *Effective Upscaling Using Family of Flux-continuous Finite-Volume Schemes for Pressure Equation*, Proceedings of a Joint Conference of the Association for Computational Mechanics in Engineering (UK) and the Irish Society for Scientific and Engineering Computation, Cecil G. Armstrong (Ed.), Queen's University Belfast, 19-20 April 2006.

4. Mayur Pal and M.G.Edwards, *Family of Flux-continuous Finite-volume Schemes with Improved Monotonicity and Convergence*, In Proceedings of ECMOR X 2006, Amsterdam, The Netherlands.

5. Mayur Pal and M.G.Edwards, *Flux-Splitting Schemes for Improved Monotonicity of discrete solution of elliptic equation with high anisotropic coefficients*, In Proceedings ECCOMAS CFD 2006, Egmond Aan Zee, The Netherlands.

6. Mayur Pal and M.G.Edwards, *Flux-Splitting Schemes for Improved Monotonicity of discrete solution of elliptic equation with high anisotropic coefficients*, International Journal for Numerical Methods in Engineering, Submitted 2006.

7. Mayur Pal and M.G.Edwards, *Quasi-Monotonic Continuous Darcy-flux Approximation for General 3-D Grids of Any Element Type*, SPE Reservoir Simulation Symposium, Houston, Texas-USA, Feb 2007.

8. Mayur Pal, D.Gupta, M.G.Edwards and C.J.James, *Flux-continuous schemes for solving EEG source localization problems*, In ACME 07 Conference Proceeding, Scotland, 2nd - 3rd April 07.

Publications Co-Authored

1. M.G.Edwards and Mayur Pal, *Positive Definite q-Families of Continuous Subcell Darcy-Flux CVD(MPFA) Finite Volume Schemes and the Mixed Finite Element Method*, International Journal for Numerical Methods in Fluids, Accepted 2007.

2. M.G.Edwards and Mayur Pal, *Symmetric Positive Definite Subcell CVD Schemes on Cell-Centred Quadrilateral Grids*, In Proceedings of ECMOR X 2006, Amsterdam, The Netherlands.

3. M. G. Edwards, Mayur Pal and Hongwen Zheng , *Quasi-Monotonic Variable Support (q1,q2)families of Continuous Darcy-Flux CVD(MPFA) Finite Volume Schemes*, SIAM Journal on Sci. Comp), Submitted 2007.

4. H.Zheng, M.G.Edwards and Mayur Pal., *Flux-continuous finite volume schemes with full pressure continuity*, In ACME 07 Conference Proceeding, Scotland, 2nd - 3rd April 07.

There is an unalterable law governing every thing and every being that exist or lives. I may not deny the law or law giver, because I know so little about it or him. God to be God must rule the heart and must transform it. It is proved, in the transformed conduct and character of those who have felt the real presence of god within. In the mist of death life persist, in the mist of untruth truth persist, in the mist darkness light persist, hence, I gather that god is life, truth light, he is love, he is the supreme good. **- M.K.Gandhi**